Geodynamic and Seismological Investigation of the South Hellenic Arc Structure

By

Georgios Chatzopoulos

Student ID: 1137510

Dissertation submitted in partial fulfilment for the degree of
Doctor of Philosophy

Department of Civil Engineering & Environmental Engineering
Brunel University London

September 2018

Abstract

This thesis examines foreshock and aftershock seismicity patterns with the accelerated seismic release model and the non-extensive statistical physics approach in the South Aegean. The convergence and subduction of the African lithosphere under the Aegean Sea plate creates the seismically active Hellenic Arc. Strong earthquakes occur frequently, with evidence of a great magnitude earthquake in the past. To evaluate and understand the large earthquake likelihood, the accelerated seismic release model (ASR) has been used as hazard estimation technique. This method uses a power law equation to quantify the cumulative energy release (or Benioff strain, or number events) from the earthquakes that occur before the large event. The mainshocks are considered as critical points while the foreshocks are evolution pattern of the critical phenomena. A theoretical model to explain the earthquake preparation process has been proposed. This is based on the energy conservation laws and non-extensive statistical physics. The analytic expressions of the proposed model indicate the existence of a common critical exponent in the ASR power law equation. In addition, the critical exponent is independent from the measured quantity and reflects the physical parameters of the critical area, such as the Euclidian dimension, the Guttenberg-Richer *b-value* and the extensivity of the system during the large earthquake preparation period. The evaluation of the proposed model has been carried out with the identification of the critical areas for three strong events in South Aegean with retrospective analysis.

The two strong event aftershocks of 2013 and a swarm sequence occurred in 2016 have been located and relocated in order to evaluate the spatiotemporal attributes of these sequences. Cross sections and fault plane solution provided in the examination of the spatial distribution of the events. By combining the detailed aftershock and foreshock catalogues, it is possible to better understand the activation mechanisms. Also, the time differences between two continuous earthquakes (interevent time) has been examined with the ideas of non-extensive statistical physical. The results suggest that a distribution of the entropic index q could explain the extensivity of the system as the q value varies with time. The use of the non-extensive statistical physics has clearly helped to better understand the behaviour of the seismicity patterns.

Acknowledgements

This work was implemented through the project IMPACT-ARC in the framework of action “ARCHIMEDES III–Support of Research Teams at TEI of Crete” (MIS380353) of the Operational Program "Education and Lifelong Learning" and is co-financed by the European Union (European Social Fund) and Greek national funds

This work was supported by the THALES Program of the Ministry of Education of Greece and the European Union in the framework of the project “SEISMO FEAR HELLARC’’, (MIS 380208).

This work was supported by ‘HELPOS – Hellenic System for Lithosphere Monitoring, Greece’’ (MIS 5002697) which is implemented under the Action ‘‘Reinforcement of the Research and Innovation Infrastructure’’, funded by the Operational Programme ‘‘Competitiveness, Entrepreneurship and Innovation, Greece’’ (NSRF 2014–2020) and co-financed by Greece and the European Union (European Regional Development Fund.

Table of Contents

Chapter 1 Introduction

This thesis' focus is to provide an examination of foreshock and aftershock seismicity patterns guided by these questions:

- Can the hazard associated with large earthquakes in subduction zones be better understood? Is there a relationship between foreshock sequences and major earthquakes?
- What is the nature of the relationship between foreshocks and major events in South Aegean?
- Can a generalized model of Tsallis entropy explain the accelerating-decelerating seismicity patterns in South Aegean?
- Can the aftershock sequences be correlated with the foreshock patterns?
- Can the aftershock and the swarm type sequence characteristics be explained by complexity theories?
- What could the process be for assessing future earthquake hazards in South Aegean?

The Hellenic Arc is the most seismically active region in Europe due to the subduction of the oceanic African lithosphere beneath the Eurasian plate, a tectonic regime shaped faults capable for great magnitude earthquakes (figure1.1) (McKenzie, 1972; Le Pichon & Angelier, 1979; Papazachos, 1990; Papazachos, et al., 2005; Le Pichon & Kreemer, 2010; Giardini, et al., 2013). It is an arcuate feature extending from the Peloponnese in the northwest to the Crete Island in the south and Rhodes Island in the northeast (Lyon-Caen, et al., 1988; Papazachos, et al., 2002). Crete lies in a prominent position in the fore-arc of the Hellenic subduction zone. It is located on top of the shallow portion of the presently active region of convergence. This reason makes Crete an excellent onshore observation point for the internal structure of the fore-arc at various depths.

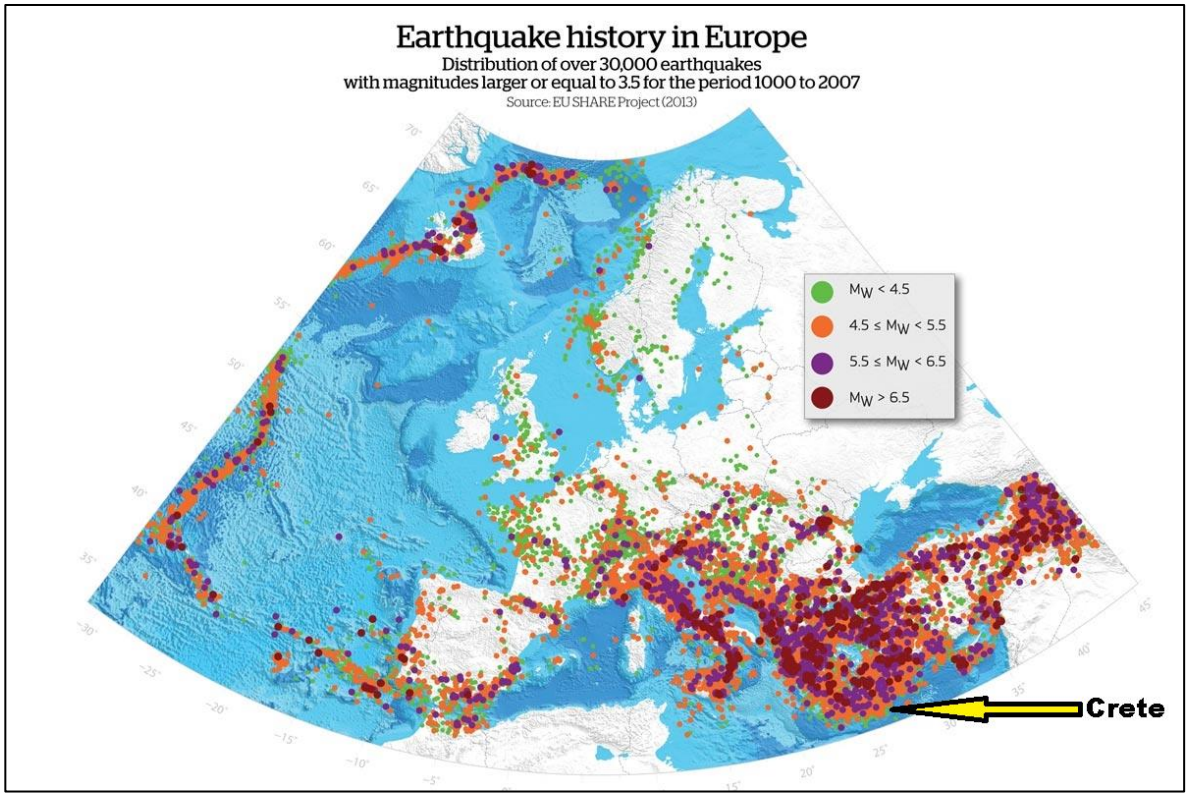

Figure 1.1 The spatial distribution and the magnitude of earthquakes in Europe. Image from (Giardini, et al., 2013)

The collision of continents is dominant in plate tectonic related features in the Hellenic Arc, yet not fully understood, especially in this complex region where the underlying structure is considered three-dimensional. Due to the plates motion there is an increased risk in the areas near the subduction zone to be affected by large earthquakes (figure 1.2). The seismic hazard is a function of the earthquake magnitude and the probability of a large event to occur. The development of a near real-time estimation method of the seismic hazard is a prominent feature of this area. This has the potential to enable the determination of the time dependent seismic hazard based on the study of accelerating seismicity phenomena at the scale of the South Aegean. The concept is that the earthquake generation process is a critical phenomenon, culminating in a main event that corresponds to some critical point (Saleur, et al., 1996; Sornette & Sammis, 1995; Bowman, et al., 1998; Rundle, et al., 2000). Fundamental prediction of this hypothesis is that, before it reaches the critical

point, a regional system of faults goes through a characteristic period of accelerating seismicity. The increased seismic release prior to a large event can be described by a power law time-to-failure relation (Varnes, 1989; Bufe & Varnes, 1993). The small and medium events are related to the "correlation length" increase of the regional microfracturing whereas the main event represents the critical point where rupture nucleates at all scales.

In this thesis, the hazard estimation model has been based on the accelerating seismicity release model as well as on the common critical exponent criterion derived by the proposed model. The new approach to produce a time dependant seismic hazard model is based on the energy conservation law and the non-extensive statistical physics. The evaluation of the model has been carried out with past data catalogues that have been revised. According to the risk assessment flowchart (figure 1.2), the earthquake catalogues are the primary tool to investigate the spatiotemporal evolution of the seismicity. The accurate earthquake parameters estimation and the data completeness of the seismicity catalogue are necessary for this hazard estimation method. In addition, an investigation to evaluate the spatiotemporal attributes of two strong event aftershock sequences in 2013 and a swarm sequence that occurred in 2016 has been carried out. The earthquakes have been located and relocated in order to examine their spatial distribution of the events and examine the temporal characteristics using non-extensive statistical physics.

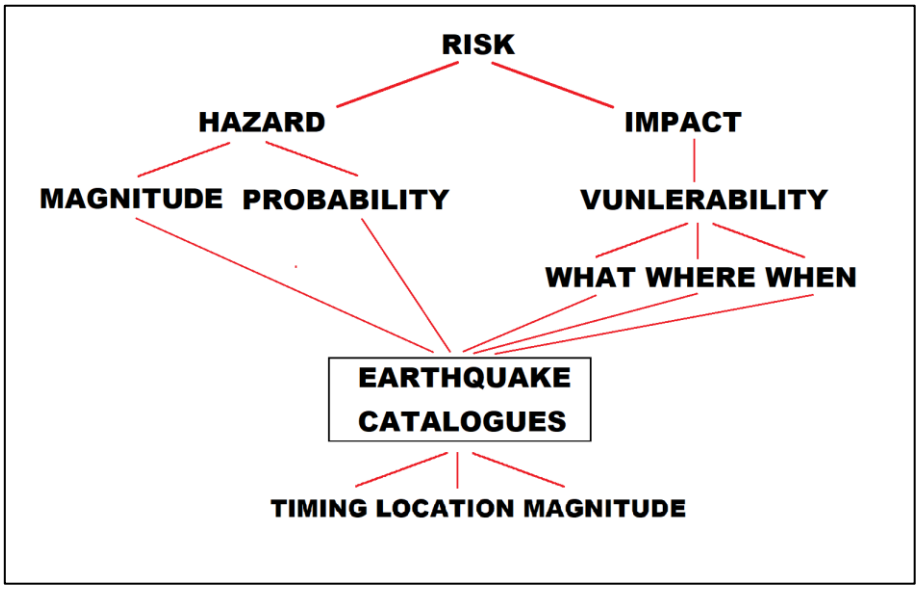

Figure 1.2 The seismic risk assessment flowchart developed for this research.

Chapter 2 Basic Theories - Literature Review

2.1 General Geophysics – Seismology

2.1.1 Tectonic boundary types

The tectonic plates theory starts early in 1620, when Francis Bacon noticed and published the observation that there is a shape similarity between the continental shelf of west Africa and the east part of South America. This observation was enough to inspire different group of scientists to investigate the possible past locations of the continents and the relative motions that led to the present-day shape (Donaldson, 2016). The tectonic plates theory describes very well the mechanisms that shapes earth's outer layers. It is considered that a plate can travel without experiencing significant deformation in the interior part of the plate due to the rigidity of materials. There are areas that have remain unchanged in terms of deformation since the Precambrian Eon, these areas are known as cratons (Grotzinger & Jordan, Thomas, 2010). However, on the edge of these blocks there are zones where different interactions can occur such as volcanic activity or earthquakes. These areas are known as plate boundaries (Morgan, 1968; Dewey, 2016). The boundaries between the tectonic plates have been defined mainly by using the location of earthquakes that occur on areas where stress can build up and then be abruptly released (Isacks Bryan, 1968). The detailed mapping of epicentres on a global scale has allowed researchers to distinguish the number of plates. The number of lithospheric plates varies in the literature. It is broadly accepted that there are seven large plates and a considerable number of smaller ones. Regardless the classification of plates, the important aspect is than not all boundaries are the same type. There are three categories based on the relative motion between them (Morgan, 1968; Turcotte & Schubert, 2002; Fowler, 2005):

A. Convergent lithospheric plate boundaries

The tectonic margins shaped when two lithospheric plates move toward to each other are known as *convergent* boundaries. The expected consequence of this block approach is the

tectonic collision of the plates. This kind of margin is considered as a destructive type because the colliding plates produce significant deformations in lithosphere. Usually one of the two plates, is submerging under the other into the mantle which consists of denser and more compressible materials. A progressive increase in temperature and pressure with depth exist in mantle. In the descending parts of the lithosphere, the materials are heated by the friction that is developing between the colliding rocks. The additional heat of the mantle helps the destruction of the subducted plate. The lithospheric part entering the mantle is under a gravitational force. Because the lithosphere is acting like elastic material, the stress is also transmitted to the surface part pulling it downwards. This act is known as *slab pull* and creates an extensive force field with normal faults (Conrad & Lithgow-Bertelloni, 2002). In the upper part of ocean trench, there are formed some masses from friction forces known as accretionary prisms, mainly consisted by the top part of the sea floor basalt and the overlying sediments which have been detached from the sinking slab. Another common tectonic feature which is observed in convergent boundaries is the relative newformed volcanic arcs. It is very common to observe high seismicity rates in these regions and earthquakes at great depth. The tectonic plates can be classified in two categories based on the material that consist them. The first type are the oceanic plates, formed from oceanic floor in mid ocean ridges, with basaltic type rocks and the overlying sediments. The second one is the continental plates consisted by continental crust with granitic type masses and the analogous sediments. Depending on the approaching plates materials, the results of the collision can form three possible tectonic regimes:

i. An oceanic plate approaches another oceanic plate

ii. An oceanic plate subducts under a continental plate

iii. A continental plate approaches another continental plate.

B. Divergent lithospheric plate boundaries

Harry Hess suggested that the mantle's convection currents are responsible for the sea floor spreading in mid-ocean ridges (Hess, 1962). The sea floor spreading causes the two

lithospheric plates move apart from each other in the divergent margins, but this discovery is considered as the fourth and final stage of the continental rifting process. The first stage of the ocean opening mechanism was a subject that drew much attention and a lot of scientists contributed to explain it. Among the possible contributions the most acceptable hypotheses are two. The one was proposed from Wilson in 1966 considering the opening of the continental crust as a result of tensional stress that stretch and cracked the lithosphere, which is consider as *passive rifting* since the acting force is applied by a far-field extension (Wilson, 1966). The other theory is introduced by Buck in 1991, which involves compressional forces that are developed from the upward motion of mantle's magma (Buck, 1991). This squeeze type action is thinning the crust and move apart of the continental blocks which categorizes the oceanogenesis mechanism as a product of *active rifting*. Whether it is an active or a passive rifting or not, after the lithosphere is lengthened and thinned, the existence of normal faults shapes a tectonic graben which is known as *rift valley.* The erosion and the additional extension of the crust widens the graben and gradually make it deeper until it reaches seawater level and covered by water which forms a small basin. In the next stage the elevated mantle's material is pushing away the lithosphere and takes its place. Due to the lower temperature occurring in the crust and atmosphere, the hot magma is slow cooling, solidifies and create new rocks.. The last stage of the spreading process, is the formation of well know mid-ocean ridge, an area where new ocean floor is produced and spread symmetrically and parallel on both sides of ridge crest.

C. Transform plate boundaries

The last type of plate margins can characterized by a conservative behaviour as the two plates that are in contact move in the same relative direction to opposite azimuth. This kind of motion, where the two tectonic plates have only lateral fracture and there is no change in the size of the plate, shapes the transform plate boundaries (figure 2.1.6a). This opposite direction motion is the reason for the formation of long (up to hundreds of kilometres in length) almost vertical angle faults like the San Andreas Fault in California, U.S.A. which is probably the most well-known example of transform faults.

2.1.2 Faults – Focal Mechanisms

A fracture in the rocks caused by brittle failure relative with a displacement is known as *fault* and its motion is related to the acting force field, which can be compressional or tensional (Allaby, 2013). The faults have length varies from a few centimetres to many hundreds of kilometres. The fracture has a direction which is measured as an azimuth on horizontal plane know as *strike,* an angle relative to the horizontal plane called *dip* while the *rake* is the direction of block which is related to stress field (Allaby, 2013; Aki & Richards, 1980). In the case of the incline faults the upper moving blocks is called the hanging wall and the lower one is the footwall. There are four fault categories which are function of angle of dip and their relative displacement (Aki & Richards, 1980). The first are the normal faults which are typical products of an extensional field, the hanging wall moves downwards in respect with the footwall, a typical dip is 45° and the rake value for pure normal fault is -90°. The second category are the reverse faults which are developed from compressional stress regimes, the in this case the stress is pushing the hanging wall to move upwards and the expected rake values are at 90°. The other category refers to the strike-slip type with vertical dip, while the rake 0° or 180° denotes if the fault is left or right lateral respectively. Usually the faults are a combination of a strike-slip fault and a normal or reverse fault known as oblique faults, which are typically formed by integration of shearing and tensional or compressional forces at the same time. The fault slip that occurs during an earthquake is usually calculated by *P* waves first-motion direction and it is described by the focal mechanism (or moment tensor or beachball or fault plane solution) which is a representation of a second order tensor with nine dipoles of forces that depends on the source strength and the fault orientation (figure 2.1.8) (Aki & Richards, 1980; Udias, 1999).

In the recent work by Thingbaijam, et al. (2017) the source parameters for various tectonic regimes have been estimated with the general orthogonal regression method (Fuller, 1987) which is considered as a more robust approach (Castellaro, et al., 2006; Lolli, et al., 2014). The ordinary least squares method is simple to use but the assumption that the independent variable has insignificant uncertainty, is a major drawback to apply in magnitude

comparison dataset. The GOR method consider that the two variables have different uncertainties (Lolli & Gasperini, 2012).

2.1.3 Elastic waves propagation and velocities

The elastic deformations are distributed in the interior of earth with the *Body waves* consisted by the Primary (P) which is the first waves arriving to a monitoring station and Secondary (S) waves which comes after the *Primary* (Timoshenko, 1953). In the *Primary waves* the particles vibrate parallel to the travel direction, this motion that generates consecutive expansions and compressions in the traveling medium and for that reason they are also called compressional waves. In the *Secondary waves* the particles of the continuum oscillate vertical to the travel direction and due to this motion, they are known as shear waves. Another category of seismic waves are the *Surface waves* which are a product of the energy transfer by the *P* and *S* waves in the free surface above the medium (Udias, 1999). In the (Pujol, 2003; Udias, 1999) or any other seismic wave related geophysical book, it is described the theoretical background and assumption to derive the equations for the seismic wave velocities. This approach is based on taking the equation of motion for the deformed particles, the law of elasticity (Hooke 1660) and the strain tensor and displacement relation into account to obtain an equation that express the motion of the particles in an elastic medium. The elastic wave equation for the *Primary (V_P)* and *Secondary (V_S)* waves are:

$$V_P = \sqrt{\frac{(\lambda+2\mu)}{\rho}} = \sqrt{\frac{(3k-2\lambda)}{\rho}} \tag{2.1.1}$$

$$V_S = \sqrt{\frac{\mu}{\rho}} = \sqrt{\frac{3(k-\lambda)}{2\rho}} \tag{2.1.2}$$

The λ is the Lame constant, the μ is the Shear modulus, the *k is* the Bulk modulus and ρ the density (Sheriff, 1984).

2.1.4 Earthquake magnitudes

In 1902, the Italian volcanologist Giuseppe Mercalli modified the Rossi–Forel scale and added two intensity levels to make the well-known Mercalli intensity scale (Tiedemann, 1992). The first instrumental scale, well-known and still in use today, was the local magnitude M_L presented in 1935 by the American seismologist Charles Francis Richter along with the contribution of the American seismologist Harry O. Wood (Richter, 1935). There different ways to express the magnitude of the earthquakes, most of them are based on the measuring the amplitude for a specific part of the seismic waves (Woessner, et al., 2010). A scale that does not get saturated was proposed by (Kanamori, 1977; Hanks & Kanamori, 1979). As the previous scales measures the logarithm of the amplitude, this one differs because it measures the logarithm of the seismic movement (Kanamori, 1983; Scordilis, 2006; Woessner, et al., 2010):

$$Mw = \frac{2}{3}\log_{10}(M_0) - constant \qquad (2.1.3)$$

The M_0 is the seismic moment the constant is 6.06 for Newton meters and 10.7 for dyne centimetre.

2.1.5 Gutenberg-Richer & Omori scaling laws

The well-known Gutenberg Richer law, that associates for an earthquake population the rate of appearance events with a specific magnitude, it is considered as one of the most important relationship in seismology (Gutenberg & Richter, 1954):

$$N(\geq Mag) = 10^{a-bMag} \qquad (2.1.4)$$

The *b-value* has been studied by various independent researchers and some of the findings are recapitulated here:

- At laboratory triaxial test, as the stress increases in the rocks the *b-value* tends to decrease (Scholz, 1968)
- The b-value reflects the heterogeneity of the Earth's interior (Mogi, 1962).
- The b-value not only decreases before the fracture of specimens but also before large earthquakes and it can associated with critical point theory (Amitrano, 2012).
- As the b value gets higher the more often small magnitude earthquakes occur. The *b-value* has been correlated with the fault type, the smallest values appear in reverse faults, the strike-slip has average values while the largest exist on normal faults (Schorlemmer, et al., 2005)
- For the California region the *b*-value becomes higher with the increase of depth (Mori & Abercombie, 1997)
- The typical *b-value* for aftershocks in the Aegean region has a mean value 1.0 ±0.2 (Kourouzidis, 2003). Studies in Japan suggest that the b-values varies from 0.7 to 1.4 for aftershock sequences (Guo & Ogata, 1997)
- The small *b-values* in aftershock sequence might indicate that the aftershock sequence may have not fully released the accumulated energy (Peng, 2011).
- The Magnitude of completeness controls the G-R law frequency magnitude distribution slope and the *a* and *b-values* (Wiemer & Wyss., 2000).

Considering the Gutenberg-Richter's law as the most important relation for the seismology, then the second most important is the Omori's law. This law explains the decay behaviour of the aftershock sequences as it connects the aftershock frequency $F(t)$ that occurred in a time window at time t, N number of aftershocks with magnitude ≥ magnitude of completeness and the d (days) is the time delay, a parameter that is used to apply correction for the missing data (Omori, 1894; Utsu, et al., 1995; Kagan & Houston, 2005; Utsu, 1961; Peng, 2011):

$$\mathrm{F}(t) = \frac{N}{t+d} \qquad (2.1.5)$$

It has been proposed (Utsu T. , 1961) that modified Omori's law is modified by introducing the parameter *p,* which measures the decay rate:

$$F(t) = N/(t+d)^p \quad (2.1.6)$$

Utsu et al. 1995 propose that the *p-values* vary from 0.9 up to 1.4 being controlled by parameters such as the heterogeneites of the crust's materials, the build up stress and the temperature. A typical *p-value* for the aftershocks on the Aegean area is 1.0 ±0.2 (Kourouzidis, 2003). Similar results have been found for the California region, mean value 1.08 (Reasenberg & Jones, 1989; Guglielmi, 2016) and for two Nepal aftershocks sequences 1.01 and 0.95 (Chingtham, et al., 2016).

2.2 Accelerated Seismic Release (ASR)

2.2.1 Criticality

The risk associated with the energy release of the large earthquakes inspired scientists to investigate the various preseismic indicators. For many years scientists have tried to predict earthquakes with different methods, mainly relying on the spatial and temporal variation of the seismic activity rate (e.g. Jones and Molnar, 1979; Papazachos, 1973). One of these methods supports the idea that during the large earthquake preparation process, there is an interval where an anomalous increase in the intermediate magnitude earthquake population (Accelerating Seismic Release-ASR) is observed (Papazachos & Papazachos, 2000; De Santis, et al., 2010; Mignan, et al., 2006; Papadopoulos & Minadakis, 2016) and others. The core idea of accelerated deformation theory is that on a stressed area there are some earthquakes usually 2 orders smaller than the large event (Bufe & Varnes, 1993) that they will contribute with seismic energy release to the preparation process of a large event. The abnormal increase of the energy flow inspired researchers to quantify this phenomenon and a significant number of empirical models aiming to explain the Accelerating Seismic Release have been proposed. Historically, the first attempt was made by Gerasimos Papadopoulos in 1988. His work considered the increase of foreshocks number occurred before large earthquakes in western Hellenic Arc region (Papadopoulos, 1988). David Varnes (1989) explored the subcritical extension theory, where the small cracks in rocks under constant pressure expand rapidly before the origin of the main fracture, with the ASR

model (Varnes, 1989). This process describes a model that follows the critical point theory (Sornette & Sornette, 1990; Rundle, et al., 2000), where the small cracks behave as the critical phenomena while the main fracture that terminates the process acts as the critical point. He also proposed a differential power law equation that expresses seismic energy release in terms of the inverse power of the time before a large event. The combined effort of Bufe and Varnes in 1993 to measure the seismic energy release and predict earthquakes in the San Francisco bay, helped to correlate the Benioff stain release with a power law time to failure relation (Bufe & Varnes, 1993):

$$Bs(t) = Bs_f - \frac{k}{m}(t_f - t)^m \qquad (2.2.1)$$

where the t_f is the origin time of the mainshock and Bs_f is the Benioff strain when $t = t_f$. Since then, the ASR model has been tested and altered by various independent scientists : (Papadopoulos, 1986; Bowman, et al., 1998; Varnes, 1989; Bufe & Varnes, 1993; Brehm & Braile, 1999; Papazachos & Papazachos, 2000; Rundle, et al., 2000; Tzanis, et al., 2000; Bowman & King, 2001; Papazachos & Papazachos, 2001; Di Giovambattista & Tyupkin, 2001; Di Giovambattista & Tyupkin, 2004; Papazachos, et al., 2002; Tzanis & Vallianatos, 2003; Scordilis, et al., 2004; Papazachos, et al., 2005; Mignan, et al., 2006; Mignan, et al., 2007; Mignan, 2008; Mignan & Di Giovambattista, 2008). Typically, the ASR analysis was retrospective, usually after a large earthquake, although there were few attempts for prediction though not all of them were successful.

The Accelerating Seismic Release model is based on the theory that the large magnitude earthquakes are generated by the summary of the energy release which is produced by several moderate size events. Based on the observation, above the ASR idea and the power law time-to-failure has been correlated with critical point concept. The preparation of an earthquake was described as a critical phenomenon that leads to a critical point which is the main earthquake occurs when fracturing becomes coherently self-organized at different scales (Sornette & Vanneste, 1992; Rundle, et al., 2000; Sornette & Sornette, 1989; Sornette & Sornette, 1990). Furthermore, the Accelerating Seismic Release hypothesis has been associated with the phase transitions theory and spinodals lines where the fault

failures are the product of a continuous evolving and correlated system (Rundle, et al., 2000). This approach also considers the earthquakes as a critical phenomenon, which occurs when fracturing becomes coherently self-organized at different scales (Sornette & Vanneste, 1992; Rundle, et al., 2000; Sornette & Sornette, 1989; Sornette & Sornette, 1990).

2.2.2 Non-Criticality

The lack of a sufficient physical model to explain the empirical power law equation of Bufe & Varnes(1993), has inspired a number of scientists to propose their own hypotheses. The Accelerating Seismic Release theory has been correlated with the Coulomb static stress transfer (King & Bowman, 2003; Mignan, et al., 2006; Mignan, 2008; Mignan, 2012). The basic principle of this theory is that every event generates a stress change which is responsible for the triggering of the next event. The Coulomb stress changes (ΔCst) in the stress field during the preparation period (Mignan, 2008b; Mignan, 2012):

$$\Delta Cst = \Delta\tau + \mu(\Delta\sigma + \Delta Po) \qquad (2.2.2)$$

where the $\Delta\tau$ and $\Delta\sigma$ are the shear and normal stress change respectively, μ the friction coefficient and ΔPo the pore pressure changes. The areas with positive ΔCst values generate new earthquakes while in the areas with negative values there is a quiescence. (Mignan, 2008b; Mignan, 2012). There are two techniques to estimate the stress field before the occurrence of the large event. The first one evolves to measure the deformation cause by the loading process while the second one proposed by King & Bowman(2003) is to estimate the stress field by reversing the faults motion (Mignan, 2008b; Mignan, 2012). While a number of scientists accept that the static stress transfer model behaves as a critical point, Mignan(2008b); Mignan(2012) supports that the preparation procedure is due the tectonic loading and the foreshocks are the results of this process.

2.3 Principles of statistical physics

Seismology, especially the part that is related with prediction and risk assessment, is acknowledged as a multidisciplinary science (Udias, 1999). The Brazilian-Greek physicist Constantino Tsallis developed a broader concept of statistical mechanics defined by Boltzmann-Gibbs (Tsallis, 1988) which has been applied in various dynamical systems including the earthquakes (Tsallis, 2009). The physicist Ludwig Boltzmann's initial formula was expressed for thermodynamic systems in equilibrium like ideal gases. The entropy is a measure of disorder, for equal probabilities it explains the possible number of states for a closed system with the formula:

$$S_B = k_B \ln W \tag{2.3.1}$$

where k_B is a constant (ideal gas constant R divided by Avogadro's number N =1.38065 × 10−23 J/K) and W is controlled by the number of states (Schmitz, 2007; Boltzmann, 1896). The American physicist Josiah Willard Gibbs took his formula to estimate the energy changes of a system into account to generalize the Boltzmann's equation (Gibbs, 1902; Schmitz, 2007):

$$S_{BG} = -k_B \sum_{i=1}^{W} p_i \ln p_i \tag{2.3.2}$$

$$with \quad \sum_{i=1}^{W} p_i = 1$$

The S_{BG} is Boltzmann-Gibbs entropy, the p_i is a set of the stage probabilities and W is the total number of possible stages.

For any two probabilistically independent subsystems Ss_1 and Ss_2, i.e. if the joint probability satisfies $p_{ij}^{Ss_1+Ss_2} = p_i^{Ss_1} p_j^{Ss_2} (\forall(i,j))$ then the S_{BG} becomes additive and satisfies the relation (Tsallis, 2009):

$$S_{BG}(Ss_1 + Ss_2) = \sum_i^W S_{BG}(x) \tag{2.3.4}$$

with $W = W_{Ss_1} + W_{Ss_2}$

$$S_{BG}(Ss_1 + Ss_2) = -k_B \sum_{i=1}^{W_{Ss_1}} \sum_{j=1}^{W_{Ss_2}} p_{ij}^{Ss_1+Ss_2} \ln p_{ij}^{Ss_1+Ss_2} \tag{2.3.5}$$

$$S_{BG}(x) = -k_B \sum_{l=1}^{W_x} p_l^x \ln p_l^x \,, \tag{2.3.6}$$

with $x = Ss_1, Ss_{21}$ and $l = i, j$

Hypothetically, the BG entropy can be used on all physical systems with complex behaviour. Important obstacles in this theory are the systems with long-range interactions and multifractal boundary conditions and structures. Focusing on systems with short memory and smooth boundary conditions that follows the BG statistical mechanics, Tsallis proposed Non-Extensive Statistical Physics (NESP) (Tsallis, 1988). The associated generalized entropic form for the discrete case is:

$$S_q = k_B \frac{1-\sum_{i=1}^W p_i^q}{q-1}, q \in R \tag{2.3.7}$$

with $\sum_{i=1}^W p_i = 1$

where S_q is Tsallis entropy and q is the entropic index that represents a measure of the non-extensivity of a system. S_q recovers S_{BG} in the limit $q \to 1$. S_{BG} is additive, whereas S_q ($q \neq 1$) is non-additive. For any two probabilistically independent systems Ss_1 and Ss_2, i.e. if the joint probability satisfies $p_{ij}^{Ss_1+Ss_2} = p_i^{Ss_1} p_j^{Ss_2} (\forall (i,j))$, Tsallis entropy S_q satisfies:

$$\frac{S_q(Ss_1+Ss_2)}{k} = \frac{S_q(Ss_1)}{k} + \frac{S_q(Ss_2)}{k} + (1-q)\frac{S_q(Ss_1)}{k}\frac{S_q(Ss_2)}{k} \quad (2.3.8)$$

The last term on the right part of the equation (2.3.8) controls the non-additivity of the system. If the q has a value less than 1, then the system is over-additive which means that the events with small probabilities (close to 0) becomes more frequent. If the q is larger than 1, then the system is under-additive and the frequent events with large probability (close to 1) are enhanced while if the q is equal with 1 then the system is described by the classic Boltzmann-Gibbs additive entropy (Tsallis, 2001; Vallianatos, et al., 2015; Vallianatos, et al., 2018). In the Michas, et al .(2013); Papadakis, et al .(2013); Vallianatos, et al. (2015); Tsallis (2009) work, it is demonstrated the method to maximize the entropy S_q with the Lagrange multipliers in order to obtain the q-logarithmic function $\ln(x) = (1-q)^{-1}(x^{1-q}-1)$ for a continuous variable x with a probability distribution *p(X) (figure 2.2.1).*

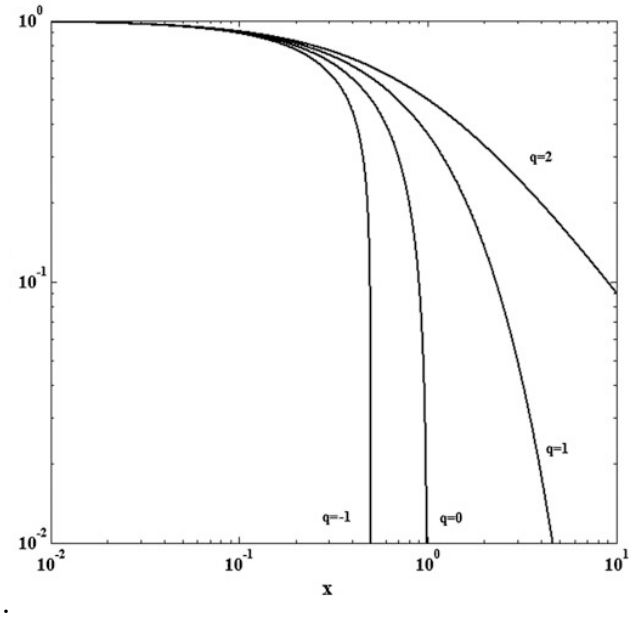

Figure 2.2.1 The log-log plot of the q-exponential distribution for various values of q. Image from (Tsallis, 2009).

2.4 Area of study

2.4.1 Evolution of Hellenic Arc

The Hellenic orogeny was created and developed through geologic time through relentless tectonic processes. Due to its complex geometry and kinematics, it has been a study case that has been considered by numerous independent scientists (Dercourt, 1964; Brunn, 1956; Mercier, 1968; Mountrakis, 2006) and references therein, the work of whom contributes to the following description:

The Hellenic orogen is divided according to orogenetic processes, which is based on the tectonic events that acted over a specific time period, starting in the pre-late Jurassic. In general, the Hellenic orogenesis consists of three arc shaped zones: the Cimmerian in the northern part of Greece, the Alpine in the middle part containing most of the South Aegean Peloponnese as well Crete island, and the Mesogean in the outer part, south from Crete (figure 2.4.1). The first orogenetic episode is dated to the pre-Late Jurassic, and is related to the convergence motions of the Cimmerian continental parts. However, so far research findings do not give a satisfactory conclusion about the relative plates motions. The second orogenesis, the Alpine, started from the Cretaceous and lasted up to the Paleogene. The main reason for this deformation was the convergence of the Apulian microplate to the Cimmerian which is responsible for the subduction Neo-Tethys. In the Alpine orogenesis there are two periods - the first occurred during the Cretaceous and the other one in the Eocene-Oligocene. The most recent orogenetic process is the Mesogean which occurred from Miocene to Pliocene and caused the subduction of the African plate under the Eurasian plate. Generally, the classification of three orogenetic zones does not mean that the limits of each process are strict and there are no effects in other zones. More specifically in the south Aegean, after the Alpine orogenetic process, a series of new tectonic events took place during the place on Tertiary is responsible for the crustal thinning and the formation of the geological windows in the Crete and Peloponnesus that reveal the lower plate units.

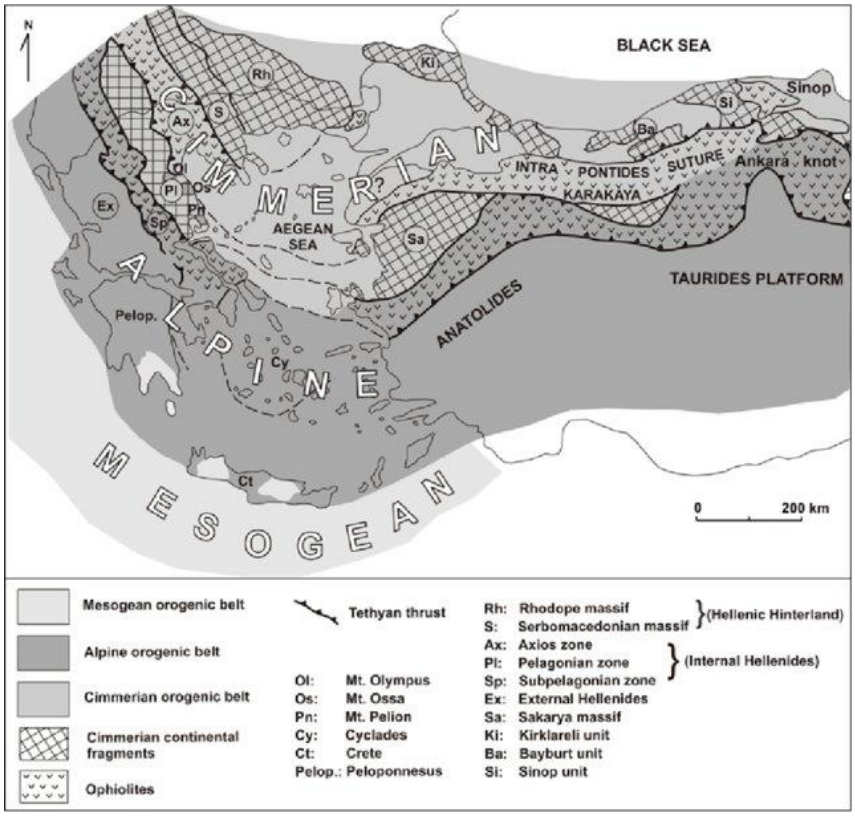

Figure 2.4.1 The three orogenetic belts that acted in the Hellenic region since pre-late Jurassic times, image from (Mountrakis, 2006).

2.4.2 Geodynamics of Hellenic arc

The Hellenic Arc, located in south-eastern Europe, it is a well-known example of a destructive boundary as there are two converging plates which submerge one under the other. In the Cretaceous – Paleogene period, the convergence of Apulian microplate towards the Cimmerian-Eurasian plate was the main reason for the closing, subduction and destruction of the Neo-Tethys ocean (Mountrakis, 2006). During this time period and parallel to the Hellenic Arc, two HP/LT metamorphic events occurred, the first in inner part during the Eocene and second in outer arc in Oligocene-Miocene (Mountrakis, 2006). Eventually the convergence of plates continued to the southern part of Greece near Crete and Peloponnesus and after the full subduction of the Apulian microplate in the Oligocene – Lower Miocene, the compressional forces folded the sediments and start to form the Mesogean ridge (Mountrakis, 2006). These sediments evolved to form a new accretionary

prism. Since the Miocene-Pliocene, the area of the old accretionary prism, which formed from the compressional stresses during the Oligocene, was under an extensional stress field, which continues until today (Mountrakis, 2006). The relative phenomena of the expanding forces are the thinning of the crust, the formation of tectonic basins and trenches and the exposure of lower formations as tectonic windows. The direction of the extensive stress field was northeast to southwest in the upper Miocene, and since the Pleistocene is north-south which leads to the formation of normal, active east-west faults. A study based in south Aegean moment tensors by Papazachos, et al.(1999); Papazachos, et al.(2002) shows that, along and in the inner part of the Hellenic Arc, there is a small zone that has different stress field. The direction of extensional stresses in this zone is east-west to east/southeast which is analogous to the direction of the compressional field that acts in the outer part of the arc. In the outer part and along the Hellenic Arc, south from Crete, there are compressional forces with east-west to northeast-southwest direction that forms reverse faults (figure 2.4.2).

The initial estimation of the movement rates due to the compression is due to the subduction of African plate (McKenzie, 1972; Le Pichon & Angelier, 1979) under the Eurasian. The estimated movement rate was 4 cm per year (Kilias, et al., 1994; Papazachos, et al., 1999; Le Pichon, et al., 1995). Recent studies using Global Position System velocity vectors show that the South Aegean plate is moving quickly (33 mm/year) towards the slow (5 mm/year) African plate (figure 2.4.3) (Reilinger, et al., 2006; Ganas & Parsons, 2009).

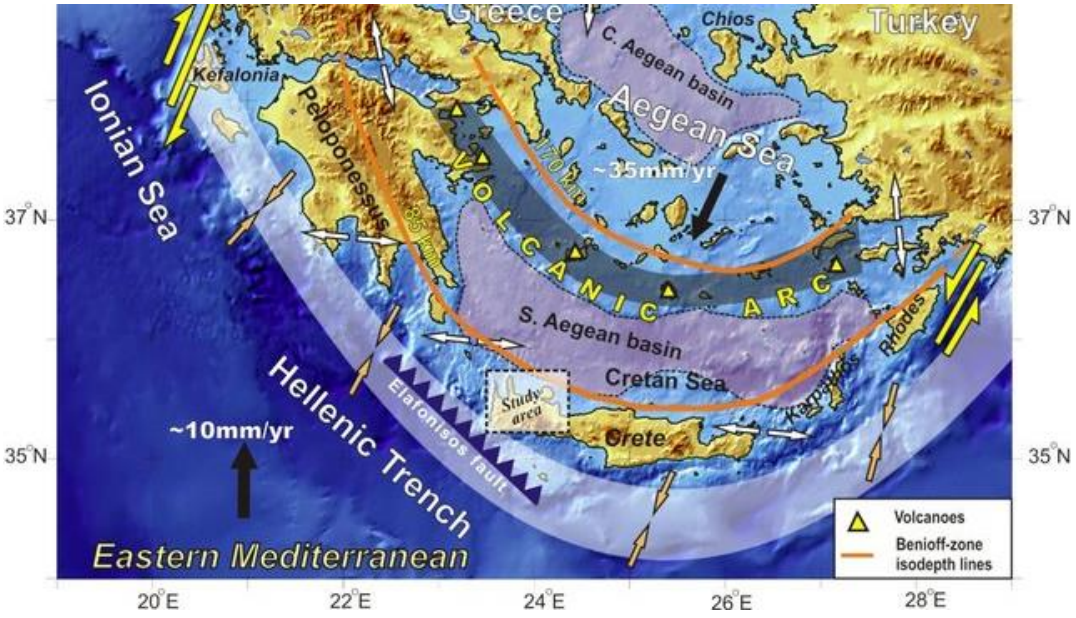

Figure 2.4.2 The current stress field in the South Aegean. Image from (Mountrakis, et al., 2012).

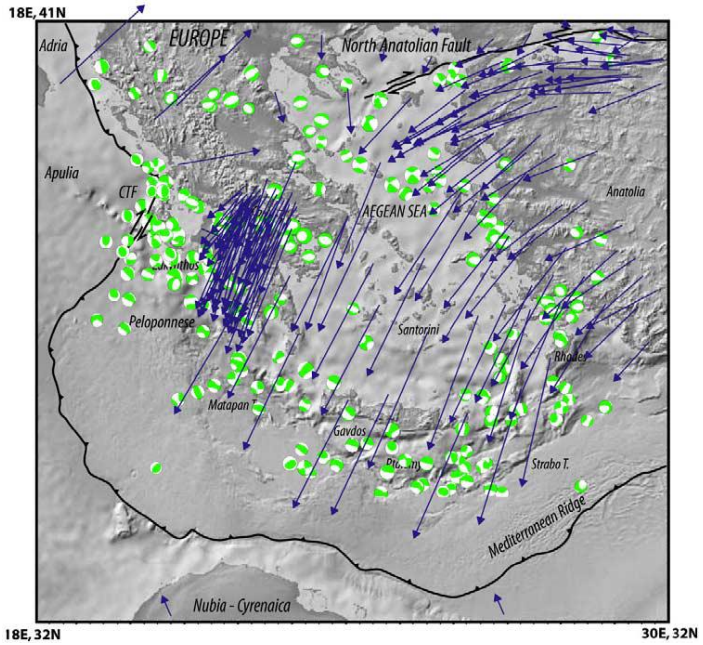

Figure 2.4.3 the GPS velocity vectors for the Aegean Area. The image is from (Ganas & Parsons, 2009) *and the caption: 'after Nyst and Thatcher [2004] and Reilinger et al. [2006], and selected earthquake focal mechanisms are from the Global CMT database'.*

Chapter 3 Pre-seismic signal Methodology

3.1 Accelerated – decelerated seismic crustal deformation.

3.1.1 The time to failure equation

The earthquake preparation process can be considered as a complex procedure where several preshock seismicity patterns occur. The extended excitation time in the large earthquakes makes the preshock phenomena easier to distinct. A very well observed and documented pattern is the one related with the accelerating seismicity. In a critically deformed region there is an increase in the generation of moderate magnitude earthquakes before the mainshock (Rundle, et al., 2000). The second pattern, which is more difficult to observe, is known as seismic quiescence and in the area that is expressed there is a characteristic decrease in the seismicity rate (Nuannun, et al., 2005; Scordilis, 2006; Nuannin, et al., 2012; Papadopoulos & Minadakis, 2016; Kulhanek, et al., 2018). The region where the decelerating seismicity pattern takes place has been discussed by Kulhanek, et al. (2018); Mignan (2012). Examination of global cases that have presented seismicity patterns before large earthquakes show that the accelerating and decelerating strain are accompanied in the critical region. The area of deceleration is located in a narrow part near the vicinity of the epicenter of the seismogenic region. The preshock seismicity patterns have been described by the term 'Accelerating (or Decelerating) Seismic Release' but the term 'Accelerating (or Decelerating) Seismic Crustal Deformation' seems to be more obvious as it reflects the physical process that takes place at the critical preshock area and this process has as results the increase-decrease of the seismicity.

The energy release during the preparation period of the large earthquakes has been expressed by the following accelerating – decelerating seismic crustal deformation equation:

$$\frac{d\Omega}{dt} = \frac{k}{(t_f - t)^{1-m}} \qquad (3.1.1)$$

or the integral form: $\Omega(t) = \Omega_f - B(t_f - t)^m$ where $B = \frac{k}{m}$ (3.1.1b)

This equation is also known as the time to failure model and it has been used by a considerable number of scientists: (Papadopoulos, 1986; Bowman, et al., 1998; Varnes, 1989; Bufe & Varnes, 1993; Brehm & Braile, 1999; Papazachos & Papazachos, 2000; Rundle, et al., 2000; Tzanis, et al., 2000; Bowman & King, 2001; Papazachos & Papazachos, 2001; Di Giovambattista & Tyupkin, 2001; Di Giovambattista & Tyupkin, 2004; Papazachos, et al., 2002; Tzanis & Vallianatos, 2003; Scordilis, et al., 2004; Papazachos, et al., 2005; Mignan, et al., 2006; Mignan, et al., 2007; Mignan, 2008; Mignan & Di Giovambattista, 2008). The cumulative Benioff strain, $\Omega(t)$ has been used as a measure of the preshock seismicity at the time t, defined as:

$$\Omega(t) = \sum_{i=1}^{n(t)} E_i^{1/2}(t) \quad (3.1.2)$$

The E_i is the seismic energy of the i^{th} preshock and $n(t)$ is the number of events till time t. The parameter t_f is the origin time of the mainshock and B and m are parameters which can be calculated by available observations. For $0<m<1$, an accelerated seismicity patterns observed, while for m>1 a decelerated pattern appears.

The most common way to measure seismic energy is by calculating through the corresponding energy-magnitude of the earthquakes relation like the one proposed for the Aegean (Papazachos & Papazachos, 2000):

$$\log E_i = 1.5 * M + 4.7 \quad (3.1.3)$$

The E_i is the energy of the i^{th} earthquake with magnitude M. The Benioff strain is roughly proportional to $E^{1/2}$ and in the literature it is the most common measured quantity. The other measures, such as the seismic moment E^1 or the number of events E^0, have been also used to describe accelerating – decelerating seismicity patterns but not so frequently.

The generalization of the cumulative Benioff strain $\Omega(t)$ introduces a new quantity

$$\Omega_\xi(t) = \sum_{i=1}^{n(t)} E_i^{\xi}(t) \quad \text{where } 0 \le \xi \le 1 \quad (3.1.4)$$

The new quantity is the generalized Benioff deformation while the ξ is the energy exponent. When the energy exponent ξ is equal with 0, then the quantity $\Omega_0(t) = N(< t)$ where the $N(< t)$ is the cumulative number of earthquakes till the time t. A ξ value equal with ½ will give the well-known cumulative Benioff strain as the $\Omega_{1/2}(t) = \Omega(t)$. Likewise, when the ξ is taking the value 1, then the quantity $\Omega_1(t)$ will represent the cumulative energy released $\sum E(t)$.

3.1.2 A First principles approach

The proposed model has been submitted and accepted in *Entropy — Open Access Journal impact factor 2.305 (2017)* (Entropy, 2018) with title: "A complexity view into the physics of Accelerating Seismic Release Hypothesis: Theoretical principles".

In a fault zone that goes under tectonic loading, the stress increases, the system of the faults has a fractal structure that obeys hierarchical scaling laws (Mandelbrot, 1983; Scholz & Mandelbrot, 1989; Turcotte, 1997). Considering the hierarchical scaling laws of fractures that takes place in the fault zone, Rundle et al. (2000) have proposed that the preparation process of the main shock can behave as a critical point phenomenon. As the fracturing becomes coherently self-organized at different scales, the system goes towards the failure time. This process develops upwards from below, following the energy scales of self-organized fractures, and is eventually concentrated in the vicinity of the hypocenter of the main shock. The seismicity patterns that have been associated with the nucleation of strong earthquakes are often recorded over a fairly large earthquake epicenter area V. It should be noted that the earthquake epicenter can lie in both central and peripheral parts of this area. The size of the area V is an order of magnitude greater than that of the earthquake source region. The stressed crustal volume V is the area where the preparation process of large earthquake occurs. For example, a Mw 6.0 earthquake with a strike slip fault length approximately 15km, has a preparation area V about 150km^2. However, in addition to the area V, the earthquake nucleation process should give rise to a potential earthquake source region called effective volume V_{eff} which is developing with time t in as the macrofractures are nucleated. The maximum size L of V_{eff} is of the same order as that of the earthquake source. In the initial phase before the seismicity patterns appear, the spatial and temporal

distribution of the seismic activity within the volume V is approximately uniform. The incoming tectonic elastic energy during the initial phase, flows into the volume V and it is released as weak earthquakes and sometimes it is possible to produce an additional aseismic deformation (e.g., creep). Considering that the crust is not a homogeneous material, it is straightforward to accept that due to the inhomogeneities of the crust, the elastic energy is concentrated in some subvolumes υ within the volume V which leads to an increase of the stress inside the subvolumes. The distribution and the size of the subvolumes are responsible for the configuration of stress field which specifies the parameters of the future main shock.

Aiming to express the energy which supports stress, the elastic energy per surface density which tectonically flows within the volume V is defined as U_s^{in}, so the incoming energy per density area (A) is $U_s^{in} = \frac{dU^{in}}{dA}$. The volume density of the elastic energy which is seismically released as a result of the earthquake activity within effective volume V_{eff} is defined as U_v^{out}. The effective volume V_{eff} is formed by the set of all the earthquake subvolumes υ within V_{eff} $(V_{eff} \mathbb{C} V)$ (figure 3.3.1), while an aseismic term $R(t)$ exists to describe the part of the inflow energy to V which is not related to the earthquake activity.

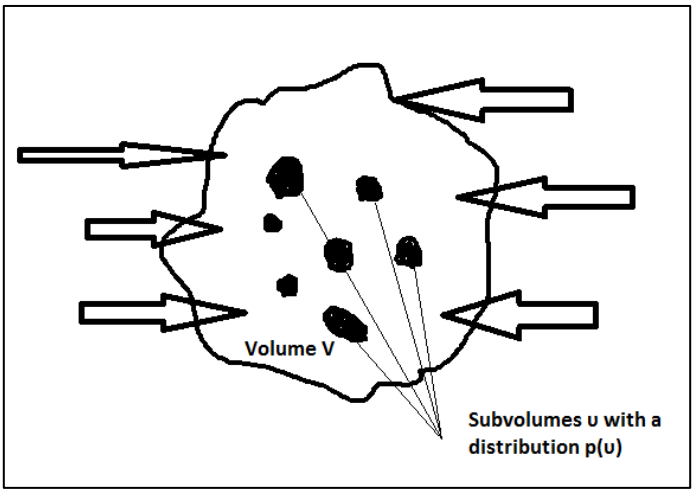

Figure 3.1.1. The tectonically-stressed volume V. Within the volume, the seismic energy is released in the hierarchically distributed subvolumes υ that form the potential earthquake source region V_{eff} (see text).

According to the fundamental principle of energy conservation, the total amount of energy in the system remains constant:

$$U_S^{in} A(V) = U_V^{out} V_{eff} + R(t) \quad (3.1.5)$$

or $$U_S^{in} A(V) = U_V^{out} V_{eff} + \lambda V \quad (3.1.5a)$$

where the aseismic term $R(t)$ is assumed as $= \lambda V$. Building on the Voight relation (1) in Voight (1989) as well as the assumption suggested in equation (4) of the Di Giovambattista & Tyupkin (2001) work and by accepting its validity for the generalized Benioff strain $\Omega_\xi(t)$, the energy release is expressed in a similar way:

$$\frac{d\Omega_\xi(t)}{dt} = \gamma [U_V^{out}(t)]^\alpha = \gamma \left[\frac{U_S^{in} A(V) - \lambda V}{V_{eff}} \right]^\alpha \quad (3.1.6)$$

The equation (3.1.6) relates the rate of the generalized Benioff deformation with the volume density of the elastic energy released and it is similar with that used in damage mechanics, where the evolution of damage variable is related with the square of the strain (Shcherbakov & Turcotte, 2003). If L is the characteristic size of the volume V, then $A(V) \sim L^{d_e - 1}$ and $V \sim L^{d_e}$ where d_e is the Euclidean dimension of V which is $d_e = 3$ when the earthquake activity in embedded in a 3 dimensional space and $d_e = 2$ when it is located in an almost 2 dimensional surface. Hereafter the term "volume" has to be viewed as the geometrical size related with the spatial distribution of earthquake events and as mentioned it is the geometrical volume in case of a 3-dimensional distribution of preshocks.

In order to proceed it is necessary to estimate the probability distribution p(υ) of the sub-volumes υ that form the effective volume V_{eff} with the use of the non-extensive statistical physics (NESP) principles in the analysis. The cornerstone of the NESP mechanics which is recapitulated here, is the non-additive entropy S_q (Tsallis, 2009; Vallianatos, et al., 2015), the entropy for a system which does not involve the mathematical addition in the sense that probabilities are proportional to the number of the elements, as it is in the classic Boltzmann-Gibbs entropy S_{BG}. The Tsallis entropy S_q is defined as:

$$S_{\mathrm{q}} = k_{\mathrm{B}} \frac{1-\sum_{i=1}^{W} p_i^q}{q-1} \qquad \mathrm{q} \in R, \tag{3.1.7}$$

or in equivalent form as $S_{\mathrm{q}} = -k_{\mathrm{B}} \int p^q ln_q p \, dx$ for a continuum variable x, with $ln_q X = \frac{X^{1-q}-1}{1-q}$ the definition of q-logarithmic function. The k_B is the Boltzmann's constant, the p_i and p(x) are the probabilities of the x, the W is the total number of microscopic configurations and the q is the entropic index. The last index is a measure of the non-additivity of the system and for the particular case when q=1, the Boltzmann-Gibbs entropy S_{BG} is obtained:

$$S_{BG} = -k_B \sum_{i=1}^{W} p_i ln p_i. \tag{3.1.8}$$

The index q = 1 gives the well-known exponential distribution (Tsallis, 2009) while for the cases where q>1 and q<1 corresponding to sub-additivity and super-additivity, gives the q-exponential distribution. Although Tsallis entropy shares a lot of common properties with the Boltzmann-Gibbs entropy, S_{BG} is additive, whereas S_q for $q \neq 1$ is non-additive (Tsallis, 2009). According to this property, S_{BG} exhibits only short-range correlations while the total entropy of the systems depends on the size of elements. Alternatively, for $q \neq 1$ the S_q allows all-length scale correlations and seems more adequate for complex dynamical systems, especially when long-range correlations between the elements of the system are present. For a system composed of two statistically independent subsystems, Ss_1 and Ss_2, the Tsallis entropy satisfies the equation (Tsallis, 2009):

$$S_q(Ss_1, Ss_2) = S_q(Ss_1) + S_q(Ss_2) + \frac{1-q}{k_B} S_q(Ss_1) S_q(Ss_2) \tag{3.1.9}$$

The non-additivity is indicated by the last term on the right side of the equation (3.1.9) and represents the interaction between the two subsystems Ss_1 and Ss_2. In order to estimate the probability distribution $p(v)$ of the seismic subvolumes v, the non-extensive entropy is maximized under the appropriate constraints, using the Lagrange-multipliers method with the Lagrangian (Tsallis, 2009):

$$L_q = = -\int_0^\infty p^q(v) ln_q p(v) dv - \lambda_o \left(\int_0^\infty p(v) dv - 1\right) - \lambda_1 \left(\int_0^\infty v P_q(v) dv - \langle v \rangle_q\right) \quad (3.1.10)$$

The first constraint refers to the normalization condition that reads as: $\int_0^\infty p(v) dv = 1$. Introducing the generalized expectation value (q-expectation value), v_q which is defined as: $v_q = \langle v \rangle_q = \int_0^\infty v P_q(v) dv$, where the escort probability is given in (Tsallis, 2009) as: $P_q(v) = \frac{p^q(v)}{\int_0^\infty p^q(v) dv}$, the extremization of S_q with the above constraints yields to the probability distribution of $p(v)$ as (Brouers & Sotolongo-Costa, 2005; Vallianatos, et al., 2014):

$$p(v) = C_q \left[1 - \frac{1-q}{2-q}\left(\frac{v}{v_q}\right)\right]^{\frac{1}{1-q}} \quad (3.1.11)$$

where C_q a normalization coefficient. The Q-exponential function is defined as:

$$exp_Q(X) = \begin{cases} [1+(1\text{-}Q)X]^{1/(1\text{-}Q)} & \text{if } (1+(1\text{-}Q)\ X \geq 0) \\ 0 & \text{if } (1+(1\text{-}Q)X<0) \end{cases}. \quad (3.1.12)$$

The normalized cumulative number of seismic subvolumes v can be obtained by integrating the probability density function $p(v)$ as:

$$P(>v) = \frac{N(>v)}{N_0} = \left[1 + \left(\frac{q-1}{2-q}\right)\left(\frac{v}{v_q}\right)\right]^{\frac{q-2}{q-1}} \quad (3.1.13)$$

where $N(>v)$ is the number of events with seismic volume larger than v. In the latter expression, if $q = 2 - \frac{1}{Q}$ leads to:

$$P(>v) = exp_Q\left(-\left(\frac{v}{v_q}\right)\right) = \left[1 + (Q-1)\left(\frac{v}{v_q}\right)\right]^{-\frac{1}{Q-1}} \quad (3.1.14)$$

which has a typical q-exponential form.

In the frame of non-extensive statistical mechanics approach the earthquake volumes bigger than a given one υ_o leads to a power law description of the distribution function and in such a case the cumulative distribution is:

$$P(>\upsilon) \cong C\left(\frac{\upsilon}{\upsilon_q}\right)^{-\frac{2-q}{q-1}} \sim \upsilon^{-\beta} \tag{3.1.15}$$

with an exponent $\beta = \frac{2-q}{q-1}$. Aiming to have an estimation of υ_o, the volume where the power law approximation of $P(>\upsilon)$ takes the value $P(>\upsilon) =1$ is selected which leads to $\upsilon_o = \upsilon_q \left(\frac{2-q}{q-1}\right)^{3/2}$. An observation is that $\beta \leq 1$ leads to $\frac{3}{2} \leq q$, in agreement with previous published results on earth physics processes in a broad range of scales from laboratory up to geodynamic one (Vallianatos, et al., 2018). It is obvious that the volume distribution $p(\upsilon)$ could lead to an estimation of $V_{eff} = \int_{V_{min}}^{V} \upsilon p(\upsilon) d\upsilon$ which for large volumes (i.e., moderate to significant events) has an asymptotic behavior $V_{eff} \sim V^{(2q-3)/(q-1)}$ or $V_{eff} \sim L^d$ where $d = d_e \frac{2q-3}{q-1}$ which generalize and justify the expression introduced in Di Giovambattista & Tyupkin (2001). The latter expression implies that when $d>0$ $(q>3/2)$ then $V_{eff} \sim L^d$ presents a fractal distribution of earthquake volumes with a fractal dimension $d_e - 1 < d < d_e$, leading to $\frac{2d_e+1}{d_e+1} < q < 2$. The latter expression suggests that within non-extensive statistical physics approach the entropic index q is bounded by the Euclidean dimension d_e of the deformed system. When $d_e = 3$, then $\frac{7}{4} < q < 2$, while for $d_e = 2$ the q is constrained in the range $\frac{5}{3} < q < 2$.

The equation (3.16), the generalized Benioff stress rate could be expressed as follows:

$$\frac{d\Omega_\xi(t)}{dt} = \gamma \left[U_S^{in} \frac{1}{L^{d-d_e+1}} - \lambda L^{d_e-d}\right]^\alpha \tag{3.1.16}$$

When the time t approaches the time to failure t_f and since $U_s^{in}(t = t_f) \neq 0$ following the (Di Giovambattista & Tyupkin, 2001) equation (6), an expansion of the incoming energy per density area U_s^{in}(t) when t approach to t_f is:

$$U_s^{in} = U_{0in} + U_{1in}\left(\frac{t_f - t}{T_c}\right) + O\left(\left(\frac{t_f - t}{T_c}\right)^n\right) \quad (3.1.17)$$

From the equation (3.1.17) it is obvious that the $U_{0in} = U_s(t = t_f)$ expresses the elastic energy of tectonic origin inserted into the deformed area close to the time of failure. The third term $O(x)$ presents all the high order terms in the expansion that are very small and could be omitted, while the parameter T_c is the characteristic time that defines the duration of main shock preparation process starting from the time where deviation of $\Omega_\xi(t)$ from linearity appears (See figure 3.1.2).

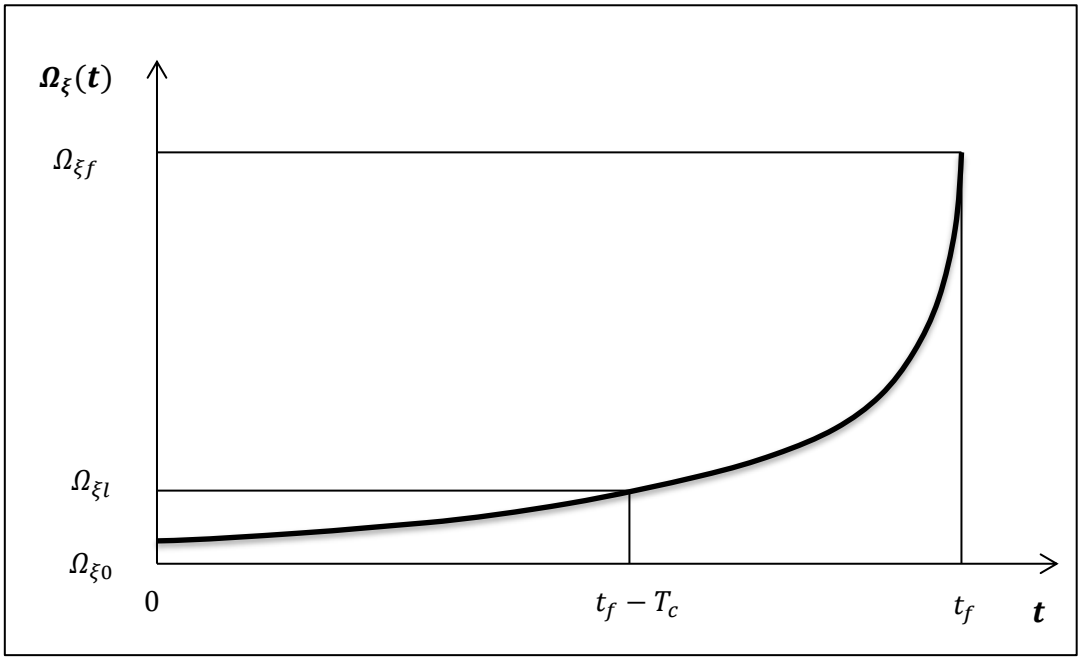

Figure 3.1.2. Graph of the evolution of the generalized Benioff strain $\Omega_\xi(t)$. The initial part is linear and the deviation from linearity starts at $t=t_f-T_c$ defining the start of the accelerating deformation stage, where T_c is the characteristic time expressing the duration of main shock preparation process.

As the time for the mainshocks approaches, the volume where energy release observed, defines a singular point (Scordilis, et al., 2004) and the analyticity assumption of $L(t)$ as $t \to t_f$ leads to:

$$L(t) = L_0\left(\frac{t_f - t}{T_c}\right) + O\left(\left(\frac{t_f - t}{T_c}\right)^n\right) \tag{3.1.18}$$

When the $t \to t_f$, the $L(t) \to 0$ and $L\left(t = t_f - T_c\right) = L_0$. Substituting equations (3.1.17) and (3.1.18) in to (3.1.16) to obtain:

$$\frac{d\Omega_\xi(t)}{dt} = \gamma\left\{\frac{U_{0in}}{\left[L_0\left(\frac{t_f - t}{T_c}\right)\right]^{d-d_e+1}} + \frac{U_{1in}\left(\frac{t_f - t}{T_c}\right)}{\left[L_0\left(\frac{t_f - t}{T_c}\right)\right]^{d-d_e+1}} - \lambda\left[L_0\left(\frac{t_f - t}{T_c}\right)\right]^{d_e - d}\right\}^a \tag{3.1.19}$$

As $t \to t_f$ then $\left(\frac{t_f - t}{T_c}\right) \to 0$. Taking into account that $d_e - d$>0 and $d + 1 > d_e$ the first term in (3.1.19) is dominated and the integration leads to:

$$\Omega_\xi(t) = \Omega_\xi\left(t = t_f\right) - \gamma\frac{T_c(U_{0in})^a}{L_0^{a(d-d_e+1)}}\frac{1}{a(d_e-1-d)+1}\left(\frac{t_f - t}{T_c}\right)^{1+a(d_e-1-d)} \tag{3.1.20}$$

Which has the classic form proposed in (Bowman, et al. (1998); Varnes (1989); Bufe & Varnes (1993); Bowman & King (2001) where:

$$\Omega_\xi(t) = \Omega_{\xi f} - B(t_f - t)^{m_\xi} \qquad \text{with } \Omega_{\xi f} = \Omega_\xi\left(t = t_f\right) \tag{3.1.21a}$$

$$\text{B}= \gamma\frac{T_c^{a(d-d_e+1)}(U_{0in})^a}{L_0^{a(d-d_e+1)}}\frac{1}{a(d_e-1-d)+1} \tag{3.1.21b}$$

$$m_\xi = a(d_e - 1 - d) + 1 \tag{3.1.21c}$$

The expression (3.1.21c) suggests that m_ξ is independent of ξ (0≤ξ≤1) used in the definition of the generalized Benioff strain $\Omega_\xi(t)$ but controlled by the Euclidean dimension d_e of the deformed system and the entropic parameter q which as a measure of long range interactions and of the complexity of the system, controls the distribution of seismic subvolumes υ and their fractality. It is worth mentioning that the shape of the acceleration curve is controlled primarily by the exponent m_ξ. Therefore, two different sized main shocks with the same m_ξ value will have the same shaped acceleration curve but with different scale.

The non-extensive statistical physics approach could be used to formulate the earthquake frequency-magnitude distribution (Sotolongo-Costa & Posadas, 2004). Moreover, Sotolonga-Costa and Posadas (2004) introduced an energy distribution function that shows the influence of the size distribution of fragments on the energy distribution of earthquakes, including the Gutenberg – Richter (GR) law as a particular case. Silva et al. (2006) revised the fragment-asperity model using a more realistic relationship between earthquake energy (ε) and fragment size. In many recent works it is indicated that the q parameter can be used as a measure of the stability of an active tectonic area (Papadakis, et al., 2014; Papadakis, et al., 2016; Vallianatos, et al., 2018). Significant increase of q indicates strong interactions between the fault blocks (earthquake volumes) and implies a transition away from equilibrium (Vallianatos, et al., 2015; Vallianatos, et al., 2016; Vallianatos, et al., 2018). The models mentioned above are modified in order to formulate a frequency-magnitude distribution, taking the earthquake volume distribution *p(υ)* into account and introducing a scale law between the released relative energy *(E)* and the earthquake volume *(υ)* as has been proposed *(E≈ α.υ)* in (Silva, et al., 2006) in agreement with the scaling relationship between seismic moment and rupture length. From equation (3.1.11) the energy distribution function of the earthquakes can be written as follows:

$$p(E) = C_q \left[1 - \frac{1-q}{2-q}\left(\frac{E}{E_q}\right)\right]^{\frac{1}{1-q}} \tag{3.1.22}$$

Since the probability of the energy is $p(E) = n(E)/N_o$, where $n(E)$ corresponds to the number of earthquakes with energy E and N_o is the total number of earthquakes, the normalized cumulative number of earthquakes is given as (Telesca, 2012):

$$\frac{N(>\mathrm{E})}{N_o} = \int_{\mathrm{E}}^{\infty} p(\varepsilon) d\varepsilon \tag{3.1.23}$$

where $N(> E)$ is the number of earthquakes with energy greater than E. Combining equations (3.1.22) and (3.1.23) the following expression for the earthquake frequency-energy distribution derived:

$$\frac{N(>\mathrm{E})}{N_o} = \left[1 - \frac{(1-q)}{(2-q)}\left(\frac{E}{E_q}\right)\right]^{\frac{2-q}{1-q}} \tag{3.1.24}$$

which for $\frac{(\mathrm{q}-1)}{(2-q)}\left(\frac{E}{E_q}\right) \gg 1$ suggests a scaling law $N(> E) \sim E^{-\frac{2-q}{q-1}}$ in agreement with the well known power law scaling $N(> E) \sim E^{-\beta}$ with $\beta = \frac{2-q}{q-1}$ (Kagan, 2010). As proposed in (Kanamori, 1978) the earthquake magnitude M and the released seismic energy E, are related as $M \sim \frac{2}{3}\log(E)$, leading to a b-value as appeared in the Gutenberg –Richter law:

$$b = \frac{3}{2}\beta = \frac{3}{2}\,\frac{2-q}{q-1} \tag{3.1.25}$$

Figure 3.1.3 presents the dependence of the b value with q as given in equation (3.1.25). Substituting $d = d_e \frac{2q-3}{q-1}$ into m_ξ as given by equation 3.1.21c) and taking (3.1.25) into account, the critical exponent is:

$$m_\xi = 1 - \alpha + \alpha\, d_e \frac{2-q}{q-1} = 1 + \alpha\, d_e \left(\beta - \frac{1}{d_e}\right) = 1 + \alpha \left(\frac{2}{3} b\, d_e - 1\right) \tag{3.1.26}$$

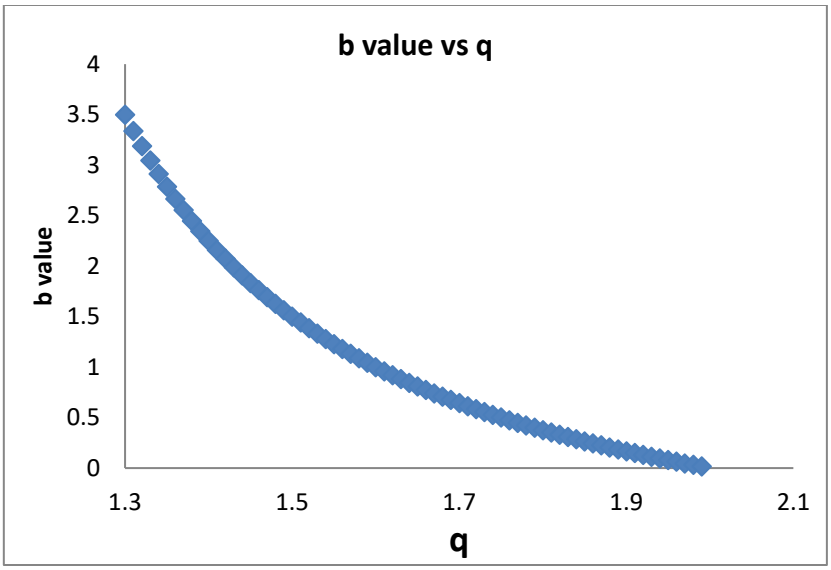

Figure 3.1.3*. The b value vs q as defined in equation (3.1.25) (see text).*

These equations connect the non-extensive parameter q and the b-value of the Gutenberg – Richter law with the m_ξ parameter of the generalized Benioff strain. Using synthetic data, Bufe and Varnes (1993) claimed a relationship between b-value and $m_{1/2}$. For the parameter m_ξ, a positive definition is required ($m_\xi > 0$) and thus $d_e - 1 < d < d_e - 1 - \frac{1}{a}$. Theoretical results and experimental observation (Papadopoulos, 1986; Bowman, et al., 1998; Varnes, 1989; Bufe & Varnes, 1993; Brehm & Braile, 1999; Papazachos & Papazachos, 2000; Rundle, et al., 2000; Bowman & King, 2001; Tzanis, et al., 2000; Papazachos & Papazachos, 2001; Di Giovambattista & Tyupkin, 2001; Di Giovambattista & Tyupkin, 2004; Papazachos, et al., 2002; Tzanis & Vallianatos, 2003; Scordilis, et al., 2004; Papazachos, et al., 2005; Mignan, et al., 2006; Mignan, et al., 2007; Mignan, 2008; Mignan & Di Giovambattista, 2008) suggest that $m_{1/2} = 0.25 - 0.30$ and $d = 2.3 - 2.4$, while m_ξ should be the same for different ξ values, in agreement with observations that indicate $m_0 = 0.3$ (Papadopoulos, 1988). Substituting $m_\xi \approx 0.3 \; and \; d \approx 2.3 \; for \; d_e = 3$ or $d \approx 1.3 \; for \; d_e = 2$ to (3.1.21c) leads to $a = 2.0 - 2.1$. From here on the $a \approx 2.0$ will have a constant value which is in agreement with damage mechanics model where the evolution of damage variable is related with the square of the strain (Shcherbakov & Turcotte, 2003).

The equation (3.1.26) along with the constrain $m_\xi > 0$ leads to a lower bound for the b value and an upper bound for the q value respectively, given as:

$$b > \frac{3(a-1)}{2ad_e} \text{ and } q < \frac{2ad_e+a-1}{ad_e+a-1} \quad (3.1.27)$$

which for α=2 and $d_e = 3$ gives $b > 0.25$ while for $d_e = 2$, $b > 0.375$. The maximum permitted value of q is q_{max} = 13/7 for $d_e = 3$ *and* q_{max} = 9/5 for $d_e = 2$. For accelerating $m_\xi < 1$ and for decelerating seismicity $m_\xi > 1$. Applying the above values in equation (3.1.26) give as result the case of accelerating seismicity for $q > \frac{2d_e+1}{d_e+1}$ which implies that in this case there is a lower bound in the observed q. The lower limit is introduced by the topological Euclidean dimension d_e of the space where the earthquakes are embedded. For $d_e = 3$ the $q > \frac{7}{4}$ while for $d_e = 2$, $q > \frac{5}{3}$. Within a similar way the $q < \frac{2d_e+1}{d_e+1}$ for decelerating seismicity. Furthermore, the equation (3.1.26) for the accelerating seismicity with $m_\xi < 1$ leads to $b < \frac{3}{2d_e}$ which (as approach to failure) for $d_e = 3$ leads to $b < 0.5$ while for $d_e = 2\ to\ b < 0.75$. The above expressions introduce a critical value for q and for b where a transition from deceleration to acceleration seismicity occurs. It is obvious that the deceleration seismicity which described by $m_\xi > 1$ which for $d_e = 3$ leads to $b > 0.5\ and\ for\ d_e = 2\ to\ b > 0.75$. The figures 3.1.4 and 3.1.5 present the dependence of the m_ξ parameter with q and b, respectively.

Furthermore, the above analysis could be applied to connect changes of m_ξ parameter to b-value variations which have been reported as precursory effects in a number of significant earthquake events (Papadopoulos, 1988; Papadopoulos, et al., 2010; Papadopoulos, et al., 2000; Kanamori, 1978). Equation (3.1.26) suggests that variations of *b* value are associated with the temporal evolution of m_ξ parameter during the main event preparation period T_c, following the b values changes as suggested in Wang (2006). By writing the $b(t)=b_o + B(t)$ where b_o represents the background *b-value* and *B(t)* reflects the time dependent part of *b-value* that varies during the preparation of the main earthquake event (see Figure 3.1.6) and substituting in (3.1.26) leads to:

$$m_\xi = m_o + \frac{2a}{3} d_e B(t) \ \ where\ m_o = 1 + \alpha \left(\frac{2}{3} b_o\, d_e - 1\right) \qquad (3.1.28)$$

For α=2, b_o=1 and $d_e = 3$ leads to $m_o = 3$ while for $d_e = 2$, $m_o = 1.67$, both results describing a decelerating stage of seismicity. As the failure time t_f approaches, observational results suggest that $m_\xi \approx 0.30 - 0.35$, leading to $B(t_f) = -1/6$ for $d_e = 3$ and $B(t_f) \approx -1/4$ for $d_e = 2$ respectively.

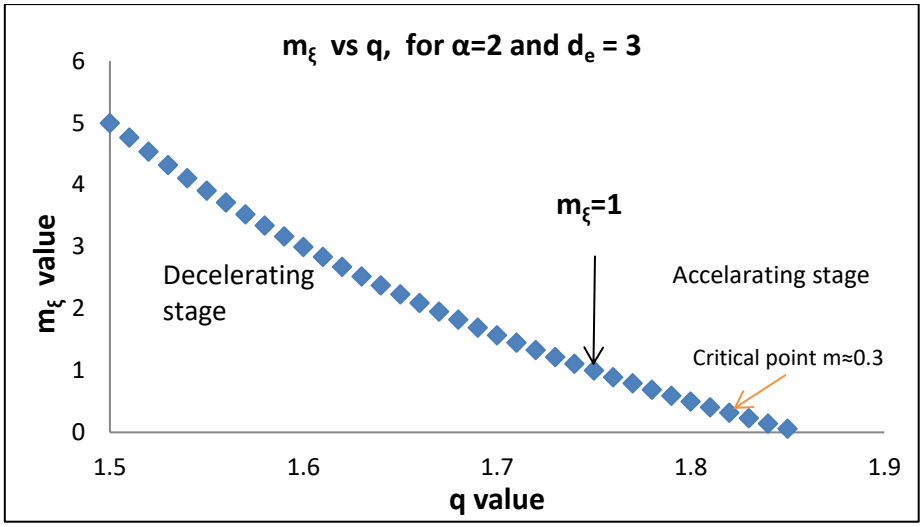

Figure 3.1.4. The dependence of m_ξ with the entropic parameter q along with the accelerating/decelerating stages (see text).

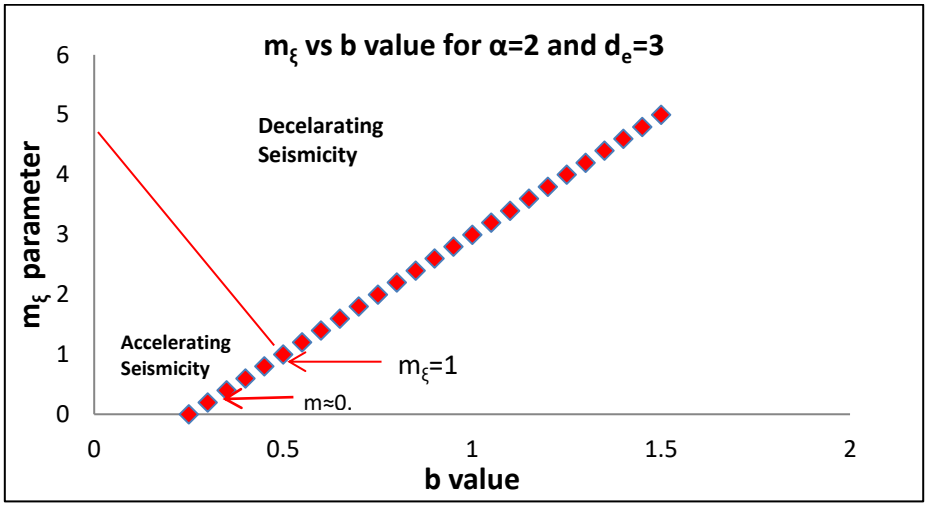

Figure 3.1.5. The dependence of m_ξ with b value along with the accelerating/decelerating ranges of the earthquake system.

Figure 3.1.6 exhibits the general pattern of the temporal variation of m_ξ parameter following the temporal variation of *b-value* as suggested in Wang (2016). Most of the time after the last main event, the m_ξ value varies around m_o, which corresponds to the average b_o value measured over a long-time period. As the b value increases from b_o to a maximum value, (a seismic quiescence appears which is in agreement with Mignan & Di Giovambattista (2008) the parameter $m_\xi(t)$ increases too following the equation (3.1.27). After passing a maximum value $m_{\xi max}$, starts a decreasing phase of b and m_ξ, crossing the value m_o and approaches the transition time t_c where $m_\xi(t_c)=1$, which defines the passing from the deceleration to an acceleration stage. At the next step $m_\xi(t)$ is approaching the value $m_\xi(t \to t_f)$ which lies in the range 0.25-0.30 and according to observations it suggests the final stage of the mainshock preparation. The latter is in agreement with (Schorlemmer & Wiemer, 2005) where *b* values based on seismicity over a period from 2006 till immediately before the Tohoku earthquake, reveals a zone of low *b-value (b≈0.5-0.6)* in and around the focal area as an indicator of highly stressed patches in the zone, in remarkable similarity to b values obtained in laboratory experiments (Lei, 2003). For $b \approx 0.5$ the equation (3.1.26) gives $m_{1/2} \approx 0.3$ in agreement with the value m=0.24±0.09 given in Xue, et al. (2012).

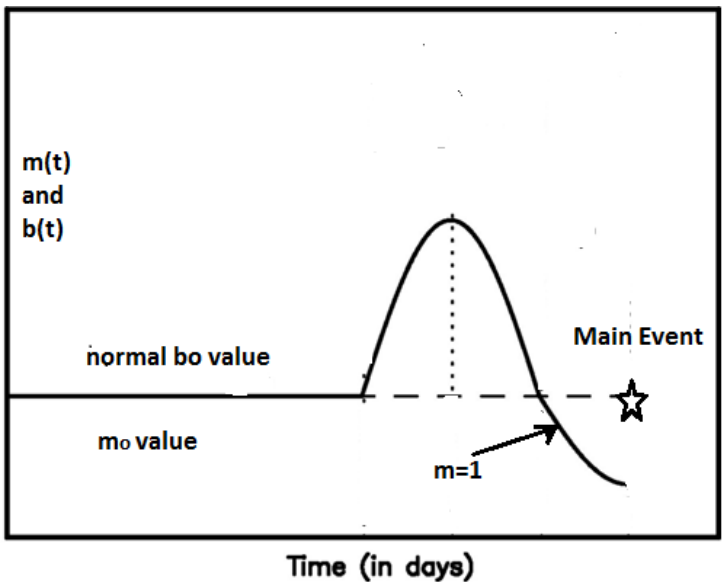

Figure 3.1.6. The pattern of the variation of b and m_ξ values with time following the mechanism of value preseismic changes proposed in Wang (2016).

3.1.3 Fundamental properties of the $\Omega_{\xi}(t)$ function.

Proceeding now to study some fundamental properties of $\Omega_{\xi}(t)$ function justified by empirical laws mainly presented in Papazachos & Papazachos (2000); Papazachos & Papazachos (2001); Papazachos, et al. (2002); Scordilis, et al. (2004); Papazachos, et al. (2005). The equation (3.1.21b) leads to:

$$\mathrm{Log}\, B = \left[\log \gamma \frac{T_c^{\,1-m_{\xi}} (U_{0in})^{a}}{m_{\xi}\, L_0^{\,1-m_{\xi}}}\right] =$$

$$\log\left(\frac{\gamma}{m_{\xi}}\right) + \alpha \log(U_{0in}) + \left(1-m_{\xi}\right)\log T_c - \left(1-m_{\xi}\right)\log L_0 \qquad (3.1.29)$$

The energy of the main shock is $E_m \sim U_{0in} {L_0}^2$ or $log E_m \sim (\log U_{0in} + 2\log L_0)$. Experimental results and theoretical estimations suggest that the preparation time has a very weak dependence on the magnitude of the main shock. Substituting to the equation (3.1.25), the scaling laws $\log E_m \cong 1.5M + const,$ and $\log L_0 \approx 0.5\, M + const$ leads to $\log B \approx \left(\frac{a+m_{\xi}-1}{2}\right) M + const.$ Since $a \approx 2$ and $m = 0.25 - 0.30$ that means that the slope is $\frac{a+m_{\xi}-1}{2} \approx 0.62 - 0.65$ which is remarkably close to that observed in a number of works (Papazachos & Papazachos, 2000; Papazachos & Papazachos, 2001; Papazachos, et al., 2002; Scordilis, et al., 2004; Papazachos, et al., 2005).

From equation (3.1.20) it is calculated the generalized Benioff strain rate $\mathrm{d}\Omega_{\xi}/_{\mathrm{dt}}$ as:

$$\frac{d\Omega_{\xi}(t)}{dt} = \gamma \frac{(U_{0in})^{a}}{L_0^{\,a(d-d_e+1)}} \left(\frac{t_f - t}{T_c}\right)^{a(d_e-1-d)} \qquad (3.1.30)$$

According to equations (3.1.20) and (3.1.30):

$$\Omega_{\xi}(t) = \Omega_{\xi f} - \gamma \frac{{U_{0in}}^{a}}{m_{\xi}} \left(\frac{T_c}{L_0}\right)^{1-m_{\xi}} \left(t_f - t\right)^{m_{\xi}} \quad \text{and} \qquad (3.1.31)$$

$$\frac{d\Omega_{\xi}(t)}{dt} = \gamma {U_{0in}}^{a} \left(\frac{T_c}{L_0}\right)^{1-m_{\xi}} \frac{1}{\left(t_f - t\right)^{1-m_{\xi}}} \qquad (3.1.32)$$

when $t_f - t = T_c$ i.e., in the start of the accelerating deformation stage, it is:

$$\Omega_{\xi l} = \Omega_{\xi f} - \gamma \frac{{U_{0in}}^{a}}{m_{\xi}} \frac{T_c}{{L_0}^{1-m_{\xi}}} \tag{3.1.33a}$$

It is physically reasonable to expect a continuity of physical parameters in the transition from the linear to accelerated crustal deformation period and to accept that at $t = t_f - T_c$ a continuity exists:

$$\left.\frac{d\Omega_{\xi}}{dt}\right|_{l} = \left.\frac{d\Omega_{\xi}}{dt}\right|_{(t=t_f-T_c)} = \gamma {U_{0in}}^{a} \frac{1}{{L_0}^{1-m_{\xi}}} \tag{3.1.33b}$$

the $\left.\frac{d\Omega_{\xi}}{dt}\right|_{l}$ is the slope of the linear part. The mean generalized Benioff rate during the accelerated (deformed) period T_c i.e., from $t = t_f - T_c$ to $t = t_f$:

$$\langle\frac{d\Omega_{\xi}}{dt}\rangle_D = \frac{1}{T_c}\int_{t_f-T_c}^{T_c} \frac{d\Omega_{\xi}(t)}{dt}\,dt = \gamma \frac{{U_{0in}}^{a}}{m_{\xi}}\left(\frac{1}{L_0}\right)^{1-m_{\xi}} \tag{3.1.33c}$$

The (3.1.33b) and (3.1.33c) leads to the conclusion that:

$$\frac{\langle\frac{d\Omega_{\xi}}{dt}\rangle_D}{\left.\frac{d\Omega_{\xi}}{dt}\right|_{l}} = \frac{1}{m_{\xi}} \approx 3 - 4 \tag{3.1.34}$$

Furthermore from (3.1.33a), if $\Omega_{\xi l} \ll \Omega_{\xi f}$ then: $\Omega_{\xi f} \approx \gamma \frac{{U_{0in}}^{a}}{m_{\xi}} \frac{T_c}{{L_0}^{1-m_{\xi}}}$. Combining the latter with equation (3.1.33c):

$$\Omega_{\xi f} \approx \langle\frac{d\Omega_{\xi}}{dt}\rangle_D T_c \tag{3.1.35}$$

which is exactly that proposed in Papazachos & Papazachos (2000); Papazachos & Papazachos (2001); Papazachos, et al. (2002); Scordilis, et al. (2004); Papazachos, et al. (2005). The Equation (3.1.35) could be written as: $\Omega_{\xi f} \approx \frac{1}{m_{\xi}}\left(\left.\frac{d\Omega_{\xi}}{dt}\right|_{l}\right) T_c$ which indicates that if the T_c and the slope of the linear part of the generalized Benioff strain is estimated, then it is possible to estimate at least the order of magnitude of $\Omega_{\xi f}$ in the time of failure.

Assuming that the last earthquake prior the main shock appears at a time $t_1 = t_f - \delta t_1$. Applying the time to failure equation (3.1.20):

$$\Omega_\xi(t_1) = \Omega_{\xi f} - \gamma \frac{{U_{0in}}^a}{m_\xi} \left(\frac{T_c}{L_0}\right)^{1-m_\xi} \left(t_f - t_1\right)^{m_\xi} \text{or} \tag{3.1.36a}$$

$$\Omega_\xi(t_1) = \Omega_{\xi f} - \gamma \frac{{U_{0in}}^a}{m_\xi} \left(\frac{T_c}{L_0}\right)^{1-m_\xi} (\delta t_1)^{m_\xi}. \tag{3.1.36b}$$

Even if this approach is general, the limit to the case *ξ=1/2* describing the Benioff strain which very commonly applied. In this case the Benioff stain of the main shock is $\Omega_{\frac{1}{2},m} = {E_m}^{1/2} = \Omega_{\frac{1}{2},f} - \Omega_{1/2}(t_1)$, which gives:

$$E_m{}^{\frac{1}{2}} = \gamma \frac{{U_{0in}}^a}{m_{\frac{1}{2}}} \left(\frac{T_c}{L_0}\right)^{1-m_{\frac{1}{2}}} (\delta t_1)^{m_{\frac{1}{2}}} =$$

$$\langle \frac{d\Omega_{1/2}}{dt} \rangle_D \left(\frac{\delta t_1}{T_c}\right)^{m_{1/2}} T_c = \frac{1}{m_{1/2}} \left(\left.\frac{d\Omega_{1/2}}{dt}\right|_l\right) \left(\frac{\delta t_1}{T_c}\right)^{m_{1/2}} T_c \tag{3.1.37}$$

Since the seismic energy is related to seismic magnitude by the relation (3.1.3), the equation (3.1.37) leads to:

$$M_m = \frac{4}{3} \log\left[\frac{1}{m_{1/2}} \left(\left.\frac{d\Omega_{1/2}}{dt}\right|_l\right) T_c\right] + \frac{4m_{1/2}}{3} \log\left(\frac{\delta t_1}{T_c}\right) - 3.13 \tag{3.1.38}$$

Using previously published numerical estimates by Papazachos & Papazachos (2000); Papazachos & Papazachos (2001); Papazachos, et al. (2002); Scordilis, et al. (2004); Papazachos, et al. (2005), the *ξ=1/2* can be used as an order of magnitude estimation for the parameter $\left.\frac{d\Omega_{1/2}}{dt}\right|_l \approx 10^6 J^{\frac{1}{2}}/y$, and assuming that the $T_c \approx 5$ years with $m_{1/2} = 0.25 - 0.30$ and the last main preshock to appear at: $\frac{\delta t_1}{T_c} \approx 0.1$ (i.e. $\delta t_1 \approx 0.5 year$), then the expected earthquake magnitude of the main event should be of the order of $M_m \approx 6.3$. In

addition, since $\frac{\delta t_1}{T_c} \leq 1$ from equation (3.1.38) the constrain $M_m \leq \frac{4}{3}\log\left[\frac{1}{m_{1/2}}\left(\frac{d\Omega_{1/2}}{dt}\Big|_l\right)T_c\right] - 3.13$, leads to the conclusion that the maximum expected earthquake in an area with background Benioff strain rate $\frac{d\Omega_{1/2}}{dt}\Big|_l$ is:

$$M_m^{max} = \frac{4}{3}\log\left[\frac{1}{m_{1/2}}\left(\frac{d\Omega_{1/2}}{dt}\Big|_l\right)T_c\right] - 3.13 \quad (3.1.39)$$

It is obvious that the ratio $\frac{\delta t_1}{T_c}$ is a crucial parameter to define the final stage of the main event preparation. In Brehm & Braile (1999) a relationship is proposed between $m_{1/2}$ and the normalized energy released R_{ne} which is defined as the total cumulative square root energy (i.e., ξ=1/2) divided by the square root of energy released by the main shock. Thus $R_{ne} = \frac{\Omega(t_f)}{E_m^{1/2}}$. From the previous expressions it is obtained that $R_{ne} = (\frac{\delta t_1}{T_c})^{-m_{1/2}}$ which leads to:

$$m_{1/2} = \frac{1}{\log(\frac{T_c}{\delta t_1})}\, logR_{ne} \quad (3.1.40)$$

In which a linear relation between m-parameter and $logR_{ne}$ is suggested with a positive slope $\frac{1}{\log(\frac{T_c}{\delta t_1})}$ (since $T_c > \delta t_1$). The figure 7 from Brehm & Braile (1999) reproduced here (as figure 3.1.7) and a red line with a slope of the order of 0.8-1.0 added in the figure seems that describe the majority of the data points. The latter slope permits an order of magnitude estimation of the ratio $\frac{\delta t_1}{T_c}$, leading to $\frac{\delta t_1}{T_c} = 0.05 - 0.1$.

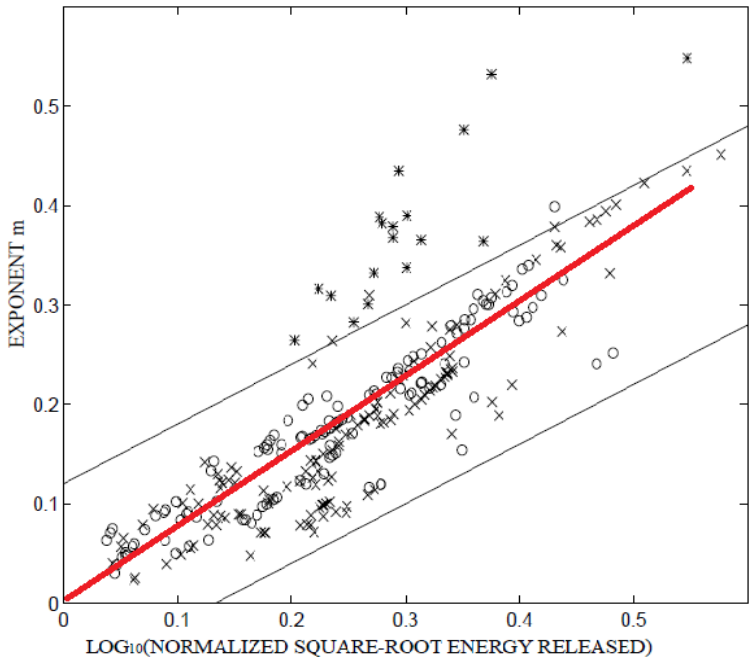

Figure 3.1.7. The $m_{1/2}$ critical exponent plotted versus the logarithm of the normalized square root of energy released as modified from Bowman, et al., 1998. The red line is with slope close to 0.8 (see text).

3.2 Earthquake catalogues

In research, the samples, or the input data in the case of a software-based analysis, are the primary material that will probably affect the outcome. It is unlikely to have detailed results if the initial findings contain artefacts. The inhomogeneities in the collection can be attributed to various reasons, as examples are the possible variation between materials of the same matter, the missing data values and the changes in the sampling methods (Smith, 2006). Focusing on earthquake related analyses such as the accelerated deformation, it is important to have high quality catalogues with accurate seismic parameters. In seismology, the common errors in earthquake parameters catalogues are associated with the wrong picked arrival times, the type location method (linear-non-linear) and the lack of representative for the area seismic velocity model (Husen & Hardebeck, 2010). In addition, the seismological centres use different reporting magnitudes scales which depend on measuring specific parts of seismic wave characteristics (Woessner, et al., 2010). The magnitude scales are not consistent in all ranges, the scale gets saturated especially in large

events and therefore a straightforward equation between the magnitude scales does not exist (Kanamori, 1983; Scordilis, 2006; Woessner, et al., 2010). The moment magnitude scale, which relays on the logarithm of the seismic moment proposed by Kanamori has a constant behaviour through the whole magnitude range (Scordilis, 2006; Johnston, 1996; Kanamori, 1977). A considerable amount of empirical approximations for converting the body wave and surface wave magnitude to moment magnitude have been proposed by various researchers (Johnston, 1996; Scordilis, 2006). Some of the proposed relations have been estimated with ordinary least-squares while others have been calculated with Fuller's General Orthogonal Regression (GOR) method (Fuller, 1987). All the possible earthquakes catalogues issues noted above put emphasis on the necessity to use only high quality and homogeneous catalogues in the accelerated seismic release method

3.2.1 The Thales project catalogue

One of the deliverables of *Thales Technical Educational Institute of Crete project* (Integrated understanding of SEISmicity, using innovative MethOdologies of Fracture mechanics along with EARthquake and non extensive statistical physics - Application to the geodynamic system of the HELLenic ARC. MIS: 380208) was the construction of a complete and homogenized in respect to magnitude catalogue for the broader area of South Aegean. A synopsis of the deliverable which is also published in (Kolligri, et al., 2014) is the following:

The *Thales catalogue* has been compilated with the seismic parameters provided by several seismological centres:

- International Seismological Centre (ISC, 2018)
- National Earthquake Information Centre of USGS (NEIC, 2018)
- Global Centroid Moment Tensor catalogue (CMT, 2018)

- National Observatory of Athens (HL/National Observatory of Athens Seismic Network, 2018), Geophysical Laboratory of the Aristotle University of Thessaloniki (HT/Aristotle University of Thessaloniki Seismological Network, 2018).

- The bulletins of the already published international and national earthquake catalogues (Papazachos & Papazachou, 2003; Engdahl & Villasenor, 2002; Karnik, 1996; Pacheco & Sykes, 1992).

In the final catalogue there were earthquakes without an original moment magnitude estimation, in these cases an equivalent moment magnitude was calculated based on the weighted mean of the converted magnitudes. The available magnitude scales M_L, M_s, and M_b of the aforesaid sources, have been homogenized with a different process to obtain a unique magnitude scale. The conversion between scales has been carried out by the already published relations (Scordilis, 2006; Baba, et al., 2000; Papazachos & Papaioannou, 1997; Scordilis, et al., 2015; Scordilis, 2005; Tsampas, 2006; Duni, et al., 2010). The moment magnitude scale has been selected as the reference scale. The M_W scale does not get saturated for a wider range of magnitudes compared to the other reporting scales. In addition, there is a straightforward relationship between moment magnitude and the logarithm of the seismic moment (Kanamori, 1977; Johnston, 1996; Scordilis, 2006; Woessner, et al., 2010).

The catalogue focus is on an area bounded by coordinates, longitude 19.0 to 30.0E and latitude 33.0 to 40.0N. The recorded earthquakes in the catalogue start from 550 BC with data obtain from historical documents while the events after 1910 up to the end of 2013 are from analogue and digital instrumental recordings. The instrumental part of the catalogue has been relocated with the HYPO71 earthquake location program (Lee & Lahr, 1972), the HYPOINVERSE 2000 algorithm (Klein, 2002) while the final relocation has been completed with the double-difference algorithm, HYPODD (Waldhauser, 2001).

The relocation process has been carried out with the use of the crust models proposed by Karagianni, et al., 2002; Karagianni, et al., 2005. A mean error exists of approximately 0.3 for the magnitude values and up to 30km for the epicentre location (Kolligri, et al., 2014). The final catalogue contains 126,907 earthquakes. 124,204 of these were shallow with depths less than 60km.

The completeness of the catalogue has been estimated with the best combination between the maximum curvature method, the goodness of fit for 90% confidence and goodness of fit for 95% confidence for a square grid with 0.2 degrees size (Wiemer & Wyss., 2000; Wyss, et al., 1999; Mignan & Woessner, 2012). In each point of grid, the number of included events were set to 50. In addition, a 50 times random resampling for each point with replace from the dataset, a method known as bootstrapping (Efron, 1979; Efron & Tibshirani, 1993) has been used to calculate the error limits. In the figure 3.2.1, the bootstrapping boarder values are presented as grey colour dashed lines, the blue vertical dashed lines indicate the time periods while the horizontal ones define the M_c of each time period. The number of seismological networks and the digital recording instruments increased gradually in the past decades (Ammon, et al., 2010), and a result is the continuous decrease of Magnitude of completeness values with time. In the time interval between 1970 and 2013, there are three different time periods where the magnitude of completeness has decreased for the investigation area, the numerical values are presented in table 3.2.1 and a Magnitude of completeness map for the last time period is illustrated in figure 3.2.2. In this thesis the time period that is examined for accelerated seismic release, is the last couple of years from 2011 up to end of 2013 for the two large events occurred in 2013 in southern and western part of South Aegean while for the 2015 event in eastern part, another catalogue has been used (next subchapter).

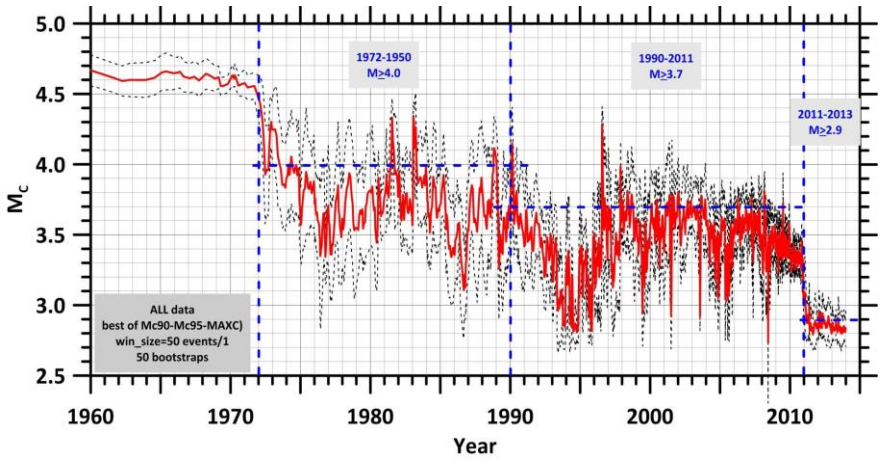

Figure 3.2.1. The time variation of Magnitude of completeness for the Aegean region during the time period 1960-2013. Since 1970, there are three time intervals with different Mc values as a result of the increase in monitoring capabilities and the number of stations (Kolligri, et al., 2014).

Table 3.2.1 The Mc variations in the Thales catalogue through the instrumental period (Kolligri, et al., 2014).

Time Period	Magnitude of completeness
1972-2013	4.0
1990-2013	3.7
2011-2013	2.9

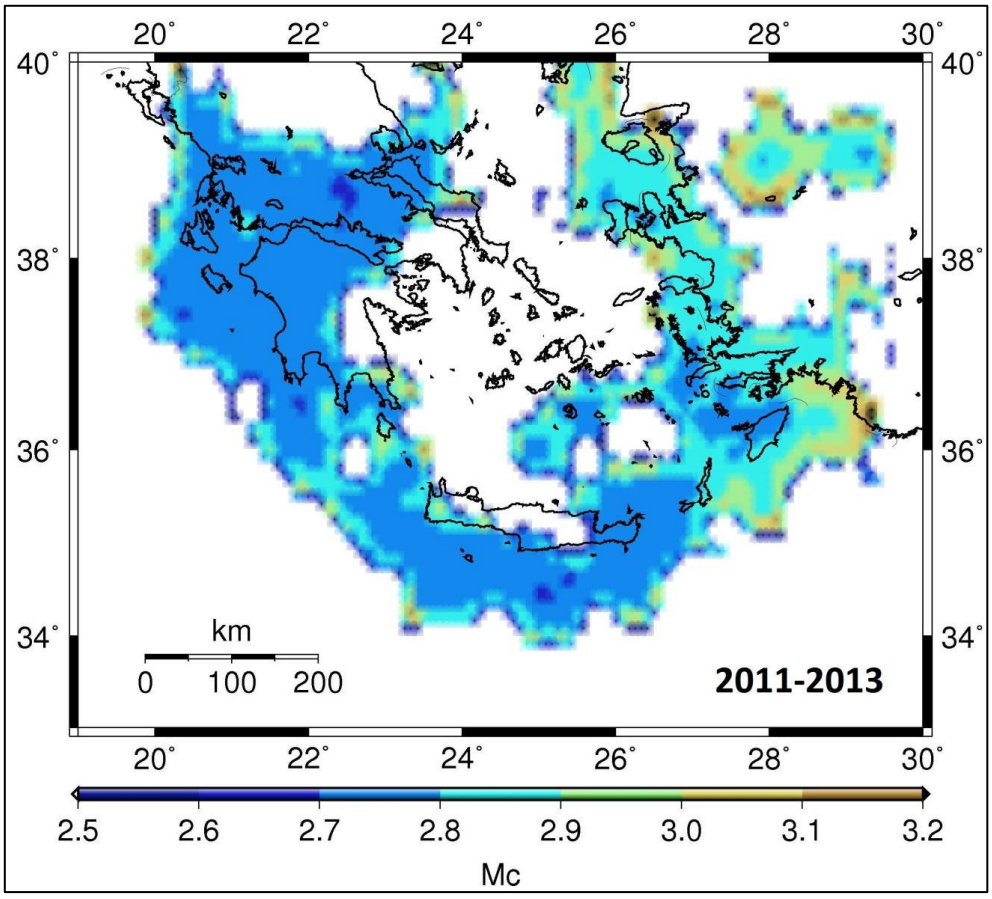

3.2.2 The 2011-2013 magnitude of completeness map, calculated with the Thales project catalogue for the Aegean area. The Mc for the western and central part appeared to have lower values compared to the eastern part (Kolligri, et al., 2014).

The Thales project catalogues covers the broader area of Aegean, but a focus has been made for the events located in South Aegean. Considering that the Magnitude of completeness has spatiotemporal variations and the catalogue completeness is crucial for the accelerated seismic release investigation, it is necessary to calculate the M_c values for the southern Aegean part having as a centre of attention the areas close to large faults. The calculation of M_c has been carried out by using a 0.2 degrees grid with 50 events as well as the "best combination" option in Z-map software (Wyss, et al., 2001) which compares the Maximum Curvature Technique and the Goodness-of-Fit Test with 90% and 95% confidence (Wiemer & Wyss., 2000; Wyss, et al., 1999; Mignan & Woessner, 2012). A new Magnitude of completeness map for the included in coordinates 33.5 – 37.0N and 20.0 – 30.0E rectangular has been calculated (figure 3.2.3). The spatial distribution of the Mc near the area of the large events (yellow stars in figure) seems to have small variation. The average value the western part of the investigation area is approximately 2.7. In the area close to the 15/06/2013 large event, the Magnitude of completeness varies between 2.4 and 3.0 while in the broader area of the southern part it has mean value 2.7 which was considered as the optimal solution for the 2013 events .

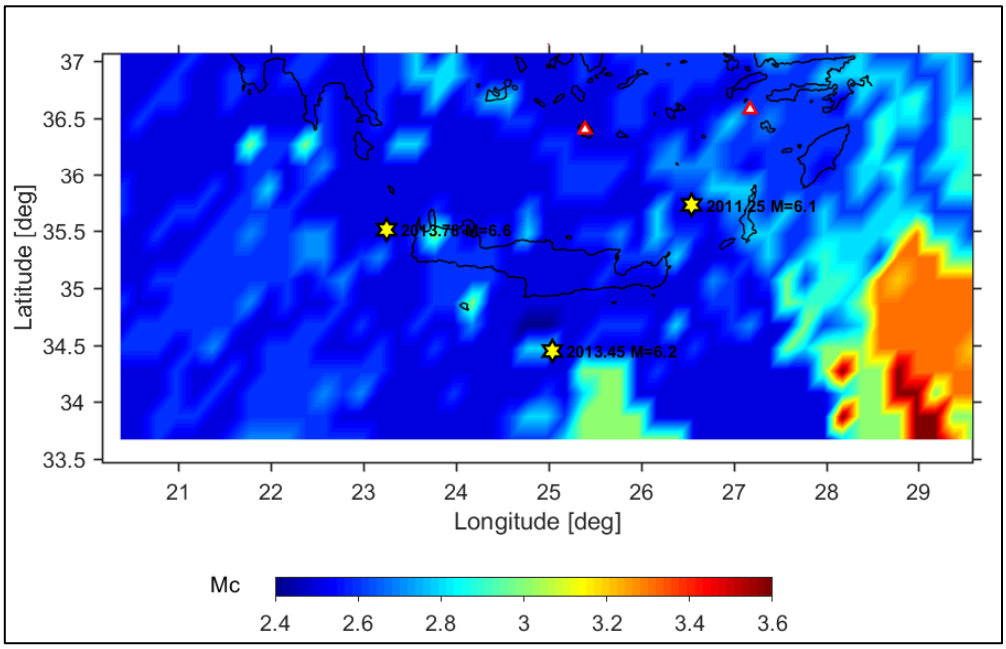

3.2.3 A detailed magnitude of completeness map for the Thales project catalogue calculated with the same parameters and method while this map is compiled only for the South Aegean area. The Mc for the western and central part, which is the focus for the 2013 events, seems to have an average Mc values around 2.7.

An additional effort to examine the completeness of the catalogue for the selected area has been made by inspecting the graphical representation of the M_c calculation method. In figure 3.2.4 there is the average value of Magnitude of completeness for the South Aegean area with the best combination option in *Z-map* software. The white squares are the Gutenberg-Richer law fitting, showing the relationship between event magnitude and frequency while the grey colour triangles are the same fitting but with a discrete curve. The Magnitude of completeness for the selected area and time period is down to 2.7 and the *b-value* is slightly less than one.

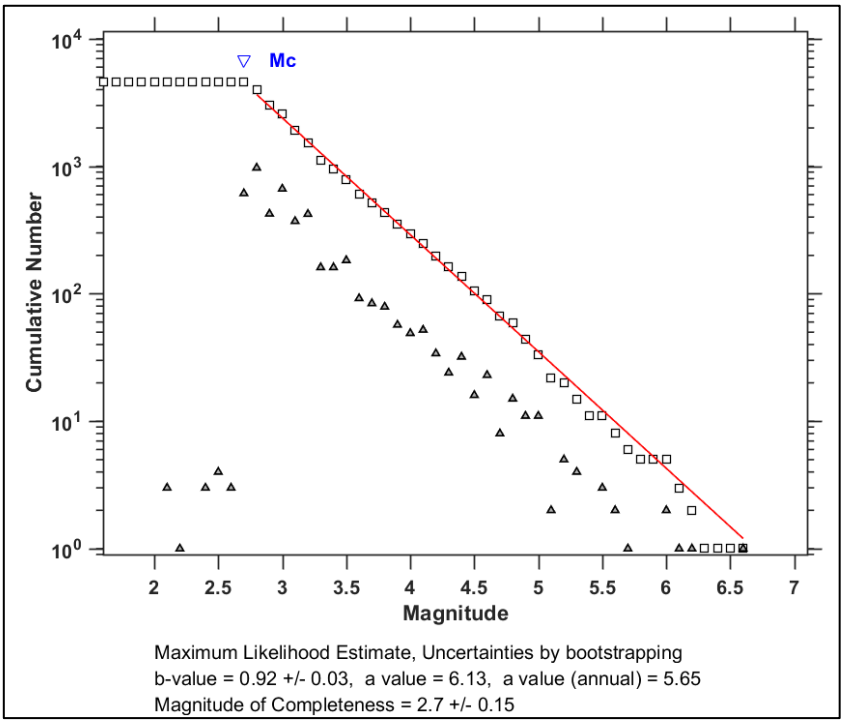

3.2.4 The graphical representation of the Gutenberg- Richer law which permits the calculation of the b-value and the Magnitude of completeness. In the South Aegean, for the time period between 2011 and the end of 2013, the best combination option with bootstrap fitting in Z-map software shown a b-value 0.92 and Mc average value down to 2.7.

The catalogue has been checked for consistency in reporting events, whereas the validation process requires the inspection of cumulative number of events curve for rate changes. The possible variation in the number of monitoring stations could lead into different event sampling which can be interpreted as acceleration or deceleration. The validation procedure

should be carried out after removing the aftershocks and swarms but without applying the M_c filter because the small events can provide information for the possible network operational changes (Wyss, et al., 2001). The cumulative number curve obtained from the Thales catalogues for the South Aegean area is presented in the left part of figure 3.2.5. The cumulative curve is almost a straight line but there are some small slope changes after the large events caused by the aftershocks (figure 3.2.5a). Aiming to remove aftershocks with a time efficient and deterministic approach, the Reasenberg window method (Reasenberg, 1985) has been used to apply a preliminary decluttering in the Thales catalogue. In this method the spatial correlation of the events is based on the magnitude of the largest event while the temporal correlation takes Omori's law into account (Molchan & Dmitrieva, 1992; van Stiphout, et al., 2012). The parameters that have been applied for the declustering method were: the minimum and maximum time period to identify clusters was set to 1 and 15 days, the Omori's law exponent p_1 was set to 0.95, the maximum epicentral error and depth was set to 5 km and 10 km and the effective cut-off magnitude and raise factor was set to 1.5 and 0.5. The declustered catalogue cumulative curve has been examined for rate changes. In *Zmap* software the new cumulative curve (figure 3.2.5b) has been separated in two equal time windows in order to inspect if there are changes in slope of the curve.

The normalized frequency versus magnitude curves and the annual rate as a function of magnitude appears to be the same for the selected time periods. The normalized frequency magnitude distribution has some small fluctuations in magnitudes above 5.5 which are expected, as in the second time window there are the 2013 large events. The results from the rate change evaluation suggest that for the period 2011 to the end of 2013 there were not any significant changes in the recording capabilities and magnitude reporting of the seismic networks that contributed in the compilation of the Thales project catalogue.

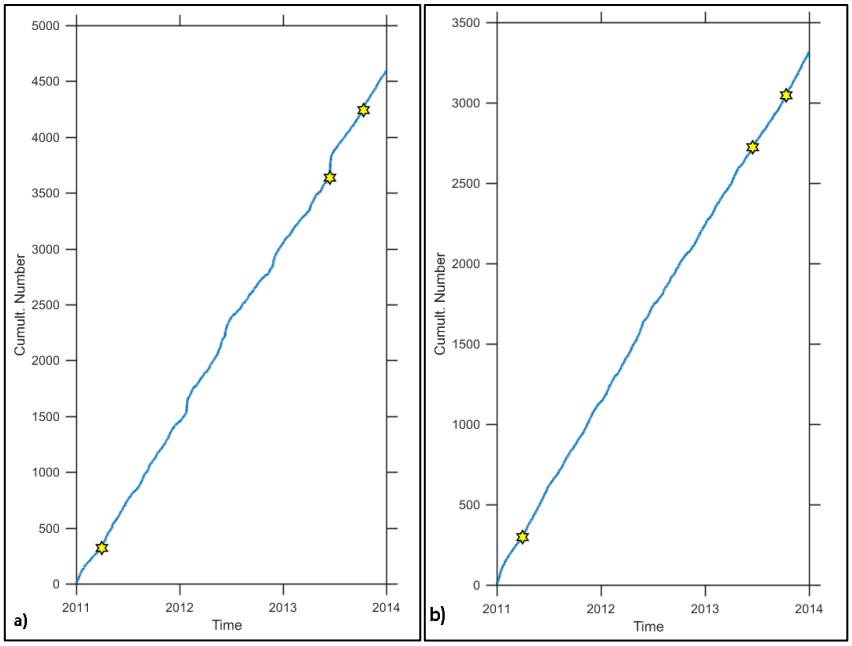

3.2.5 a) The Thales catalogue 2011 to the end of 2013 South Aegean cumulative number of events. b) the declustered catalogue cumulative number of events. The yellow stars are the events with magnitude larger or equal to 6.0 (figure obtained from Zmap).

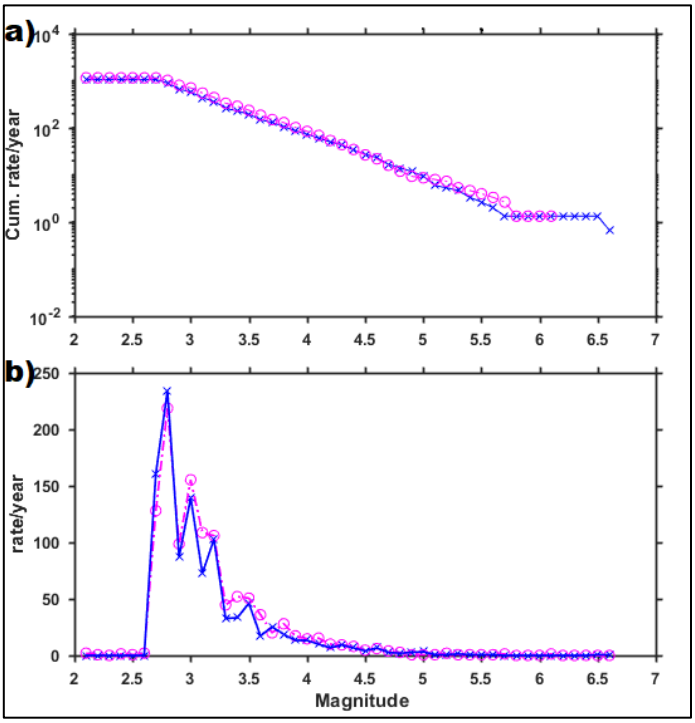

3.2.6 The cumulative (a) and the non-cumulative (b) annual number of events as a function of magnitude. The magenta o shaped points are representing the first time window (2011 -2012.5) while the blue x shaped points are from the second time window (2012.5- end of 2013) (figure obtained from Zmap).

3.2.2 The NOA-IG catalogw3ue

In 1893, the Institute of Geodynamics of the National Observatory of Athens (HL/National Observatory of Athens Seismic Network, 2018) known as (NOA-IG or NOA) started the first seismic network in Greece. The Hellenic Seismic Network with FDSN code HL and doi:10.7914/SN/HL initially was operating with analogue instruments. Most of the old seismometers have been replaced with the modern broadband ones after 2000. The NOA-IG has a dedicated webpage (NOA, 2018) that provides automatic earthquake locations from the SeisComP3 software (Helmholtz Centre Potsdam, GFZ German Research Centre for Geosciences, 2018) as well as manual location parameters by seismologists. There is also other seismological related information such as the focal mechanism derived from the waveform inversion of moderate-strong events. The quality control of the available sensors is achieved with the use of the PQLX software (Incorporated Research Institutions for Seismology, 2018) which uses a probability density function (PDF) to calculate the distribution of Power Spectral Density (PSD) for the seismic noise (Mc Namara & Boaz, 2005). To enhance its monitoring capabilities, the NOA receives waveforms in real time from other neighbour seismological networks and the waveforms are stored in a dedicated node of the European Integrated Data Archive (EIDA) hosted by NOA (ORFEUS the European Infrastructure for seismic waveform data in EPOS, 2018). The EIDA contributing networks for Greece and south-eastern Mediterranean region are the (HL/National Observatory of Athens Seismic Network, 2018), the (HT/Aristotle University of Thessaloniki Seismological Network, 2018), the (HP/Seismological Laboratory of the University of Patras, 2018), the (HA/Seismological Laboratory of the National and Kapodistrian University of Athens, 2018), the (HI/Institute of Engineering Seismology and Earthquake Engineering, 2018), the (HC/Hellenic Seismological Network of Crete, 2018), the Cyprus Broadband Seismological Network (CQ/Cyprus Broadband Seismological Network, 2018), Strong Motion Network of the Aristotle University of Thessaloniki (EG/EUROSEISTEST Strong Motion Network, 2018) and the Montenegrian Seismic Network of the Montenegro Seismological Observatory (ME/Montenegrian Seismic Network of the Montenegro Seismological Observatory, 2018).

Although the provided catalogue is not relocated with appropriate crust models, the large number of available recordings helps to have good estimation of the earthquake parameters. This catalogue has been used only to investigate the accelerated seismic release prior to the 16/04/2015 large event. Following the same procedure as the Thales project catalogue, the calculation of M_c for the NOA catalogue has been carried out using the same options and parameters. The search grid had spacing 0.2 degrees with 50 events in each point and there was a 50 times bootstrapping. The "best combination" option in Z-map software (Wyss, et al., 2001) compared the fitting techniques and kept the one with better results. The Magnitude of completeness spatial distribution on the eastern part of the investigation area (figure 3.2.7) between Crete and Rhodes island (28.0 - 36.0) has Magnitude of completeness range from 1.9 to 2.9. The area near the large events as well as the Gutenberg-Richer frequency magnitude relationship fitting (figure 3.2.8) suggest an average M_c value 2.5.

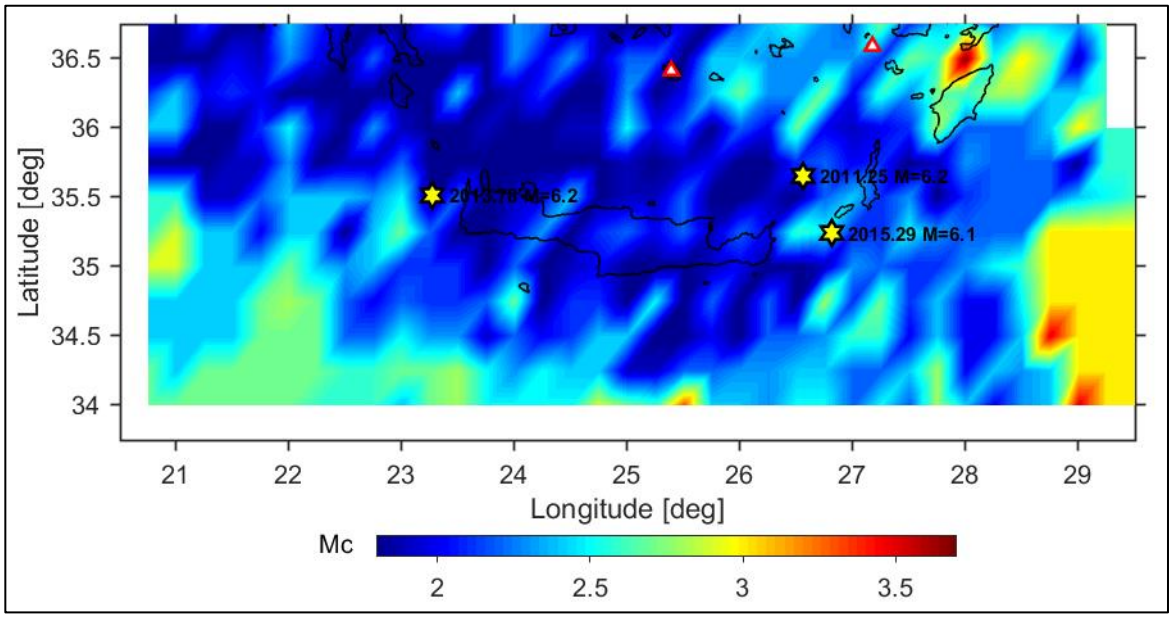

Figure 3.2.7 A detailed magnitude of completeness map compiled from the NOA catalogue for the South Aegean area. The Mc for the eastern part, which is the focus for the 2015 event, seems to have an average Mc values around 2.5 (figure obtained from Zmap).

The NOA catalogue for the South Aegean limited in the time period 2011 to 16/04/2015 has almost 15000 events (figure 3.2.9a). The catalogue has been declustered with the Reasenberg method with the same parameters as the ones used for the Thales catalogue.

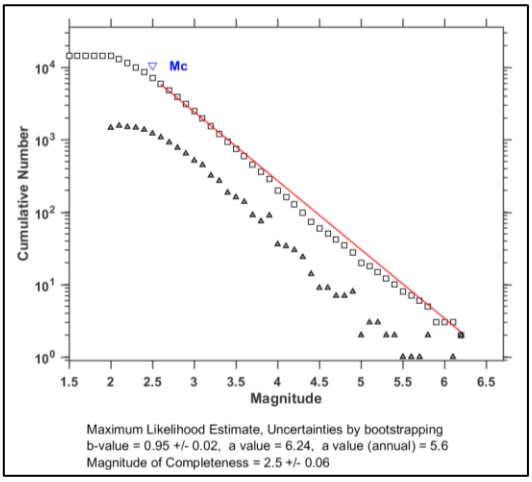

Figure 3.2.8 The Gutenberg- Richer law fitting for the time period is between 2011 and the April of 2015. The calculation methods in Z-map software shows a b-value 0.95 and Mc average value down to 2.5.

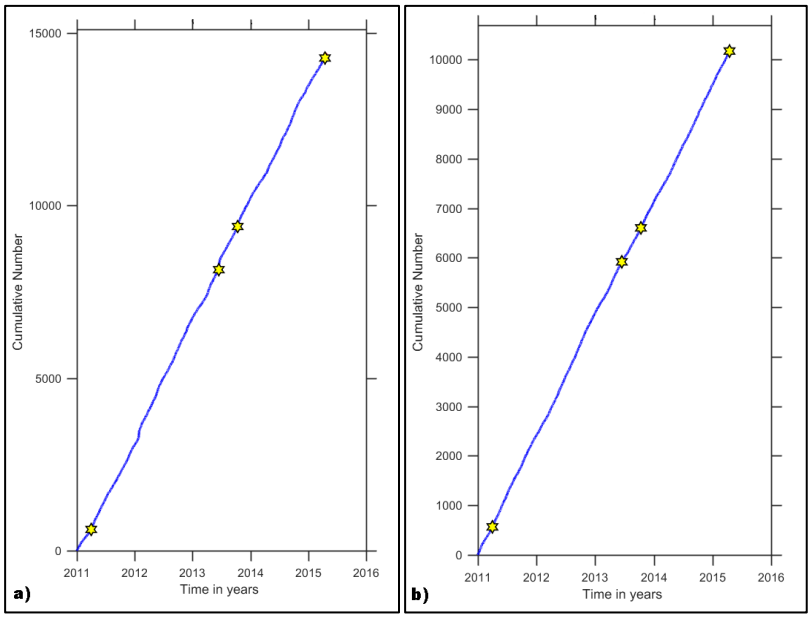

Figure 3.2.9 The a) diagram is obtained from the NOA catalogue for 2011 to 16/04/2015 South Aegean cumulative number of events. The b) has the declustered catalogue cumulative number of events which have been used to inspect the possible variation in the sampling method. The yellow stars are the events with magnitude larger or equal with 6.0 (figure obtained from Zmap).

On the declustered catalogue the cumulative number curve (figure 3.2.9b) has been inspected for slope changes. Two equal time windows (2011 -2013.2 and 2013.2-2015.3) have been used to identify the possible rate changes. The cumulative and non-cumulative plot of the frequency-magnitude distribution for the two time windows appears to be the same. The normalized frequency magnitude distribution has some small fluctuations in magnitudes above 5.5 which is normal, considering that in the second time window there are the 2013 and 2015 large events. Therefore, the conclusion is that there were not any significant alterations in the seismic network recording capabilities and magnitude reporting.

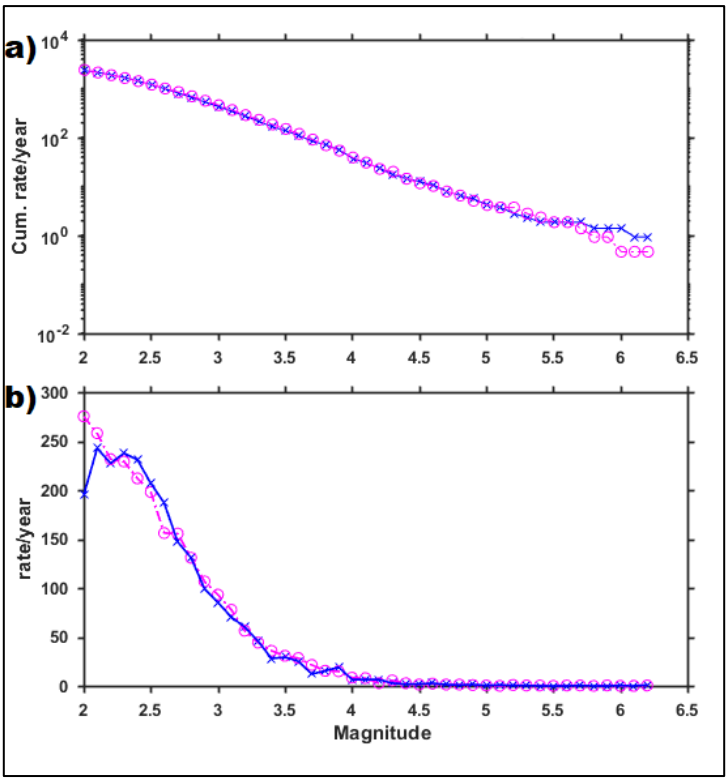

Figure 3.2.10 The cumulative (a) and the non-cumulative (b) annual number of events as a function of magnitude. The magenta o shaped points are representing the first time window (2011-2013) while the blue x shaped points are from the second time window (2013- 16/04/2015) (figure obtained from Zmap).

A final test to check the quality of the NOA catalogue have been carried out by comparing the cumulative number curves obtained from the NOA and the Thales catalogue. The two catalogues have different end day, minimum magnitude and depth limits. In order to compare them the maximum depth was set to 40km, the end period of NOA catalogue was reduced to end of 2013 and the minimum magnitude for both catalogues was set to 2.7. The depth limit was set to keep only the crustal events while the Magnitude of completeness of the Thales catalogue was the one that set the magnitude threshold in the two catalogues. The two cumulative curves are plot together in the figure 3.2.11. The blue line represents the NOA while the red the Thales catalogue. The cumulative number curves have strong shape similarities, there are only small changes in the slope of the NOA line after the 2013 events. The catalogues in this test have not been declustered so it appears that the NOA catalogue has more events for the 2013 aftershock sequences.

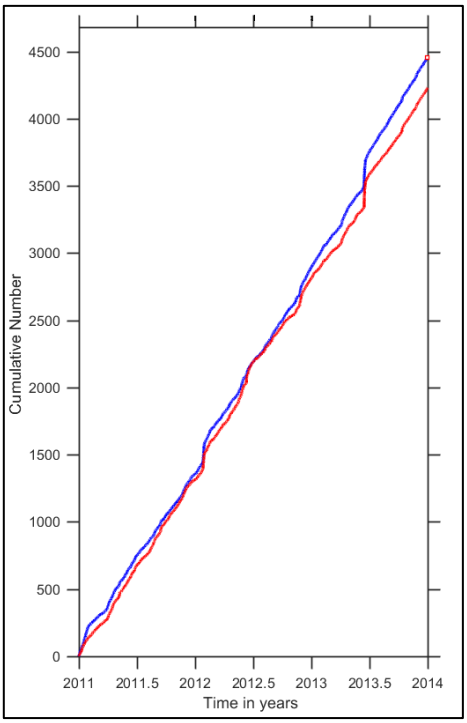

Figure 3.2.11 The cumulative number curves for the Thales (red line) and NOA (blue line) catalogues. Filters as the minimum magnitude 2.7 and maximum depth 40km have been applied to have the same number of events in the examined period 2011- end of 2013 (figure obtained from Zmap).

3.2.3 The HSNC catalogue

The HSNC has a descent earthquake database with good data completeness for the period the examined period from the beginning of 2008 until the end of September 2015 as it is presented in figure 3.2.12. The calculation of M_c has been carried out by using a 0.1 degree grid with 100 events as well as the "best combination" option in *Zmap* software (Wyss, et al., 2001). The Mc values close to Crete Island is down to 2.0 at the majority of the western part and it takes values between 2 to 2.7 at the central and southern part of the island, while the larger but still small values down to 3.0 are presented in the eastern part of the HSNC coverage area (Chatzopoulos, et al., 2016). Despite the fact that the network has good data completeness, the catalogue has not been used in accelerated seismic release research. The main reason is that the seismic stations have been under upgrades-changes the past years, which means that there are possible inhomogeneities in the reported magnitude values. In addition, the increase in the number of stations could give a false alarm of accelerated deformation as the number of the recorded events has been increased which is noticeable in figure 3.2.13, where the slope of the cumulative number curve changes after 2011.

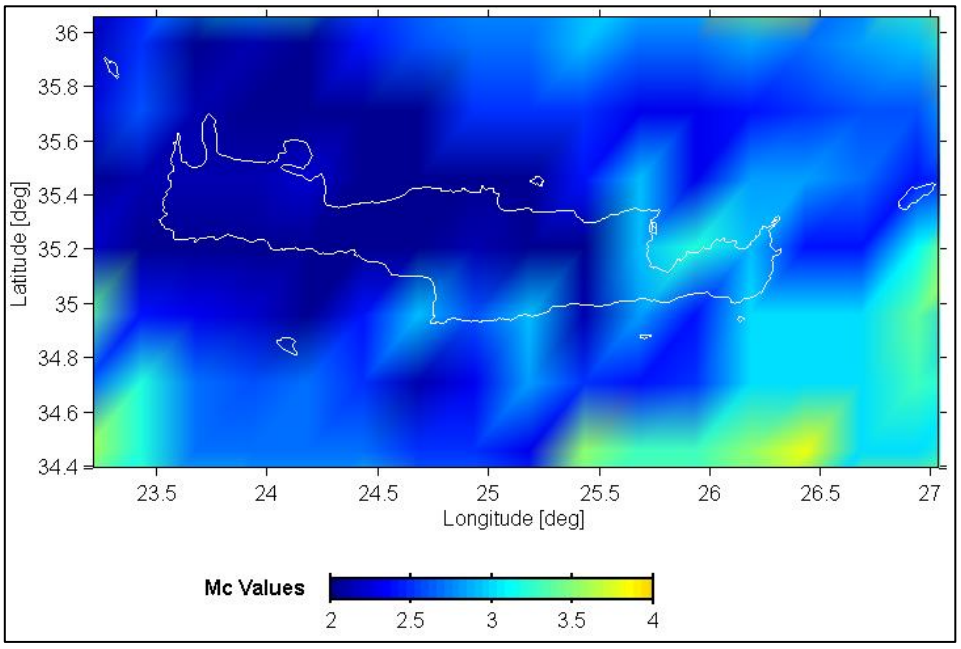

Figure 3.2.12. The Magnitude of Completeness map for close vicinity of the Crete Island area. The map has been composed in Z-map software with best combination option using the manual catalogue of the HSNC from 2008 until end of October 2015 (Chatzopoulos, et al., 2016).

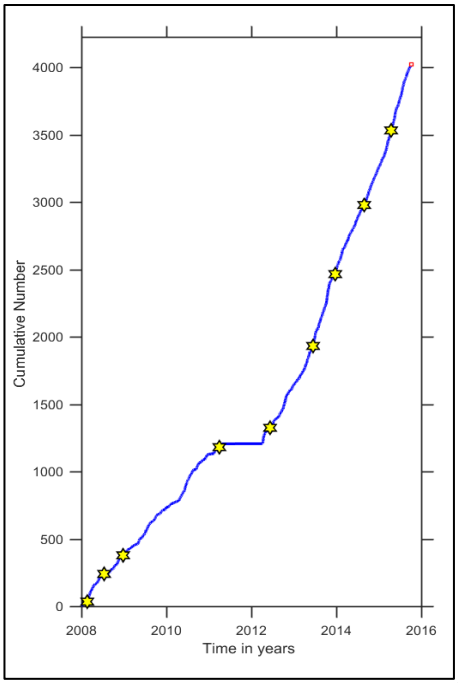

Figure 3.2.13 The cumulative number of events of the HSNC catalogue for the time window 2008 to mid of 2015. The yellow stars are the events with magnitude larger or equal with 6.0. (figure obtained from Zmap).

3.3 Methodological Aspects

3.3.1 The ASR software

Aiming to test the theoretical framework and the validity of the common critical exponent in real data, the Thales and the NOA catalogues have been used to evaluate the seismic hazard in the South Aegean region with the use of the accelerating seismic release method. The first attempts to quantify the seismic energy release in this research have been carried out with the use of an old accelerated seismicity scanner which was written in Fortran code. This program, even though it was written in an old programming language and it was very small in terms of size, had a search process that was very time consuming even for a modern computer with a strong processor and large RAM capacity. The use of graphics in Fortran code is avoided as they are difficult to write. In addition, the figure creation process is slow and usually an external application is needed to plot the results (Padman, 2007). Every attempt to scan an area such as the South Aegean can last from many hours to days

which was dependent on the number of events in the catalogue as well as the other searching parameters such as the grid, the search radius around a point, the maximum depth and the minimum number or earthquakes. For the research purposes of this thesis, a new GUI program which has better search algorithm, optimized for speed and has functions that enables to scan the area for a common critical exponent (the Fortran scanner was searching only in Benioff strain) has been created in the MATLAB (MATLAB-Mathworks, 2018). The program is divided in several script-functions assigned to carry out different tasks. The basic structure and commands of the new GUI software are presented in the next subchapter, the whole script is in appendix which has help comment lines starting with *%* (`% comment`).

3.3.2 The features of the software- Brief explanation of the code

The procedure of executing the software as well as a summary of the most basic functions, commands and the reasons for using each of them will be provided. The analysis of accelerated seismic release first step is to execute the *`main.m`*, which is a function that launches a singleton pattern which is a software design pattern with one instance that connects all the available search parameters with the rest functions (Gamma, et al., 1994). The purpose of the *`main.m`* is only to prepare the research process in a visual and user-friendly environment (figure 3.3.1). It contains mostly visual related commands and some code that is useful for converting-controlling the catalogue data. On the top left corner there are two pushbuttons designed to load a map and the earthquake catalogue. The map needs to be a coastline type file with two columns (x, y) that define the shape of the borderlines. The one that has been used in this research is obtained by (National Oceanic and Atmospheric Administration , 2015). The catalogue files have five variables with the earthquake parameters depth, magnitude, time, longitude and latitude. The time format of the catalogue yyyy-mm-dd HH:MM:SS (yyyy is year with four digits, mm the month, dd the day etc) have been converted to a serial date number with `datenum` command (datenum-MathWorks, 2018). Both files need to be created and saved in *.mat format. In the appendix there is a code that enables the conversion of a tab delimited text file to a

MATLAB catalogue compatible with the accelerated deformation software (`catmaker.m`).

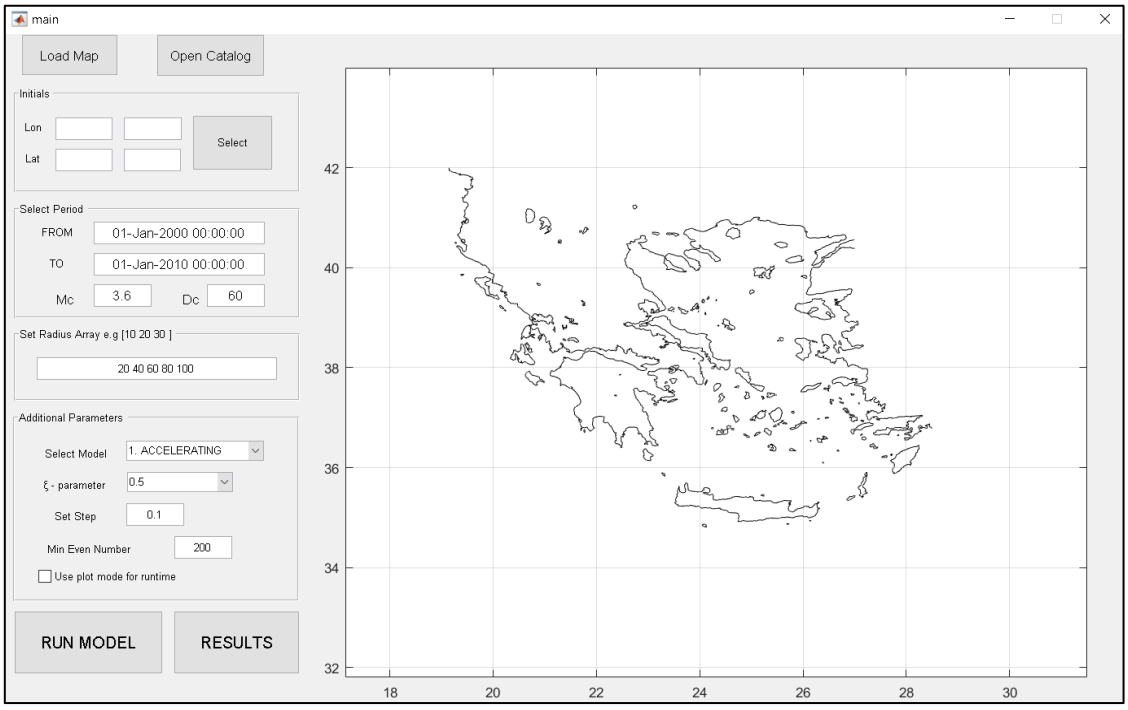

Figure 3.3.1 The analyses procedure start by launching the function `main.m` which is a singleton pattern that enables the scanner preparation with visual inspection and edit of the research parameters.

Below the map and catalogue pushbutton there are four boxes to insert the numerical values of the coordinates for the search area. An additional pushbutton enables the graphical selection of the research rectangular. The next option controls the catalogue events by applying filters such as the starting and the ending time of the excitation period as well the minimum magnitude and maximum depth of the events. The rest of the parameters are for optimizing the accelerated-decelerated seismic crustal deformation model (see below). In this software, the identification of the possible seismicity patterns has been carried out with circular shape areas. There are options that control the size of the searching area by customizing the number and the size of the search circles. Below these options there are settings to arrange the minimum number of events, the grid size and the seismicity pattern (acceleration or deceleration) that will be used. So far, the aforesaid options have been used

and extensively tested by other researchers (see 3.3.1). The Bufe & Varnes (1993) work proposed that the seismic release can be calculated directly from the seismicity catalogues by converting the earthquake magnitude to energy or Benioff strain or event count. An option that enables to fit the data in power law sense for the different energy exponents has been used. This option permits using the critical exponent m_ξ as a validation tool for the results. In a successful seismicity pattern identification, for all $0 \leq \xi \leq 1$ the critical exponent should have similar values $m_\xi \approx 0.3$ for acceleration and $m_\xi > 1$ for deceleration. By pressing the RUN MODEL pushbutton, the process starts and in the MATLAB command window information is presented regarding the search progress as well as statistics for the completed iterations (figure 3.3.2). A last visual detail is a checkbox that enables the graphical representation of the power law fitting against the linear fitting (figure 3.3.3) which is a nice to have option, but it is better to use it for small areas as it makes the search process slow.

```
line: 35.2, 15.10 s, C:[0.25-0.75], n:[0.16-0.35],r:[0.81-1.00]
line: 35.3, 18.72 s, C:[0.25-0.75], n:[0.14-0.53],r:[0.80-1.00]
line: 35.4, 21.78 s, C:[0.23-0.94], n:[0.14-0.53],r:[0.80-1.00]
line: 35.5, 26.24 s, C:[0.23-0.94], n:[0.14-0.53],r:[0.79-1.00]
line: 35.6, 28.81 s, C:[0.23-1.02], n:[0.14-0.53],r:[0.76-1.00]
```

Figure 3.3.2 The analysis progress as it is displayed in the MATLAB's command window. From left to right there are the latitude of the grid point that has been scanned, the time to complete this line, the minimum and maximin for curvature (c) critical exponent (n) as well as the power law fit correlation coefficient (r).

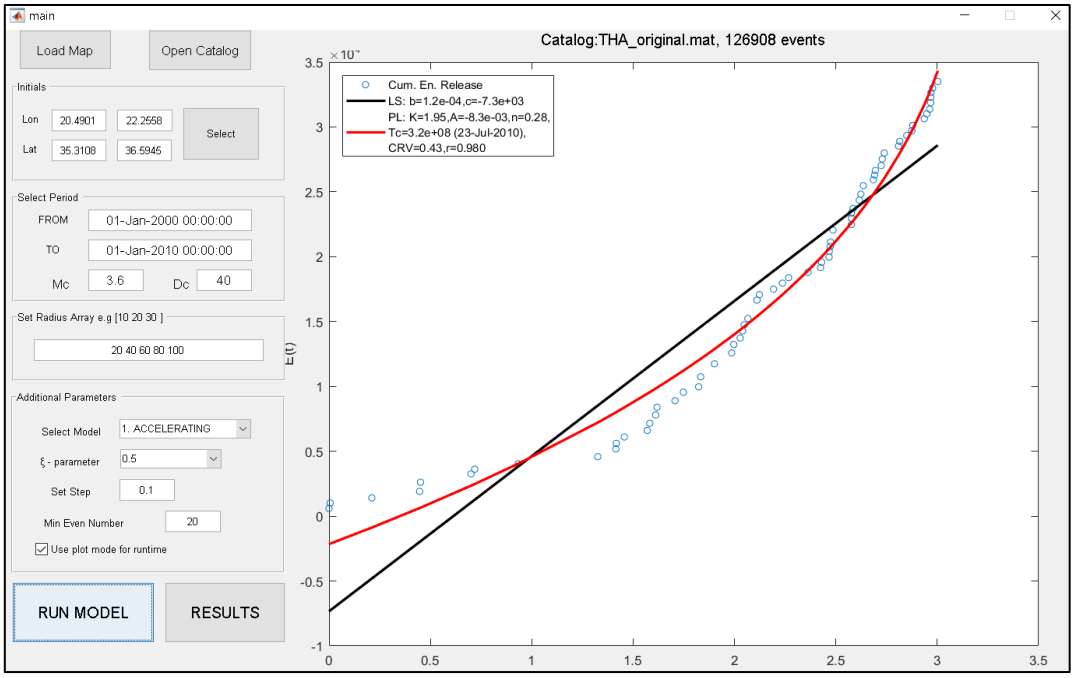

Figure 3.3.3 The graphical representation of the power law fitting (red line) against the linear fitting (black line) and with blue circles are the events.

When all parameters are set in the `main.m`, the search starts by activating the ACCscanner.m where two `for` commands are responsible for the search grid (for-MathWorks, 2018):

```
% create the grid with user defined step
for yepi=ystart:step:yend
    for xepi=xstart:step:xend
```

The scanner follows a loop in a loop sequence. The grid of the under-investigation area is defined by the step. The internal loop examines the longitude of the defined area between `xstart` and `xend` while the external loop is for the latitude. In every iteration, it searches for a latitude value through all the possible longitude coordinates, as the iteration is completed goes to next latitude value. Aiming to avoid keeping in memory unnecessary data and make the script faster, a series of initiation commands have been used. An example of the initiation process, is the matrix preparation according to the available data:

```
% Initialize local model array parameters for speed
La = length(radarray);
CVR = zeros(1,La);
```

The `length` command finds the largest number of elements in a vector (length-MathWorks, 2018). In this case, the length of the radarray is the number of the search circle radii that have been assigned to scan in every grid point. The `zeros` command is used to create a matrix with zeros, an option that helps to have a preallocation and a constant matrix size which can improve code execution (zeros-MathWorks, 2018). In this instance, for every iteration it creates a one row matrix with the columns number based on the search circles. Another example with an `if` expression that uses a logical operator to execute other commands (if-MathWorks, 2018) :

```
%index the area according to a specific radius
idx = find(D<=radarray(i));


% run the model if the number of events is satisfied
if length(idx)>=min_events
```

An index `(idx)` is created with the find command which returns the nonzero elements of matrix or an array of data that meet an operator defined condition (MathWorks, 2018). In this example for every iteration, the find command is used to search and keep the circles that include events. The Euclidian distance D between the grid point and epicentre of the events should be less or equal to the circle radius in order to satisfy the distance criterion.
The if statement is used to permit the indices having more than the minimum number of events (`min_events`) to execute the `GetCurvature.m` function that is responsible for fitting the data in the power law model.
The `GetCarvature.m` function of the scanner is optimized to calculate the Benioff strain by fitting the data in a power law sense. The Benioff strain for each event is calculated with the use of energy-magnitude equation (3.1.3):

$$\log E_i = 1.5 * M + 4.7$$

where E the is the energy of the i[th] earthquake in joules, M is the magnitude of the event (Papazachos & Papazachos, 2000), or as it is used in the MATLAB script code:

```
Es=10.^(1.5*M) + 4.7);
[bt,Es]=qbenioff(t,Es,ksi);
```

The initial variable `Es`, the energy of each earthquake calculated from the magnitude M, becomes an input in qbenioff internal function along with time `t` and `ksi` (ξ), the energy exponent. The qbenioff function uses a simple `for` loop to calculate the cumulative energy and at the same time it uses the `ksi` to transform the energy values into Benioff strain or cumulative number of events that permits to calculate the different values for the critical exponent m_ξ. The cumulative energy (or Benioff strain or number of events) is fitted in the power law function pwlawfunc with the nonlinear regression solver `nlinfit` which applies the nonlinear least squares algorithm proposed by Levenberg-Marquardt (nlinfit-Mathworks, 2018). The Levenberg-Marquardt method is a robust technique, but it may achieve slow converge or even not work when there are large fitting residuals (Seber & Wild, 2003). The robustness of the nlinfit algorithm has been enhanced based on the work of DuMouchel & O'Brien (1989) and Holland & Welsch (1977). The estimated residuals after each fitting iteration, are used with a least squares algorithm that recalculates the function's weights. The fitting procedure is separated in two steps aiming to avoid having large residuals and increasing the fitting speed. The first part involves a preliminary fitting with the initial values for the power law function the ones predefined in `beta`. The next step is to do a second fitting with initial values the ones obtained from the results of the preliminary fitting:

```
%make a preliminary estimation for ACC or DCC respectively
if model==1, beta = [2 0 0.33 max(t)]; end
[Bf,r,J,COVB,mse] = nlinfit(t,Es/max(bs),pwlawfunc,beta);
```

```
% fit power-law model function non-least squares case
[Bf,r,J,COVB,mse]   =   nlinfit(t,Es/max(bs),pwlawfunc,[bf(1)
bf(2) bf(3) bf(4)],statset('MaxIter',100));
```

Where `r` are the fitting residuals, the `J` is Jacobian matrix with all the first-order partial derivatives, `COVB` is the estimated variance-covariance matrix for the estimated coefficients and the mse is an estimation of the variance of the error.

As mention in 3.1.1 the 'legacy' version of the accelerated deformation software compiled in Fortran has an optimization method like the `lsqcurvefit` in MATLAB which assumes that the data have a least squares regression solution (lsqcurvefit-MathWorks, 2018). The two methods `nlinfit` and `lsqcurvefit` have strong similarities in terms of optimization, someone can argue which is better but without a fitting comparison in a real study case, there is no conclusion which one is more suitable for this research. A series of random tests in real catalogues shown that the second method present rough fitting in the boundary values especial when the couple last events have a considerable magnitude difference with the previous ones. The `lsqcurvefit` solution for the time to failure power law equations, turns the curve upwards in the edges like a U shape. This effect is more noticeable in the energy versus time fitting which might be the reason for making the Benioff strain more popular among the scientists especially before a couple of years ago where the computational power and fitting algorithms were more limited. Despite the craggy fitting, the legacy software has been tested for accelerating seismic patterns with the common critical exponent criterion and there were not any satisfactory results as the critical exponent was underestimated due to the fitting. A random example where the two methods are applied for the same events with the identical conditions and initial parameters are in figure 3.3.4. The blue circles are the events, the black line is the linear fitting which is used to calculate the curvature parameter, the red line is the power law fitting with the `nlinfit` while the blue one is for the `lsqcurvefit` method.

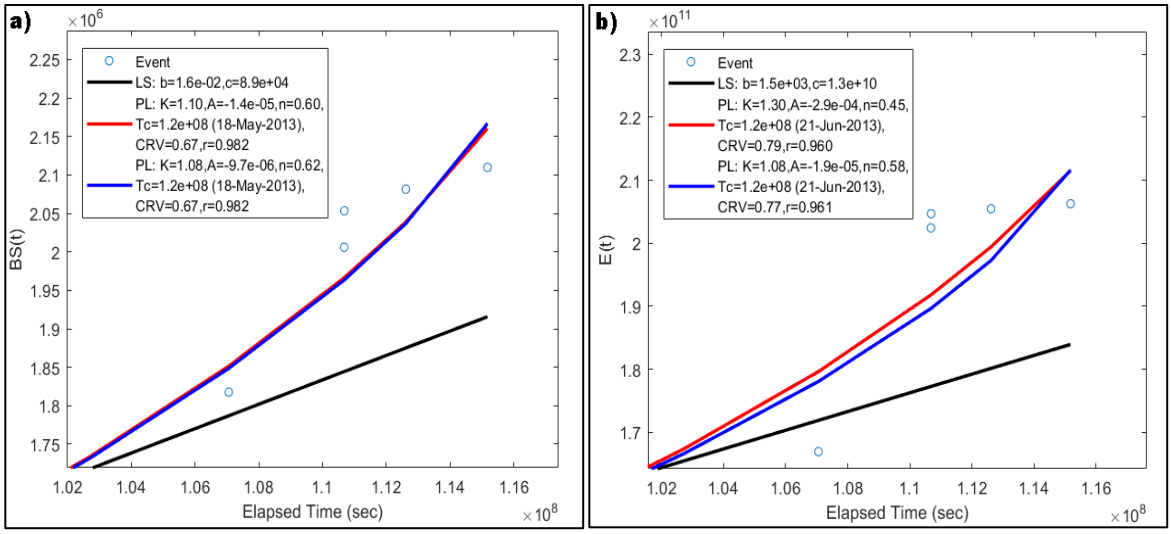

Figure 3.3.4. The evaluation of the fitting results and the capabilities of the `nlinfit` *(red line) and* `lsqcurvefit` *fitting methods for the Benioff stain exponent* $\xi = 1/2$*(a) and for the energy* $\xi = 1$*(b). It is clear that the second one (blue line) has a rough fitting in both cases (Benioff strain and Energy).*

In each step, the curvature parameter $C(Rc)$ as well as the critical exponent n for different radius around a point is computed. The curvature parameter is the root mean square error of the power low fitting against the root mean square error of the linear fitting proposed by Bufe & Varnes (1993). The root mean square error of the two fittings is estimated by:

```
% Calculate the Power Law and Linear Fit RMSs
RMSlin=norm(Es-LNfit);
RMSpow=norm(Es-PLfit);
```

The `norm` is used to find the Euclidean length (norm-MathWorks, 2018). The `Es` is the cumulative Benioff strain release (or energy of the earthquakes or the cumulative number of events) while the `LNfit` and `PLfit` are the linear and the power law fitting respective. The curvature parameters `CRV` is calculated by:

```
% Get the curvature parameter C=(Power law fit)/(Linear fit),
CRV=RMSpow/RMSlin;
```

The optimal radius is considered to be the one with the lowest curvature parameter. Although the software is set to consider the one with the smallest curvature as the optimal radius, for the successful cases the radii that have been excluded by the software have been manually examined. Sometimes, at the same grid point two different size circles could give similar results, the size difference was small like 2-3 or less radius. If the lowest curvature parameter option does not filter the results, then it seems that the larger circles tend to miscalculate the critical time. An example from the 12/10/2013 case is presented in figure 3.3.5. The fitting on the left diagram (a) is achieved with a 16-radius circle while the other one is with an 18-radius (b). The aforesaid initial criteria for the seismic pattern identification are satisfied for both cases, there is a common critical exponent for all ξ $(0\leq\xi\leq1)$, the correlation coefficient is more than 0.97 and the curvature parameter is less than 0.55. In this example the first fitting has 48 events while the second one has 56 as the search circle is larger. The curvature parameter has slightly lower value in first case which indicates a clearer accelerating pattern. The smaller circles were considered as better solutions as the critical time estimation was closer to the real one.

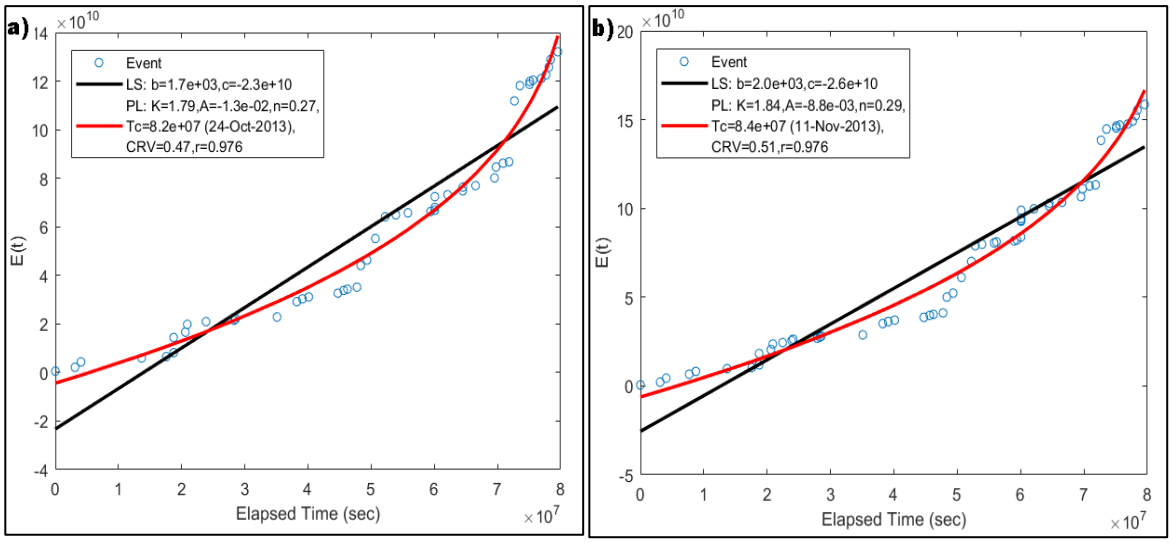

Figure 3.3.5. The same search parameters with slightly larger circle in (b) gives acceptable results but with a miscalculation in the estimated time of the mainshock.

An estimation of the power law fitting accuracy is checked by the correlation coefficient:

```
% get correlation coefficient R^2
Crmat = corrcoef(PLfit,Es); R = real(Crmat(1,2)^2);
```

The `corrcoef` is used to find the correlation between the variables power law fitting `PLfit` and the cumulative quantity `Es` (corrcoef-MathWorks, 2018). The correlation coefficient accepted values are set as R ≥0.95.

The inspection of the result has been carried out in `Accres.m` which creates or uses the existing singleton pattern (figure 3.3.6). This is another visual inspection window that enables to control the amount of the presented results by applying some filters. The available options are to set the accepted values for the curvature parameter, the critical exponent and the correlation coefficient of the power law fitting. Each grid point that has a fitting, regardless of the fitting results is noted with a different color on the original curvature critical exponent and filtered. The color scales changes according to the range of the results. The options that have been used to filter the result are discussed in the next subchapter (3.3.3).

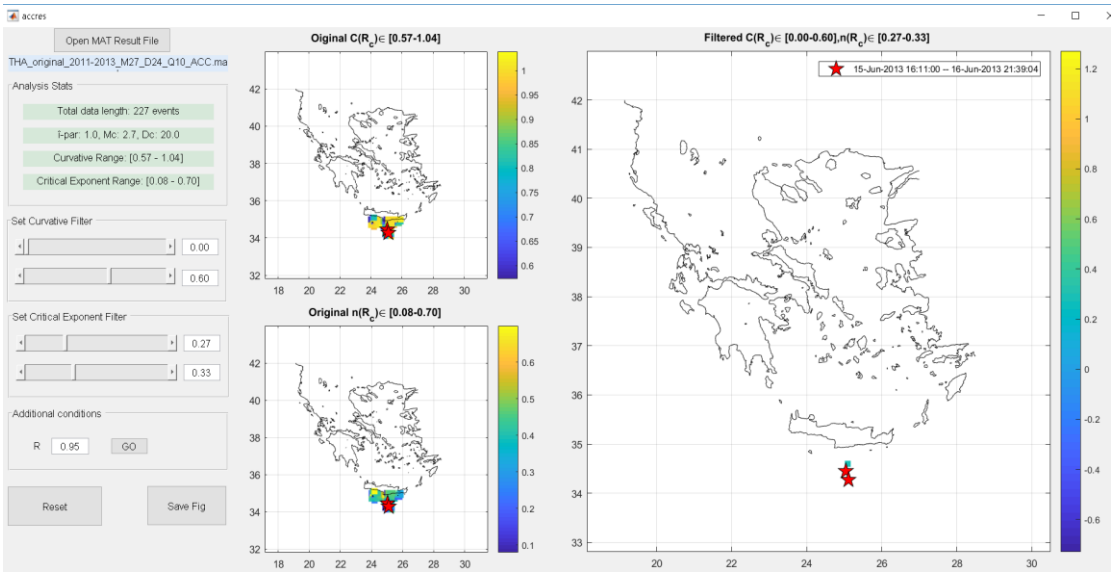

Figure 3.3.6 The accres.m is used to inspect the results and constrain the fitting parameters. On the left side there are filters as well as two small maps with the unfiltered curvature and critical exponent values. On the right side there is a large map showing the locations that satisfy the curvature critical exponent and the correlation coefficient limits.

3.3.3 Procedure – Parameters' selection

The accelerated seismic release time to failure model and the related software have been used mainly as a tool to predict large events, but a large amount of researchers has use it in a retrospective approach mainly after a strong earthquake, in order to examine the possible accelerated areas and/or establish a theoretical model (Papadopoulos, 1986; Bowman, et al., 1998; Varnes, 1989; Bufe & Varnes, 1993; Brehm & Braile, 1999; Papazachos & Papazachos, 2000; Rundle, et al., 2000; Tzanis, et al., 2000; Bowman & King, 2001; Papazachos & Papazachos, 2001; Di Giovambattista & Tyupkin, 2001; Di Giovambattista & Tyupkin, 2004; Papazachos, et al., 2002; Tzanis & Vallianatos, 2003; Scordilis, et al., 2004; Papazachos, et al., 2005; Mignan, et al., 2006; Mignan, et al., 2007; Mignan, 2008; Mignan & Di Giovambattista, 2008). In this thesis framework, the accelerated-decelerated seismic crustal deformation software has been used a posteriori as a validation method for the existence and the use of the common critical exponent m_ξ to identify the preparation period. According to the proposed theory (3.1.2), the area which undergoes accelerated seismic release will have a specific time window where the critical exponent will be $m_\xi \approx 0.3$. This should occur for every energy exponent ξ selected in the range [0,1]. More specific the values 0, 1/2 and 1 were selected since they represent the cumulative number of events, the Benioff strain and the cumulative seismic energy respectively. In the under-study area of South Aegean, during the period 2013-2015 three strong earthquakes occurred. These events were examined for power law patterns with the use of the common critical exponent m_ξ. The strong event was excluded from the analysis, all the examined time windows had an end date always just a couple hours before the mainshock. The starting times of the three seismicity patterns were unknown. A trial and error approach was necessary in order to determine the initial time of any possible precursory activity. In the literature there two approaches. The older one supports the idea that the accelerated seismic release needs a large amount of time such as 15-20 or even more years (Bufe & Varnes, 1993; Papazachos & Papazachos, 2000; Di Giovambattista & Tyupkin, 2004; Tzanis & Vallianatos, 2003; Scordilis, 2006), while the most recent one identifies the excitation period of much shorter catalogues (De Santis, et al., 2010; Mignan, 2008b; Tiampo, et al., 2008; Papadopoulos & Minadakis, 2016). Considering the latest additions in

the seismicity pattern literature, the trial and error search for the starting time was up to 10 years before each mainshock.

The minimum number of events that have been used to define a power law pattern varies in literature. In Bowman, et al., 1988 work it is stated that the accelerated seismic release model can predict a foreshock with a small number like 4. Mignan uses M_{min}= 6 (Mignan, et al., 2006) while in the research (2008) there is Bowman's later suggestion that the accelerated seismic release will work better with M_{min}=10. Hardebeck after testing the M_{min} = 4,6,8 and 10 found out that the minimum number of events does not affect much the curvature parameters, which means that the curvature parameter is not strongly influenced by M_{min} (Hardebeck, et al., 2008). In the aforesaid research the minimum magnitude was set based on Bowman's proposal that takes the magnitude range into account. The use of as few as the proposed minimum number of events is based on the assumptions that the preshock catalogue has earthquakes with magnitudes 2 units smaller than the large event (Bufe & Varnes, 1993). This theory works only if you already know the magnitude of the expected mainshock. In an instance where someone is trying to identify an accelerated deformation process of a future event, the 2 units smaller magnitude rule could lead to no/or wrong results. On the other hand, using events that have small magnitudes in combination with low values of M_{min} will also produce false alarms. In this thesis, with the purpose of having a balanced in terms of sensitivity accelerated seismic release fitting, the minimum number of events was set to 25. In the literature the minimum magnitude of the preshocks that can produce power law phenomena varies. The early works on accelerated seismic release suggest the use of moderate magnitude earthquakes while the later researchers De Santis, et al. (2010); Mignan (2008b); Papadopoulos & Minadakis (2016) have used smaller values like $M_{min}\geq3.0$. Within the present thesis, the minimum magnitude has been tested and all the available values down to the magnitude of completeness of each catalogue have been examined.

The process to identify the seismicity pattern start when the whole catalogue and a coastline type map have been loaded in the accelerated seismic release software (figure 3.3.7). The Thales catalogue with seismic events for the broader Aegean area, to focus on the investigation area a rectangular that includes all events for longitude from 20.0 to 30.0 and the latitude from 33.5 to 37 was selected (figure 3.3.7). The main reason for selecting

to investigate the whole South Aegean was to evaluate with real data the identification capabilities of the accelerated-decelerated seismic crustal deformation software. In addition, the idea of searching for seismicity patterns only in the area around the epicentre of the mainshock could lead to biased results in the retrospective analysis as well as to the forecast attempts. The first couple of runs were rough estimations, aiming to check if there are seismicity patterns before the large earthquakes of 2013 and 2015. The area was scanned with large spaced square grid 0.1 degrees, a few circles have been used with 5km increase in size and the trial starting time was decreased by 6 months in every iteration. Afterwards, an additional focus has been applied in the regions where the first results suggest that there are seismicity patterns. In order to have enhanced resolution and detailed results in the accelerated decelerated seismicity crustal deformation output maps, the square grid size was reduced to 0.05 degrees and the size of the expanding search circles was increasing by 2km in each attempt. The time window had a fixed end point, while the starting point was defined with the trial and error approach. Initially, the iteration has been carried out with a narrow time window, beginning approximately 3-4 months before the mainshock and its size was increased by one month after every completed run. In the case where a time window had multiple starting points with the same results, the earlier starting point was used.After the identification of the possible seismic acceleration time window the process has been continued until there were no other positive results for more than 8-12 months. The end and starting time are numbers that depend on the existence of events in the specific time, circle size and grid point. The catalogue with the events of a successful seismic pattern identification may have different, smaller limits than the ones assigned in the software.

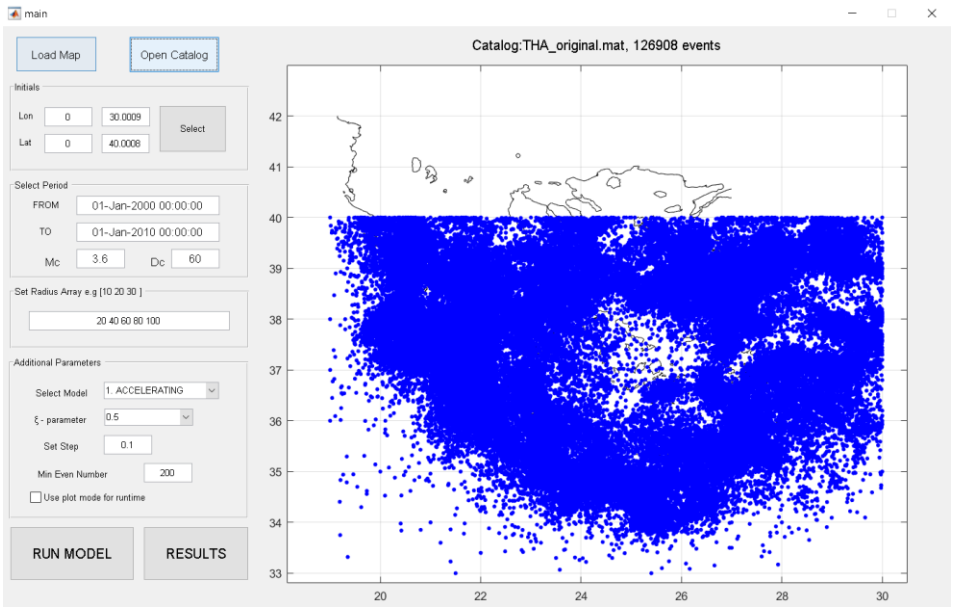

Figure 3.3.7. The Thales project seismicity catalogue and the coastline for Greece have been loaded to the software.

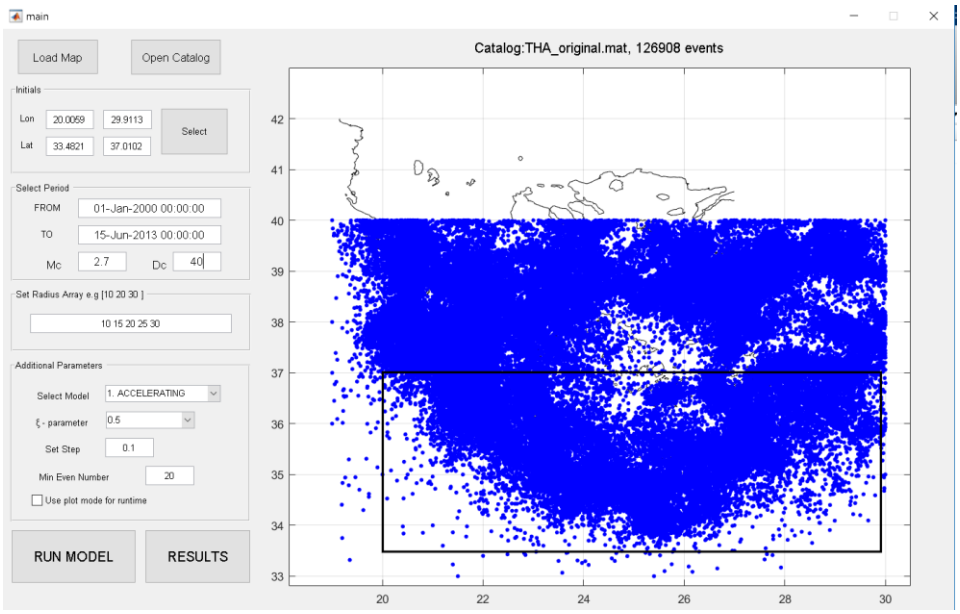

Figure 3.3.8 the catalogue was limited to the South Aegean region. Additionally, different magnitude and depth limits have been tested (see text).

A similar idea occurs for the search shape and its size. In the literature the search shape varies, ellipses lobes and other shapes have been proposed. The actual search shape in the

three dimensions is different, for example a circular search area is actually a cylinder as the surface and the maximum depth shapes upper and lower bound of the search volume. This observation adds another variable in the search parameters, arising the basic questions: which shape will work better to identify the seismicity patterns and is there a limit in the size? In the work of Bowman & King (2001); Tzanis & Vallianatos (2003); Mignan (2008b) where the spatial distribution of the preshock events is limited to small size (approximately 15-20km) lobe shaped areas with positive stress changes. Aiming to approximate the aforesaid pattern and with the assumption that the fault type and the area of the large event are unknown, circular shaped areas with small diameters have been used to include the events with the possible positive stress changes. Additionally, different depth limits have been tested in the seismicity pattern search. The initial idea was to use only crustal events with depth from 0 up to 40km but taking the aforesaid researches into account and with purpose to narrow the height of the 'cylinders', other depth limits like 10 20 30 km have been tried.

In order to accept the produced results a series of criteria has been applied. A grid point was considered that it successful identified seismicity pattern when for each of the three ξ energy exponent (0, ½, 1) cases, there were the same:

- time window (starting and ending time)
- circle size as well as the number of events
- minimum magnitude and maximum depth

Additionally, the successful grid points should have curvature parameter $C \leq 0.55$ for all cases and the correlation coefficient of the power law fitting should be $R^2 \geq 0.97$. The most important parameter was the critical exponent. The results should have an m_ξ with values between 0.25 and 0.33.

Chapter 4 Aftershocks - swarm sequences in the front of Hellenic Arc

4.1 The HSNC network

4.1.1 HSNC monitoring area

The Hellenic Seismic Network of Crete (HSNC) was established in the front of the Hellenic Arc in 2004. The main purpose of the network is to contribute to the monitoring of seismicity in a convergent boundary tectonic regime caused by the subduction of the ocean lithospheric part of the African plate (ocean floor remnants of Tethys sea) under the Eurasian continental shelf (McKenzie, 1972; Reilinger, et al., 2006). The recent studies of the GPS velocity vectors show that the South Aegean plate is moving quickly (33 mm/year) towards the slow (5 mm/year) African plate (Reilinger, et al., 2006; Ganas & Parsons, 2009). The monitoring area is located within a rectangular defined by coordinates, longitude from 20.0 to 30.0 and latitude from 34.0 to 37.0. In this area, it is estimated that more than 60% of the total seismic energy in Europe is being released. Historically, there is evidence that earthquakes with magnitudes up to 8.3 have occurred (Papazachos, 1990). Based on the work by Ambraseys (2001), the relatively recent strongest shallow events that have occurred since 1900, have magnitudes estimated up to M_s = 7.3.

4.1.2 Evolution of the HSNC network

Initially the network had four Guralp CMG-40T 1 second triaxial orthogonal sensors for vertical and two horizontal dimensions with flat response to velocity from 1 to 100 Hz installed in western and central Crete. Within a time period of less than a decade (2004–2012) the seismic network expanded from four to twelve online stations (figure 4.1): KNDR (Koundoura Palaiochora), FRMA (Ferma Ierapetra), CHAN (Chania), KSTL (Kastelli Heraklion), PRNS (Prines Rethimnon), KTHR (Kythira island), TMBK (Tympaki Heraklion), STIA (Sitia Lasithi), KOSK (Kos island), RODP (Rodopos Kolimbari), THT2 (Santorini island), and GVDS (Gavdos island) but with mixed broadband and short period

sensors (Chatzopoulos, et al., 2016). Some of the original Guralp CMG-40T 1 second seismometers were replaced by new Guralp CMG ESPC 60 and 120 seconds seismometers (Hloupis & Vallianatos, 2013) which have a flat to velocity from 0.017 Hz (60 seconds) and 0.0083 Hz (120 seconds) to 50Hz. During the network expansion time, many changes have been made to increase the seismic network capabilities, in some cases by adopting new, more suitable location for the seismometers. In the time interval of next two years (2012-2014), another three short period sensors (STIA, FRMA and GVDS) were replaced by broadband ones and at the same time, two new stations KLMT (Kalamata) and HRKL(Heraklion) were added to the seismic network in order to provide a wider and better in quality coverage area. In the middle of 2015 two more station' seismometers (PRNS and KSTL) were changed from short period to broadband ones, leaving only one short period sensor (RODP) in the network (Chatzopoulos, et al., 2016). All 14 stations are registered to the International Seismological Centre (ISC, 2018) and the network is listed in the International Federation of Digital Seismograph Networks (FDSN, 2018) with the assigned permanent network codename HC. In all the network's stations, since its first operation, the sensors are connected with 3rd generation REF TEK 130-01 DAS digitizers (Ref Tek, 2018) to digitize and transfer the seismic signal to the collector server (Hloupis & Vallianatos, 2013). In the beginning the digitizers were set to continuously record seismic data at 125 Hz, but eventually near the end of 2013, this number was reduced to 100 Hz due to enormous amount of data stored in servers after the network's expansion and also to be compatible with neighbour seismic network collaborators (Chatzopoulos, et al., 2016). At the end of 2015, aiming to increase seismic readiness and provide more knowledge-information to scientific community, the civil protection authorities and the citizens, the HSNC started operating a permanent strong ground motion network in the urban environment of Chania and its southern basin. The network is equipped with fourteen sensors, mostly Trimble's Ref Tek 130 along with some Satways' GSense 16bit. These provide a dense network with increased spatial resolution in the monitoring area. The analysis of the strong motion data enables the peak ground acceleration to be calculate and presented in *shakemaps* (Chatzopoulos, et al., 2018).

4.2 Seismic signal acquisition

4.2.1 Acquisition methods for HSNC equipment

All the installed stations in Crete are able to communicate with the central data collection server by using private wired Asynchronous Digital Subscriber Lines (ADSL) Multi-Protocol Label Switching (MPLS) lines. To prevent the loss of data packages from possible technical difficulties in ADSL line the HSNC has back up ISDN lines to ensure the minimal data loss due to connection problems. If the ADSL line is down for some reason, the ISDN back up mechanism does a dial-up call to access the internet and transfer the seismic data until the broadband connection is restored. When the HSNC started its operations, there was a problem in communications with distant stations that were located on other islands (GVDS, KTHR and THT2), because the wired lines did not exist in these locations or they were cost inefficient. The HSNC is using its own private satellite line for these remote stations, which use the iDirect satellite hubs (idirect, 2018) to communicate the satellite links (VSAT) (Hloupis et al., 2013). All the incoming continuous recording data that are transmitted from the stations' digitizers (REF TEK 130) are gathered in the main data collection server. In this archive-dedicated server, the *REF TEK Protocol Daemon (RTPD)* is installed, which is the REF TEK's commercial software package. The *RTPD* which connects through UDP port 2543 with the DAS digitizers, uses error-correction modules to ensure the incoming data integrity from DAS as well as from the other collaborating seismic networks. Additional algorithms are designed to monitor the conditions of each station and provide useful information regarding the GPS status, the data transmission delay, the RAM usage of the DAS, the input voltage and the back-up battery condition. The incoming data remain in this server for about 4-6 months and after that they are moved and stored in back-up servers.

4.2.2 Data exchange with the other networks in the area

The HSNC continuous monitors the South Aegean. Its operations rely on collecting seismic data from its 14 stations as well as from ten more stations that belong to neighbouring networks. At the end of 2013, in order to increase its monitoring capabilities, the HSNC

had signed bilateral agreements with three neighbour seismic networks. The main collaborating network is the National Observatory of Athens that provides the stations VLI (Velies Lakonia), MHLO (Milos Island), APE (Apeiranthos Naxos), ZKR (Zakros Crete), KARP (Karpathos Island) and ARG (Archangelos Rhodes) (HL/National Observatory of Athens Seismic Network, 2018). The Seismological Station belongs to the Department of Geophysics of Aristotle University of Thessaloniki (History of the Department of Geophysics - AUTH, 2018) which provides the stations KRND (Kranidi Argolis) and NIS1(Nisyros island) (HT/Aristotle University of Thessaloniki Seismological Network, 2018). The last collaborator is the Kandilli Observatory and Earthquake Research Institute (KOERI, 2018), from Bosphorus University located in Turkey that provides 5 stations but due to network's needs it uses the BODT (Bodrum Mugla) and DAT (Datca Mugla) only (KO/Kandilli Observatory and Earthquake Research Institute, Bosphorus Univ., 2018). A map showing the HSNC topology of as well as the collaborating seismic networks is illustrated in figure 4.1.

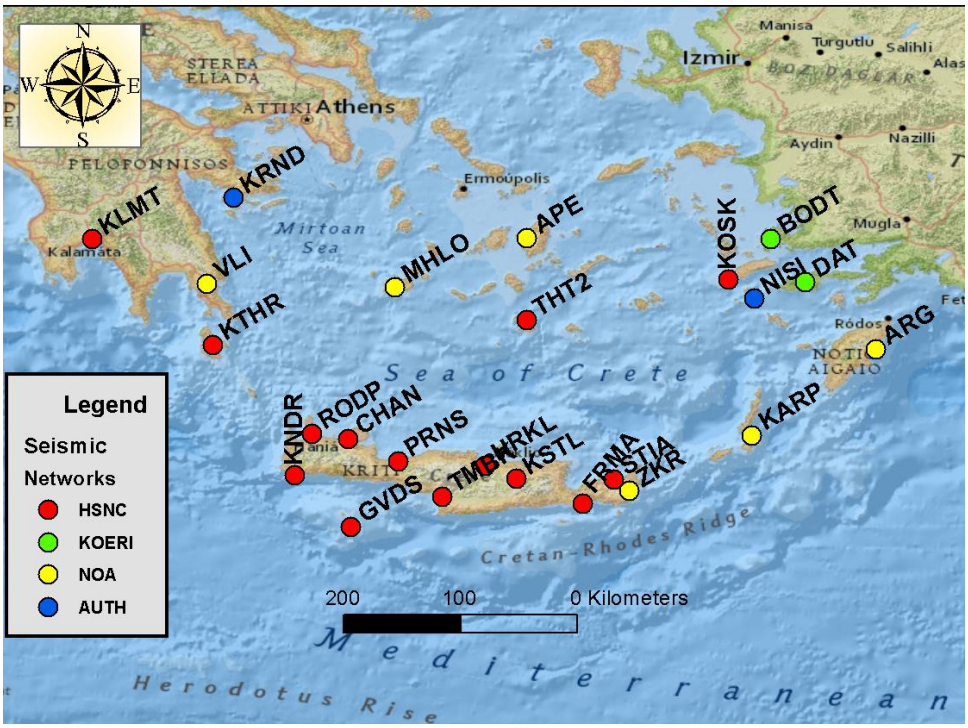

Figure 4.1 The spatial distribution of the HSNC stations as well as the other data exchange seismic network stations.

According to the FDSN, et al. (2012), the defined international format to exchange seismological data is the *SEED* (Standard for the Exchange of Earthquake Data), that files contains all the information that is necessary to reproduce the seismic waveform. A commonly used format due to its limited size, is the *miniSEED*, which is a dataless *SEED* volume and a response file is needed to access the data (FDSN, et al., 2012). Aiming to ensure a constant exchange of seismic data, a *SeisComp3* server is used. The data from neighbouring networks are available with the *seedlink* data broadcast protocol that uses small packets with size 512-byte *miniSEED*. The seismic data are available to all *seedlink* servers that are able to connect to the specific TCP IP, usually in port 18000. It is necessary to change the format of the data in order to feed them to *RTPD* collection server. The *sl2rtpd* protocol is used to transform the broadcast *miniSEED* data from *seedlink* to REF TEK format.

4.2.3 Automatic Earthquake Monitoring Systems

The automatic processing of seismic signal in the HSNC is achieved by employing two earthquake monitoring systems the *SeisComP3* developed from Helmholtz Centre Potsdam, GFZ German Research Centre for Geosciences and GEMPA GmbH (Helmholtz Centre Potsdam, GFZ German Research Centre for Geosciences, 2018) and the *Earthworm* from USGS Menlo Park in the United States (Earthworm, 2018). For the purposes of the HSNC operations, the automatic systems have been set to run independently with data feeding directly from the *RTPD* data collection server and they process the same seismic signals in parallel mode. The two earthquake monitoring systems work with different automatic phase picking algorithms. The *SeisComP3* uses as primary picker the classic short-time-average amplitude of a seismic signal for a moving-time window versus the long-time-average amplitude *(STA/LTA)* algorithm. The *Earthworm* works with the Allen algorithm, where the phase picker is applied in an envelope function of the *STA/LTA* ratio (Olivieri & Clinton, 2012; Allen, 1978; Trnkoczy, 2009) The envelope function in waves is a smoothing technique for border values (Johnson, et al., 2011). Each of the earthquake monitoring systems is assigned to have increased sensitivity for a specific monitoring area as it has lower trigger values for specific stations. The *Earthworm* monitoring system is

calibrated to identify seismic events better on onshore and in a close to Crete region while the *SeisComP3* works better for locating earthquakes in the broader area of South Aegean. After detecting an event, the automatic earthquake monitoring systems create a bulletin with a preliminary analysis and this distributed to the in-charge analyst, the registered users, the collaborating networks and the local authorities. At the same time that the analyst is being informed about an event, a script procedure is initiated, it takes less than 5 minutes after the automatic detection to send the necessary waveform files to perform the manual analysis of seismic event (further details provided in 4.3.1). Additionally, with a view to informing the rest of scientific community and the public, a dedicated webpage is set up with all available seismic parameters (origin time, latitude, longitude, depth and magnitude) for the automatic and manual solution. The webpage is updated after every new event (HSNC, 2018) (Chatzopoulos et al., 2016).

4.3 Earthquake data processing

4.3.1 Seismic waveform files

In the HSNC the manual earthquake analysis procedure is carried out by inspecting and phase picking in raw, REF TEK data archive format, seismic signal files. There are two possible ways to obtain a waveform file, the first one involves the automatic earthquake monitoring systems while the second one is controlled by the analyst needs. Every time one of the automatic systems is triggered by a possible detection, it is programmed to execute several scripts to aid the analysis process. If the automatic system identifies a possible event, a script is designed to do three basic tasks, the first job is to check and inform the earthquake databases, then it sends emails with the preliminary analysis to the seismic network users and the last task is to launch another script which is in the REF TEK data collection server. The script in the *RTPD* server execute the REF TEK's Interface Software Suite command *arcfetch* for each station. This command creates several data files (based on the number of stations) by copying from the archive data (continues waveforms) the selected time window (in HSNC the time window is set to 4 minutes length). The whole package of waveform files is stored in one Tape Archives file (*.tar) and it is send to the

users with a File Transfer Protocol command (FTP). Aiming to separate the source of the waveform package files, different codenames are assigned related with the triggered automatic earthquake monitoring system. The *EW_data* prefix denotes that the file comes from an *Earthworm* triggering while the *S3_data* from a *SeisComp3* triggering. The third option to obtain seismic signal files is available through a Graphical User Interface (GUI) designed for Windows operating system (figure 4.3.1). The GUI named *executioner* launches another script that runs the *arcfetch* command in REF TEK data collection server but this time with the user's choice for the starting date of the time window. This non-automatic method is used for events that have not been detected by earthquake monitoring systems. The GUI software has been used to bring earthquake data files after the manual inspection of the 24h raw waveforms for the aftershocks that have not been detected. Another use of the *executioner* program is for the cases where the initial waveform file has a time window that does not include the whole seismic signal, so it is necessary to bring a new file with the same event but with a better time window. The name of waveform files obtained from the GUI software had prefix *data* while the rest of the filename denotes the origin time of the event separated by underscores (Year_Month_Day_Hour_Min_Sec). An example of each of the three possible data files codenames is illustrated on table 4.3.1. A typical waveform file has a 3500- 5200kb size which is based on the available number of station data files and the length of the time window.

Table 4.1 The types of the HSNC seismic signal files.

Origin	**File name**
Manual-executioner	data_2015_10_21_07_26
Automatic-Earthworm	EW_data_2015_10_19_16_28_57
Automatic-SeisComp3	S3_data_2015_10_21_23_11_52

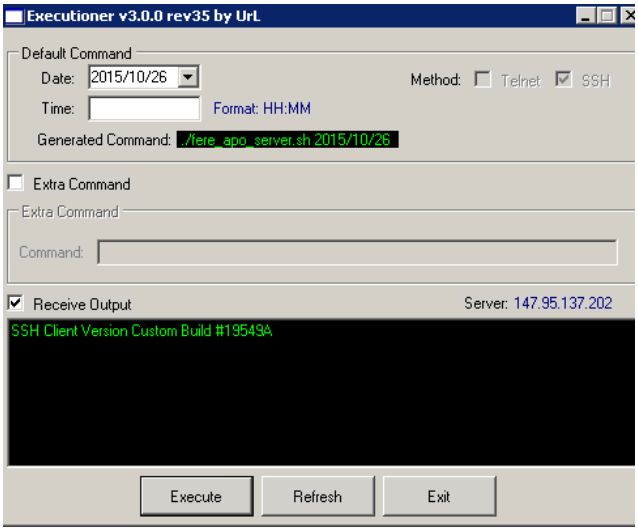

Figure 4.3.1The GUI 'executioner' that activates a script to manually bring waveform files. This software has been used to collect seismic signal files for the aftershock and swarm sequences.

4.3.2 Seismic signal analysis software

The analysis of the preliminary manual results on the HSNC is being carried out with the REF TEK's commercial GUI software (*COMPASS*) which is compatible with all kinds of Windows environments. The requirements of using the software are very limited as it doesn't require a fast processor or a large amount of memory, for example a Pentium 4 CPU and 30 Mb RAM (20 stations 4-minutes recording) are more than enough to run the software. In addition, the software is standalone and does not need an installation. The *COMPASS* is able to read and load waveforms from various types of files including the most common used formats such as *REF TEK, SAC, SEED, ASCII, SEGY* and many others. To use files other than SEED it is necessary to have the instrument response files that contain information such as location of the sensor, the orientation of the sensor components as well as the transfer functions and channel sensitivities. The *COMPASS* software is user-friendly with a large variety of menus that allow the analyst to carry out the standard analysis tasks in a time efficient way. The phase picking is achieved with the use of *P* and *S* phase arrivals for local- regional events. The origin time is calculated as the subtraction between the P wave arrival times (t_P) with the product of the time difference of *S* and *P* arrival times $(t_S - t_P)$ versus the velocity ratio (V_P/V_S) *-1*. The earthquake epicentre is located by minimizing the differences between observed and theoretical arrival times. The

magnitude computation for local magnitude is based on the distance from the epicentre to the station as well as to the logarithm of the recorded maximum seismic wave amplitude while for surface magnitude the wave's dominant period is also needed. Except the basic operations, the REF TEK's seismic analysis software has various options that helps the user to process the seismic waveform or save it in a different format. For example, in the time domain menu there are options that remove the DC offset and apply different kind of frequency filters, mathematical tools as well as smoothing, cut signal, and decimation options. In frequency domain menu there are Fast Fourier Transform, Power Spectral Density and spectrogram diagrams, also an emulation of a seismometer to another with the use of transfer functions. Other useful tools are the seismic wave velocity ratio *Vp/Vs* obtained by plotting the time difference of *P* and *S* arrivals of each station in a diagram known as Wadati plot (Wadati, 1933) and the single station Horizontal versus Vertical Spectral Ratio (HVSR) which can be used on ambient vibration (Nakamura, 1989) or on seismic signal (Lermo & Chavez-Garcia, 1993). The main disadvantage of the software is that it has only two predefined travel time tables, the IASPEI 91 (Kennett & Engdahl, 1991) and one named 'regional' which is based on a less accurate 1D version of AK173 model (Kennett, 2005). These travel time tables are not the most suitable for detailed results in the Hellenic subduction zone and they are good only for a preliminary solution.

4.3.3 Seismic signal processing

The first step to start the analysis procedure that will determine the earthquake parameters of an event, is to extract the Tape Archives file and load the seismic waveforms into the REF TEK's seismic analysis software. The modern monitoring instruments sense the ground vibrations with electromagnetic transducers and the produced output is electrical voltage. The analogue information of the coil-magnet, the electromotive force should pass through an analogue-to-digital conversion system, a digitizer so it can be converted in the digital seismic signal. The output of this process depends on sampling rate while during the conversions it is possible to have offset, gain, and non-linearity errors (Fiore, 2018) Taking the seismic waveforms is an analogue-to-digital product into account, before the phase picking procedure it is necessary to prepare the seismic waveforms. Usually a mean

removal base line correction is used in order to align all waveforms to the same level. In the *COMPASS* there are several tools specialized to remove offset. A common used option to fix the DC offset is the Mean Removal tool which removes average value from the measured signal. Aiming to cut the unnecessary noise, a filter in the frequency domain is applied. The filter application is used to improve the signal to noise ratio and make the seismic wave phases arrivals easier to distinguish for phase picking (Bormann & Wielandt, 2013). The REF TEK's software has different infinite impulse response (IIR) and finite impulse response (FIR) filters. The IIR filters are causing a time-delay in the filtered signal while FIR ones can produce a fake preseismic signal (Mollova, 2007) so the IIR are preferred. The filters are divided in four categories based on frequency signals that are allowed to pass through the filter (Lowpass, Highpass, Bandpass and Bandstop). Plotting the response curve of the amplifier versus frequency, the flat part that can pass through the filter is known as *pass band*, the rejected part is the *stop band* while the area between the pass band and the stop band is the *transition band.* The order of the filter is a measure of the response rate, which is described by an integer value, the higher the order of the filter the more steeply is the frequency attenuation. The class of the filter controls the shape of the transition region and represents the dumping factor (Fiore, 2018). Among the four basic types of filters, the most common used frequency filter in the HSNC is the Bandpass one. The second order of the filters is preferred because it is not so steep in the transition band and it does not significantly alter the output. Additionally, a large order filter may cause a phase shift of signal (Diehl, et al., 2011). An example of how a higher order filter could affect the outcome is illustrated in figure 4.3.2 where the same raw waveform is being filtered with a 2^{nd}, 3^{rd} and 4^{th} order filter. It is noticeable as the order increases; the *P* phase arrival (black line) becomes less clear a fact that can cause errors in phase picking process.

The adopted class is the common used Butterworth, it is an IIR active signal processing filter named after Stephen Butterworth who proposed a series of analogue signal processing filters with flat response to a specific frequency region (Butterworth 1930). The lower and higher cut off frequencies are set to 1 and 6 Hz and the order is 2 so the phase shift of signal is the minimal (figure 4.3.3). The filter parameter that controls the pass band frequencies has been tested in a considerable number of events and the selected ones are the best choice to fix the SNR for the HSNC stations.

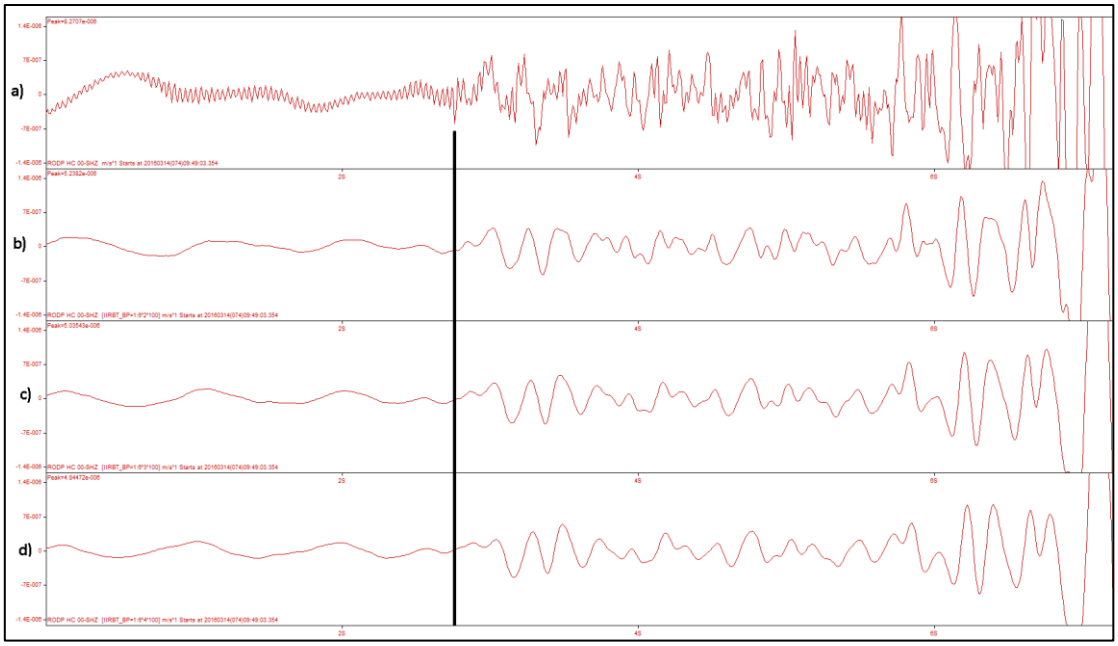

Figure4.3.2 The effect of a higher order filter in the seismic signal waveform. In the raw signal applied a 2nd ,3rd and 4th order filter. The black line indicates the P phase arrival.

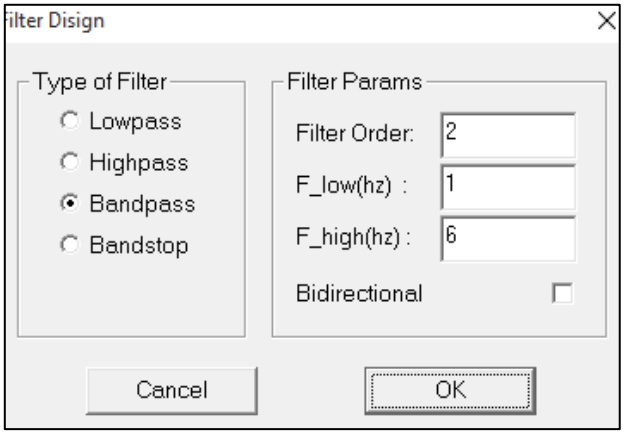

Figure 4.3.3 The Butterworth filter type and the rest parameters such as order and cut-off frequencies.

In some cases where the magnitude of the earthquake is moderate to strong and the event epicentre is near the research area, it is possible to proceed to the analysis without using filters because the SNR is sufficient enough to distinguish the phase arrivals. Most times, due to the long period marine noise and anthropogenic high frequency noise of the HSNC station location, the filters were mandatory. When filters are applied, the software copies

and separates the waveforms that have filters by adding brackets with the filter parameters (figure 4.3.4).

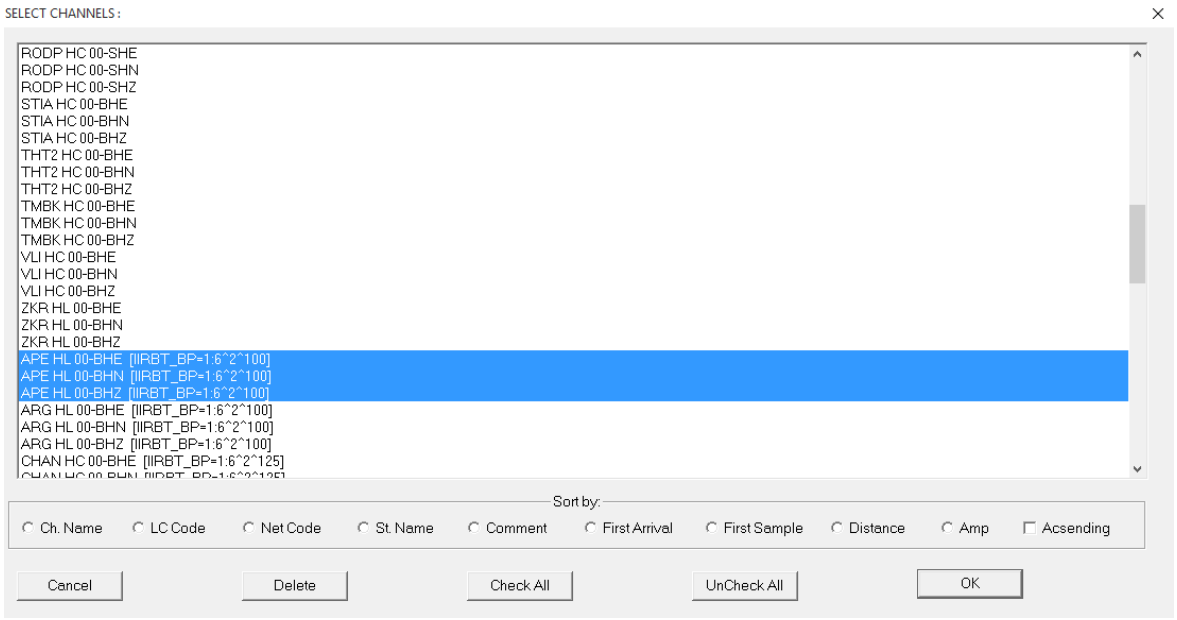

Figure 4.3.4 The software copies three components for each station, the raw waveforms are on the upper part while on the lower are the ones with the applied filters.

4.3.4 Phase picking procedure

Before the phase picking procedure, a visual inspection of all stations could give a good idea and help the analyst to understand approximately where the epicentre is and approximately how strong it is. The closer the earthquake is to a station the shorter the length between *P* and *S* phases is. The magnitude estimation is analogous to the number of station where the event is recorded. The second stage of the manual analysis is the phase picking. Selecting to work with the stations that contain a seismic signal with good signal to noise ratio makes the hand-picking routine easier. Visually, the *P*-wave arrival is characterized by a significant amplitude exceeds of the background noise which can be used for a probabilistic phase picking (Diehl, et al., 2011). Aiming to accurately define the beginning of the P-phase, the waveform is zoomed to a 2-5 seconds time window that contains a part of background noise in the left side, about in the middle is the *P*-wave arrival while in the right side are the rest of the *P*-phases (reflections-refractions). The *P*-

waves phase picking needs an additional attention in the case of large magnitude earthquakes. Usually the software that is used to inspect the waveform tries to fit the whole amplitude of the waveform on screen. In this instance, it is possible that the arrival of *P*-waves could look like background noise due to scaling. A custom scaling should be used to stretch in a vertical sense the waveform in order to carefully inspect it. In addition, in the case where a filter is applied, it will be helpful for the analyst to compare the two waveforms to ensure that there are no significant changes in the shape of the waveform (figure 3.3.5).

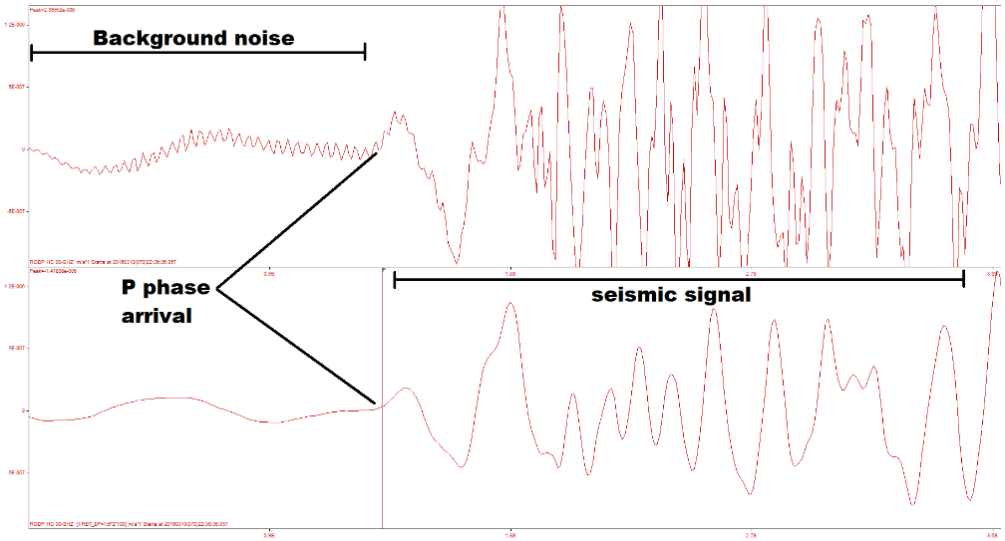

Figure 3.3.5 The seismic signal with (down) and without filters(up) is inspected for alterations in the waveform shape form the filter application.

The same routine is followed to mark the *S*-phases but this time the picking procedure has a certain degree of difficulty because the S-wave arrival is overlapped by the P-wave coda (Woessner, et al., 2010; Diehl, et al., 2011). Based on my analyses and teaching experience, I have determined that there is a time window that it is easier for analysts to separate the *P*-wave coda with the *S*-wave arrival. The time window is not the same for every earthquake, it depends on the length of the earthquake recording and usually it can be identified by selecting to focus in the waveform area just a couple of seconds before the primary waves of the earthquakes and a few seconds after the point where the maximum amplitudes of the secondary waves have arrived (figure 4.3.6). This zoom technique creates a time window where on the left side there is a part of the background noise, the P-wave arrival, in the

middle there is a part of the P-wave coda and the beginning of S-waves while on you right side there are the maximum amplitudes. Visually, the *S*-wave arrival is characterized by larger amplitudes, the wave's period increases, and the shape of the recorded waves becomes less edgy.

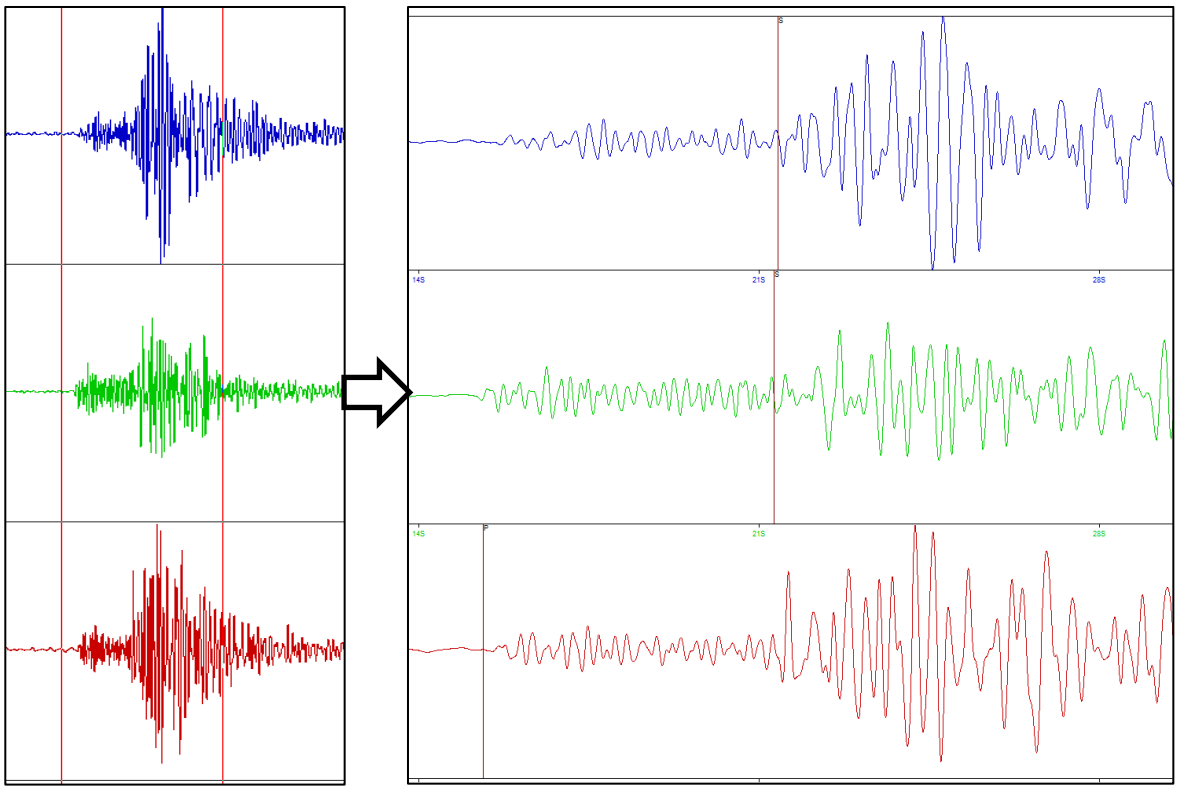

Figure 4.3.6 The zooming techique,a window that contains the P and S wave maximum amplitudes that helps to identify the different phase arrivals.

The first stage of phase picking procedure is complete when in all the available the phase arrivals stations have been marked. The first attempt to find the epicentre and calculate the rest of the earthquake parameters can be carried out by executing the build in location algorithm. In the *COMPASS* software, in the Location menu, there is a GUI solution for using the epicentre location software in an easy way (figure 4.3.7). Most options of the 'Hypocenter Location' window, are predefined by the developer. The only customizable features in the upper right part of windows (Settings and Limits) are minimum and maximum search depth, the azimuthal distance between epicentral and the nearest station to the event as well as the two available travel time tables. For the HSNC monitoring area of

the South Aegean, the typical limit values for search depth are from 0 to150 kilometres and from 0 to 15 degrees delta from the first station. In some cases, when it is necessary to constrain the solution (not suitable crust model) and increase the quality of the solution, the values 0 to 120 kilometres in depth and 0 to 12 degrees in distance are used. When clip limits are set, there is only one pushbutton to calculate the earthquake parameters. In the left upper part of 'Hypocenter Location' window in the 'Statistic' tab, there are the channels (components) that have been used for phase picking. Usually based on seismic waves motions, the *P* arrivals are marked on *Z* component as they are better recorded in this channel, while the S arrivals on the other two horizontal ones. Next to them are the time residuals that are derived from phase picking, these depend on settings and the earthquake solution. There is the distance in Delta and kilometres from epicentre on the 3rd column while the 4th column 'Phase' denotes which phase was picked by the analyst. The 'Phase' column can be compared with the 1st column 'Channel' to ensure that there is not a phase picked in wrong component by mistake. On the left lower part of the window 'Solution Result' there are the calculated seismic parameters: origin time, latitude and longitude depth, while inside a parenthesis next to each parameter are the estimated errors.
The phase picking time residuals should be as small as possible but due to the limited control of the software parameters, the acceptable errors for the preliminary analysis should be less than ±1 second (figure 3.3.7). In case a channel presents an error with higher than the expected value, then the picked phase is re-examined. There are a few possible reasons capable of increasing the time residuals associated error. Excluding the primary factor, the human mistake, it is very often to have errors caused by a not so suitable crust model for the investigating area. In some of these cases, the errors in phase picking can be close or above the ±1 second. A relocation procedure with more accurate crust model and an algorithm with adjustable parameters might fix these time residuals and improve the quality solution. Another not so common problem but sometimes very difficult to understand, is a problem caused by a malfunctioning GPS. As the time accuracy of the recordings is dependent only on the GPS, an internal error in the chipset can cause a delay in the timestamp error and a drift in the timeseries. This case is identifiable only with trial and error method while the only solution to fix the seismic parameter estimation was to remove the phases from the problematic station.

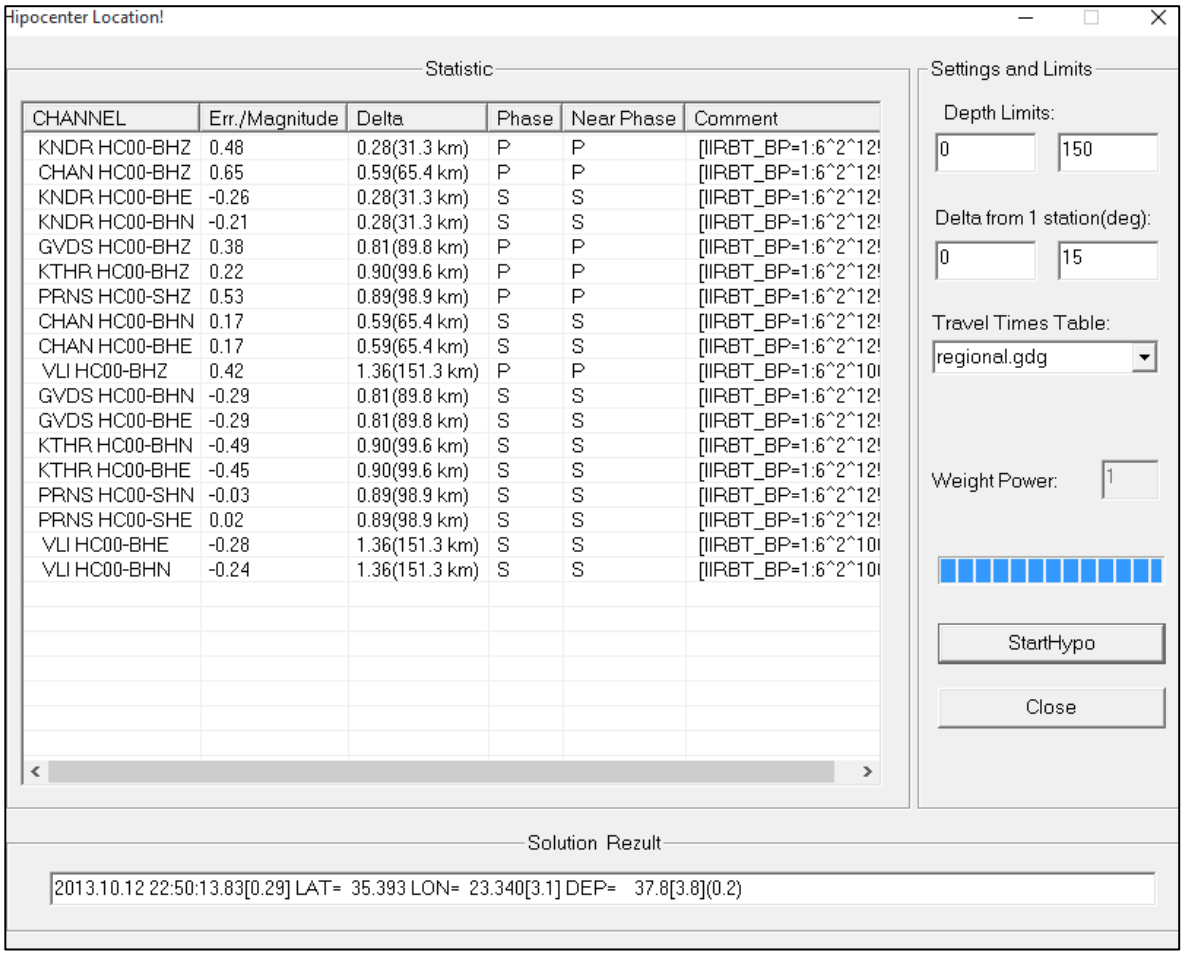

Figure 4.3.7. The GUI hypocenter solution window. On the upper part are the phases with the corresponding time residuals while on the lower part are the calculated earthquake parameters with the associated errors in parenthesis.

A final technique to check the quality of the marked arrival times, which is independent of the travel time tables, is the Wadati diagram (Wadati, 1933) presented in figure 4.3.8. The plot is constructed by using the velocity ratio of Primary waves against the Secondary waves (V_P/V_S) for each station. The dependent axis represents the travel time difference of the *S* and *P* waves (t_S - t_P) while the independent one has the time difference between *P* travel time and origin time (t_P - t_0) according to:

$$\frac{V_P}{V_S} = \frac{t_S - t_P}{t_P - t_0} + 1 \qquad (4.1)$$

The Wadati plot assumes the medium has one homogeneous layer but it is also valid for a multilayer case as long as the velocity ratio is constant (Hurukawa, 2012). This linear fitting is sensitive to border values and may indicate wrong information, so it is better to use it when there is a sufficient number of stations. The stability of the fitting will increase when the sensors are evenly distributed in different distances from the epicentre. Ideally for close distance events, there is the assumption that the velocity ratio equal with 1.73. The *P* and *S* wave velocities are correlated with the elastic constants such as the Young's modulus the Poisson's ratio the bulk modulus, the rigidity modulus the Lame's constant and the density (Sheriff, 1984):

$$\frac{V_P}{V_S} = \left(\frac{1-\sigma}{\frac{1}{2}-\sigma}\right)^{1/2} \tag{4.2}$$

The Poisson ratio σ for the crustal rocks may vary from 0.20 to 0.35, a typical value is the 0.25 which is also observed as mean value for the Mesozoic-Cenozoic orogenetic belts (Zandt & Ammon, 1995). In the REF TEK's software the velocity ratio for $\sigma = 0.25$ is represented with the green line while with black dashed lines are the best fitting based on observed arrivals and the observed arrivals combined with the origin time. The typical values for the velocity ratio in the South Aegean region based on the literature varies from 1.65 to 1.80 (Hatzfeld, et al., 1990). Hatzfeld et al. research in western part of the Hellenic arc Wadati plots suggest a $V_P/V_S=1.78\pm0.02$ (Hatzfeld, et al., 1990). Two years later, the De Chabalier et al. work for western Crete present similar results as they have calculated a velocity ratio 1.80 (De Chabalier, et al., 1992). Papazachos and Nolet have used a mean $V_P/V_S=1.75$ for their nonlinear tomography in the Hellenic arc (Papazachos & Nolet, 1997) and the same ratio have been used by Meier et al. to obtain the 1D velocity models for western and central Crete (Meier, et al., 2004). Nikolintaga et al. have used the first HSNC station recordings to obtain the 1D crust models for the South Aegean, their Wadati plots suggest a velocity ratio equal with 1.78 (Nikolintaga, et al., 2007). The same ratio has been used by Becker et al. to obtain the *1D* velocity models for central Crete with recordings from permanent stations as well as ocean bottom seismometers (Becker, et al., 2010).

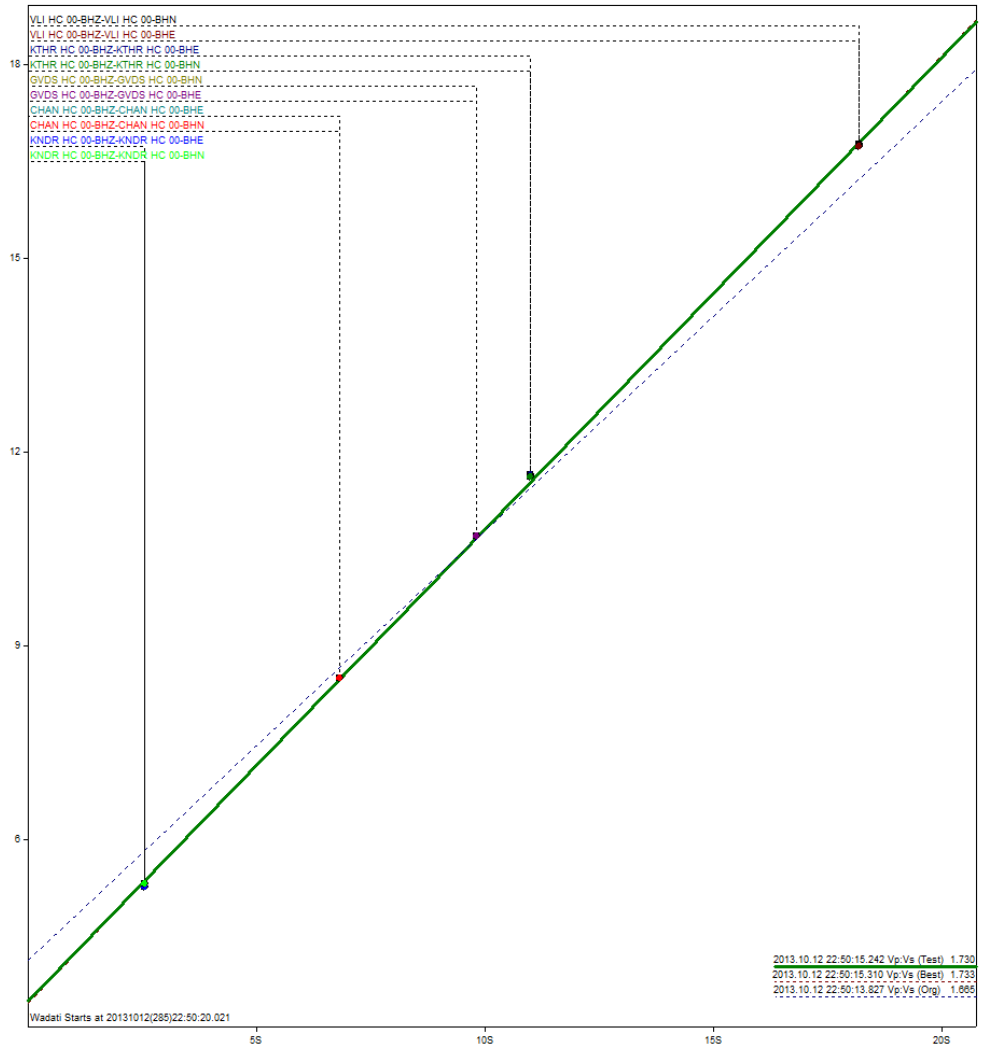

figure 4.3.8. The Wadati plot, the green line is V_P/V_S 1.73, the different colour dots are the velocity ratio of each station.

4.3.5 Magnitude estimation

The two largest seismological networks in Greece (HL,HT) are reporting all the events with the local magnitude (M_L) which is based on S waves maximum amplitudes and the moderate-large events with moment magnitude (Mw) which derives from seismic moment. The HSNC also reports all events in local magnitude, whereas the moment magnitude is estimated with spectral analysis and it used only for strong-large events. To calculate local magnitude of the located event, an emulation is required to make all the available types of sensors look like the original standard seismograph. The *COMPASS* software has a list of

transfer functions, that are designed to use the response files to change the raw waveforms from the original recorder to a standard type sensor, in this case a typical Wood Anderson seismometer is selected. The software has an option to control the signal to noise ratio level of the transformed waveform with a *Hs(f)/Ha(f) Db* ratio derived by subtracting the frequencies of the complex part of the transfer function from the standard instrument against the corresponding one of the original recorder. In the new emulated waveforms (figure 4.3.9) the local magnitude is calculated by selecting the maximum amplitudes on the S wave part of the earthquake with the hand tool (figure 4.3.10). The magnitudes are calculated for each station that has been previously used for S wave phase picking. The reported local magnitude of the event is defined as the average value of all the magnitudes. Since in the magnitude marking procedure it is required to find the maximum amplitude in the waveform and define the stations' instrument type, the whole process seems to be easier and faster than the phase picking. The software has 3 options for the sensor transfer functions, with ***A*** denoting the short period instruments, ***C*** the broadband sensors while the middle period seismometers are noted with ***B*** (figure 4.3.10).

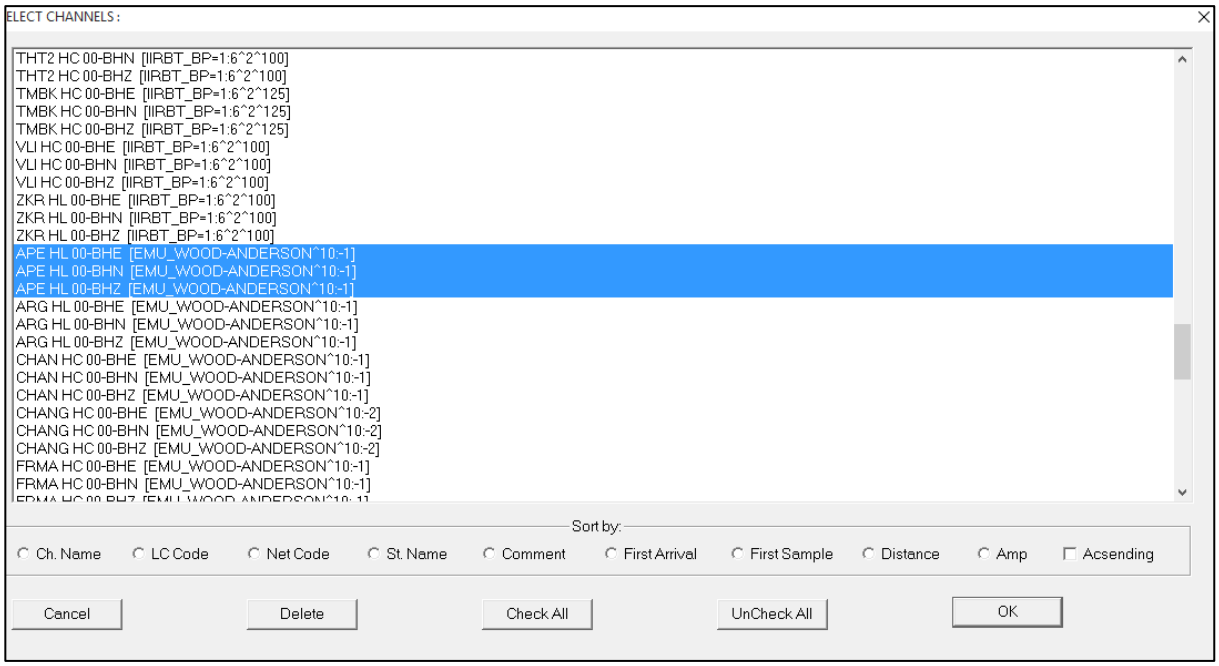

Figure 4.3.9. The original recordings are emulated to look like that they are from a typical wood anderson seismomter and they appears in the list with the [EMU_WOOD_ANDERSON] brackets.

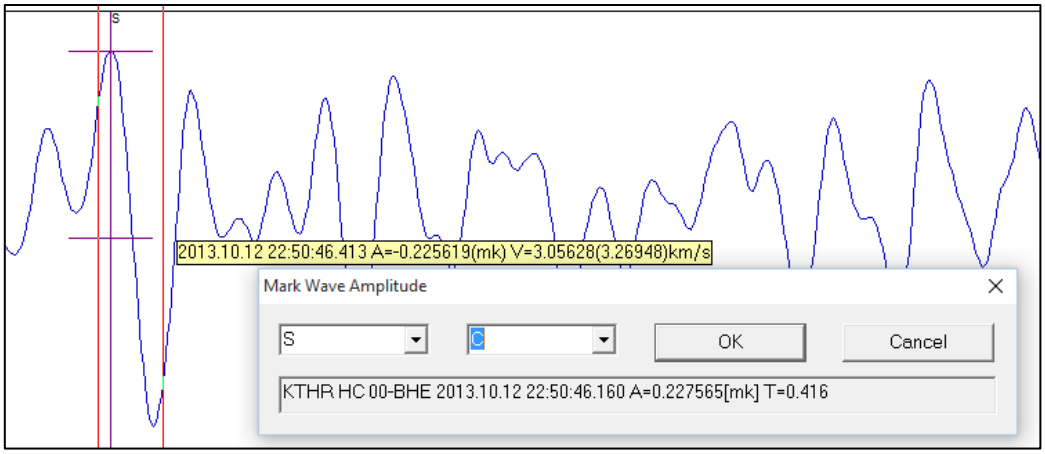

Figure 4.3.10. The hand tool selection of the maximum amplitudes as well as the type of insturment

The only difficulty that requires some attention and knowledge on the local site conditions magnitude calculation procedure, is that sometimes it is possible to have uneven results between the station's values. An example is when the distance between a station and the epicentre is too close due to the local magnitude estimation relationship. Approximately, in the moderate or large events with station-epicentral distance less than 30-40 km the local magnitude scale gets saturated and the determined magnitude is underestimated while for smaller in magnitude events, the underestimation occurs in shorter epicentral distances and it is possible to have negative magnitudes for very small magnitude and short distance events. An example is from 12/10/2013 mainshock (aftershocks also have the same problem) where the closest station KNDR tend to present considerable smaller local magnitude, 5.2 while the same time the average value from the rest of the stations is 6.2 (figure 4.3.11a). The only solution to fix this problem was to keep the *P and S* arrival times and exclude the magnitude estimation for this station in the whole aftershock sequence. In some other cases the magnitude can be overestimated, especially when the stations are located on a hard rock with an overlaid layer of soft sediments. This is possible due to the different site effects caused by the seismic velocity contrasts that could amplify the seismic wave amplitudes. Such a case is noticeable on PRNS station that has a constant overestimation in magnitude for the 16/04/2015 mainshock and aftershocks, the local magnitude estimation (figure 3.3.11b) is considerable higher (6.95 average value of the station) compared to the rest of the stations which have an average value of 6.0.

a)

CHAN HC00-BHE	C ML= 5.7(0)
CHAN HC00-BHN	C ML= 5.7(0)
GVDS HC00-BHE	A ML= 6.6(0)
GVDS HC00-BHN	A ML= 6.5(0)
KNDR HC00-BHE	C ML= 5.2(0)
KNDR HC00-BHN	C ML= 5.2(0)
KRND HT00-BHE	C ML= 6.5(0)
KRND HT00-BHN	C ML= 6.4(0)
KTHR HC00-BHE	C ML= 6.0(0)
KTHR HC00-BHN	C ML= 6.0(0)
TMBK HC00-BHE	C ML= 6.5(0)
TMBK HC00-BHN	C ML= 6.5(0)
VLI HC00-BHE	C ML= 6.0(0)
VLI HC00-BHN	C ML= 6.1(0)

b)

FRMA HC00-BHE	C ML= 6.1(0)
FRMA HC00-BHN	C ML= 6.1(0)
IDI HL00-BHE	C ML= 5.9(0)
IDI HL00-BHN	C ML= 5.9(0)
KSTL HC00-SHE	C ML= 6.5(0)
KSTL HC00-SHN	C ML= 6.5(0)
NIS1 HT00-BHE	C ML= 6.3(0)
NIS1 HT00-BHN	C ML= 6.2(0)
PRNS HC00-SHE	C ML= 6.9(0)
PRNS HC00-SHN	C ML= 7.0(0)
STIA HC00-BHE	C ML= 5.8(0)
STIA HC00-BHN	C ML= 5.8(0)
ZKR HL00-BHE	C ML= 5.7(0)
ZKR HL00-BHN	C ML= 5.6(0)

Figure 4.3.11 a) A magnitude underestimation example from 12/10/2013 mainshock. b) A magnitude overestimation example from the 16/04/2015 mainshock

Aiming to have a good estimation of the local magnitude, it is necessary to examine all the reported magnitudes to check if there is a trend and avoid having magnitudes values with large variations. As criterion for good reporting magnitudes the HSNC has a rule to keep magnitude values with a deviation of ± 0.3 of the mean magnitude which is determined after careful inspection of all the event parameters. In addition, to avoid using stations with constant reporting problems, there was a personal communication with the former network operator Ilias Papadopoulos that helped to understand which stations of the HSNC and the other collaborating seismic networks have magnitude reporting problems.

4.3.6 Evaluation of HSNC reporting Magnitude

The HSNC could be characterized as a relatively young network as it has been operating for less than 15 years (compared to other networks that operated in the Greece area such as the NOA since 1840 (Brief Historical Note - NOA, 2018) and the AUTH since 1976 (History of the Department of Geophysics - AUTH, 2018). Although the network is relatively new, a lot of effort has been made from its personnel to keep up with the latest ideas and standards of the seismological networks. Despite the continuous hard work to increase the quality of the seismic network, most of the seismic stations have not been installed in ideal sites (underground vaults or inside boreholes) due to the limited amount of

funds. Most of the HSNC sensors have been placed in the basement of unoccupied or low activity buildings (figure 4.3.12).

Figure 4.3.12. The HSNC sensors installed in empty of low anthropogenic activity building. Images from the TMBK(a), KNDR(b), CHAN(c) and KTHR(d) stations.

The initial idea for this cost-effective choice relays on the assumption that these kinds of installation conditions are more than enough for estimating the earthquake parameters. This hypothesis is not approved by everyone, an anonymous referee from Chatzopoulos, et al., 2016 work was interested in the magnitude reporting process and he/she asked for an evaluation of the reporting magnitudes values. Aiming to ensure the quality of the HSNC's computed magnitudes, 1500 same event magnitudes from the two aftershock sequences of 2013 have been compared to the reported magnitudes of the two largest seismological centres in Greece, the NOA and AUTH (figure 4.3.13).

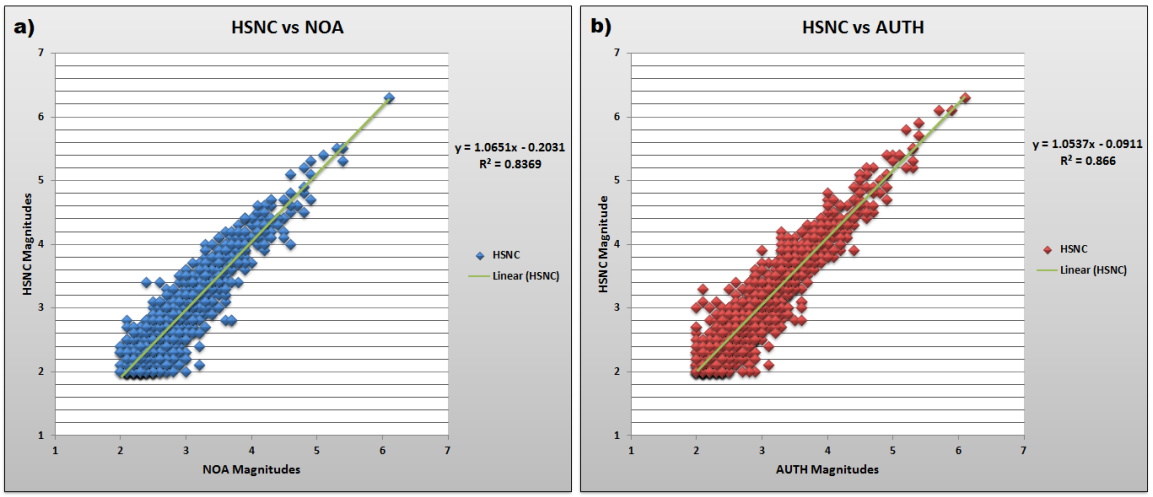

Figure4.3.13 The local magnitude calculated from manual solutions of the HSNC versus the local magnitude of the NOA (left plot) and the AUTH (right plot). A least square line was fitted in each of the available dataset. In both cases a slight overestimation is observed.

Typically, the HSNC is using the moment magnitude scale only for strong or major magnitude events. An additional effort to investigate the magnitude reporting quality of the HSNC stations has been carried out by calculating the M_w for moderate and strong events using only the HSNC stations and compare it with the moment magnitude results obtained from the NOA manual solutions catalogue. The estimation of M_w for the strong and moderate events has been carried out with the Seisan earthquake analysis software (EARTHQUAKE ANALYSIS SOFTWARE-SEISAN, 2018). The seismic moment is correlated with the moment magnitude with the Kanamori relation (Kanamori, 1977; Hanks

& Kanamori, 1979). The seismic moment M_0 has two possible ways to be calculated, the spectral analysis and the waveform inversion (Stork, et al., 2014). The spectral analysis option has been adopted for this framework with the use of Brune's source model (Brune, 1970). The stress drop can be found by fitting manually 3 points to separate the displacement spectrum in two linear parts. There is also the automatic fit option which seems to be more reliable from the manual fit when the residuals of the automatic spectral fit are less than 0.2 (Ottemöller, et al., 2017). An example of the stress drops estimation with spectral fit is presented in figure 4.3.14. The upper curve is the signal spectrum while the lower one is the noise spectrum the f_0 is the corner frequency that separates the displacement spectrum in two flat response areas.

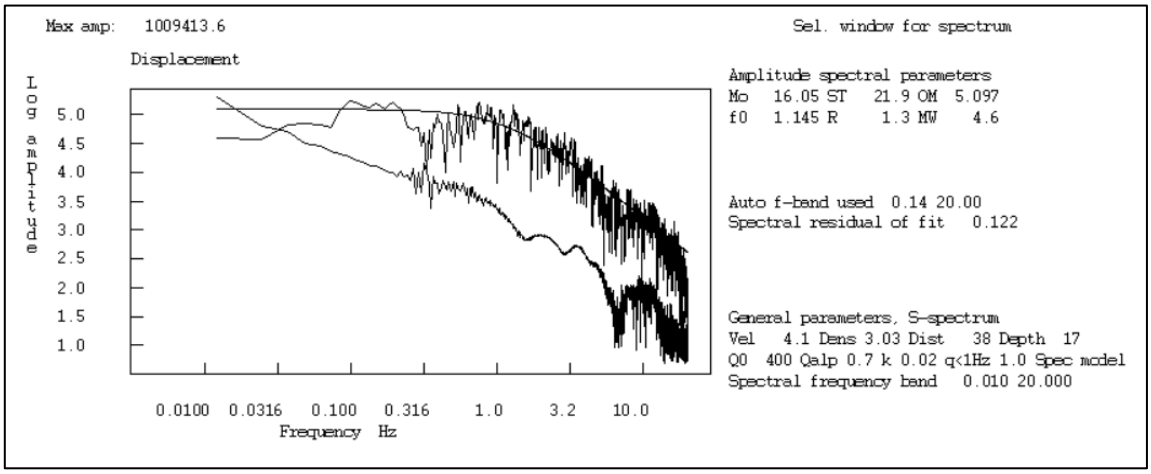

Figure 4.3.14 The automatic fit of the stress drop in the displacement spectrum is used to calculate the seismic moment which relates to the moment magnitude with the Kanamori 1977 equation.

For the time period between the end of 2015 and the mid of 2017, the 30 most well recorded events from the vicinity of the South Aegean were selected to calculate the moment magnitude. The comparison of the calculated moment magnitudes against the ones that have been reported from NOA are presented in figure 4.3.15. The results suggest that there is a small overestimation in larger than 5.0 magnitudes while at the same time there is an inadequate underestimation in the rest of the magnitude range.

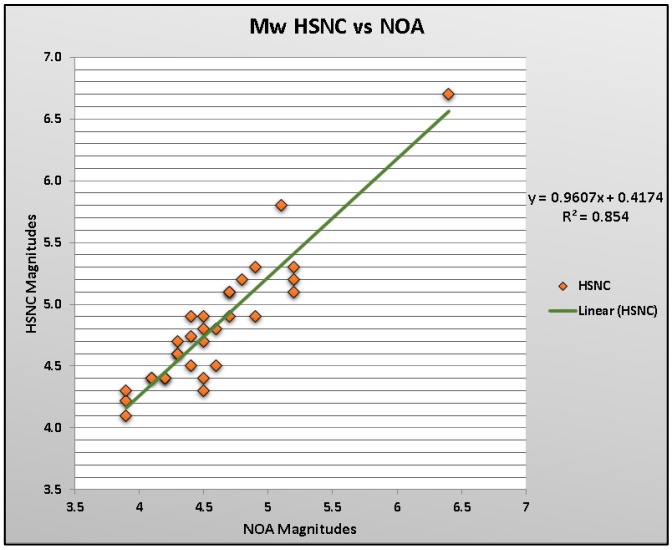

Figure 4.3.15 The moment magnitudes calculated with the HSNC stations versus the one reported from the NOA.

4.4 Relocation Process

4.4.1 The reasons to use relocation techniques

Since its first operations the HSNC has adopted REF TEK's commercial software to define the initial seismic parameters. Although the software is easy to learn, user friendly and suitable for marking seismic wave phases, it has some limitations. One of them is that for the location procedure, as it uses a locator which relays on the difference between theoretical and picked arrival times. Normally this is not wrong with an appropriate travel time table but the provided 'regional' model in the software has a generic crust model for subduction zones and this is not the most suitable for the Hellenic Arc. The manual preliminary results have a certain degree of accuracy, but this is not satisfactory for the HSNC which focuses on monitoring the seismically active front of the Hellenic Arc. Although the Hellenic subduction zone created by the convergence of the Eurasian – African lithospheric plates, has all the typical characteristics of an ocean-ocean plate convergence regime, there are some challenging tectonic, morphological and geological settings that make the investigation more difficult. Along the boundary area, the subducting slab can be divided into two different segments as they have different dipping angles

(Papazachos, et al., 2002). Geologically the South Aegean region and especially Crete, is characterized by continuous nappe units which construct a non-uniform material (Mountrakis, 1986; Kilias, et al., 1999) with different velocity layers. In addition, along the inner part of the Hellenic Arc there is a extensional stress field with the normal faults that started acting in the mid Quaternary and that formed the deep sedimentary basins (Papazachos, et al., 1999; Piper & Perissoratis, 2003) which add a low velocity layer in the upper crust. Therefore, the application of a general subduction velocity model will not fit well with the available data. A possible solution to increase the spatial resolution of the earthquake parameters is to have several local models dedicated for specific areas. Another obstacle is that the crust model file of the REF TEK's software is compiled in binary format, so it is difficult to be modified without the necessary software-developer knowledge.

Aiming to satisfy the need for increased accuracy in earthquake parameters, more sophisticated and customizable earthquake location software has been adopted. On the one hand there are the linear iterative methods (will address them in section 4.4.2) while on the other hand the recent studies suggest the use of 3D velocity models with non-linear location algorithm such as the NonLinLoc (Lomax, et al., 2000; Husen & Smith, 2004; Latorre, et al., 2016). The nonlinear locators need more computational power (which is not a problem nowadays) and they don't depend on the initial solution compared to linear methods (Husen & Hardebeck, 2010). A major drawback of using the non-linear methods is the lack of a detailed 3D model. In cases where a 3D grid velocity model has not been calculated, the software has an algorithm that creates one based on the available 1D models. Someone can argue that the linear iterative methods have similar techniques to use multiple 1D crust files like a 3D.

The 1D velocity models main disadvantage is that they are not suitable for large areas because of the possible inhomogeneities and lateral variations of the velocity (Husen, et al., 2003). Considering the following assumptions, that the research area is small in size with no complex structures and large velocity changes, like the area constrained by the events of an aftershock sequence around a fault, then in this case the relocation procedure will have pretty similar results either by using a linear location method with a 1D model or by adopting a nonlinear algorithm with 3D model constructed from many 1D crust files.

4.4.2 The relocation software

A series of earthquake location software based on Geiger's iterative least squares linear method (Geiger, 1912) with similar characteristics have been published by USGS (Klein, 2002). Some of the well-known locators are the Hypo71 (Lee & Lahr, 1972), the HYPOELLIPSE (Lahr, 1989) and the Hypoinverse-2000 (Klein, 2002). The Geiger's method assumes an arrival time function (Maochen, 2003):

$$f_i(x, y, z, t) = t + \frac{1}{V}\sqrt{(x_i - x)^2 + (y_i - y)^2 + (z_i - z)^2} \quad (4.3)$$

The x, y, z are the coordinates of the hypocentre while the x_i, y_i, z_i are the coordinates of the ith seismometer, V is the seismic wave velocity and t is the origin time. The 4.3 equation is solved with the use of partial derivatives:

$$\frac{\partial f_i}{\partial u} = \frac{u_i - u_0}{V\sqrt{(x_i - x)^2 + (y_i - y)^2 + (z_i - z)^2}} \text{ with } u = x, y, z \text{ and } \frac{\partial f_i}{\partial t} = 1. \quad (4.4)$$

The quality of the solutions relay on the partial derivatives, the trial location as well as the applied constrains (Husen & Hardebeck, 2010). Another popular software from USGS is the HypoDD which try to estimate the travel time difference for pairs of earthquakes that have been recorded from the same stations (Waldhauser, 2001). In this method the reliability of the solution depends on spatial distribution of the earthquakes as it works better for close distance events as well as the location accuracy of the primary event of the pair (Husen & Hardebeck, 2010).

In this research, the Hypoinverse-2000 location software has been used as the primary software to create relocated aftershock sequence and swarm catalogues. Most researchers use the HypoDD after the Hypoinverse-2000 relocation to achieve better results. Taking the small relocation errors from the Hypoinverse-2000 results into account as well as the

spatial distribution of the aftershock (see Chapter 5.2), I decided not to use the HypoDD software.

4.4.3 The relocation files and parameters.

The Hypoinverse-2000 uses a number of input files. A brief description of them as well as the purpose and the available adjustable parameters based on the manual follows (Klein, 2002): A typical run needs the phase file, the crust model, the station file and optionally the control file. All the input and output files have ASCII format. The phase file contains information about the phase arrival times, each phase picking which has been recorded in a station, it is written in a separate line. This kind of files also contains the direction of the first motion, the maximum peak to peak amplitude and its period and some weights for each phase. The control files have all the three letter commands that define the input-output files, the data format, the limits of the acceptable values as well as other options that are needed for running the program. Some of the parameters were common for all the relocation procedures. The velocity ratio was set to 1.75 after examining the Wadati diagrams (see subchapter 5.2). The distance weighting of each station was set to start from the 4^{th} iteration with cut off distance 100km. The distance weighting function is a cosine taper, the parameters that control the tapered window was 1 and 2, which means the stations with 2 * 100 distance doesn't receive weight while the ones between 100 and 200 receive reduced weight. This option ensures that the contributing sensors to the relocation process have small epicentral distances. As the distance of a station-epicentre increase, the seismic waves attenuate, the signal becomes weaker in terms of signal to noise ratio and the waveform becomes longer as the *P-S* interval increase due to the *S* wave velocity which makes the phase picking harder. Moreover, the seismic rays from distant events may pass from different formations, layers that have other velocity and thickness values from the examined area. The same type of tapered function applies for the phase residuals in order to remove phases with high timing errors. The root-mean-square residual cut off was set as 2 while the window length constants was 1 and 2. The initial values for distance and RMS residual weighting have been obtained through personal communication with the network operators of NOA and AUTH, and some small changes were applied after several tests on the results. The initial trial depth has been found with the trial and error approach. The

accepted trial depth values were selected by the one that produce the smallest relocation errors and did not stuck the events to a specific layer of the crust model.

A special attention is given to the station files that contain information like the stations coordinates, altitude and the station delay errors. The Hypoinverse assumes that the earth is flat with no elevation, in order to take the lateral velocity variations and elevation delaying effect into account, the phase delays should be included in the station file. In each relocation case to fix the station timing errors, several events (50 to 100 depends on the available dataset) with the smallest errors and the largest number of phases have been used to define the station timing residuals. The events that participate in station error corrections must have the most accurate coordinates and gathered in a limited volume. Typically, these criteria are satisfied with the mainshock and the largest aftershocks because these events have been recorded in large distances with many *P* and *S* phases. The events that have been recorded with many phases from different distance stations, are more constrained and they are less independent in the velocity model. The station calibration process is achieved with a Fortran program that calculates the station timing errors. The script finds the origin time from the Wadati plots which mean that it is independent from the velocity model and then calculates the 'new' observed travel times. The new travel times are compared with the theoretical ones in order to estimate that station corrections (Karakostas, et al., 2012). This procedure requires to run the Hypoinverse-2000, relocate the events, execute the station correction algorithm, apply the station corrections and start from the beginning the same procedure until the new obtained station corrections are very small ≈0.02 second. If the station corrections did not become inadequate after a series of iterations, then the software cannot converge to a solution so there is a problem in the crust model or in the picked phases.

The crust file has two columns, one with the speed of *P* waves in km/sec and one with the thickness of the layer where the speed remains unchanged. In the literature there are the 1D crust models, the most recent are provided from the work of Meier, et al. (2004) for the western, southwest and southern Crete and the work of Becker, et al. (2010) for the central-eastern part of Crete. To obtain more updated crust models, that have been used for relocation of the 15/06/2013 and 12/10/2013 aftershock sequences, a personal communication was established with Professor Karakostas V. from AUTH who has

extensive experience in relocation techniques. The provided crust models (table 4.2) are from Meier, et al. (2004) but they have been modified by Professor Karakostas and they have been published in Chatzopoulos, et al. (2016) and Papadimitriou, et al. (2016).

Table 4.2 The modified crust that has been used to relocate the 15/06/2013 and 12/10/2013 aftershock sequences.

Vp (km/sec)	Depth (km)	Vp (km/sec)	Depth (km)
4.6	0	4.2	0
5.4	1	5.7	1
5.7	2.5	6.3	3
6	5	6.4	8
6.1	8	6.45	12
6.2	11	6.5	20
6.3	15	6.8	25
6.6	20	7.3	30
7	25	7.9	33
7.5	30		
8	33		

The Hypoinverse has a number of commands and files that are used to control the magnitude estimation. These options have not been used as the magnitudes that have been calculated with the REF TEK' software and the Figure 4.3.13 results suggest that the magnitude estimations are pretty accurate.

4.4.4 VELEST software

In 2016 a swarm sequence occurred in the onshore part of western Crete. The sequence lasted about two months with having a considerable number of minor and moderate events. The events first location has been carried out with REF TEK's commercial software, but there was an obstacle for the relocation procedure. In the specific area, there were no records for similar type of swarm behaviour and a 1D crust model did not exist. In the literature there were some tomographic researches (Makris, et al., 2013; Kokinou, et al., 2006) that could get a general idea for the interior of this area in order to derive an

approximate velocity model, but this solution did not give any satisfactory results. The station corrections keep increasing after several tries and the events after relocation stuck to specific velocity layers. Instead of trying to establish a rough crust model based on the literature, the already proposed 1D models (Meier, et al., 2004; Chatzopoulos, et al., 2016; Papadimitriou, et al., 2016) for the neighbour areas have been tested. The new results were better than the first attempt, the horizontal and the time residual errors were small, but the vertical ones were considerable large. The next step was to create a 1D model with the VELEST version 3.3 software (Kissling, et al., 1995). The VELEST has two different modes, the single and the joint event solution. The second mode is used to estimate a minimum 1D model by taking the time residuals into account. The software is trying to minimize the residuals for a set of events by continuous inversion of the hypocentres, the station corrections and the velocity model in each iteration.

The software parameters and options are the same provided by (Kissling, et al. (1995) user manual and the procedure to derive 1D models is well descripted in (Kissling, et al., 1994). The only parameters that have been adjusted were VELADJ from 0.2 to 0.1 which is responsible for the changes in the velocity model in each iteration as well as the ZADJ from 5 to 1 which controls the depth change in each iteration. These adjustments have been applied to increase the detail in the converge procedure as the 1D model estimation have been completed with more and smaller steps. The first relocation has been carried out with Hypoinverse-2000 software, the 1D crust model was the same for 12/10/2013 western Crete. The 462 events with the smallest relocation errors have been converted to VELEST phase file format with a MATLAB script. An algorithm to transform the file did not exist and for the purpose of this thesis one was created and provided in appendix (hyp2velest.m). The selected events have horizontal errors less than 1.7km and depth errors less than 3km. The input 1D model was the same one used in the first relocation. A series of simultaneous five iteration inversion with the use of the coupled hypocentre method have been completed before the 1D model with the smallest time residual error was derived. All the new 1D models as well as the ‘best’ solution, have been used in Hypoinvese-2000 to carry out the second relocation. Numerical results of the strongest events relocation errors before and after the use of model calculated from VELEST as well as the 1D velocity model are presented in the 5.2.4 subchapter.

Chapter 5 Results

5.1 Foreshock patterns

5.1.1 Theoretical Model

The large earthquake organization patterns that exhibit faults with scaling properties described by a self-organized criticality model (Bak & Tang, 1989; Bak, et al., 2002) as well as the recent work on earthquake properties with Tsallis entropy (Tsallis, 2009; Vallianatos, et al., 2015; Vallianatos, et al., 2016), were the motivation to apply the non-extensive statistical physics approach to the earthquake occurrence. A theoretical model that explains the energy concentration and release in the crustal rocks has been proposed in section 3.1.2. The new model is a result of jointed theories, the classical first principles approach with the energy conservation laws that has been combined with the non-extensive statistical physics. Based on the NESP and the Tsallis entropy, a framework that produces the collective pattern of seismicity has been introduced to describe the macroscopic behaviour of the complex seismic systems that present strong correlations among their elements.

Summarizing the results from the proposed model in subchapters 3.1.2 and 3.1.3: In existing published work (Bowman, et al., 1998; Varnes, 1989; Bufe & Varnes, 1993; Bowman & King, 2001), a power law time-to-failure equation has been used to describe the cumulative energy release before significant earthquakes (3.1.1b):

$$\Omega(t) = \Omega_f - B(t_f - t)^m \quad \text{where} \quad B = \frac{k}{m}$$

The analytic expressions of the energy flow and storage inside the stressed crustal volume during the earthquake preparation stage demonstrate that the earthquake subvolumes follows a fractal distribution. The non-extensive statistical physics approach shows that the entropic index q is correlated with the subvolumes and it is bounded by the Euclidean dimension d_e of the deformed system which leads to the equivalent equation (3.1.21a):

$$\Omega_{\xi}(t) = \Omega_{\xi f} - B(t_f - t)^{m_{\xi}}$$

The $\Omega_{\xi f}$ is equal with Ω_{ξ} for the time of failure as $t = t_f$, while the B and the critical exponent for the proposed model is (3.1.21b and c):

$$B = \gamma \frac{T_c^{a(d-d_e+1)} (U_{0in})^a}{L_0^{a(d-d_e+1)}} \frac{1}{a(d_e-1-d)+1}$$

$$m_{\xi} = a(d_e - 1 - d) + 1$$

Taking the Gutenberg-Richer law, Kanamori energy-magnitude relation and Kagan number of events-energy equations into account, the relation between *b-value* and entropic parameter q is derived (3.1.25):

$$b = \frac{3}{2} \frac{2-q}{q-1}$$

For a fractal dimension $d = d_e \frac{2q-3}{q-1}$ and by taking the equation 3.1.25 into account, the critical exponent becomes (3.1.26):

$$m_{\xi} = 1 + \alpha \left(\frac{2}{3} b \, d_e - 1 \right)$$

An analytic expression that connects the critical exponent m_{ξ} of the power law time-to-failure model with the Tsallis entropic parameter q and the b value of Gutenberg – Richter law has derived. Moreover, according to the equations (3.1.21c): $m_{\xi} = a(d_e - 1 - d) + 1$ the critical exponent is independent of the ξ *(0≤ξ≤1)* which have been used in the definition of the generalized Benioff strain $\Omega_{\xi}(t)$. The m_{ξ} is controlled by the Euclidean dimension d_e of the deformed system and the entropic parameter q which as a measure of long range interactions and of the complexity of the system. This leads to the conclusion that for the

accelerated crustal seismicity patterns an $m_\xi \approx 0.3$ should exist for all ξ *(0≤ξ≤1).* To validate the aforesaid assumption, the critical exponent was tested with real numerical examples from South Aegean (see section 5.1.2).

The upper and lower bound of the parameters q and b created according the geometrical limitations, the positive definition of m_ξ and the condition of the system (accelerating with m_ξ<1 or decelerating with m_ξ >1). Based on the range of the q and the b values that could drive the system into an accelerating stage and to failure, the precursory variations of m_ξ as resulted by any precursory b-value anomaly proposed by Wang (2016) is explained.

It is proved in section 3.1.3 that mean generalized Benioff rate during the accelerated period T_c (3.1.34):

$$\frac{\langle \frac{d\Omega_\xi}{dt} \rangle_D}{\left. \frac{d\Omega_\xi}{dt} \right|_l} = \frac{1}{m_\xi} \approx 3 - 4$$

the $\left. \frac{d\Omega_\xi}{dt} \right|_l$ refers to the generalized Benioff strain rate during the linear part.

While if the $\Omega_{\xi l} \ll \Omega_{\xi f}$ then (3.1.35):

$$\Omega_{\xi f} \approx \langle \frac{d\Omega_\xi}{dt} \rangle_D \, T_c$$

Based on the literature, the associated average generalized Benioff strain rate during accelerating period connected with the background seismicity rate and a model to estimate the expected magnitude of the main shock has been proposed (3.1.38) and (3.1.39):

$$M_m = \frac{4}{3} \log \left[\frac{1}{m_{1/2}} \left(\left. \frac{d\Omega_{1/2}}{dt} \right|_l \right) T_c \right] + \frac{4m_{1/2}}{3} \log \left(\frac{\delta t_1}{T_c} \right) - 3.13$$

$$M_m^{max} = \frac{4}{3} \log \left[\frac{1}{m_{1/2}} \left(\left. \frac{d\Omega_{1/2}}{dt} \right|_l \right) T_c \right] - 3.13.$$

The calculations based on Tsallis entropy and the energy conservation law, gives a new view on the empirical scaling laws. The results of the proposed model in section 3.1.2 and 3.1.3 connect the empirical law parameters of the time-to-failure power-law expression with a unified theoretical framework based on the ideas of non-extensive statistical physics.

5.1.2 Numerical results

In 2013 and 2015, three strong earthquakes with moment magnitude range from 6.0 to 6.4 and the associate foreshocks/aftershocks have been occurred in the west, east and central part of the Hellenic subduction zone (figure 5.1.1). The proposed theoretical model has been tested with two real event catalogues: the Thales and the revised catalogue of NOA. The Thales catalogue used for the 2013 events only since it contains no data for the subsequent years. The time period before the strong events was examined for precursory seismicity patterns using the concept of the common critical exponent in the excitation period.

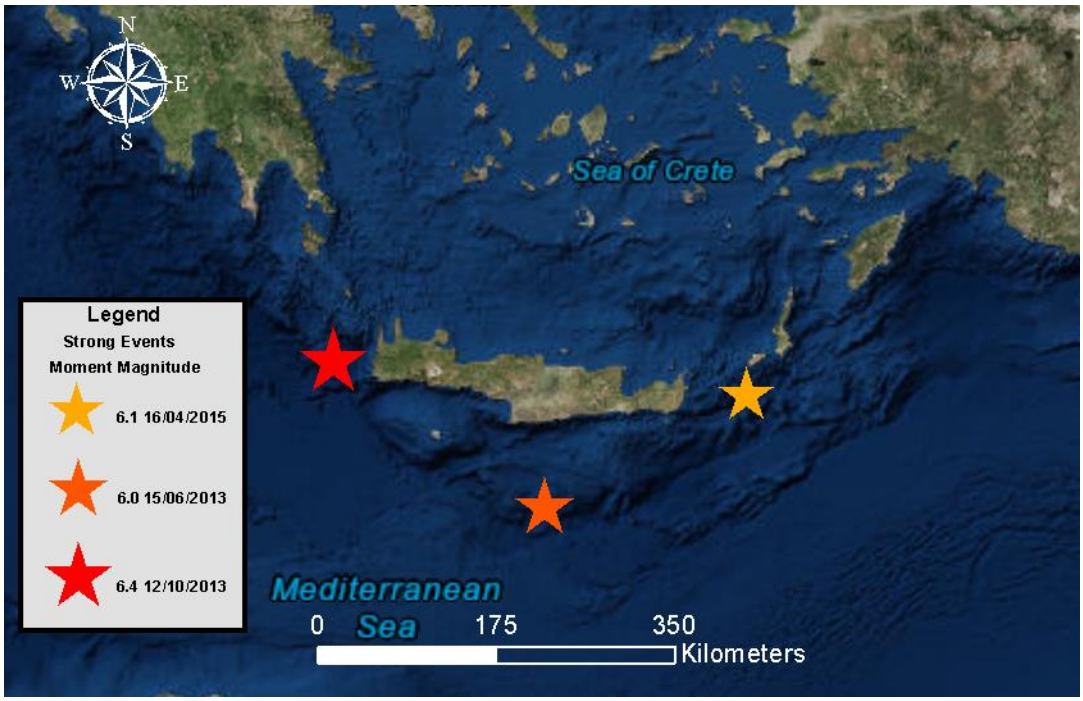

Figure 5.1.1 The three strong events occurred in 2013 and 2015 in the South Aegean (map data are managed in ArcGIS (Esri, 2018).

The new code written in MATLAB programming environment (see section 3.3.2) was used to scan the South Aegean area for accelerating seismic crustal deformation. In the new GUI scanner, the fitting algorithm solves the power law equation with a non-linear regression approach which gives a better and smoother fitting in the Benioff strain, seismic energy release and number of event curves as it is described in section 3.3.2. In the same section it is described the `accres.m` function that has been used to filter and inspect the seismicity pattern results. Aiming to define the geographical area and time window ($t = t_f - T_c$) where the accelerated seismic release pattern is well identified, the aforesaid criteria mention in section 3.3.3 have been applied. The first couple searches have been carried out with a 0.1 square grid, this value was reduced to 0.05 for the areas where a seismic pattern has been identified. Setting the search grid half of the proposed in literature size, helped to have an increased spatial resolution. This method produced more accurate and better power law fitting results. Before every large event a time window where the critical exponent $m_\xi \approx 0.3$ for $0 \leq \xi \leq 1$ has been point out. Aiming to increase further the detail of the results, the search grid was reduced to 0.01. The new results have even lower curvature parameter, most times better correlation coefficient and more accurate estimation of the critical time. An example from the 12/10/2013 seismicity pattern identification is illustrated in figure 5.2.2 where the detailed search with 0.01 grid, identified a better solution.

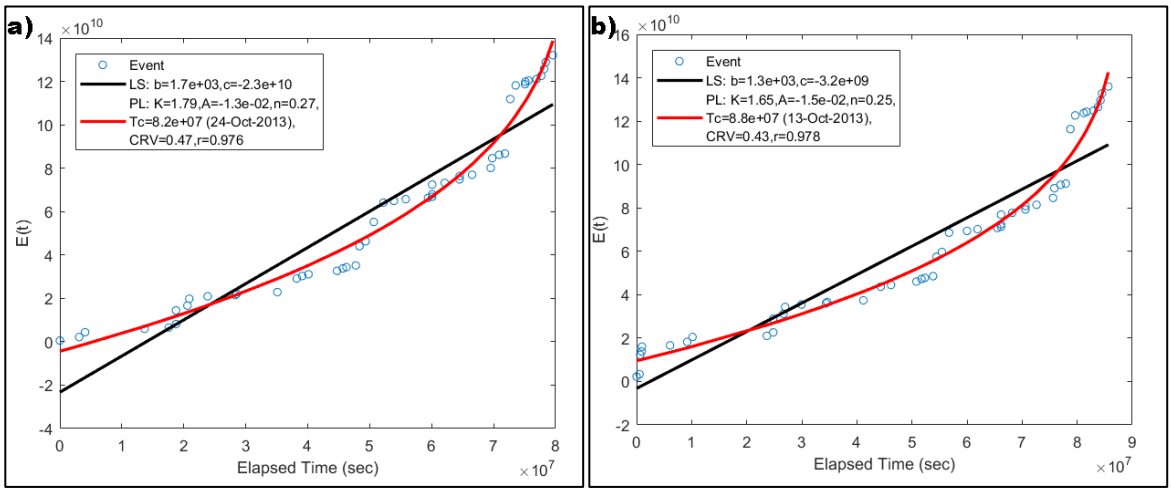

Figure 5.1.2 a) The results obtained by fitting a 16 km radius circle in the grid point 23.10, 35.15 and b) the result from a 15km radius circle in the point 23.12, 35.15.

The summary of the parameters that produce the optimal results such as the starting-ending time, the minimum magnitude, the maximum depth as well as the size and centre of the circles that have used in the successful seismic pattern identification are presented in table 5.1.1. Most times, close to the 'best' results grid point, there are solutions with slightly worse power law fitting, but with acceptable identification criteria. These happen because the search shape and size does not approximate exactly the critical region and by 'moving' the search circle it includes or excludes some events. Small diameter expanding circles have been used separated the accelerated – decelerated seismic patterns in the deformed region.

Table 5.1.1 The parameters that defined the accelerated seismic pattern.

Case	Starting time	End time	Radius (km)	Depth (km)	M_c	Longitude degrees	Latitude degrees	N	catalogue
15/06/2013	18/01/12	24/05/13	15	40	2.7	25.04	34.83	29	Thales
12/10/2013	04/01/11	21/09/13	15	40	2.7	23.12	35.15	49	Thales
16/04/2015	16/01/11	06/04/15	14	40	2.5	27.47	35.46	26	NOA

In order to find the seismic pattern starting point, the trial and error method have been carried out up to 10 years before each mainshock. The 15/06/2013 case was an exception in the aforesaid approach because a previous strong event limited the search catalogue. According to the NOA' revised catalogue, near the 15/06/2013 epicentre (34.336, 25.063 and depth 31.8km) there was another large event in 01/07/2009 with comparable magnitude (ML=5.8) and coordinates (34.350, 25.400 and depth 30km) while the focal mechanisms were almost the same. These limited the search for the 15/06/2013 seismic pattern starting time

The figures 5.1.3, 5.1.7 and 5.1.11 present the accelerating seismic crustal deformation results with the use of the new software for the 15/06/2013, 12/10/2013 and 16/04/2015 strong events respectively (see section 3.32). In each figure, from (a) to (c) there is the

different critical exponent result: number of events, Benioff strain and seismic energy release respectively. On the maps, the different coloured squares are the grid points with a successful solution while the red star denotes the large events. These squares are the centre of the search circles and their colour is based on the values denoted on a scale bar next to the map. The main map which in the right side, present the filtered results while the two small ones on the left side of the singleton are the unfiltered curvature and critical exponent values. These figures have been compiled using the 0.01 square grid for the whole vicinity of the South Aegean. As it is noticeable for all study cases, the results for the energy exponent m_ξ for ($\xi = 1$) are limited compare to the other two exponents. This happens because it is more difficult to have a good power law fitting for the energy exponent as the magnitude difference of the events increase much more the fitting distance between them.

Figures 5.1.4, 5.1.8 and 5.1.12 illustrating the results obtained from the main maps (5.1.3 figures), focused in the critical area. The inspection of the curvature-m_ξ exponents results: number of events (a), Benioff stain (b) and seismic energy (c) suggest that there is a common area where the aforesaid criteria are satisfied. The events that satisfy the parameters from the table 5.1.1 for the foreshock seismic patterns are illustrated in figures 5.1.5, 5.1.9 and 5.1.13 while the power law fittings for the different critical exponents are presented in figures 5.1.6, 5.1.10 and 5.1.14.

In the first strong earthquake (15/06/2013), the critical region has been identified north of the mainshock epicentre. The excitation period was quite narrow; the power law has optimal fitting with an about 1.5-year time window. The Benioff strain optimal fitting is slightly overestimating the critical time, ten days later while the seismic energy release underestimates the critical time by 8 days. The second strong event (12/10/2013) has a more stable power law fitting with more events, lower curvature compared to the first one and the critical area (located at SSE) is closer to the epicentre. The preparation period was more than 2.5 years and the Benioff strain and seismic energy release fitting give a critical time few and 1 days respectively later than the actual critical time. The last strong event (16/04/2015) has a very good Benioff strain power law fitting, the estimated critical time is 1 day later while the seismic energy fitting underestimates the critical time by 11 days. The preparation period was about 4.2 year and this seismic pattern was identified with almost the minimum events.

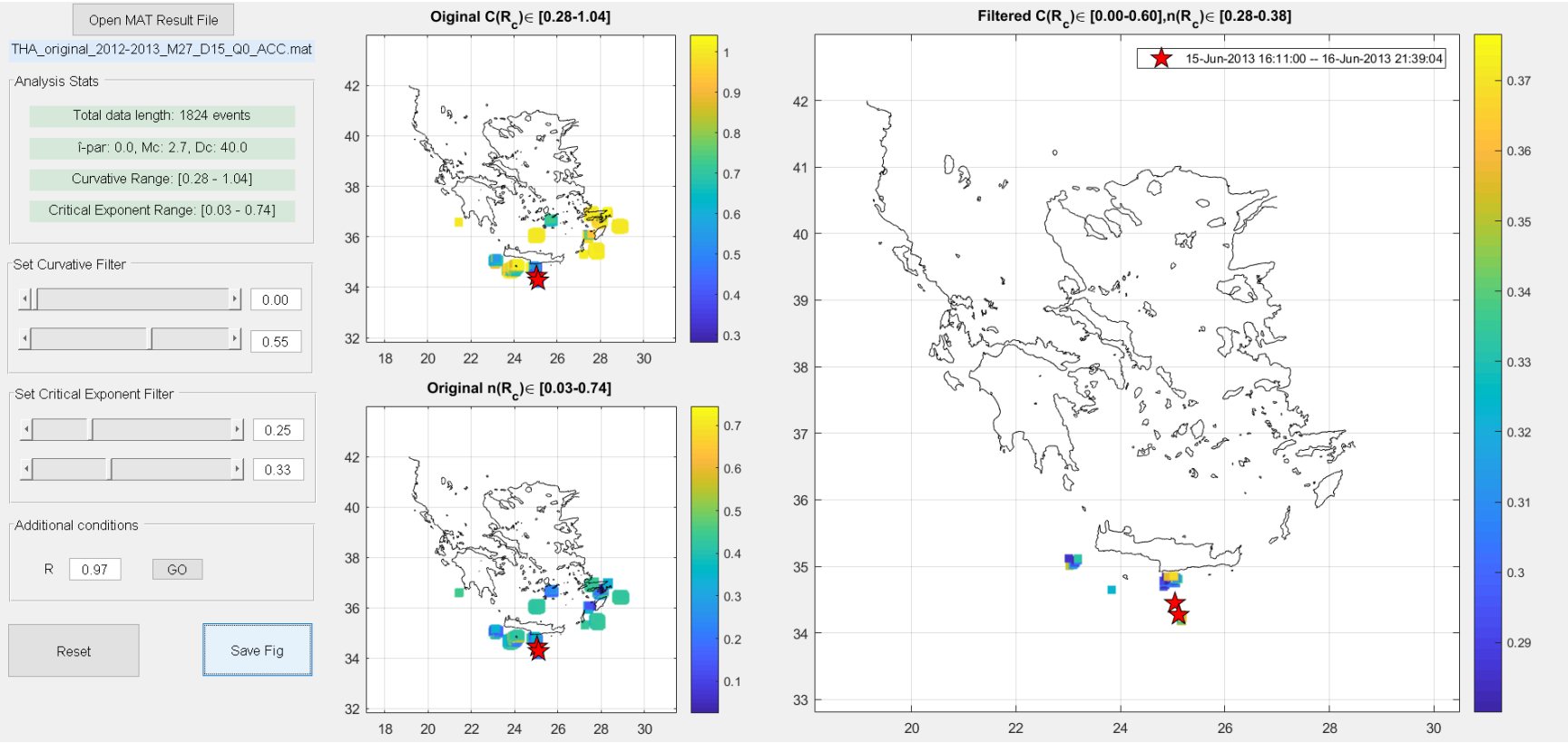

Figure 5.1.3a) The scan results of the accelerating seismic crustal deformation for $\xi = 0$ energy exponent before the 15/06/2013 mainshock. On the left panel there are some search statics as well as the filters that have been applied in the main map.

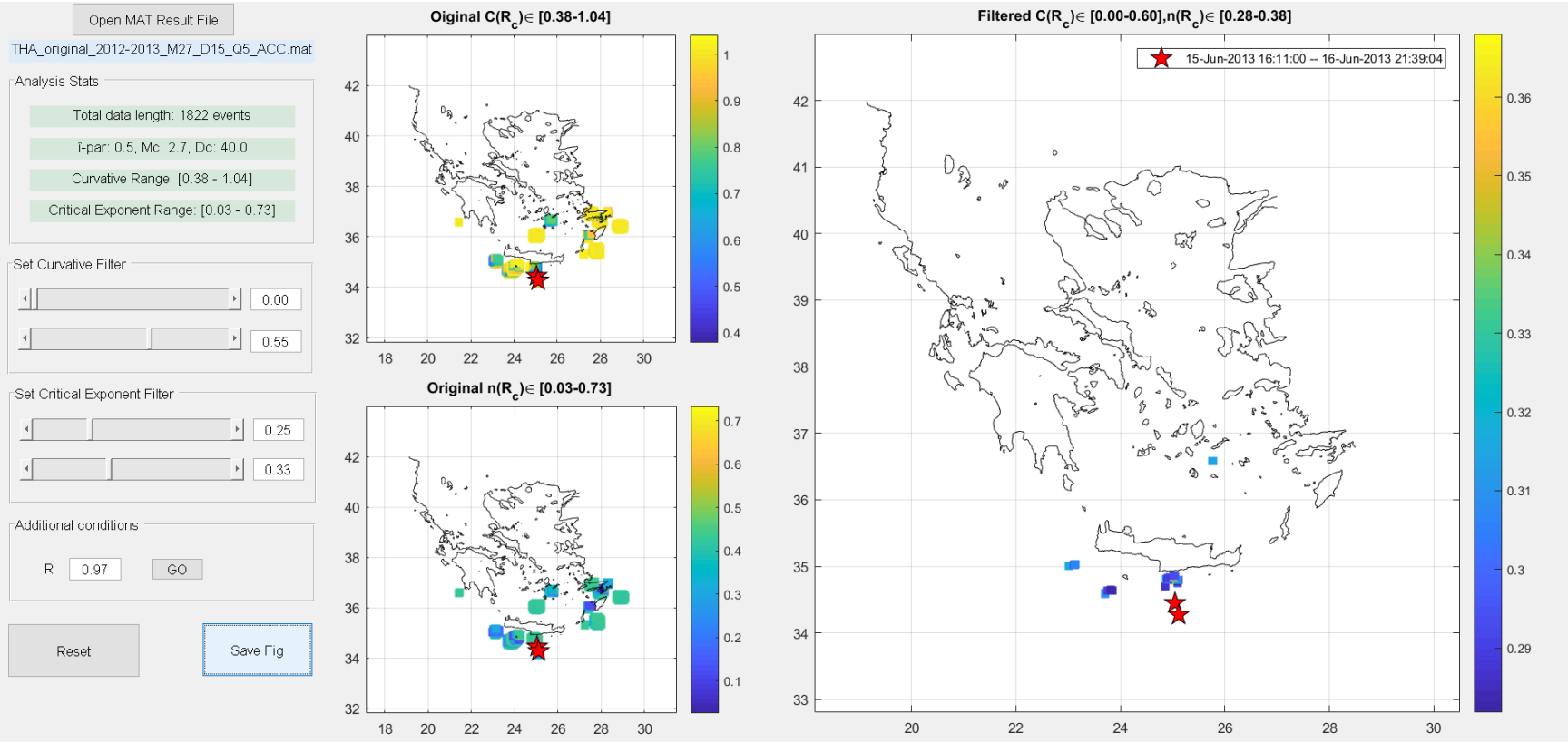

Figure 5.1.3b) The scan results of the accelerating seismic crustal deformation for $\xi = 1/2$ energy exponent before the 15/06/2013 mainshock. On the left panel there are some search statics as well as the filters that have been applied in the main map.

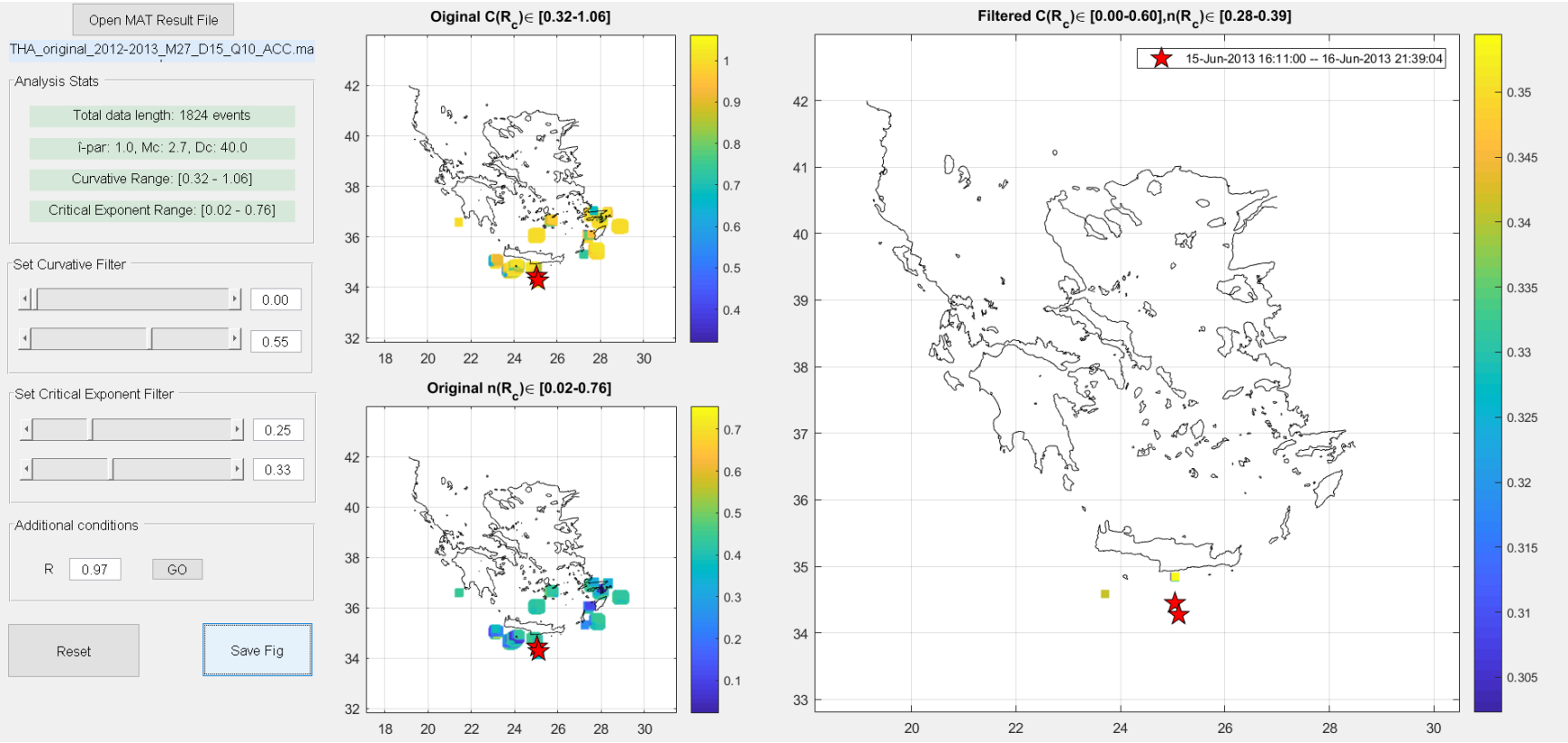

Figure 5.1.3c) *The scan results of the accelerating seismic crustal deformation for $\xi = 1$ energy exponent before the 15/06/2013 mainshock. On the left panel there are some search statics as well as the filters that have been applied in the main map.*

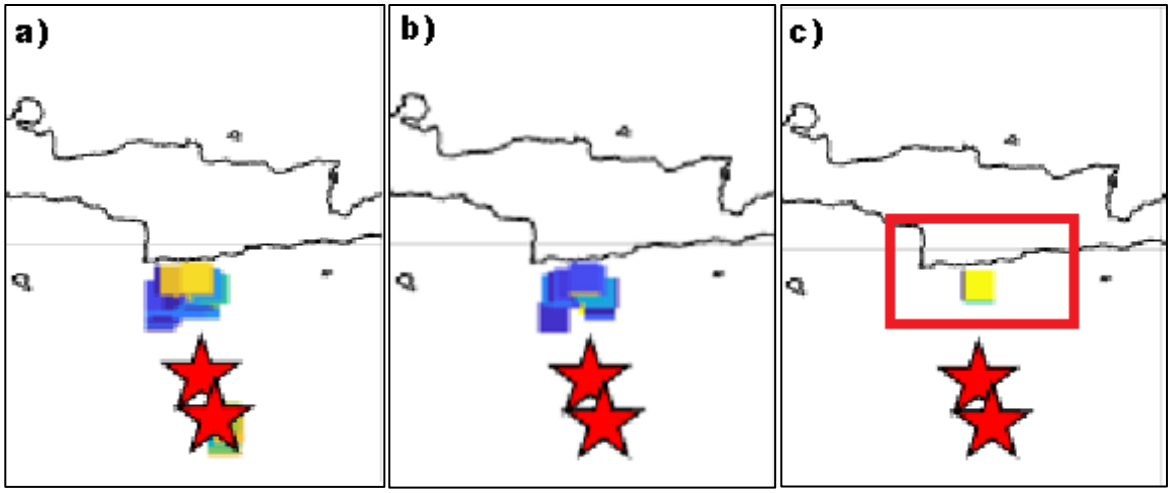

Figure 5.1.4 The filters application in the curvature parameter, critical exponent and power law fitting correlation coefficient for the 15/06/2013 foreshock results. The red box denotes the centre of the circle where the common critical exponent has the optimal fitting.

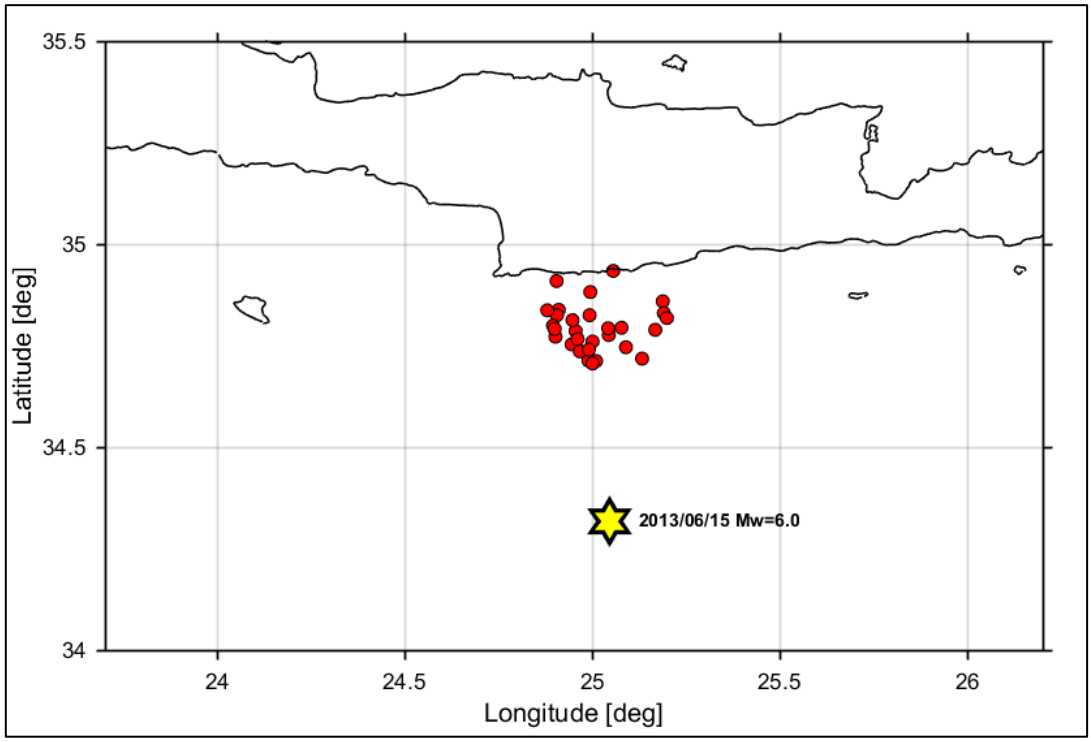

Figure 5.1.5 The epicentres of the earthquakes that identified as the15/06/2013 strong event foreshocks. (figure obtained from Zmap).

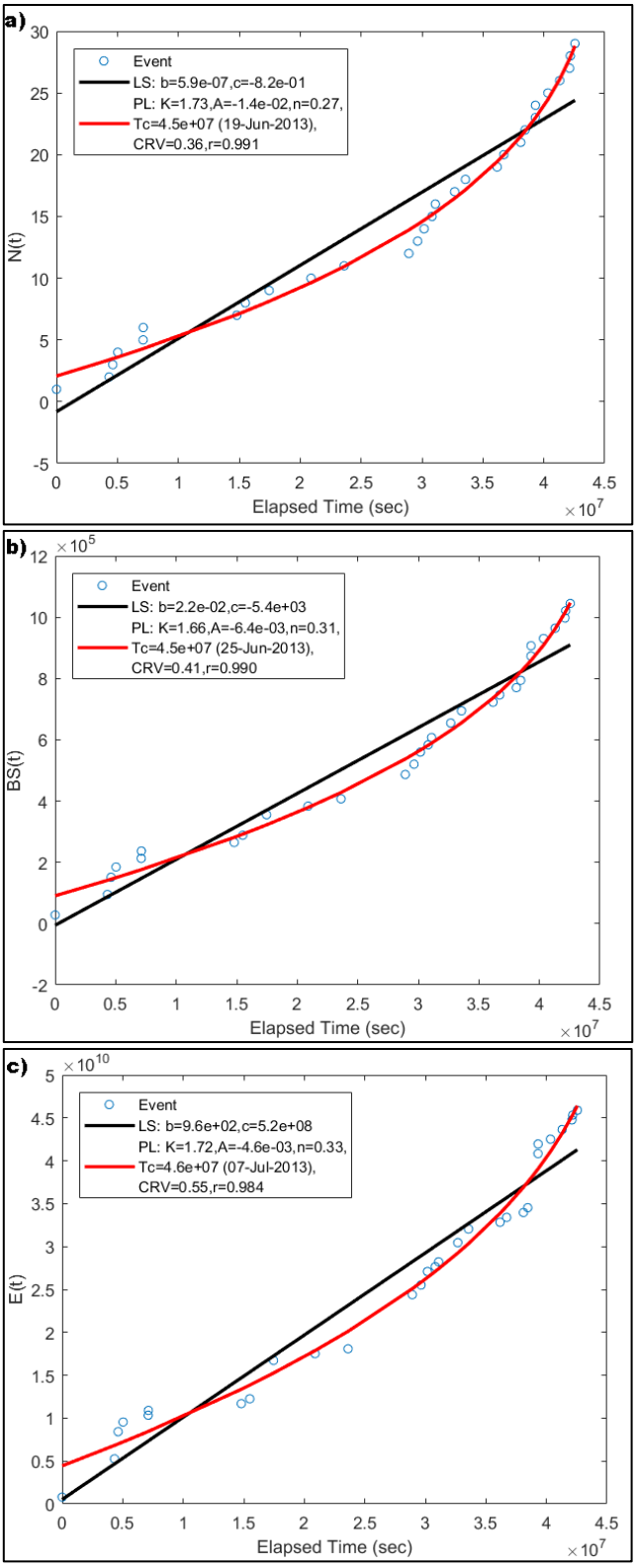

Figure 5.1.6 The power law (red) and the linear (black) fitting of events (blue circles) for $m_\xi = 0$*(a),* m_ξ*=1/2 (b) and* m_ξ*=1 (c) (See section 3.3.2).*

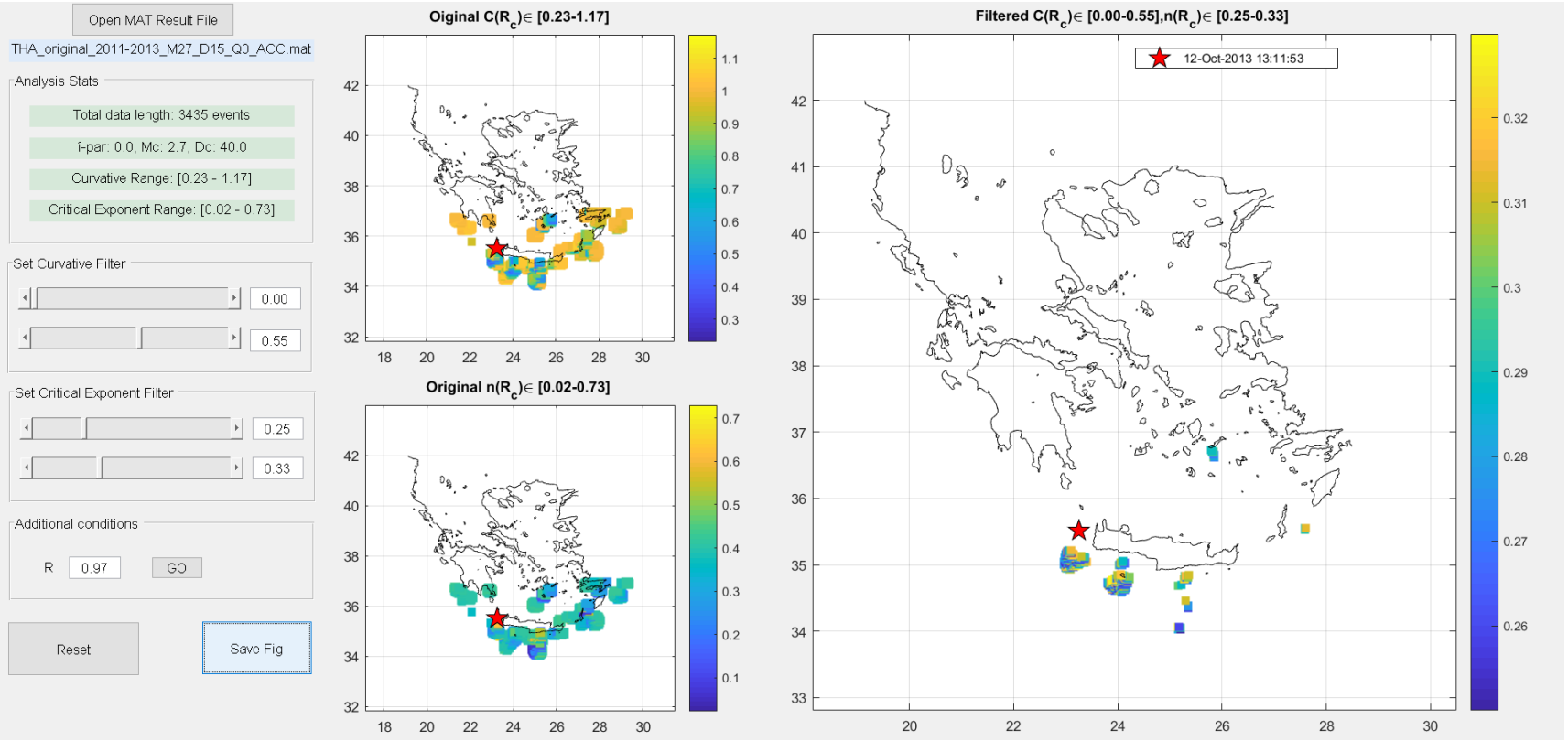

Figure 5.1.7a) *The scan results of the accelerating seismic crustal deformation for* $\xi = 0$ *energy exponent before the 12/10/2013 mainshock. On the left panel there are some search statics as well as the filters that have been applied in the main map.*

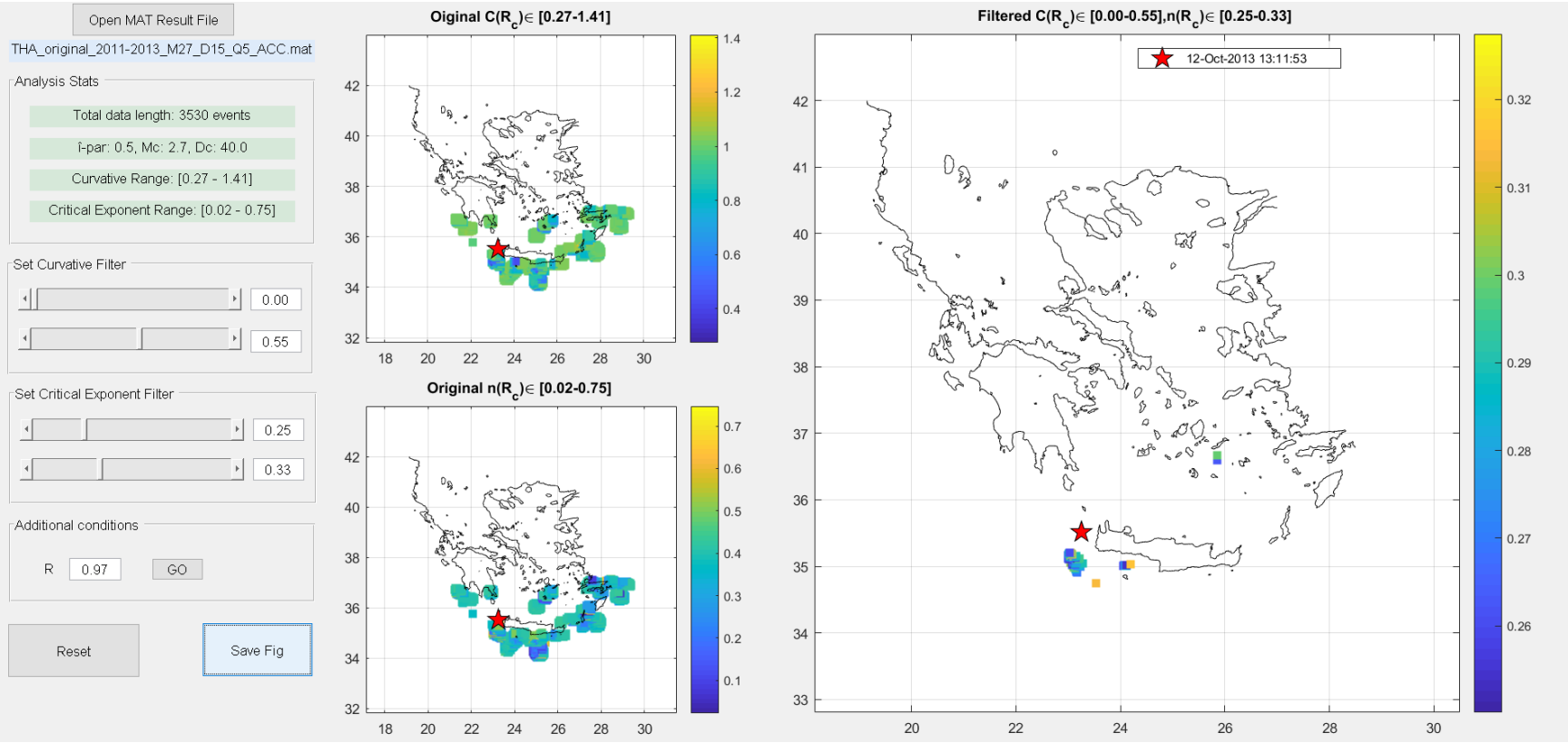

Figure 5.1.7b) *The scan results of the accelerating seismic crustal deformation for* $\xi = 1/2$ *energy exponent before the 12/10/2013 mainshock. On the left panel there are some search statics as well as the filters that have been applied in the main map.*

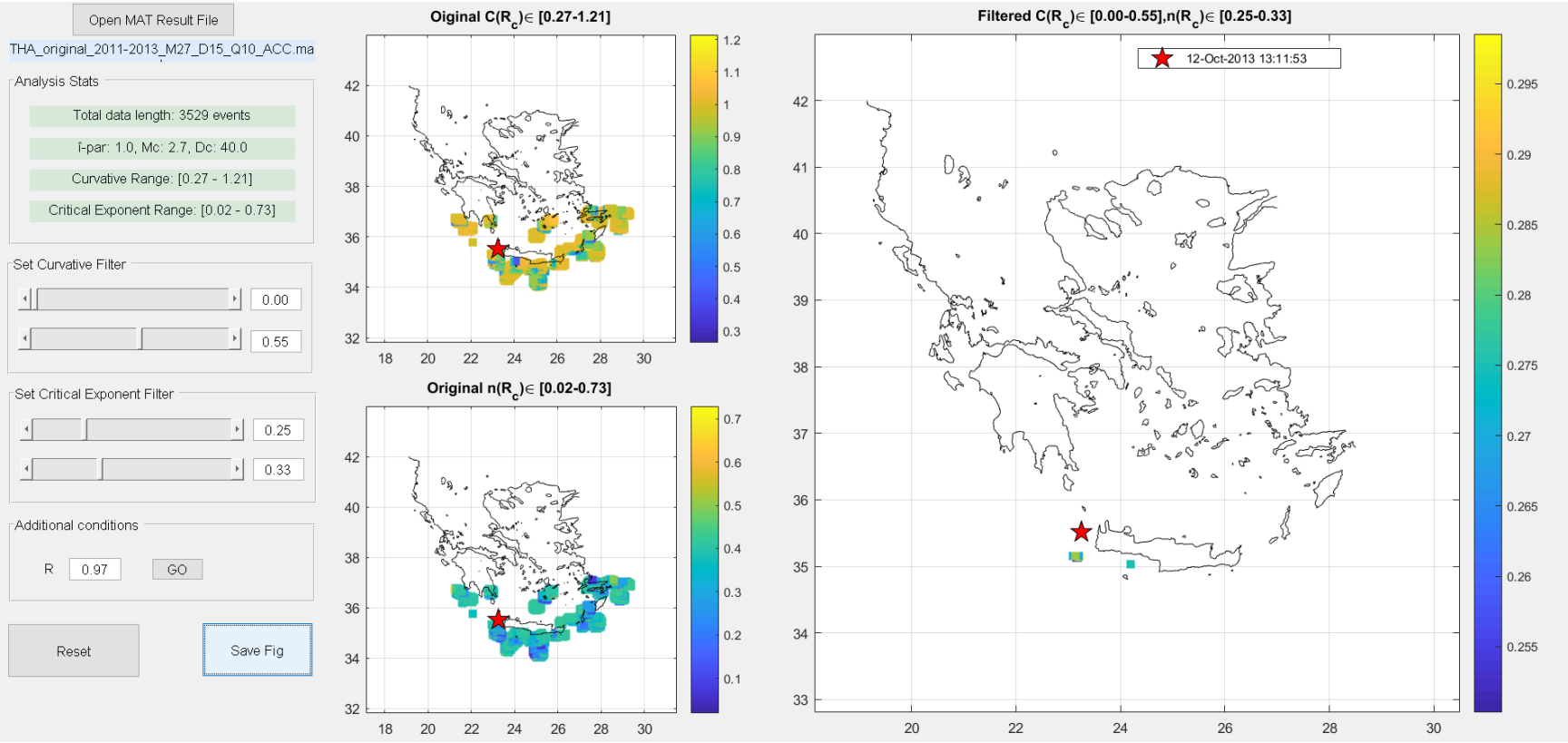

Figure 5.1.7c) *The scan results of the accelerating seismic crustal deformation for* $\xi = 1$ *energy exponent before the 12/10/2013 mainshock. On the left panel there are some search statics as well as the filters that have been applied in the main map.*

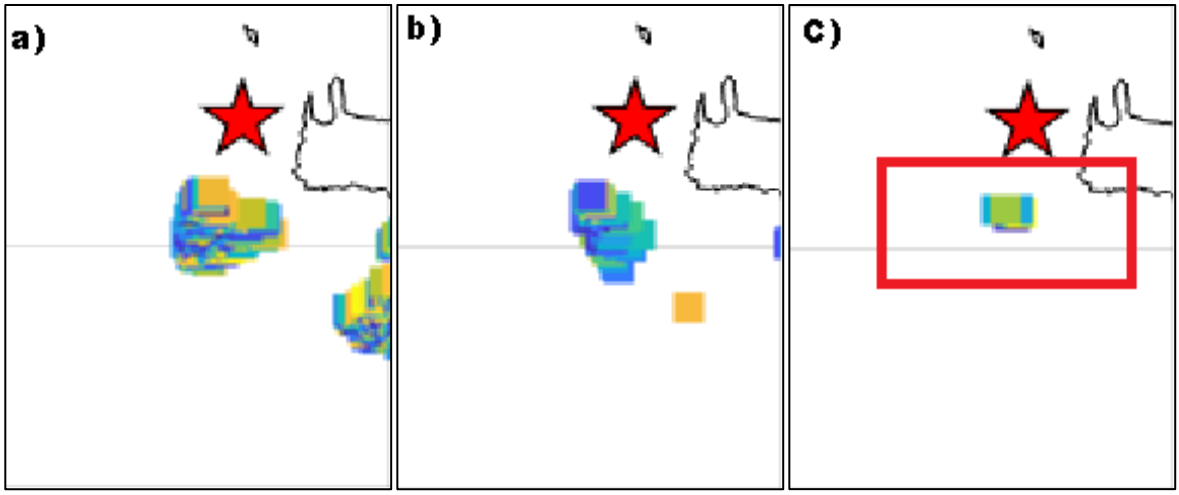

Figure 5.1.8 The filters application in the curvature parameter, critical exponent and power law fitting correlation coefficient for the 12/10/2013 foreshock results. The red box denotes the centre of the circle where the common critical exponent has the optimal fitting.

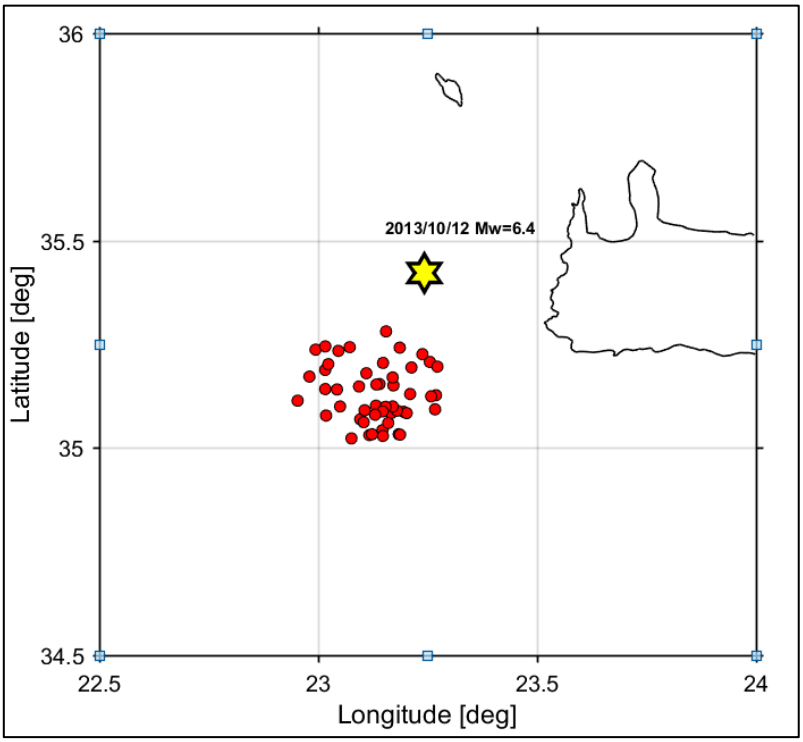

Figure 5.1.9 The epicentres of the earthquakes that identified as the 12/10/2013 strong event foreshocks. (figure obtained from Zmap).

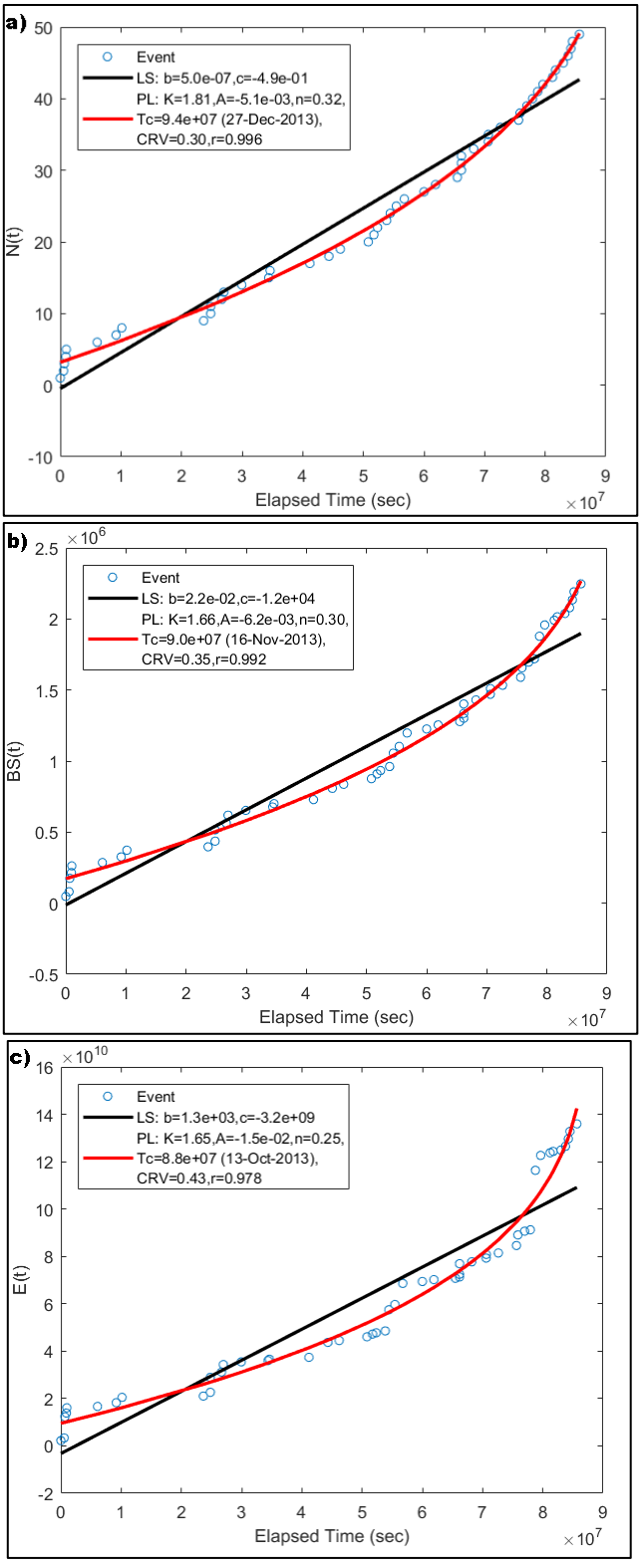

Figure 5.1.10 The power law (red) and the linear(black) fitting of events (blue circles) for $m_\xi = 0$*(a),* m_ξ*=1/2 (b) and* m_ξ*=1 (c) (See section 3.3.2)*

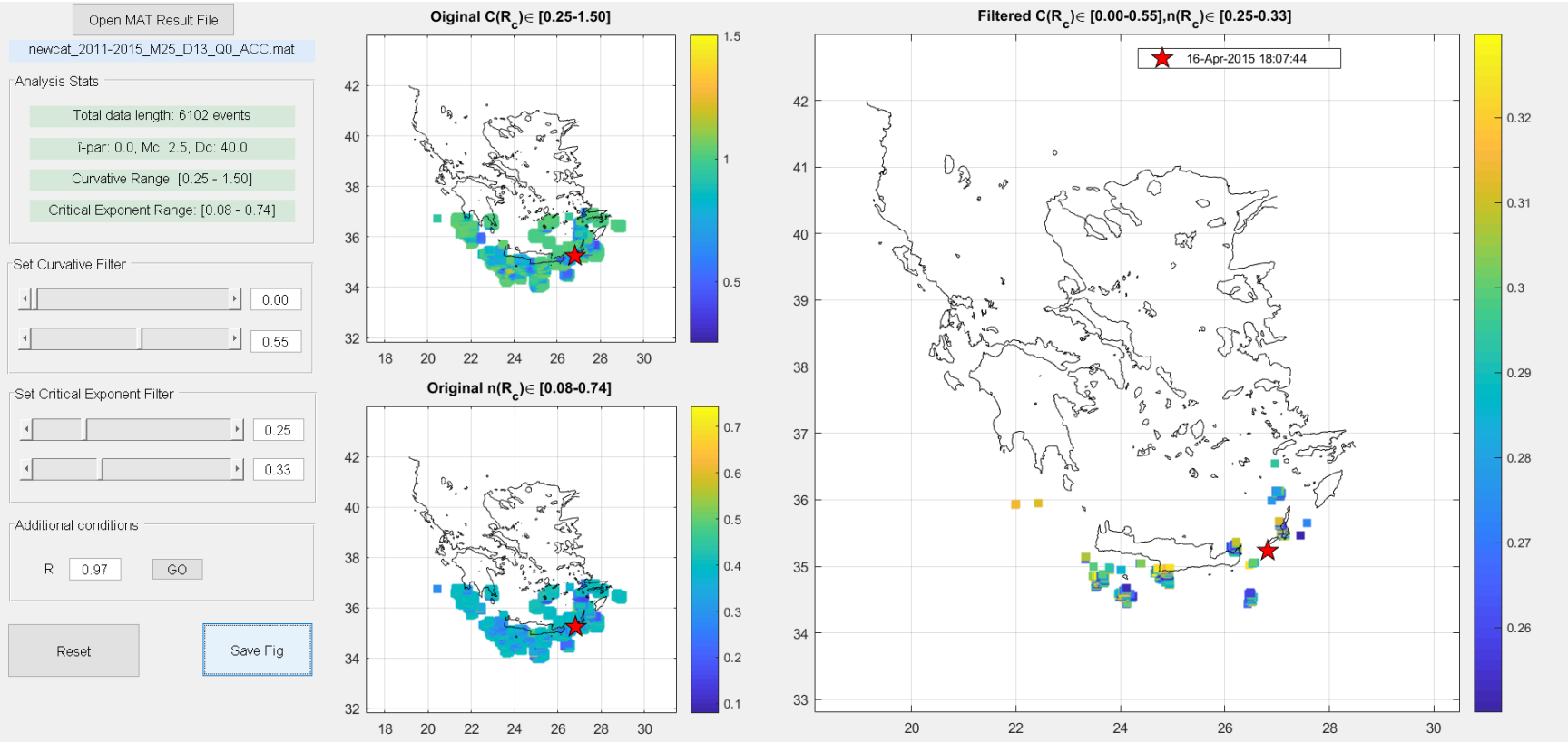

Figure 5.1.11a) *The scan results of the accelerating seismic crustal deformation for* $\xi = 0$ *energy exponent before the 16/04/2015 mainshock. On the left panel there are some search statics as well as the filters that have been applied in the main map.*

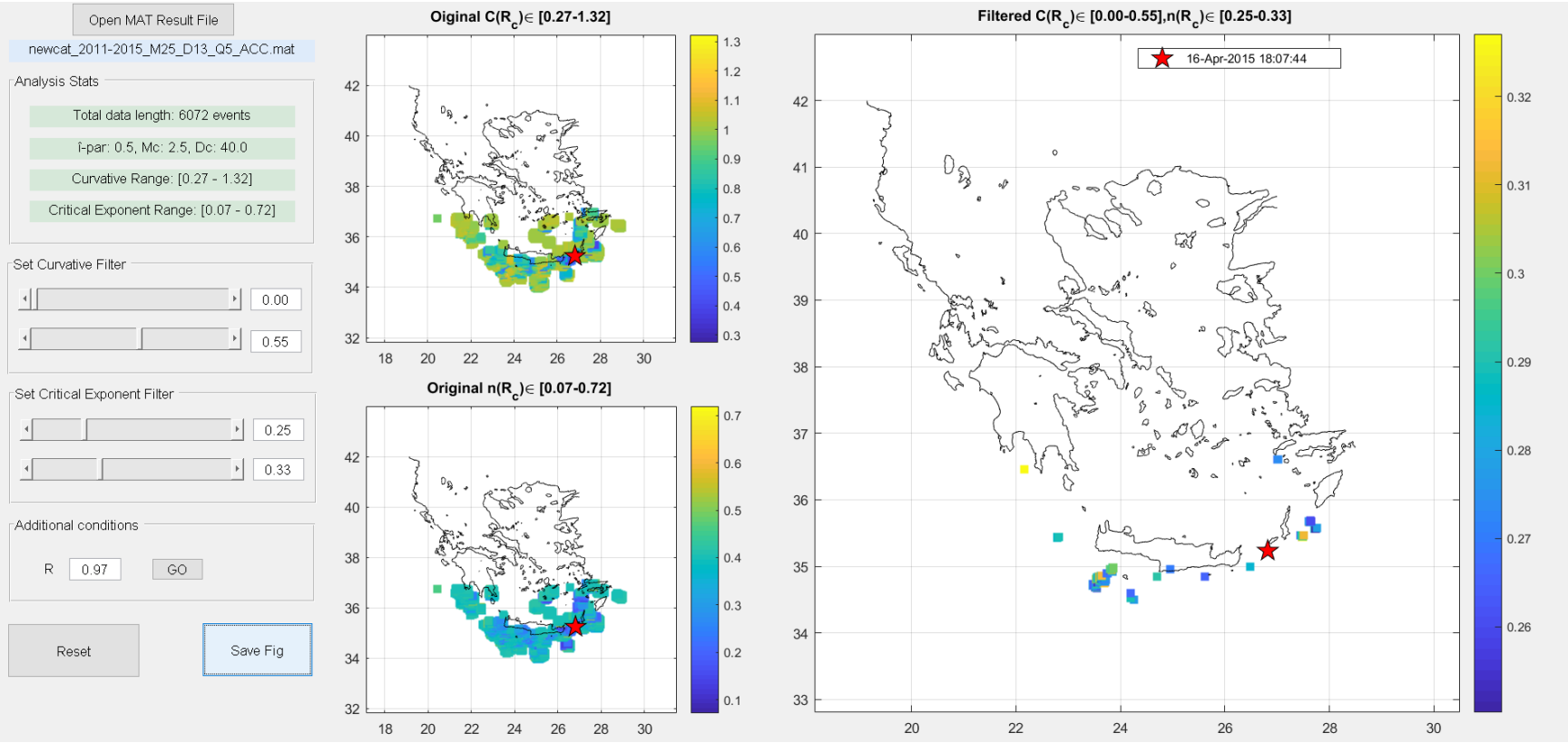

Figure 5.1.11b) *The scan results of the accelerating seismic crustal deformation for* $\xi = 1/2$ *energy exponent before the 16/04/2016 mainshock. On the left panel there are some search statics as well as the filters that have been applied in the main map.*

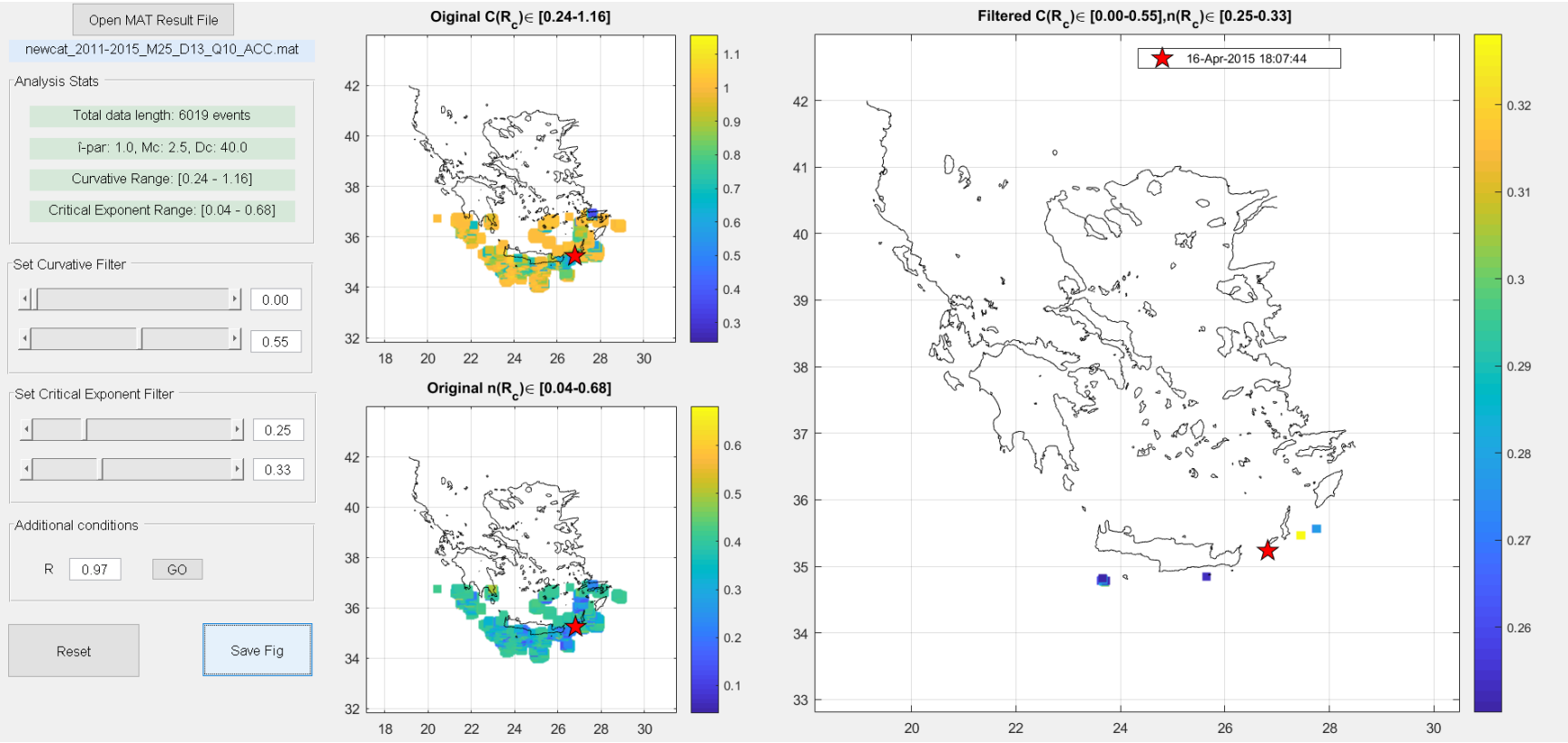

Figure 5.1.11c) *The scan results of the accelerating seismic crustal deformation for* $\xi = 1$ *energy exponent before the 16/04/2016 mainshock. On the left panel there are some search statics as well as the filters that have been applied in the main map.*

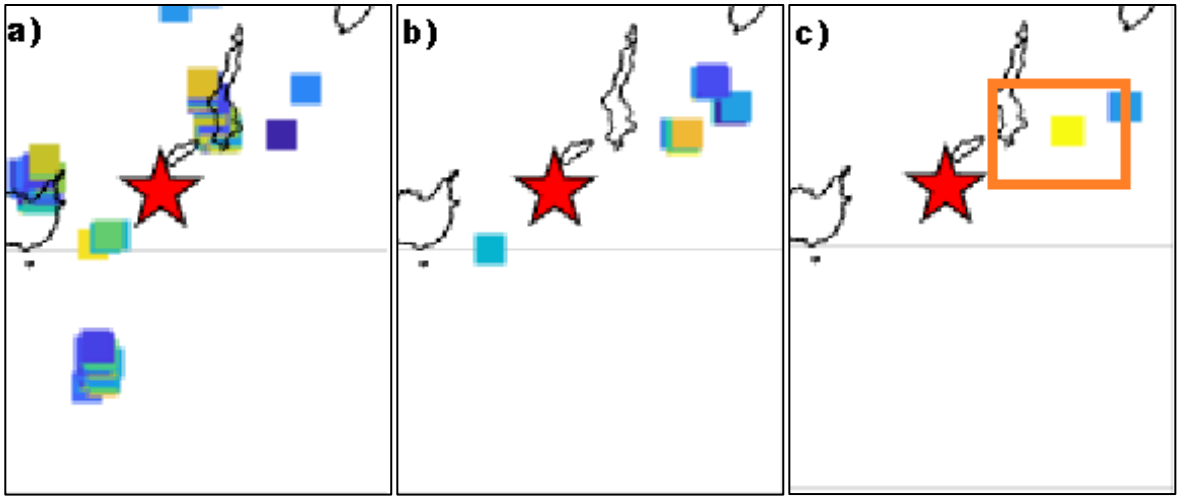

Figure 5.1.12 The filters application in the curvature parameter, critical exponent and power law fitting correlation coefficient for the 15/06/2013 foreshock results. The red box denotes the centre of the circle where the common critical exponent has the optimal fitting.

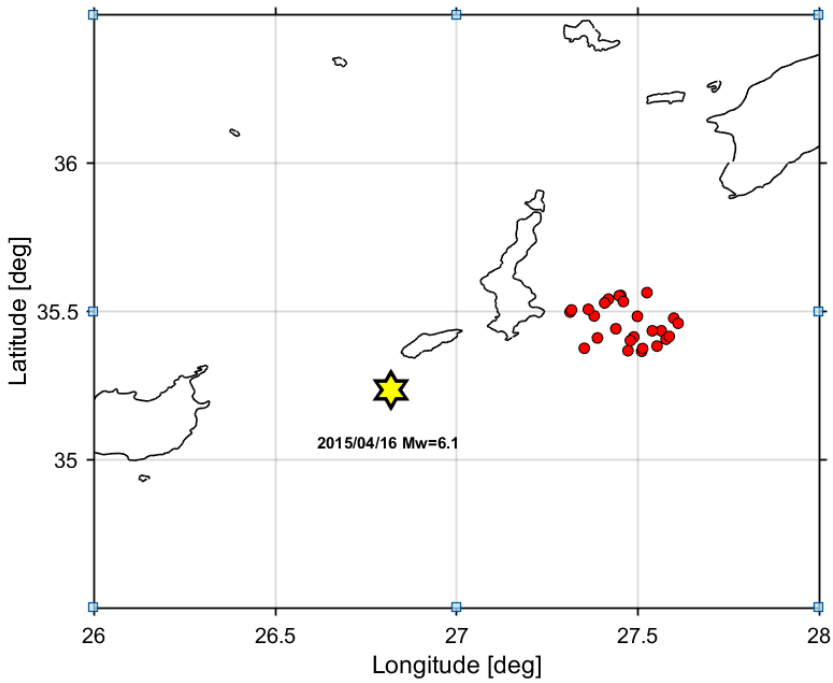

Figure 5.1.13 The epicentres of the earthquakes that identified as the 16/04/2015 strong event foreshocks (figure obtained from Zmap).

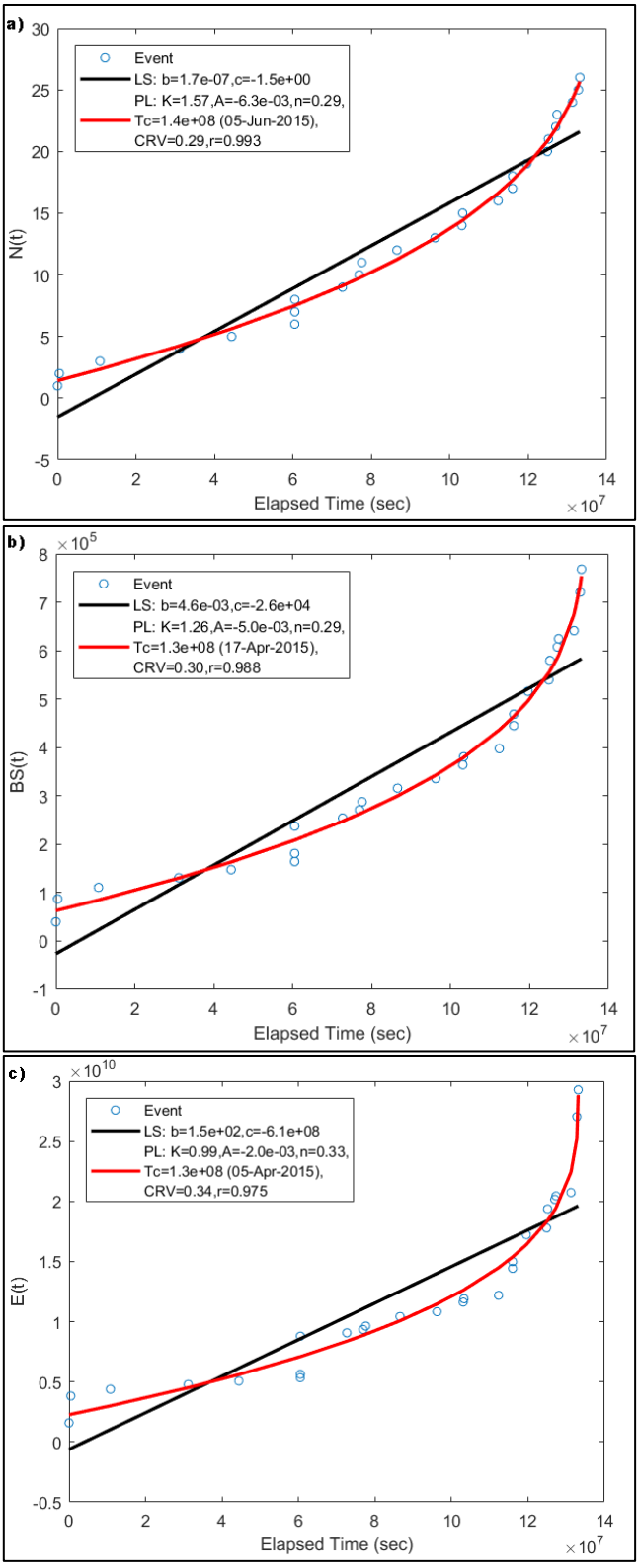

Figure 5.1.14. The power law (red) and the linear(black) fitting of events (blue circles) for the different critical exponents (See section 3.3.2).

An attempt to evaluate the equations 3.1.38 and 3.1.39 and estimate the magnitude of the critical events based on the critical exponent and the seismicity pattern durations has been made. Considering the first event of each catalogue, which is presented in table 5.1.1, is approximately the point where the deviation from linearity starts ($\mathrm{t} = \mathrm{t}_f - T_c$) and the last event is the time $t_1 = t_f - \delta t_1$. Taking equations (3.1.38), (3.1.39) and the values from table 5.1.1 into account, an estimation of the expected minimum and maximum magnitudes of each foreshock sequence is presented on table 5.1.2.

Table 5.1.2 The expected large event magnitudes estimated from equation 3.1.38 and 3.1.39

Case	M_w	M_m	M_{max}
15/06/2013	6.0	5.31	5.88
12/10/2013	6.4	5.58	6.23
16/04/2015	6.1	5.7	6.55

The maximum magnitude values for the Thales catalogue fitting result are close but they slightly underestimate value compared to the ones that have already occurred. In comparison, the NOA catalogue results are within the limits of the expected minimum and maximum magnitude. These estimations may vary as there is an uncertainty in the starting point of the seismicity pattern and the shape of the critical area. The average Benioff strain value that has been used is for the whole Greece area, but it is possible that it may vary for the South Aegean region. The critical exponent has a crucial role in the final expected calculations which emphasize the importance to have an as possible as accurate calculation.

5.2 Aftershocks and swarm sequences in South Aegean

Two strong earthquakes with magnitude greater than 6.0 occurred in the vicinity of Crete Island in 2013 (figure 5.1.1). The first results of these two aftershock sequences have been published in (Chatzopoulos, et al., 2016). Since then, a more detailed analysis has been carried out and the results have been re-examined in order to improve the quality of the data. In the meantime, in the beginning of 2016, an onshore swarm sequence appeared in

the western part of the island. All the events of the aforesaid sequences have been manually located and relocated by the author of this thesis.

A particular effort has been made to produce complete and good quality catalogues to be able to analyse the spatiotemporal properties of these events. In these datasets, the classical seismological investigation such as Gutenberg-Richer and Omori's law, histograms and focal mechanism have been applied as well as the innovative theories of the non-extensive statistical physics.

5.2.1 The 15/06/2013 aftershock sequence

The first strong event with moment magnitude M_w = 6.0, occurred in the front of the Hellenic Arc on 15 June 2013 at 16:11:02 Universal Time Coordinated (UTC). The epicentre of the mainshock was located on longitude 25.045E and latitude 34.317N while the depth was estimated as being shallow at about 14 km (figure 5.1.1). The location of the earthquake was offshore, south from central Crete and the distance from nearest town (Tympaki) was about 85 km. A second moderate to strong earthquake with moment magnitude M_w = 5.8 occurred approximately 29 hours after the mainshock on 16/06/2013 at 21:39:05 UTC. The location of this large event has coordinates 25.092E and 34.239N, it was south-southeast from the mainshock while the depth of the hypocenter was shallow about 6.1 km. The mainshock was followed for more than 515 recorded aftershocks in a time period of about 23 days. In figure 5.2.1, the time histogram was set to present the daily rate of events with the starting point being the time of the mainshock. In the time interval between the strong and the second moderate-strong event, more than 210 aftershocks occurred, with the magnitude ranging from micro (1.9–2.9) to light (4.1–4.8), with a considerable number of events in minor range (3.0–3.9). About 24 hours after the moderate M_w 5.8 event, there was a sharp decrease in the aftershock rate. About 370 aftershocks occurred during the first 48 hours while the remaining approximately 145 events were distributed in a period of about 21 days.

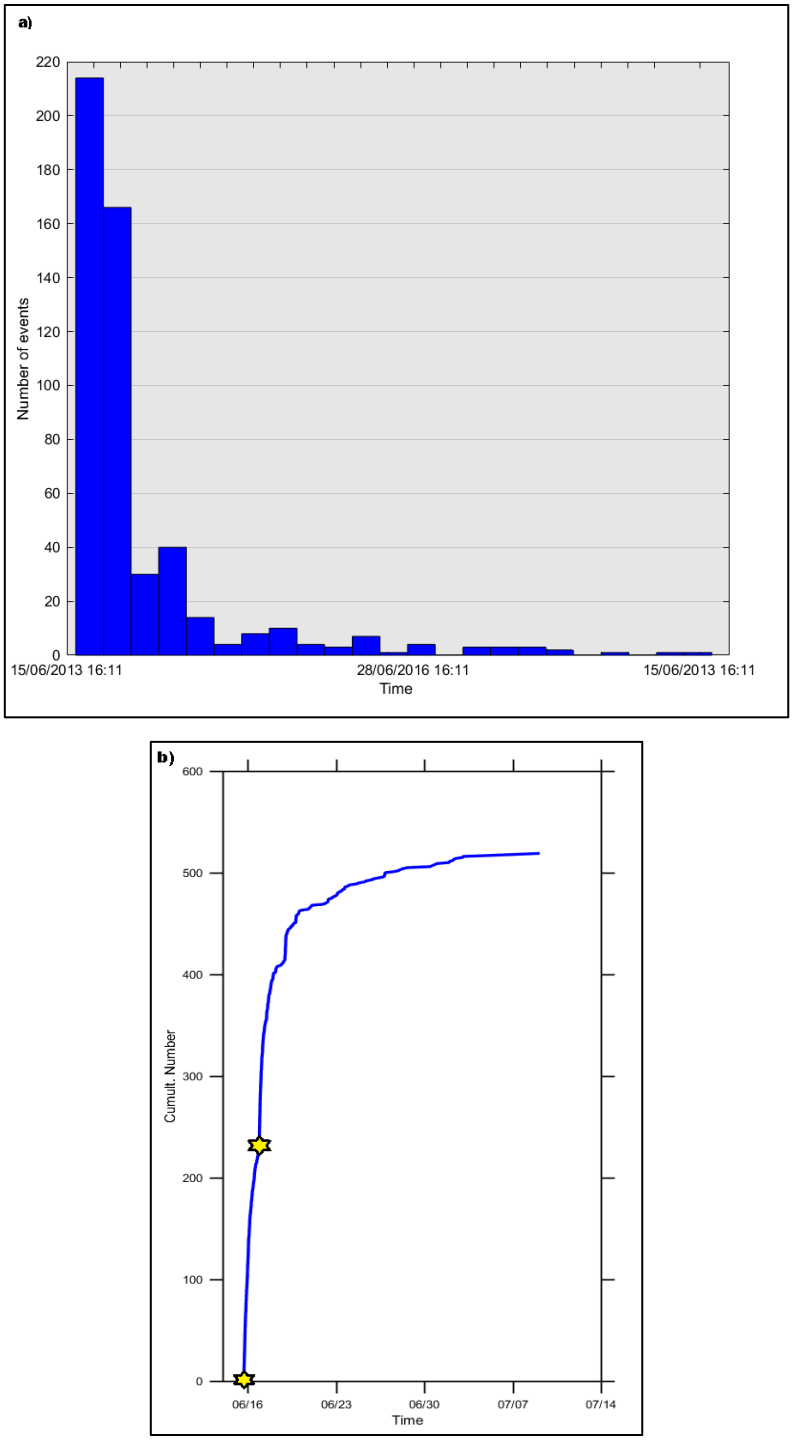

Figure 5.2.1a) In the diagram there is the time histogram that present the daily rate of the aftershock sequence after the 15/06/2013 strong event. b) The cumulative curve of the 15/06/2013 aftershock sequence, the yellow stars denote the large events with moment magnitude M_w= 6.0 and 5.8 (figures obtained from Zmap).

The examination of the cumulative curve in figure 5.2.1 shows that the second large event noted as the yellow star near the 180th event, increased the rate of aftershocks as there is a small slope change in the curve. This is an indication that the second large event triggered another aftershock sequence. The slope of the curve has a noticeable change approximately in the 450 events, where the rate of cumulative numbers becomes slower until the stop of the sequence. In figure 5.2.2a the magnitude histogram is presented while in the b) there is the depth histogram. The distribution of the magnitudes suggest that the majority of the events had micro to minor magnitudes while the light magnitude events were limited. The aftershock sequence magnitudes have a normal distribution, a little skewed to the right and the model magnitude values are the 2.4 and 2.6. The depth histogram shows that the data are also normally distributed with a little positive skewedness. The majority of the events have been reported in depth between 4 and 17km which is near the depth values of the two large events (7 and 14km).

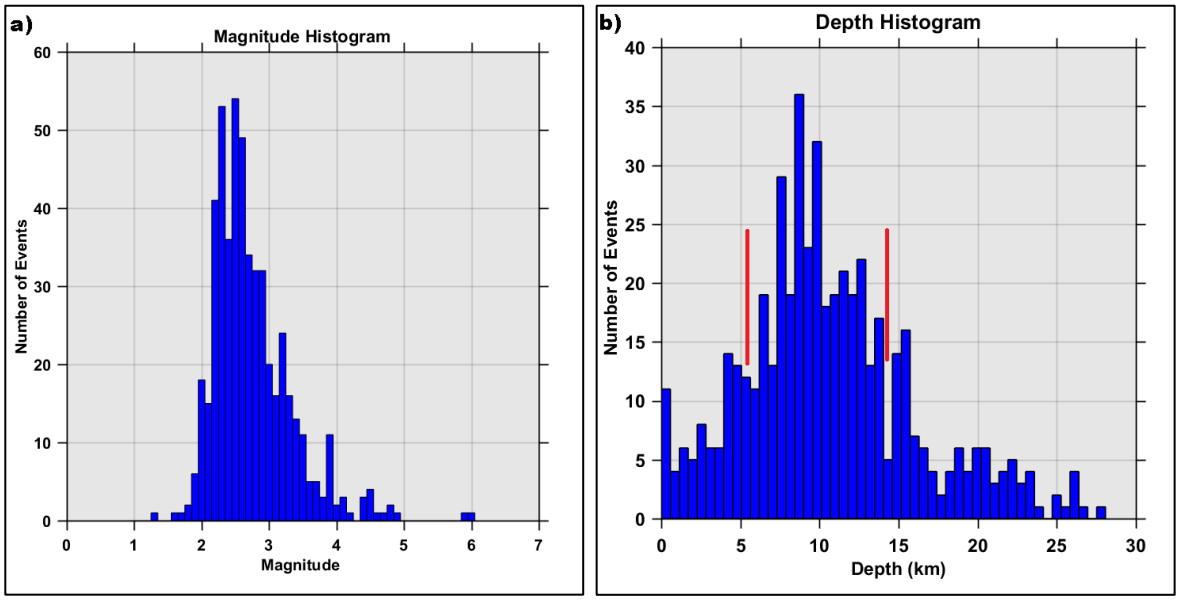

Figure 5.2.2a) the magnitude and b) the depth histogram of the 15/06/2013 strong earthquake and its aftershock sequence (figures obtained from Zmap). The red lines indicate the depth of the two largest events.

The magnitude versus depth and versus time are illustrated in figure 5.2.3. The a) figure shows that the magnitudes are well distributed in the whole depth range and there is no

pattern that could suggest an error in magnitude estimation. Some of the events are in zero depth, these happens if there are not enough *P* and *S* phases or there is a problem in the phase picking procedure (one or more phases have picked wrong due to bad signal to noise ratio) or the velocity model in not suitable for this shallow depth. The 5.2.3b diagram shows that the maximum magnitude tend to decrease with time.

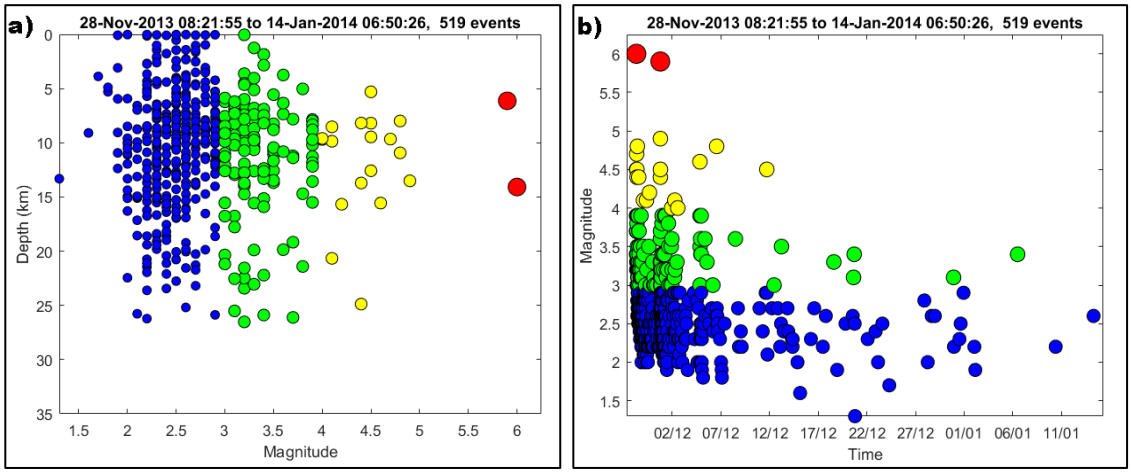

Figure 5.2.3a) The magnitude versus depth diagram and b) the magnitude versus time diagram of the 15/06/2013 aftershock sequence. The circles colour and the size change with magnitude.

Aiming to understand if this second large event is an aftershock or a new activation, the Omori's law, the focal mechanism of the fault as well as some other statistical parameters were examined. First, the catalogue was spatially and temporally limited to contain only the main event and the aftershocks. The Magnitude of completeness has been estimated M_c = 2.4 with the use of best combination option in Zmap software as explained in section 3.2.1 with 50 times bootstrapping without using the mainshock (figure 5.2.4a) and without using mainshock and the second largest event (figure 5.2.4b). The large events have been removed from these catalogues in order to examine only the aftershock characteristics. The *b-value* of the Gutenberg-Richer law for the aftershock sequence is 0.77 which might indicate that the aftershock sequence may have not fully released the accumulated energy (Peng, 2011). Typical *b-values* for aftershocks in the Aegean region as it is noted in section 2.1.5, have mean value 1.0 ±0.2 (Kourouzidis, 2003). The magnitude of completeness has been used to limit the catalogue and apply the modified Omori's law. The first attempt to

define the decay parameters for the whole aftershock sequence did not have the expected typical values. The fitting was poor with a large root-mean-square value almost 18 and the p parameter had very high value p = 2.67 compared to the typical values for aftershocks (see in section 2.1.7). The same fitting applied on the aftershocks after the 16/06/2013 M_w = 5.8 event.

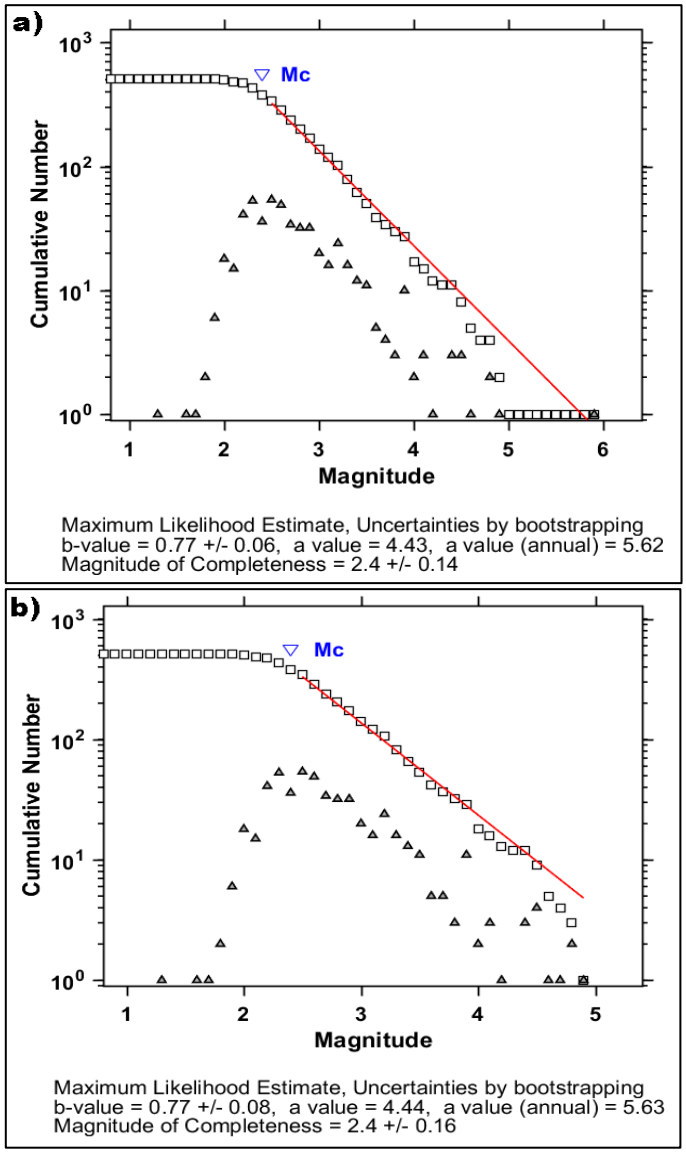

Figure 5.2.4a) The Gutenberg- Richer law fitting without the mainshock obtained from the best method in Zmap software as descripted in section 3.2.1. b) The same fittings without the mainshock and the second largest event (figure obtain by zmap).

In the second attempt the application of the modified Omori's law was considerably better, the fitting RMS was about 5.0 and the obtained *p-value* = 1.16 which is typical for aftershock sequences. The p=1.16 indicates a relative slow decay which is in agreement with the time histogram and the cumulative number of events (figure 5.2.1) as after 48 hours there is a significant decrease daily rate.

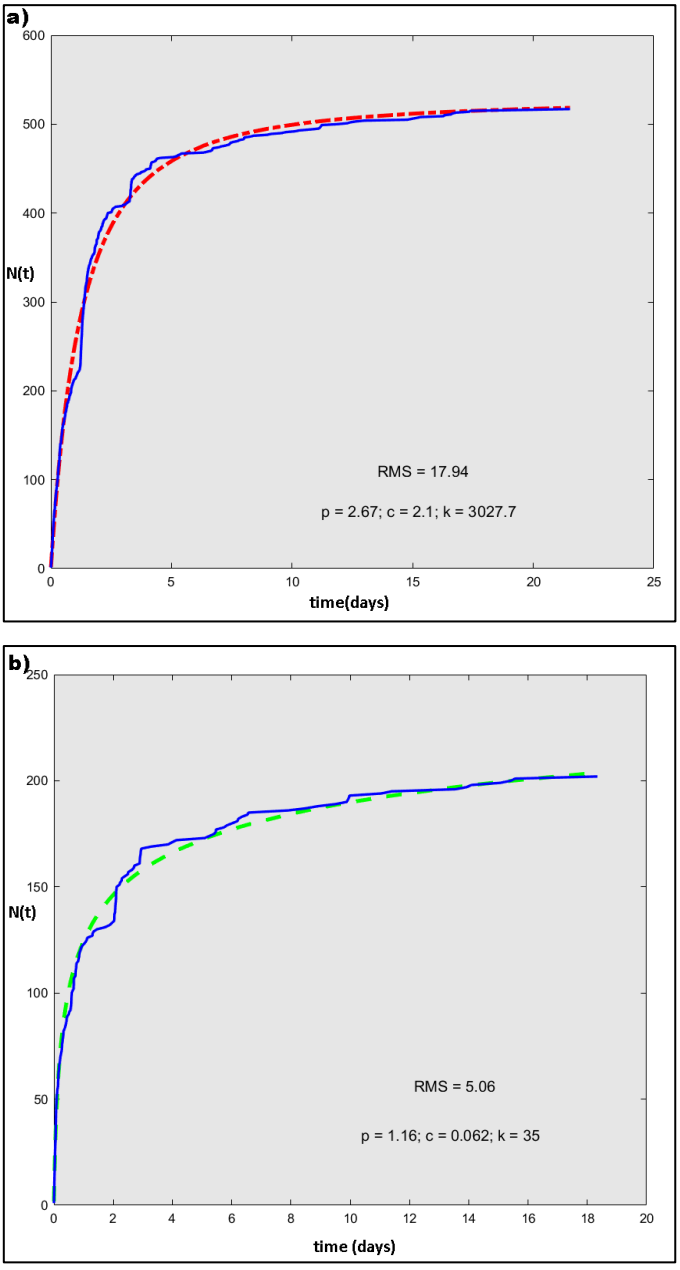

Figure 5.2.5a) the modified Omori's law fitted for the whole aftershock sequence and b) the same fitting for the aftershocks after the 16/06/2013 M_w = 5.8 event. (figures obtained from Zmap)

The mainshock as well as the spatial distribution of the aftershocks are presented in figure 5.2.6. In the same figure there are also the fault plane solution of the mainshock as well as the trace of the two cross sections.

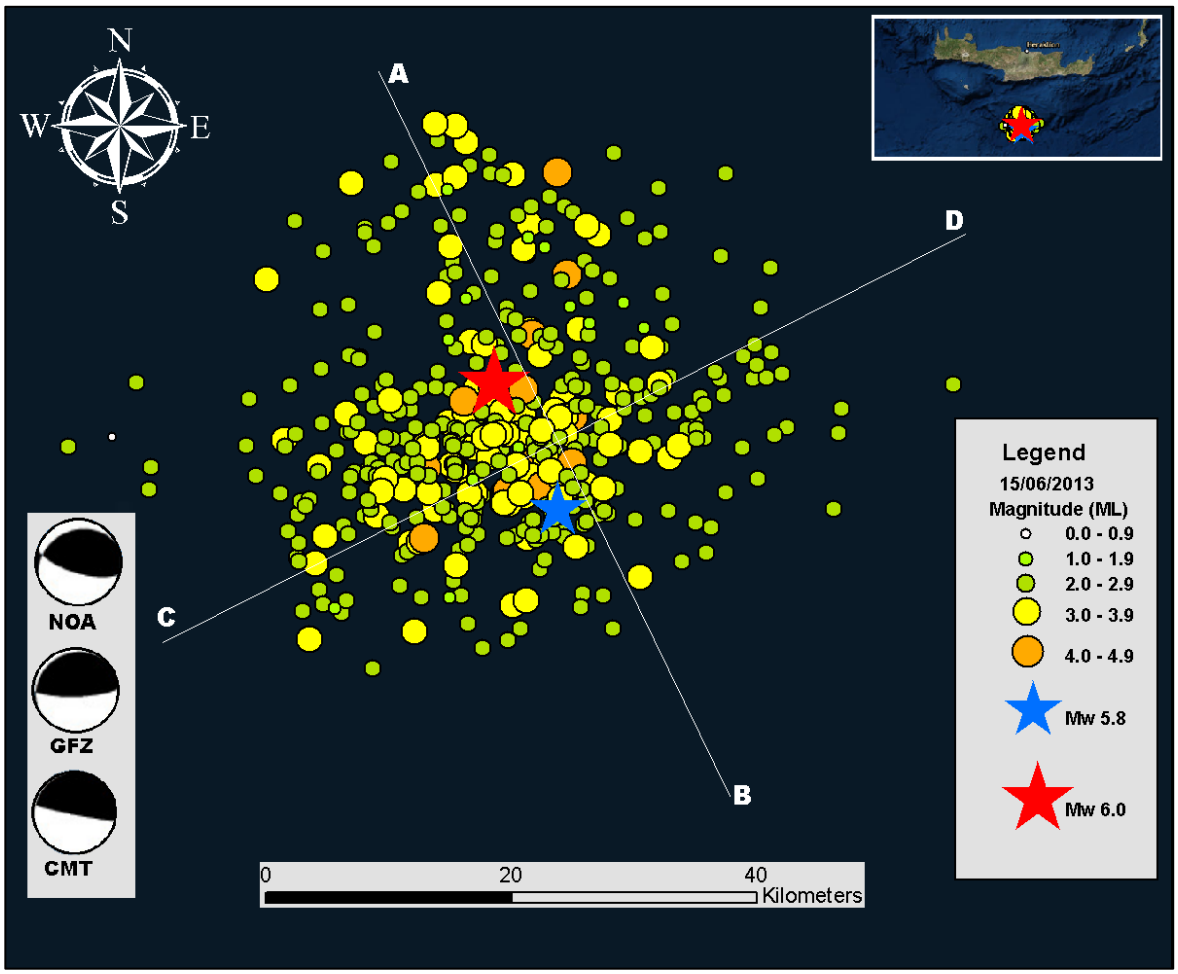

Figure 5.2.6 The spatial distribution of the 15/06/2013 aftershock sequence, the moment tensor of the mainshock and the trace of the two cross sections the strong and moderate magnitude events are denoted with a star while the smaller events indicated by circles. The size and the colour of the circles or the stars scales with the magnitude (map data are managed in ArcGIS (Esri, 2018)).

The HSNC does not calculate focal mechanism yet, so the provided focal parameters are from the manual solution (NOA, 2018) of the NOA network (HL/National Observatory of Athens Seismic Network, 2018), the Global Centroid-Moment-Tensor (CMT, 2018) which follows the method descripted in (Dziewonski, et al., 1981; Ekström, et al., 2012) and the Helmholtz Centre Potsdam GFZ German Research Centre for Geosciences (GFZ, 2018).

The table 5.2.1 has the double couple solution for the strongest events of the 15/06/2013 sequence.

Table 5.2.1 The fault plane mechanism form the NOA, CMT and GFZ centres.

Event	Magnitude	Strike 1	Dip 1	Rake 1	Strike 2	Dip 2	Rake 2	author
15/06/2013	6.1	246	27	52	107	69	109	NOA
15/06/2013	6.3	235	7	100	100	85	95	CMT
15/06/2013	6	244	16	66	88	76	96	GFZ
15/06/2013	4.4	282	11	-87	98	79	-91	NOA
16/06/2013	5.8	301	74	-117	183	31	-32	NOA
16/06/2013	6	222	7	20	112	87	97	CMT
16/06/2013	5.8	216	13	17	110	86	103	GFZ
18/06/2013	4.5	300	47	-118	158	50	-63	NOA
19/06/2013	4.7	298	54	-139	181	58	-44	NOA
19/06/2013	4.8	310	74	-114	189	29	-34	GFZ

The focal mechanism solution of the mainshock in respect with the NOA and GFZ parameters and the aftershocks distribution has the fault plane solution with strike ≈245 while for the dipping angle it is suggests being less than 30 degrees. According to fault plane and the section 2.1.3 this in not a typical reverse (dip=45 and rake=90), the smaller dip value 27 shows a fault type between thrust and reverse. If the dip is calculated by the cross section in figure 5.2.7, it is approximately 35 degrees, so it is more like a reverse fault. The rake≈59 that means the fault type is mainly reverse with a left lateral strike slip component (dip=90 and rake=0). The large activation that occurred 29 hours later than the mainshock, according to the NOA moment tensor occurred in a normal fault with a strike slip component while the global CMT and GFZ suggest a reverse fault. The largest

aftershock fault plane solutions according to NOA and GFZ are on normal faults. This subject is examined in discussion.

The cross sections are used to inspect the vertical distribution of the events. They are usually set to be parallel and perpendicular to strike of the fault in order to show the geometrical characteristics. In figure 5.2.7 the cross section that is vertical to the strike is presented. The location of the large events as well as the hypocentres of the aftershocks placed on the fault plane surface indicate the dipping angle of the fault. According to the figure 5.2.7, the dip is estimated about 35 degrees which is in good correlation with the moment tensor provided by the NOA seismic network. The actual value is very difficult to obtain as the fault is not pure reverse, it has a strike slip component which makes the earthquake distribution more scatter in the vertical cross section. According to the spatial distribution of the events, there is only one large fault that have been activated during this aftershocks sequence. In figure 5.2.8 which is the parallel to strike cross section, the hypocentres of the aftershocks shape the fracture surface of the fault in the sense of the rake. The cross-section images have been adjusted to have as possible as equal vertical and horizontal dimensions, so the presented image is more realistic.

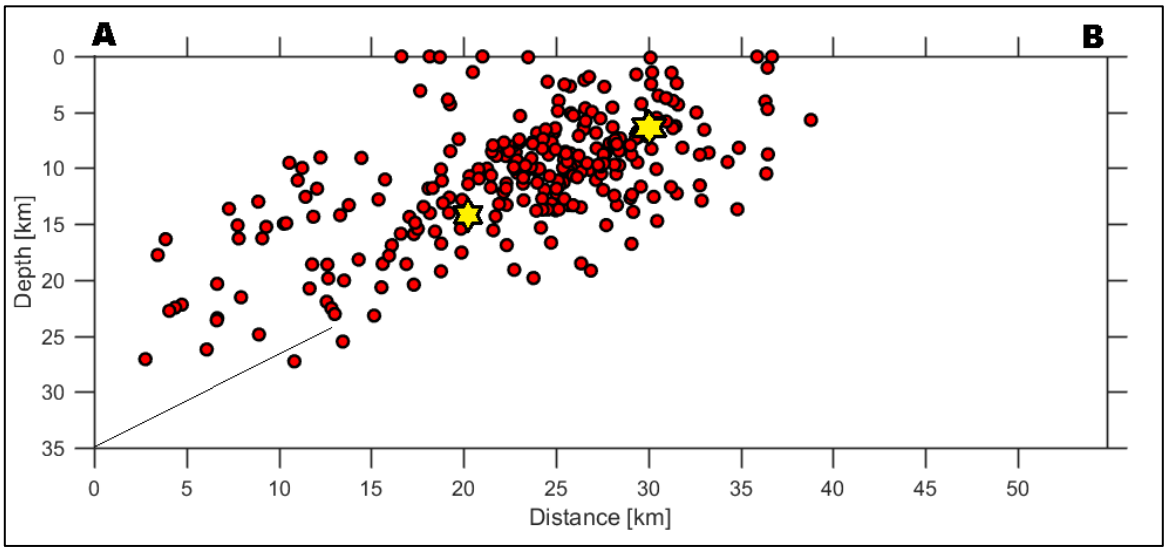

Figure 5.2.7 The perpendicular to the strike cross section that reveals the vertical spatial distribution of the 15/06/2013 events as well as the fault geometry (figure obtained from Zmap). The black line denotes the dip of about 33-35 degrees.

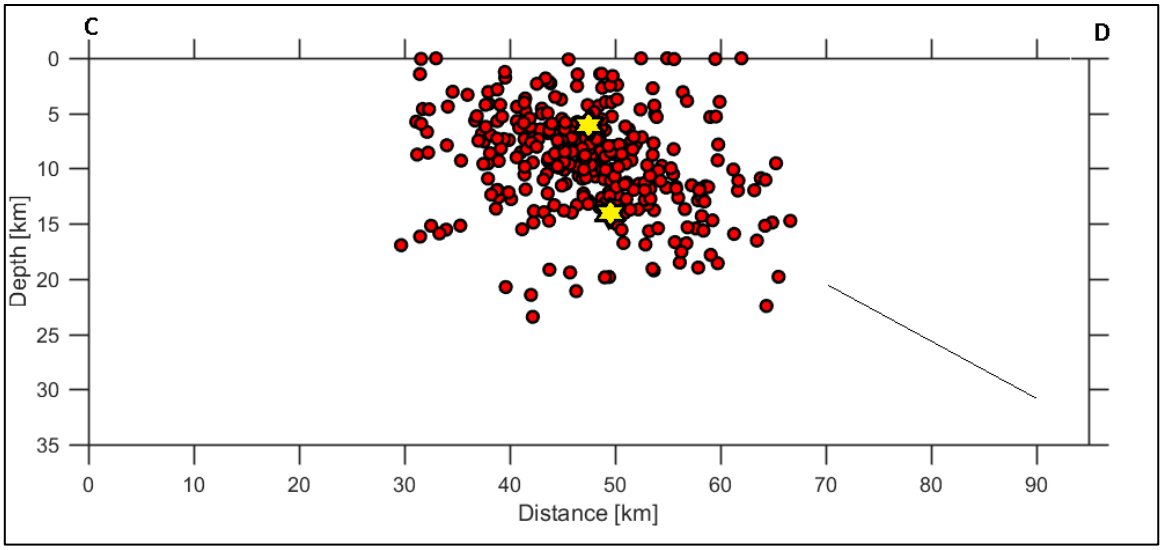

Figure 5.2.8 The parallel to the strike cross section that reveals the vertical spatial distribution of the 15/06/2013 events as well as the fault geometry (figure obtained from Zmap). The black line denotes the direction of rake.

The absence of events in the edge of the cross-sections, the very clear spatial limits is artificial as the earthquakes that were far from the fault were removed. The width of the cross sections is 15km. The fault parameters such as the length L , the width W and the rupture area S can be estimated from the moment magntitude (see section 2.1.3). According to these equations, the rupture length of the mainshock should be about 11km and the width of the fault about 9.5km. The NOA has created a digital fault database for the Greece area based on the available publication since 1972 (Ganas, et al., 2013). The faults of the southern part of central Crete are presented in figure 5.2.9. An attempt to correlate the fault parameters of the large earthquake with one of the recorded faults has been made.

The two large events and the strongest aftershock from the HSNC catalogue as well as the same two large events from NOA's revised database has been placed on the map. The location of the orange pin with the number two inside (M_w =5.8) and the faults geometry from cross section in figure 5.2.7, suggest that the fault highlighted yellow colour is likely the one that has been activated. The relocated results of the HSNC catalogue appears to match to the fault GR0173 with length 10.43km obtained from Mascle, et al., 1982 which is similar with the results (11.3km) from Thingbaijam, et al., 2017 equations, but the fault type is not very clear as the image quality from the original puplication is low.

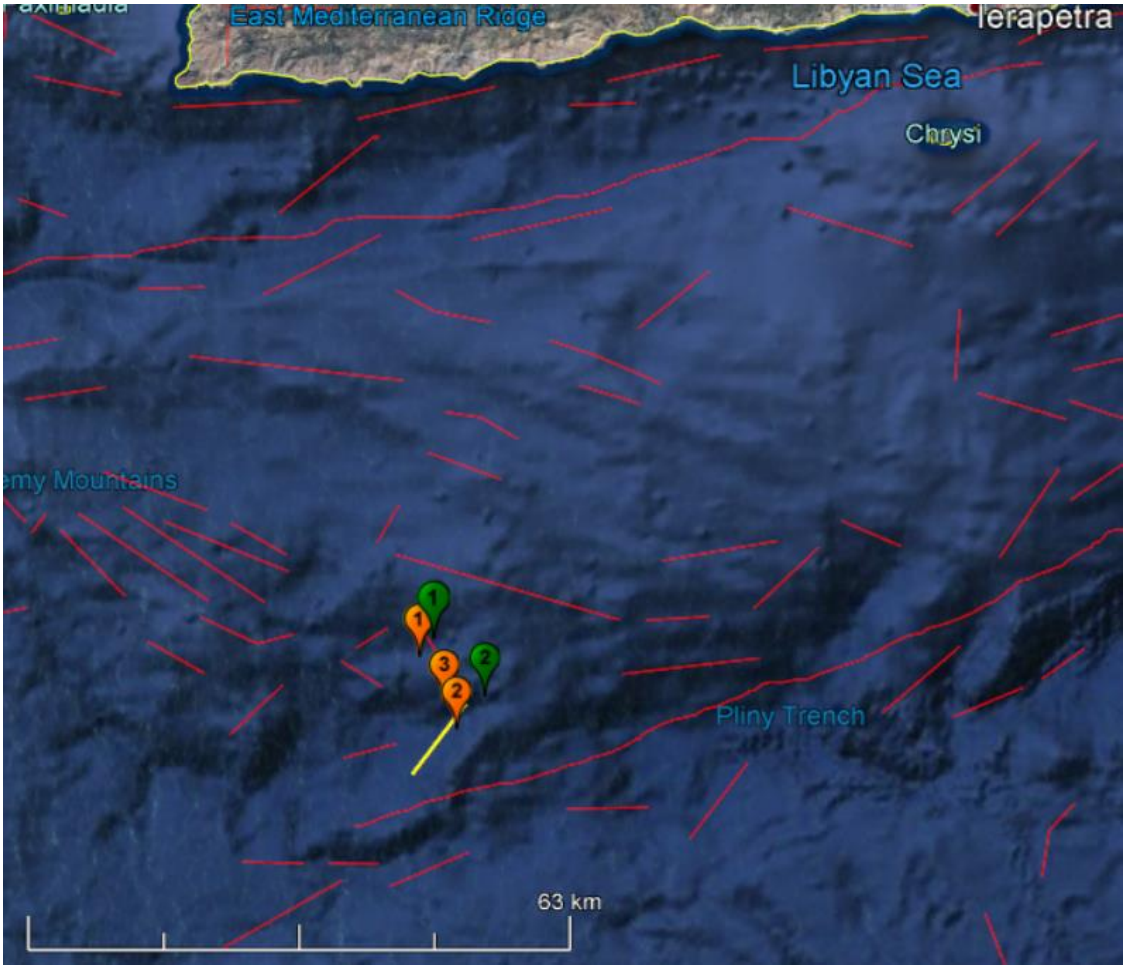

Figure 5.2.9 The recorded faults from NOA database denoted with red lines (Ganas, et al., 2013). The orange pins are the epicentres of the three largest events from the HSNC' aftershock sequence catalogue while the green ones are from the revised solution of NOA for the 15/06/2013 event. The numbers on the pins denotes the order of appearance (data processed in Google Earth (Google, 2018)).

The relatice recent PhD thesis of Shaw (2012) mention that in these area, there are shallow depth (<20km) splay reverse fauls with steep diping angle more than 30 degrees, which is very similar with the numbers provided from the 15/06/2013 vertical to strike cross-section. In order to relocate the main event as well as the aftershocks, it was necessary to calculate the velocity ratio V_P/V_S. The ratio is obtained from the slope of the Wadati diagram (Wadati, 1933). A script in MATLAB has been used to read the Hypoinverse-2000 input phase file and compute the velocity ratio for every event. Aiming to have a reliable mean

velocity ratio, a filter has been added in the script, so the mean V_P/V_S been calculated with all the event that have been recorded in at least six stations. The arrival times have been normalized by the software based on the minimum *P* arrival time of each event, so they could plot in the same Wadati diagram (figure 5.2.10) and the mean velocity ratio for the 15/06/2013 aftershock sequence is 1.7487 ≈ 1.75.

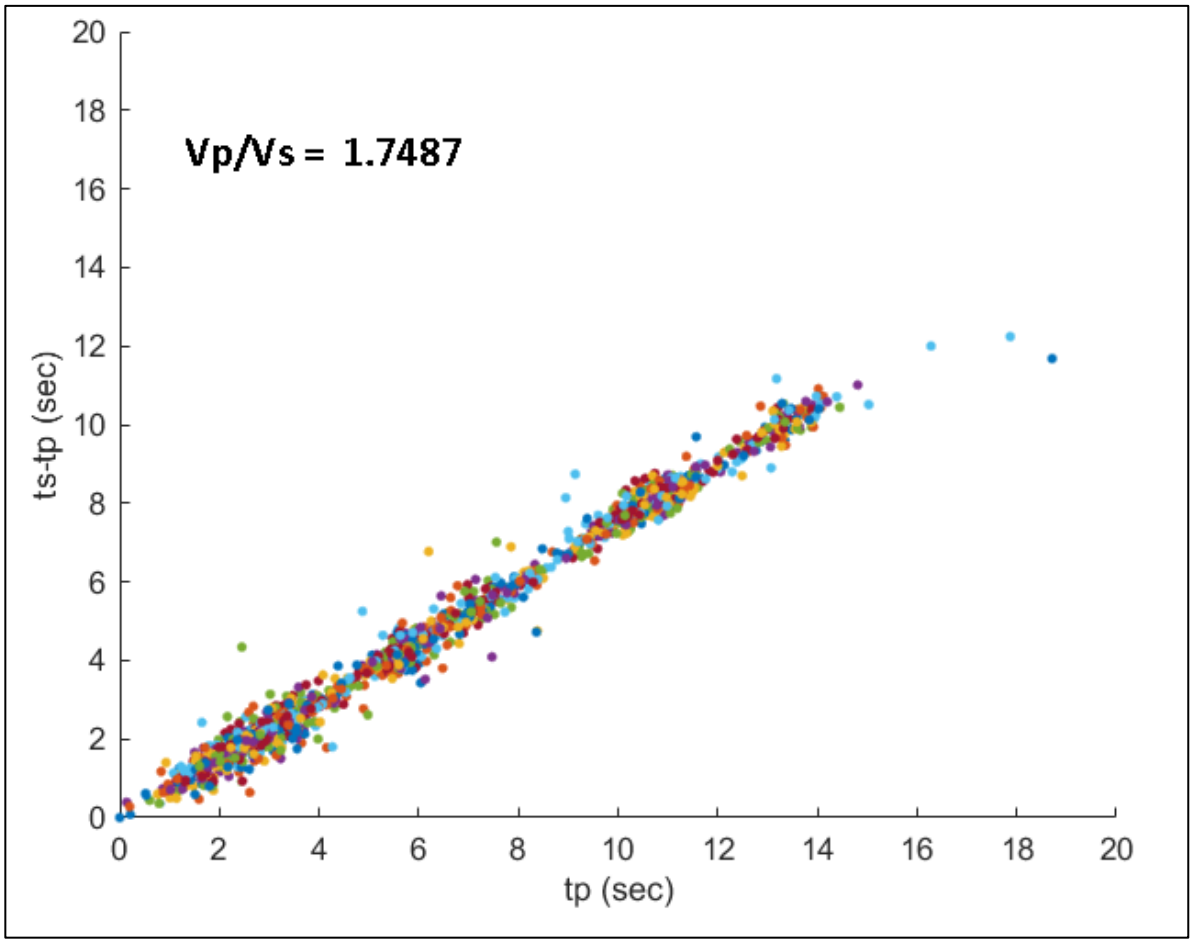

Figure 5.2.10 The Wadati plot for the 15/06/203 events that have been recorded in more than six stations. The mean velocity ratio has been estimated 1.7487.

One of the important steps in the relocation procedure is to fix the station correction which will help to reduce the lateral velocity variations and the possible elevation delaying effects. During the station corrections estimation procedure, it is possible to identify corrections with values much higher than one second. In this case, either the station is too

far from the epicentre, or there is a problem in the picked arrival times, or the crust model does not fit well. The final station file that has been used to relocate the 15/06/2013 events is presented in table 5.2.2. The correction applied in the relocation procedure appears to have typical values. The stations close to epicentre have small correction while the stations with much bigger distance like KNDR and CHAN have increased values. The relocation process results can be validated with the visual inspection of the spatial distribution of the earthquakes by doing cross sections also with numerical examination of the relocation associated errors. The root-mean-square error of the time residuals as well as the horizontal and vertical errors should be as low as possible. The errors of the ten strongest events are presented in table 5.2.3.

Table 5.2.2 the Hypoinverse-2000 station file input file with the calculated station corrections for the 15/06/2013 relocation.

Stations	**Latitude (Degrees)**	**Longitude (Degrees)**	**Altitude (m)**	**Station Correction (sec)**
ZKR	35 06.88N	26 13.02E	270	0.17
TMBK	35 04.35N	24 45.97E	10	0.26
GVDS	34 50.60N	24 03.49E	178	-0.15
PRNS	35 20.67N	24 25.58E	232	0.03
STIA	35 12.12N	26 05.45E	31	0.05
KSTL	35 12.54N	25 20.25E	176	-0.06
FRMA	35 01.12N	25 51.33E	10	-0.07
KNDR	35 14.09N	23 37.49E	25	0.45
HRKL	35 18.69N	25 6.10E	90	0.04
CHAN	35 31.15N	24 2.55E	34	0.45

Table 5.2.3 The relocation errors of the 10 largest events of the 15/06/2013 sequence.

Date	Time	Magnitude ML	Depth (km)	RMS (sec)	Horizontal error (km)	Vertical error (km)
15/06/2013	16:11:02	6.0	14.08	0.18	0.5	0.7
16/06/2013	21:39:05	5.8	6.13	0.23	0.6	0.8
16/06/2013	21:43:17	4.9	13.51	0.30	0.9	0.9
19/06/2013	19:05:09	4.8	10.93	0.20	0.6	0.6
18/06/2013	22:27:07	4.6	15.56	0.22	0.7	0.6
16/06/2013	21:47:36	4.5	9.46	0.30	1.2	1
22/06/2013	8:50:15	4.5	5.3	0.29	0.8	1
15/06/2013	16:59:38	4.4	24.88	0.30	1.1	1.8
16/06/2013	21:42:42	4.4	13.71	0.25	0.8	0.7
16/06/2013	8:15:18	4.2	15.67	0.19	0.6	0.7

The non-extensive statistical physics q parameter has been calculated to examine the temporal characteristics and scaling relations of the 15/06/2013 aftershock sequence. The distribution of the time differences between two continuous earthquakes is known as interevent time T_{ij} and it is defined as: $T_{ij} = T_{ij}(\mathrm{j}) - T_{ij}\,(i)$ where $j = i + 1$ and i is the number of the event. It has been proposed by Abe & Suzuki (2005); Michas, et al. (2013); Papadakis, et al. (2013); Vallianatos, et al. (2012) that in an earthquake population with consecutive event, the cumulative distribution of the spatiotemporal properties such as the interevent times and hypocentral distances can be explained by non-extensive statistical physics. More specific the cumulative distribution frequency (CDF) of the interevent times P(>T) or hypocentral distances can be described by a q-exponential distribution. In the Abe & Suzuki (2005); Michas, et al. (2013); Papadakis, et al. (2013); Vallianatos, et al. (2015); Tsallis (2009) work, it is demonstrated the method to maximize the entropy S_q with the Lagrange multipliers in order to obtain the q-logarithmic function:

$$P(>T) = [1 + (q-1)\frac{T}{T_q}]^{-\frac{1}{1-q}}$$

$$ln_q[P(>T)] = (1-q)^{-1}(p^{1-q}-1) = -\frac{T}{T_q}$$

while the T_q is a q-scaling factor. This function has been used in the 15/06/2013 aftershocks cumulative interevent times distribution ($P > T$).

The interevent times of the aftershocks has been calculated, converted into cumulative interevent times along with the cumulative distribution which has been used as an input in for the `nlinfit` solver in order to estimate the q parameter. The method is straightforward: define the magnitude of completeness, remove the events that have smaller magnitudes than the M_c, select the aftershocks time window and use the cumulative distribution to obtain the q-exponential function parameters. As Abe & Suzuki (2005) demonstrated, the q-exponential parameters q and T_q depend on magnitude, the Magnitude of completeness has a crucial role in the estimation of the q entropic parameter. The q is larger than 1, which means that system is under-additive this has been noted before by Papadakis, et al. (2013); Michas, et al. (2013); Chochlaki, et al. (2018); Abe & Suzuki (2005); Vallianatos, et al. (2012). The q>1 means that the frequent interevent times that with large probability (close to 1) are enhanced as the aftershock sequence decays. A challenge to identify the length of the aftershock time window occurred. As the aftershock sequence decays with time, the last couple days the frequency-time distribution of the events becomes very small. In this case the exact time point where the sequence end can be unclear as the aftershocks are mixed with the background seismicity. In order to define the limit of the aftershock catalogue, different dates have been tested. During this procedure, it was noticed that the q-value had large variations dependent on the selected time window.

Aiming to validate if the q-variations are data artefact; the magnitude of completeness has been re-calculated after 50 and 100 events from the end of the catalogue have been removed. The GR-law fit in figure 5.2.11 show that the *b-value* and the M_c haven not change in a way that could explain the dependence of the q with time. The new findings have been also examined with the expanding and the moving windows methods. In the expanding windows approach, different combinations window sizes and techniques such remove events from the ending point or from the starting point have been applied. The results from the 'normal' expanding windows method are presented in the figure 5.2.12,

where the time windows are having the starting point fixed, the beginning of the catalogue and the ending point is up to 260(a), 280(b), 300(c), 320(d), 340(e) and 360(f) events. On the contrary, in figure 5.2.13 it is presented the 'reverse' method, having fixed the end point, the events have been removed from the beginning of the catalogue and the number of remaining events are 340(a), 320(b), 300(c), 280(d), 260(e) and 240(f). In order not having the same window in these two methods, in the reverse mode the first window (1 to 360) was excluded from the search. In the figure 5.2.14 are the results from the moving window approach. A large window with 180 events have been selected to be statistically stable and have an as much possibly as accurate fitting while the overlap window was small, 25 events due to the limit of the catalogue. The results in the presented figures have very small fitting error values which are less than 0.0018 with 99% confidence. The correlation coefficient has been calculated with the same command in MATLAB as in section 3.3.2.

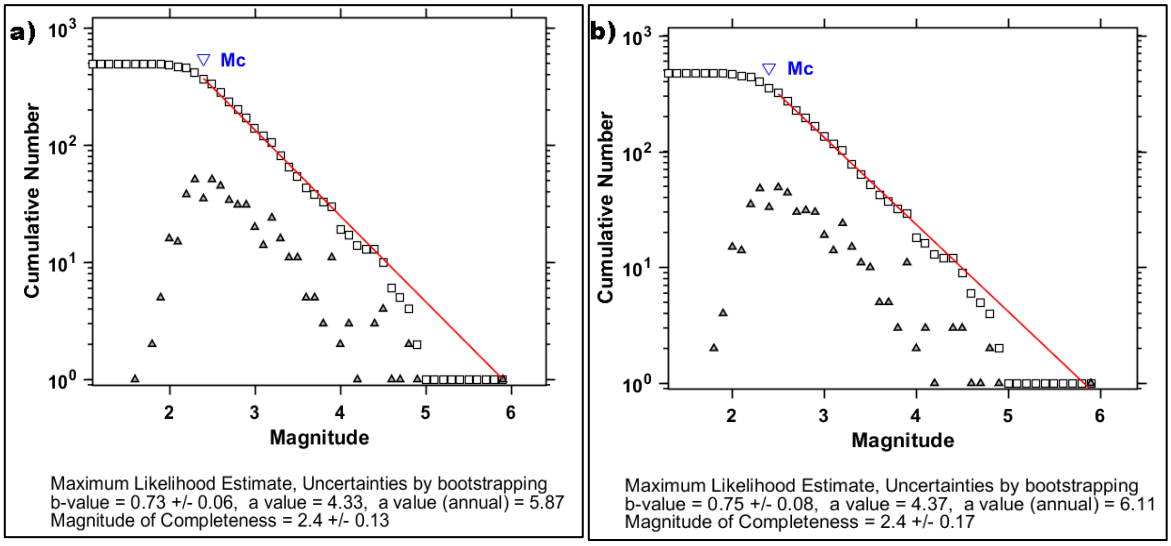

Figure 5.2.11 The magnitude of completeness and the b-value for the 15/06/2016 aftershocks after removing 50 (a)and 100(b) events respectively (figures obtained from Zmap).

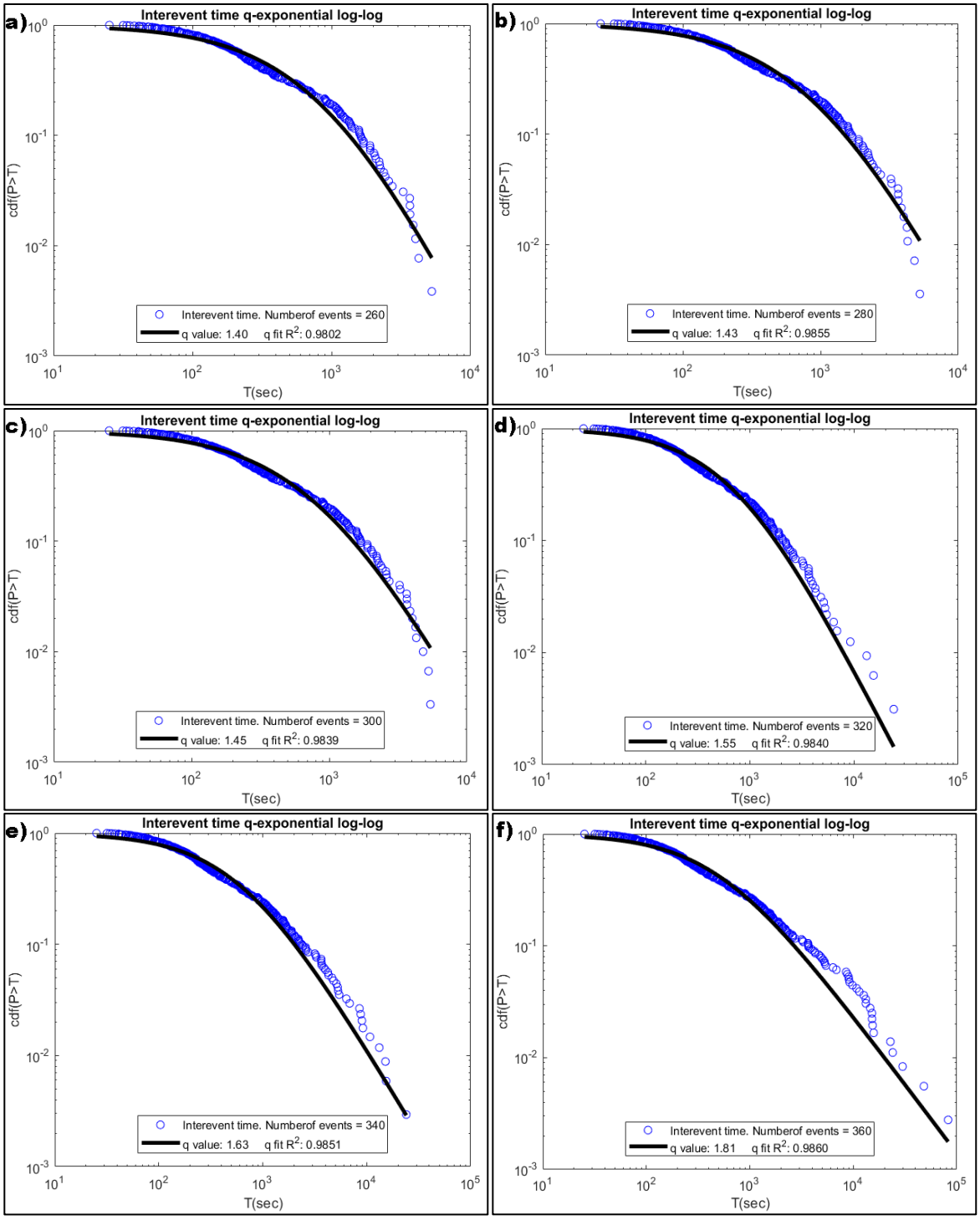

Figure 5.2.12. The normal expanding time window results for 260(a), 280(b), 300(c), 320(d), 340(e) and 360(f) events: a) q=1.40±0.0055 up to ±0.0125, b) q=1.43±0.0048 up to ±0.0107, c) q=145±0.0055 up to ±0.0118, d) q=1.55±0.0055 up to ±0.0115, e) q=1.63±0.0052 up to ±0.0106, f) q=1.81±0.0049 up to ±0.0099.

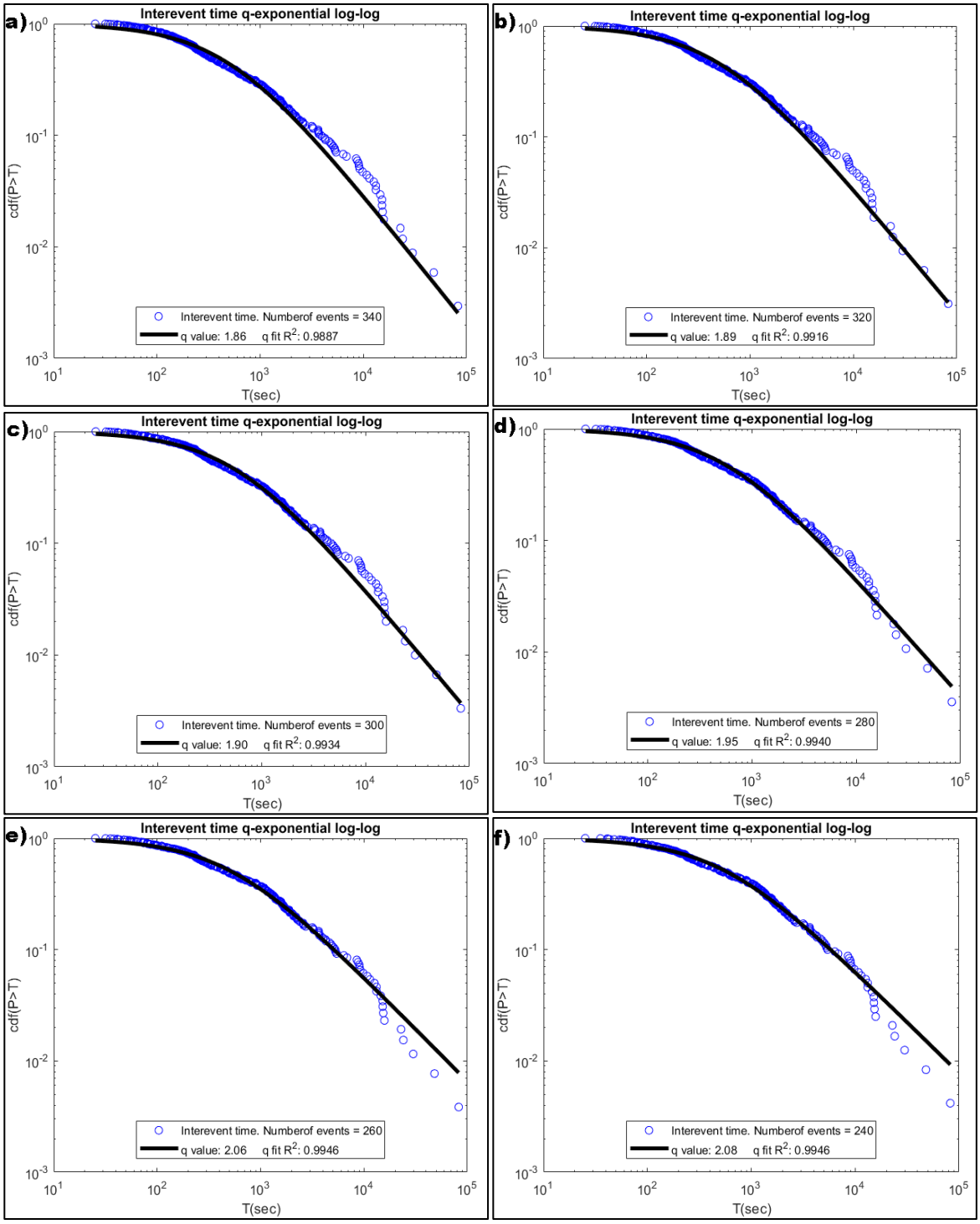

Figure 5.2.13. The reverse expanding time window results for 340(a), 320(b), 300(c), 280(d), 260(e) and 240(f) events: a) q=1.86±0.0039 up to ±0.0081,b) q=1.89±0.0029 up to ±0.0060, c) q=1.90±0.0022 up to ±0.0048, d) q=1.95±0.0020 up to ±0.0044, e) q=2.06±0.0040 up to ±0.0177, f) q=2.08±0.0041 up to ±0.0177.

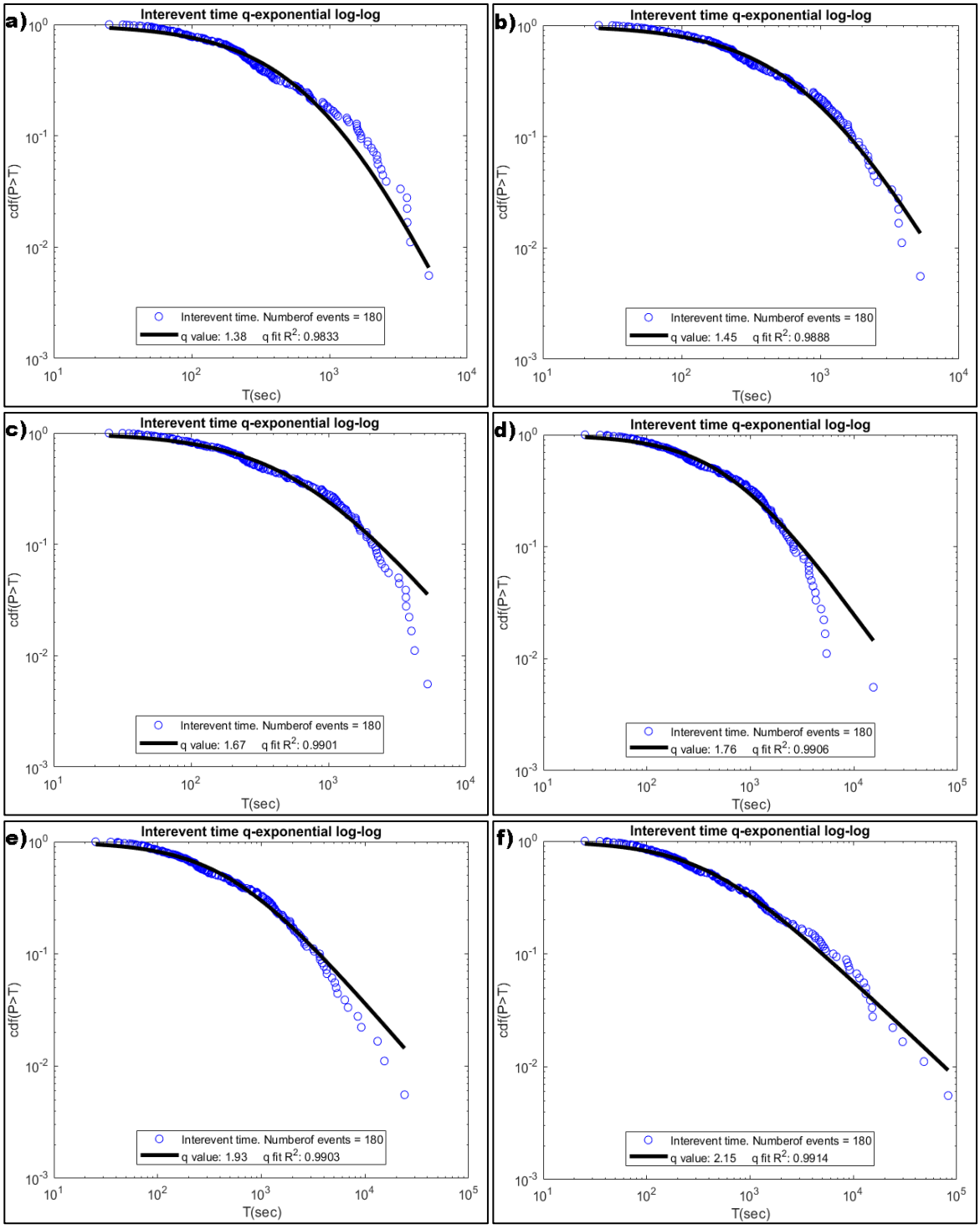

Figure 5.2.14. The moving time window results, the window moves 25(a), 50(b), 75(c), 100(d), 125(e) and 150(f) events : a) q=1.38±0.0051 up to ±0.0137, b) q=1.45±0.0034 up to ±0.0091, c) q=1.67±0.0030 up to ±0.0081, d) q=1.76±0.0028 up to ±0.0077, e) q=1.93±0.0029 up to ±0.0079, f) q=2.15±0.0036 up to ±0.070.

5.2.2 The 12/10/2013 aftershock sequence

The second strong event of the 2013 occurred in the western part of the Hellenic Arc on 12 October 2013 at 13:11:54 UTC with moment magnitude M_w = 6.4. The epicentre of the mainshock was located on coordinates 23.242E and 35.21N (figure 5.1.1). In contrast to the first event of 2013, this hypocenter was estimated in intermediate the depth about 47 km. The location of the earthquake was offshore, west from western part of Crete while the distance from the nearest town (Kissamos) was about 45 km. This event has attracted interest due to the number of different foreshocks observed (Contadakis, et al., 2015; Vallianatos, et al., 2014). The time histogram (figure 5.2.15) as well as the cumulative number of events shows that the mainshock was followed by more than 350 recorded aftershocks in a time interval of 25 days. The time histogram was set to present the daily rate of events with the starting point being the time of the mainshock. It is noticeable that only on the first day there was a considerable amount of seismic energy released. About half of the aftershocks (170) occurred within the first 24h and after that the aftershock activity was low.

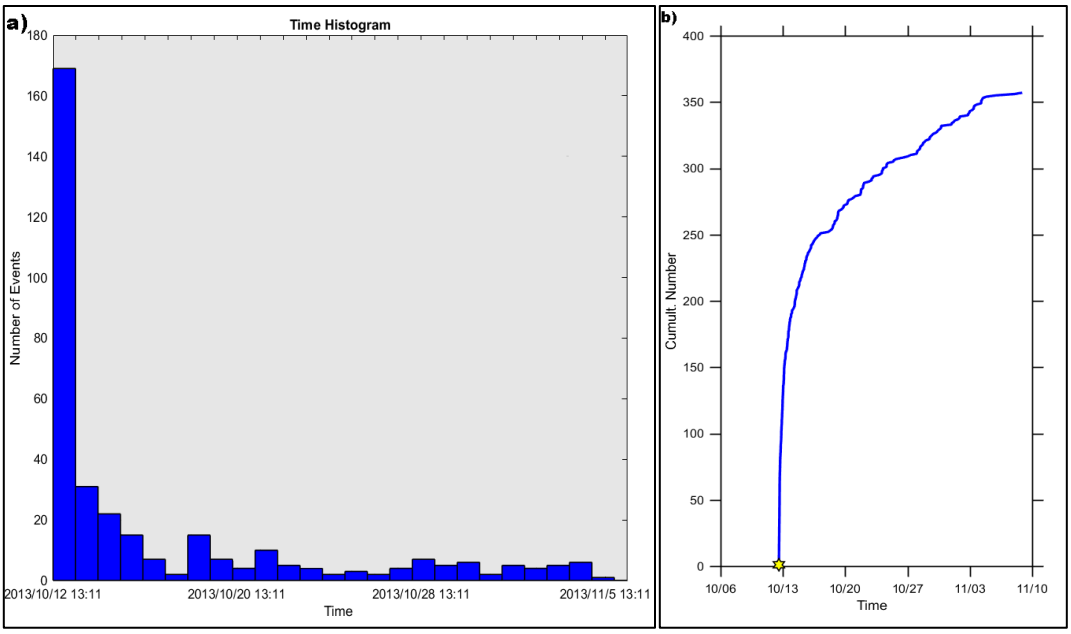

Figure 5.2.15 a) The time histogram that present the daily rate of the aftershock sequence after the 12/10/2013 strong event. b) The cumulative curve of the 12/10/2013 aftershock sequence, the yellow star denotes the large event with moment magnitude M_w= 6.4. (figures obtained from Zmap).

The magnitude and depth distribution histograms of the 12/10/2013 aftershock events are illustrated in figure 5.2.16. The examination of the aftershock catalogue shows that the magnitudes range between micro and minor from 1.1 to 3.9, while only three of the events had magnitude from 4.0 to 4.1 occurred in the first 48 hours. The aftershock sequence magnitudes seem to have a normal distribution a little skewed to the right and the most common magnitude values are the 1.8 and 1.9. The depth histogram suggests that most of the events have been distributed normally between the 22 and 59 km depth while a large portion of the events are at depth shallower than the depth where the mainshock occurred.

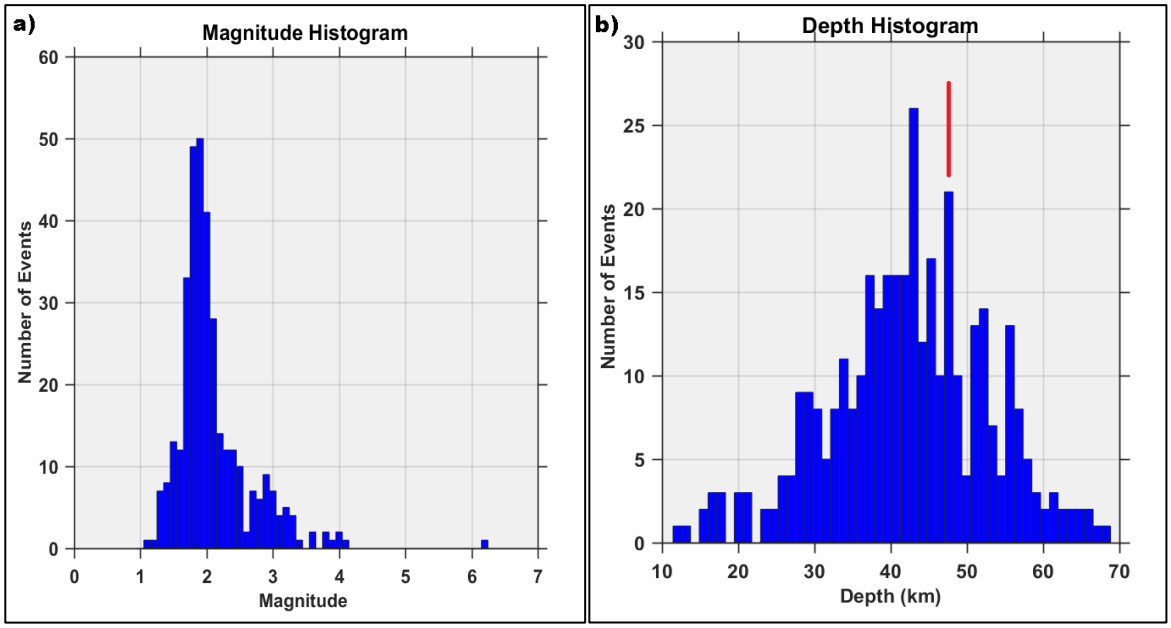

Figure 5.2.16a) the magnitude and b) the depth histogram of the 12/10/2013 strong earthquake and its aftershock sequence. The red line indicates the depth of the largest event (figures obtained from Zmap).

The magnitude versus depth and versus time are illustrated in figure 5.2.17. The first figure (a) shows that the magnitudes are well distributed in the whole depth range while the largest aftershocks are located close to the mainshock and there are no patterns that could suggest that there is an error in the magnitude estimation. The second (b) shows that the maximum magnitude tends to decrease with time and events with light magnitude occurred only the first two days.

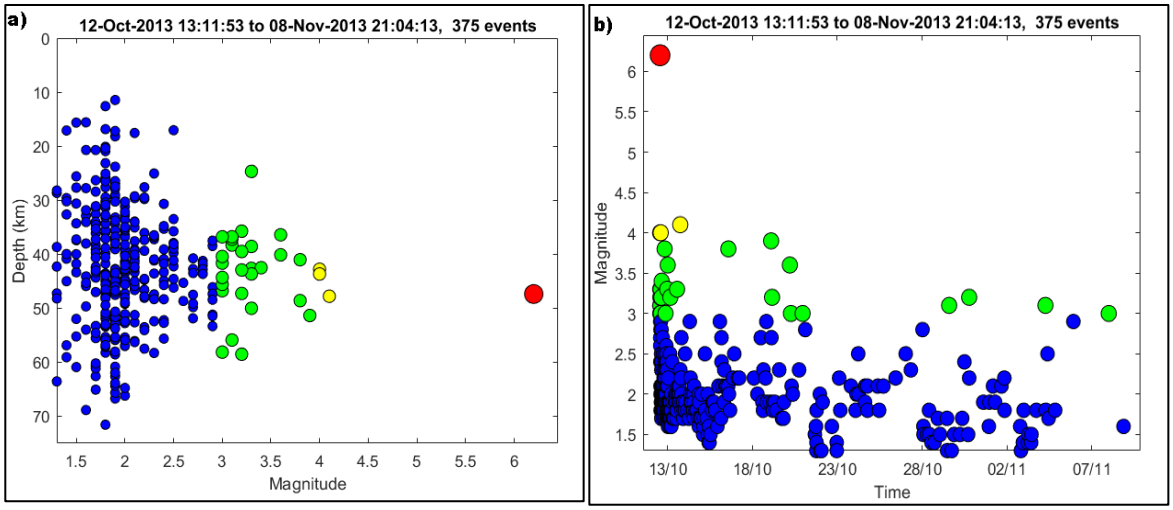

Figure 5.2.17 a) The magnitude versus depth diagram and b) the magnitude versus time diagram of the 12/10/2013 aftershock sequence. The circles colour and the size change with magnitude.

Omori's law has been used to examine the aftershock decay rate. The procedure to find the decay rate parameters was the same as the 15/06/2013 sequence (see section 5.2.1). Initially, the catalogue was limited spatially and temporally to contain only the main event and the aftershocks. The best combination option in *Zmap* software with 50 times bootstrapping estimated the Magnitude of completeness equal to 1.7 (figure 5.2.18). The Gutenberg-Richter law b-value of the aftershock sequence is 0.96 which is a typical for an aftershocks sequence (see section 2.1.5). The magnitude of completeness has been used to limit the catalogue and apply the modified Omori's law. The fitting was very good as the RMS was about 5.0 while the obtained *p-value* was 1.1 which is typical for aftershock sequences. The 12/10/2013 *p-value* is slightly smaller than the one obtained by the 15/06/2013 sequence which shows the second aftershock sequence had a relative faster decay (figure 5.2.19). It is worth mentioning that even though the mainshock was considerably larger than the one of the 15/06/2013 sequence, the aftershocks of the 12/10/2013 were fewer and they had smaller magnitudes which can be attributed to the intermediate depth of the mainshock.

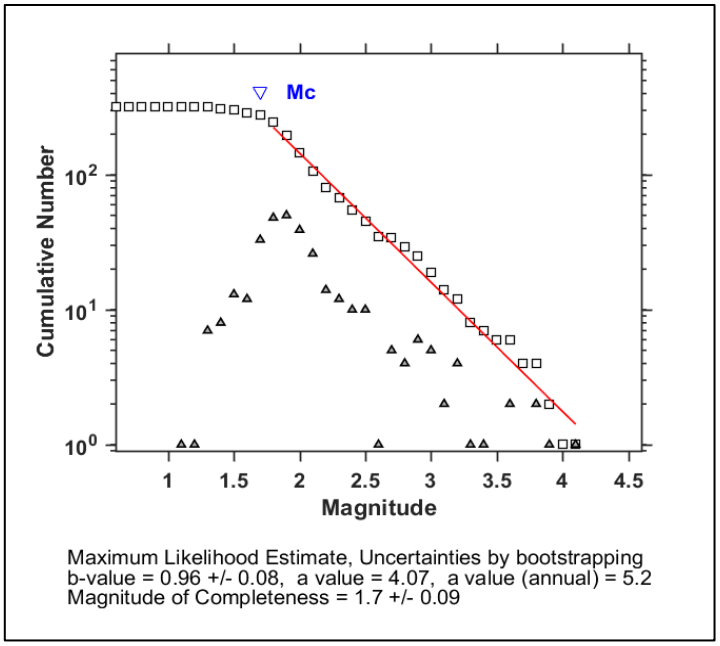

Figure 5.2.18. The best method comparison from the Zmap software has been used to examine the frequency magnitude distribution without using the mainshock. The aftershock sequence GR law fitting has given b-value 0.96 and the Magnitude of completeness is down to 1.7.

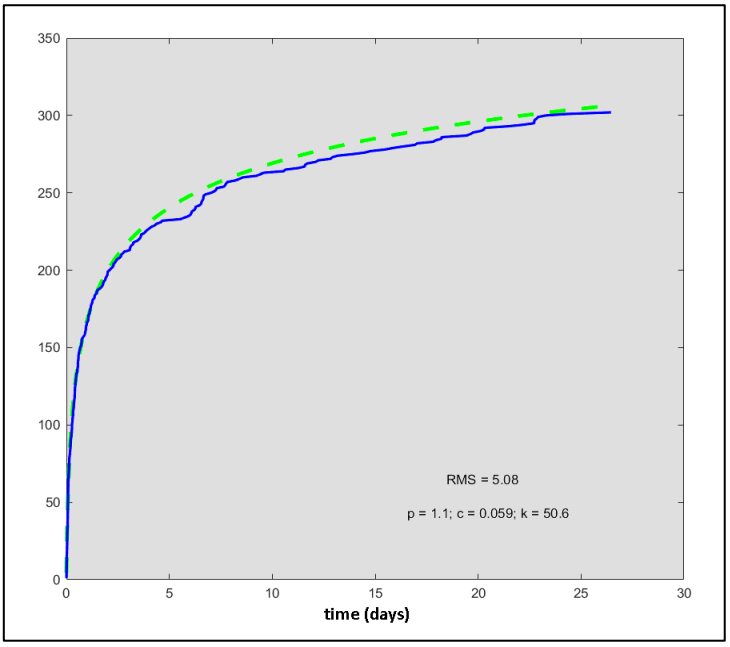

Figure 5.2.19 the modified Omori's law has been applied to estimate the decay rate parameters for the 12/10/2013 aftershock sequence (figures obtained from Zmap).

The mainshock as well as the spatial distribution of the aftershocks are presented in figure 5.2.20. In the same figure the fault plane solutions of the mainshock has been placed as well as the trace of the two cross sections. The provided focal parameters on table 5.2.4 are from the manual solution (NOA, 2018) of the NOA network (HL/National Observatory of Athens Seismic Network, 2018), the Global Centroid-Moment-Tensor (CMT, 2018) which follows the method descripted in (Dziewonski, et al., 1981; Ekström, et al., 2012), the Helmholtz Centre Potsdam GFZ German Research Centre for Geosciences (GFZ, 2018) and Centre Polynesien de Prevention des Tsunamis (CPPT, 2018).

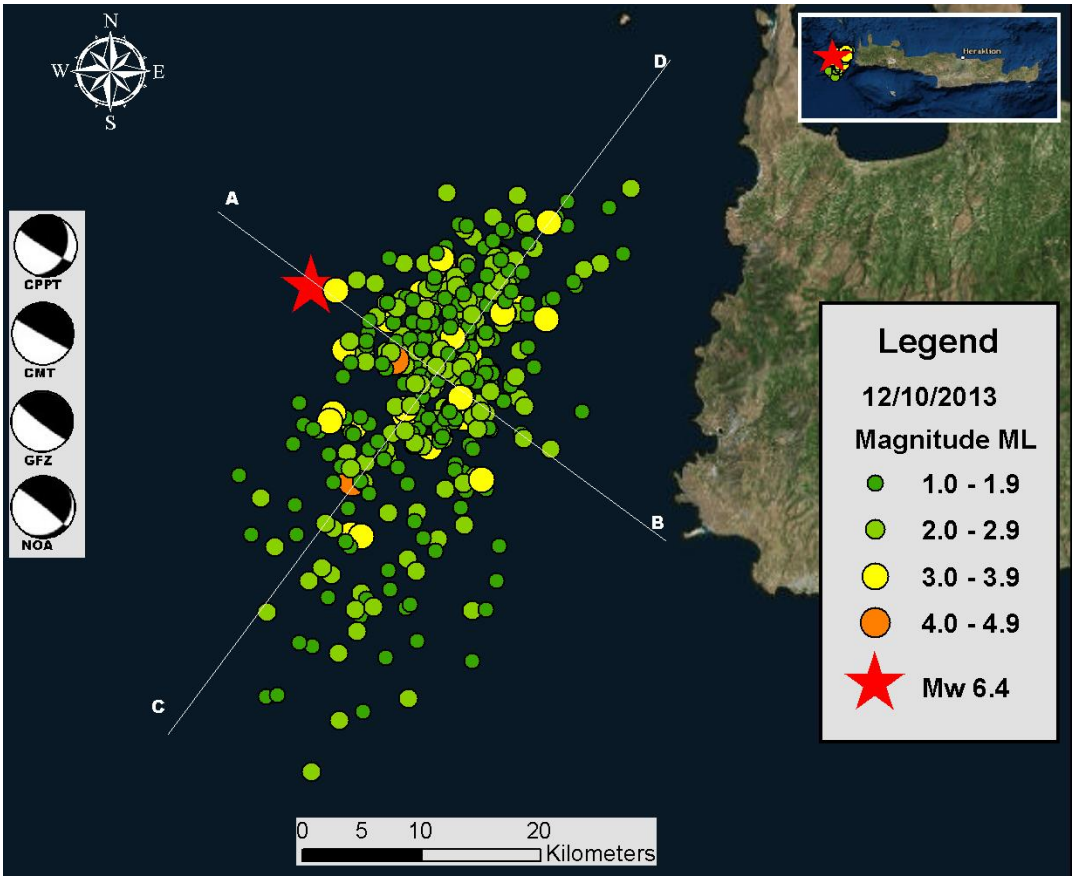

Figure 5.2.20. The spatial distribution of the 12/10/2013 aftershock sequence, the moment tensor of the mainshock (NOA, 2018) and the trace of the two cross sections. The strong event is denoted with a red star while the smaller events with circles. The size and the colour of the circles scales with the magnitude (map data are managed in ArcGIS (Esri, 2018)).

Table 5.2.4 The fault plane solutions for the 12/10/2013 mainshock.

Event	Magnitude	Strike 1	Dip 1	Rake 1	Strike 2	Dip 2	Rake 2	author
12/10/13	6.4	50	20	-168	309	86	-70	NOA
12/10/13	6.2	122	85	54	25	36	171	CPPT
12/10/13	6.7	119	87	88	340	3	130	CMT
12/10/13	6.5	128	84	96	262	8	44	GFZ

Studying the table 5.2.4 it clear that there are some fault plane solutions with considerable differences between the reported fault plane solutions. To determine which is the most representable for the 12/10/2013 case, cross section the spatial distribution of the events have been examined (figures 5.2.20, 5.2.21 and 5.2.22). The strike of the faults is about 120 (or 300) degrees, based on the location of the epicentres. If the angle of dip is calculated using graphical manner from the cross section in figure 5.2.21 which presents the cross section that is vertical to the strike, then it is estimated being around 80 degrees.

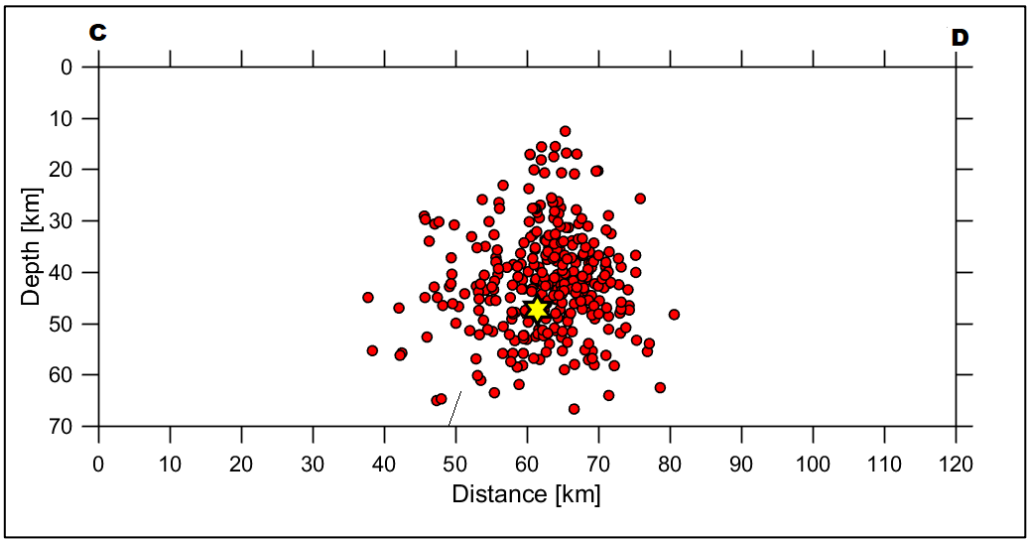

Figure 5.2.21 The perpendicular to the strike cross section that reveals the vertical spatial distribution of the 12/10/2013 events as well as the fault geometry (figure obtained from Zmap). The black line denotes the dip around 80 degrees.

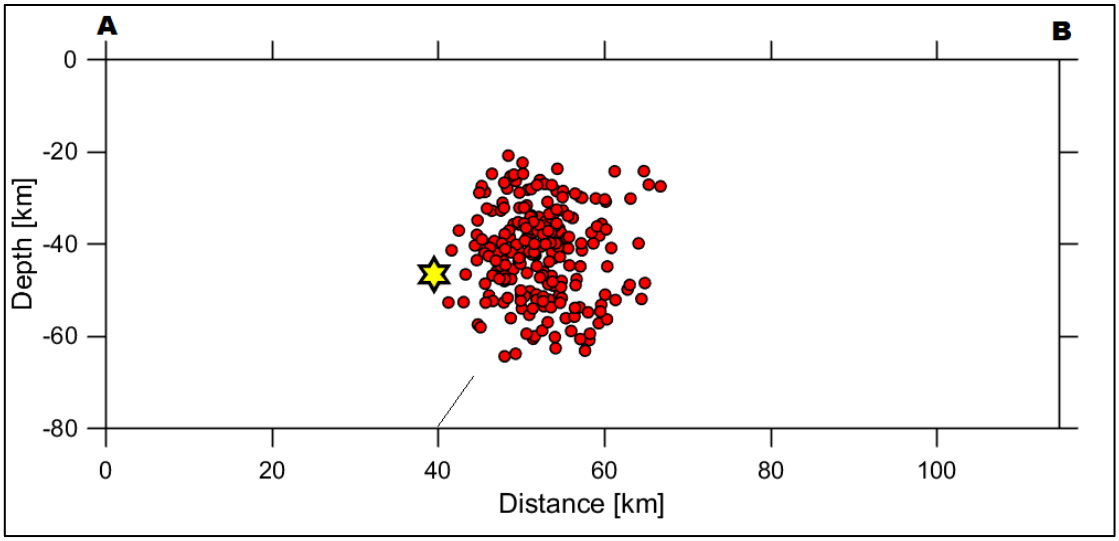

Figure 5.2.22 The parallel to the strike cross section that reveals the vertical spatial distribution of the 12/10/2013 events as well as the fault geometry (figure obtained from Zmap). The black line denotes the direction of rake.

In the vertical to strike cross section it is noticeable a possible second fault which will addressed in the discussion. According to figure 5.2.22 the spatial distribution of the events indicates a rake direction about 45-50. The CPPT fault plane solution explains better the focal mechanism so the fault is a reverse with a left lateral component (see section 2.1.3). The cross-section images have been adjusted to have as possible equal vertical and horizontal dimensions, so the presented image is more realistic. The absence of events in the edge of the cross-sections, the very clear spatial limits is artificial as the earthquakes that were far from the fault were removed. The width of the cross sections is 15km.

According to equations from Thingbaijam, et al. (2017) the fault length should be about 17.3km while the width 13.1 km. An attempt to correlate the fault parameters of the large earthquake with one of the recorded faults in the NOA digital fault database has been made. In the area where the large event the strongest aftershock was occurred (figure 5.2.23) there is a fault (GR0265) that had similar parameters (length, strike and mechanism). Based on the Mascle, et al. (1982) work, this is a reverse fault is a about 19.7km which is very similar to the results obtain from Thingbaijam, et al. (2017) work.

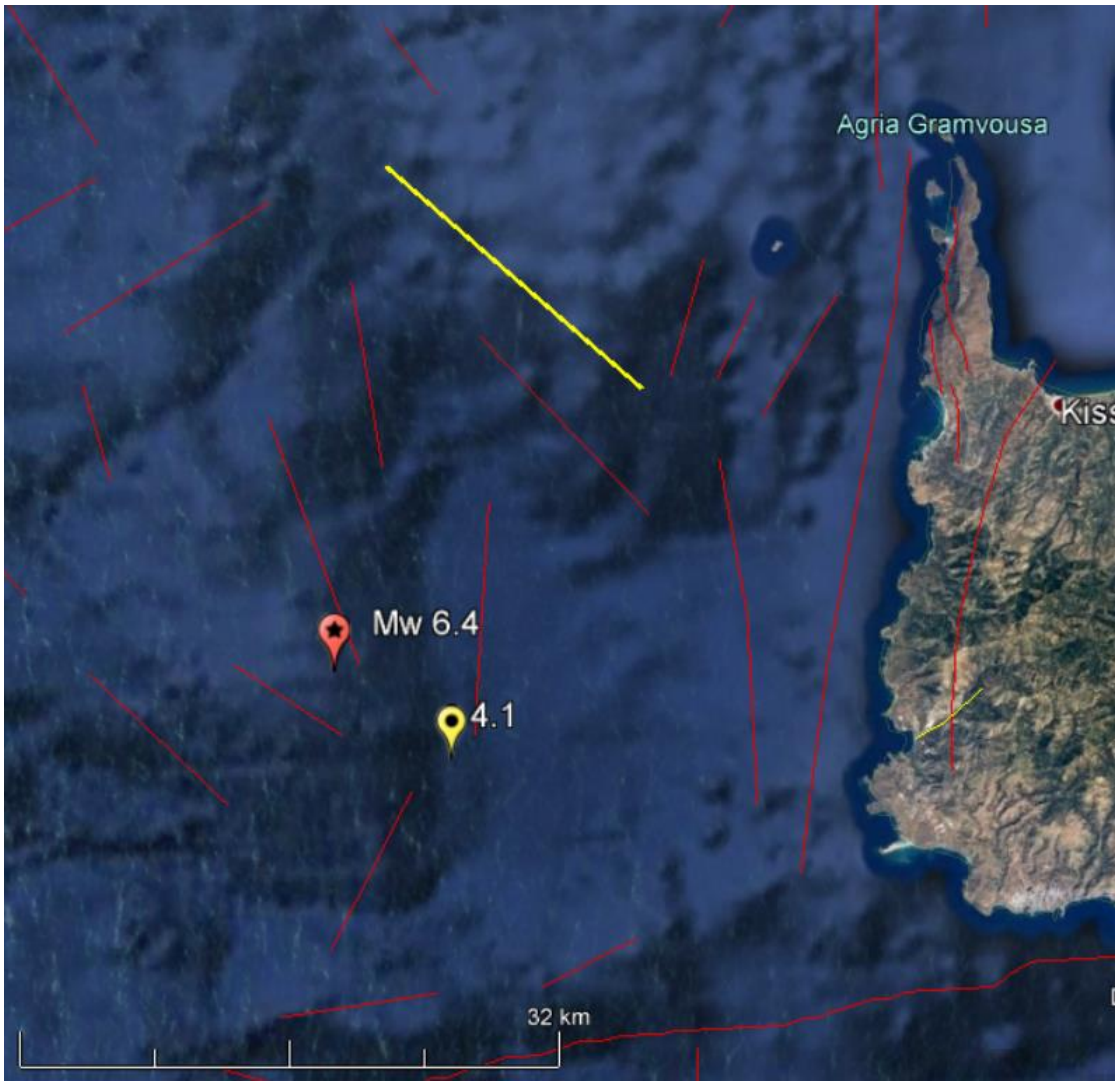

Figure 5.2.23 The registered faults in the NOA database (Ganas, et al., 2013) *denoted with red lines while with yellows is likely the one that has been activated. The epicentres of the strong event of the 12/10/2013 sequence is marked with a red pin with a star and its largest aftershock is with the yellow pin (data processed in Google Earth* (Google, 2018).

Aiming to relocate the main event as well as the aftershocks of the 12/10/2013 sequence, the velocity ratio VP/VS was calculated. The ratio is obtained by the same procedure as for the 15/06/2013 sequence (section 5.2.1). Wadati diagrams have been plotted with the MATLAB script for every event and the obtained mean value has been used in the relocation process. The same criteria has been used so that the mean *VP/VS* has been calculated with all the event that have been recorded at least in six stations. The arrival

times has been normalized so they could plot in the same diagram (figure 5.2.23) and the mean velocity ratio for the 12/10/2013 sequence is 1.7459 ≈ 1.75

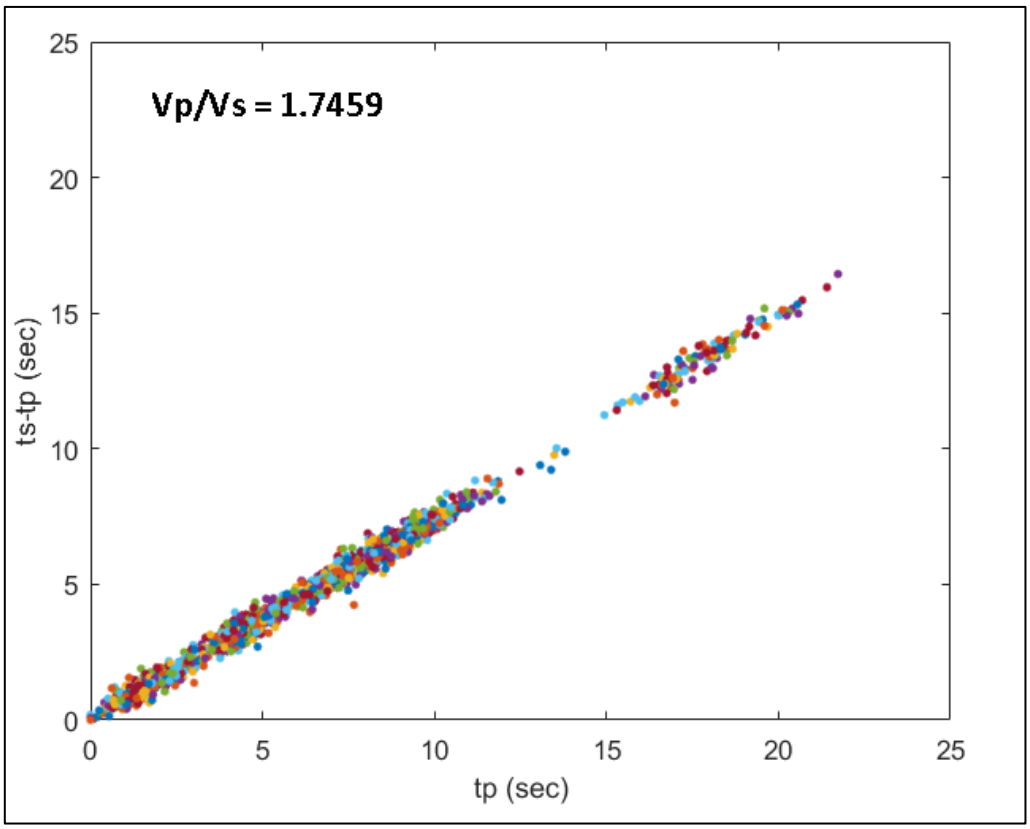

Figure 5.2.23 The Wadati plot obtained from the 12/10/2013 even. The mean velocity ratio has been estimated 1.7459.

The station correction file that has been used to relocate the 12/10/2013 events is presented on table 5.2.5. The software that uses Wadati plots to compare the theoretical and observed arrival times has produced the station corrections that have acceptable values. Most of the stations close to the epicentre have small time correction while the far station such as the HRKL, PRNS and VLI have increased values. The root-mean-square error of the time residuals as well as the horizontal and vertical errors have very low values. The errors of the ten strongest events are presented in table 5.2.6.

Table 5.2.5 the Hypoinverse-2000 station file input file with the calculated station corrections for the 12/10/2013.

Stations	Latitude (Degrees)	Longitude (Degrees)	Altitude (m)	Station Corrections (sec)
MHLO	36 41.39N	24 24.10E	175	0.31
GVDS	34 50.61N	24 05.41E	164	0.04
PRNS	35 21.89N	24 30.09E	51	-0.31
CHAN	35 31.15N	24 02.55E	34	0.28
RODP	35 33.37N	23 45.28E	308	0.06
KNDR	35 14.05N	23 37.29E	10	-0.19
VLI	36 43.09N	22 56.22E	220	0.32
KTHR	36 15.64N	23 00.25E	315	0.15
HRKL	35 18.69N	25 06.10E	90	0.54

Table 5.2.6 The relocation errors of the 10 largest events of the 12/10/2013 sequence which are very small in all cases.

Date	Time	Magnitude ML	Depth (km)	RMS (sec)	Horizontal error (km)	Vertical error (km)
12/10/2013	13:11:54	6.2	46.74	0.16	0.7	0.8
13/10/2013	17:43:52	4.1	47.05	0.15	0.5	0.6
12/10/2013	13:17:00	4	40.68	0.19	0.7	0.9
12/10/2013	14:05:51	4	44.2	0.16	0.6	0.8
19/10/2013	2:19:21	3.9	52.83	0.11	0.6	0.7
12/10/2013	19:36:26	3.8	48.74	0.13	0.5	0.5
16/10/2013	13:47:59	3.8	41.17	0.22	0.8	1
13/10/2013	0:01:24	3.6	33.98	0.13	0.5	0.7
20/10/2013	4:49:48	3.6	39.88	0.18	0.6	0.8
12/10/2013	15:27:05	3.4	41.89	0.14	0.7	1

The non-extensive statistical physics q parameter has been estimated to examine the temporal characteristics and scaling relations of the 12/10/2013 aftershock sequence. The cumulative interevent times $P(>T)$ of the aftershocks has been calculated to estimate the q. Aiming to examine if there are variations in the Magnitude of completeness and Gutenberg-Richter b-value, the frequency-magnitude distributions have been re-plotted after removing 50 and 100 events from the end of the catalogue. The GR-law fit in figure 5.2.24 show that the b-value and the M_c have changed after removing 50 events from the catalogue. These variations have been considered when the interevent times have been calculated. Having in mind the q-variations that have been noted in the 15/06/2013 aftershock sequence, the q value has been computed for different time windows and the same techniques as the previous sequence have been applied as in section 5.2.1. The only difference is that due to the new M_c value, the catalogue was limited considerably, and the window size has been reduced. In figure 5.2.25 there are the results from the 'normal' expanding windows method, starting from the beginning of the catalogue and change the ending point while in figure 5.2.26 there are the 'reverse' method, having fixed the end point and remove event from the beginning. In the figures 5.2.27 are the results from the moving window approach. A large window with 150 events have been selected to be statistically stable and have an as accurate as possible fitting while the overlap window was small, with 20 events due to the limited size of the catalogue.

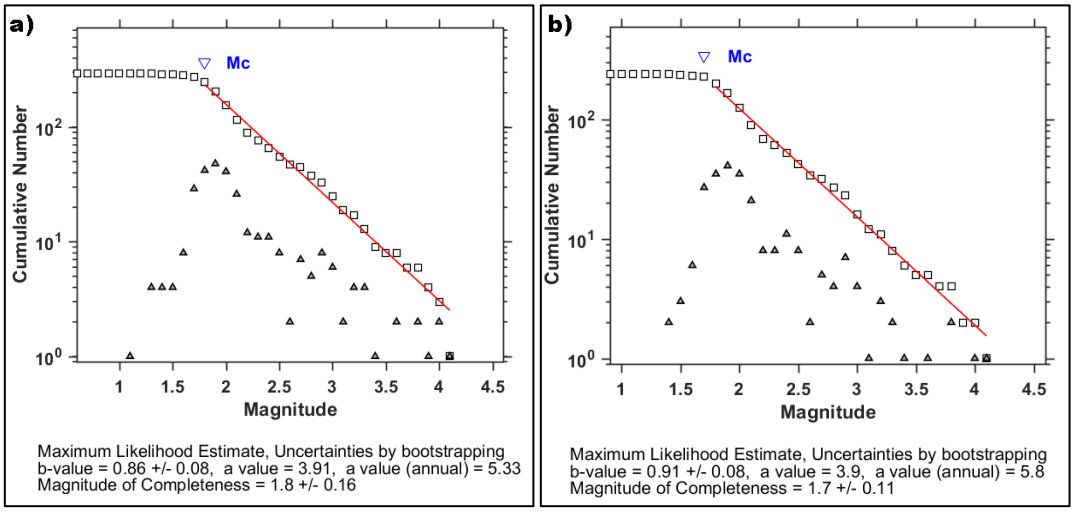

Figure 5.2.24 The magnitude of completeness and the b-value for the 12/10/2016 after removing 50(a) and 100(b) events respectively (figures obtain from Zmap).

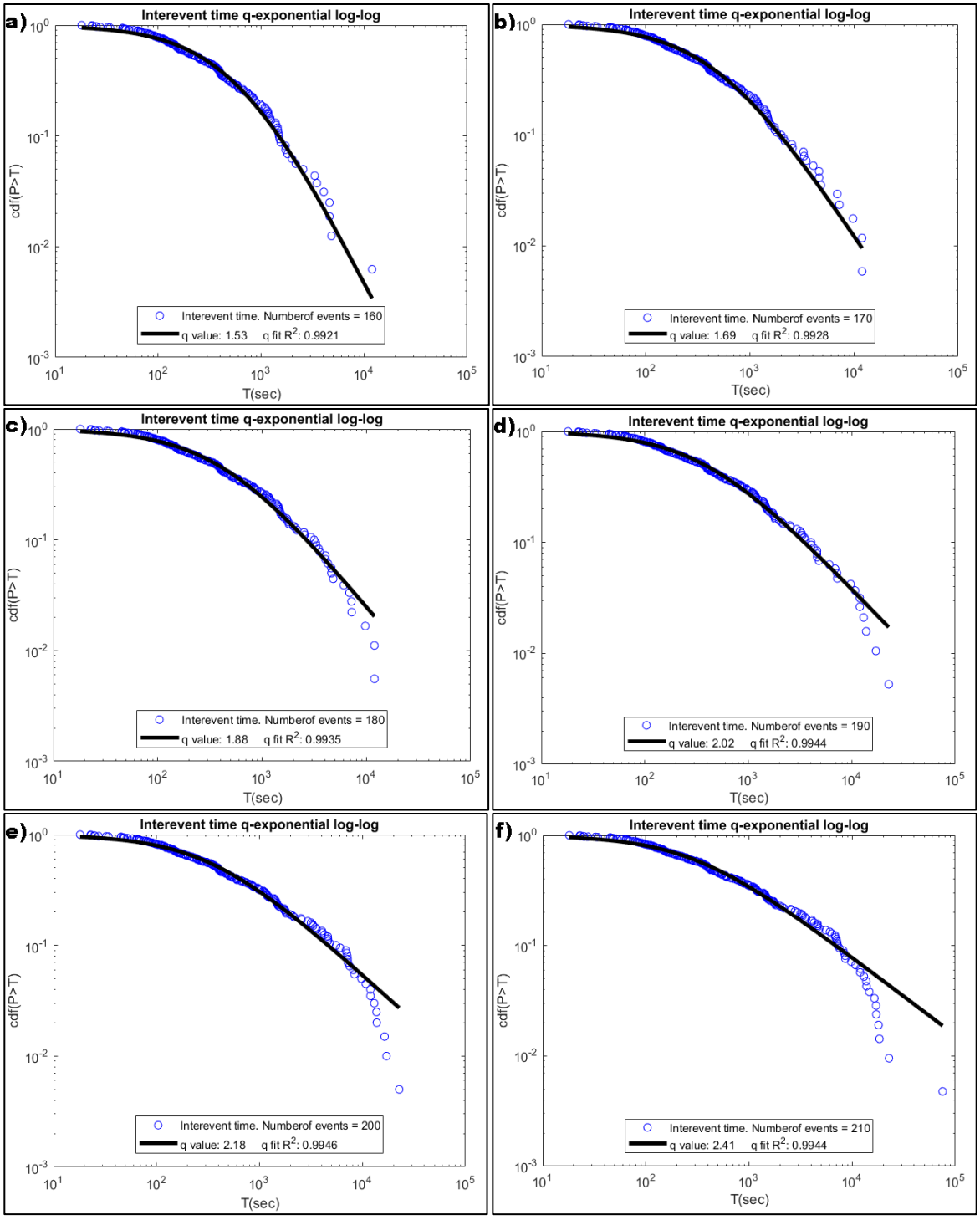

Figure 5.2.25. The normal expanding time window results for 160(a), 170(b), 180(c), 190(d), 200(e) and 210(f) events: a) q=1.53 ±0.0023 to ±0.0066, b) q=1.69 ±0.0021 to ±0.0060, c) q=1.88 ±0.019 to = 0.0053, d) q=2.02 ±0.017 to = 0.0044 and e) q=2.18 ±0.0017 to ± 0.0043 and f) q=2.41 ±0.0018 to ± 0.0044.

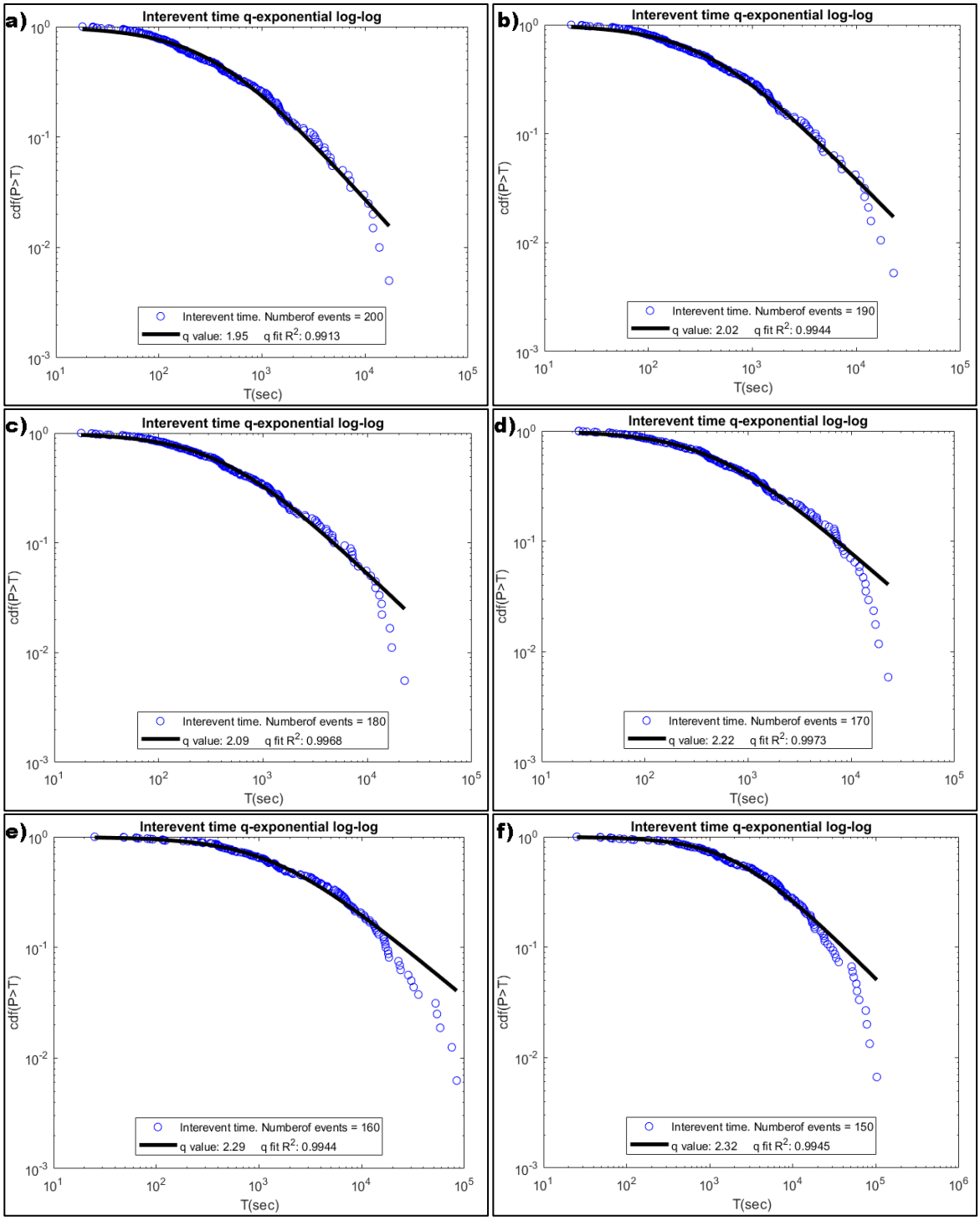

Figure 5.2.26. The reverse expanding time window results for 200(a), 190(b), 180(c), 170(d), 160(e) and 150(f) events: a) q=1.95 ±0.0017to ± 0.0044, b) q=2.02 ±0.013 to ± 0.0037, c) q=2.09 ±0.0009 to ±0.0025, d) q=2.22 ±0.0008 to ±0.0032, e) q=2.29 ±0.016 to = 0.0047 and f) q=2.32 ±0.0015 to ± 0.0047.

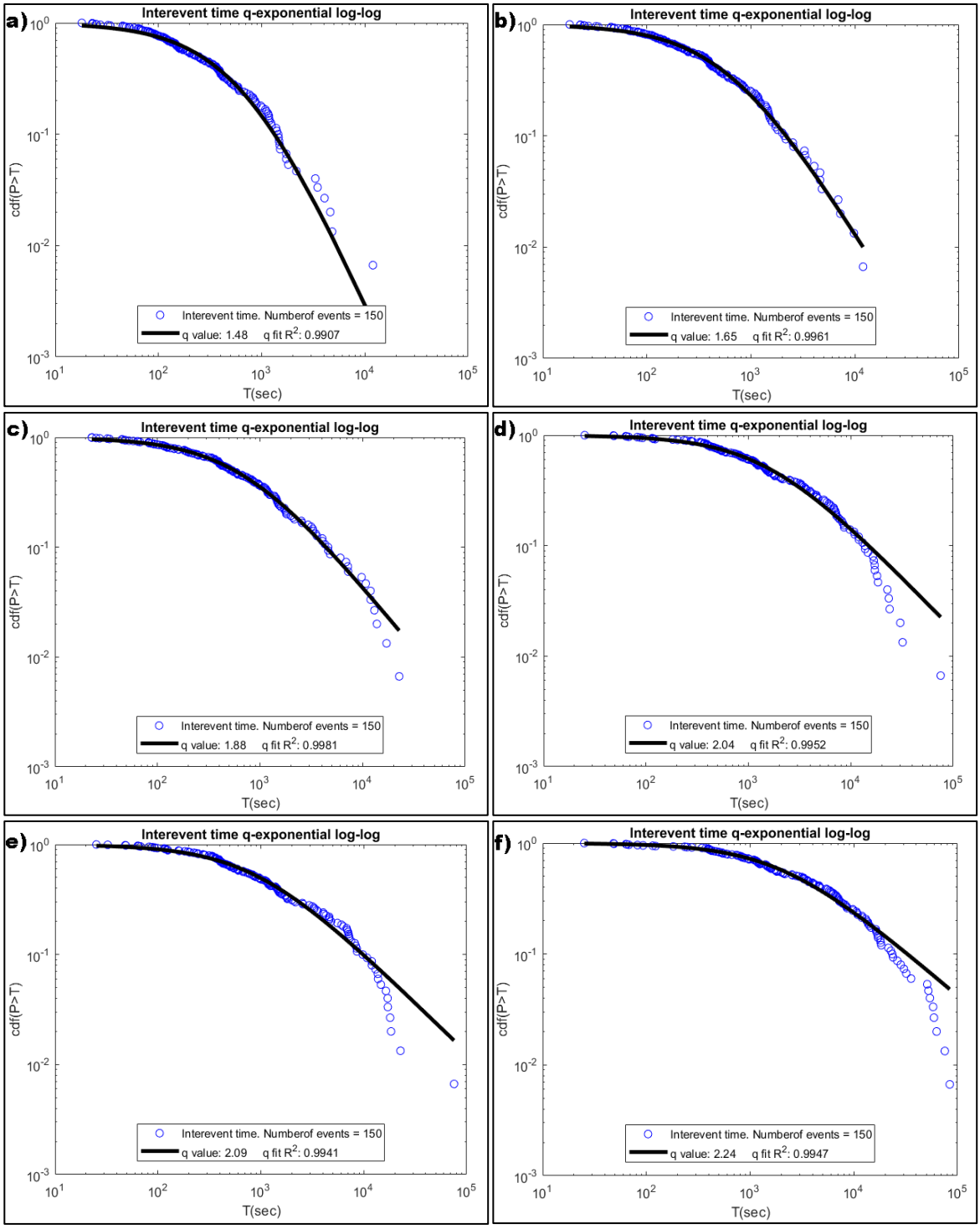

Figure 5.2.27. The moving time window results, time moves 20(a), 40(b), 60(c), 80(d), 100(e) and 120(f) events: a) q=1.48 ±0.0027to ± 0.0080, b) q=1.65 ±0.011 to ± 0.0033, c) q=1.88 ±0.0005 to ±0.0016, d) q=2.04 ±0.0017 to ±0.0051, e) q=2.09 ±0.014 to = 0.0041 and f) q=2.24 ±0.0015 to ± 0.0045.

5.2.3 The 2016 Chania swarm sequence

A swarm type sequence occurred in the western part of the Crete, with estimated starting time based on the first event recorded in this location on 31 January 2016 at 00:00:37 UTC with local magnitude M_L = 1.7. The 24-hour recording has been examined for about two months before the first event without been able to identify another event in the same zone. In the beginning the earthquakes were scattered in time with small magnitudes, not all of them have triggered the automatic monitoring system. Due to the small epicentral distance from the Chania city, these events have been used as testing material for the new strong ground motion networks of the HSNC (Chatzopoulos, et al., 2018). The number of events increased rapidly after the 05/03/2016, before this date it was not possible to spatiotemporally correlate them with a swarm sequence. The strongest event with M_w =4.6 has took place before the 'middle' of the of the swarm excitation period on 12/03/2016 at 12:40:39 UTC. The epicentre was located on longitude 23.599E and latitude 35.366N and the hypocentre was approximately 16km deep. The location of the earthquake was on the western onshore part of Crete, 15km south-southwest from nearest town (Kissamos). The daily rate of events time histogram (figure 5.2.29) as well as the cumulative number of events shows that the sequence started with a slow release of seismic energy for the first 35 days approximately. Afterwards, there was a sharp increase in the cumulative number. About 260 events occurred in the six-day period before the main event (M_w 4.6). The relaxation was smooth, and about 300 events were distributed evenly within a 14-day window.

The magnitude and depth distribution histograms of the swarm sequence are illustrated in (figure 5.2.30). The examination of the aftershock catalogue shows that the magnitudes range between micro and minor from 1.0 to 3.9 while there were only three of the events that had magnitude above from 4.0. The magnitudes seem to have a normal distribution where was slightly skewed to the right and the most common magnitude values were the 2.0 and 2.1. The depth histogram suggests that most events have been distributed normally between the 5 and 30 km depth, while there are some events at an apparent 0 km depth that have not relocated properly as explained in section 5.2.1.

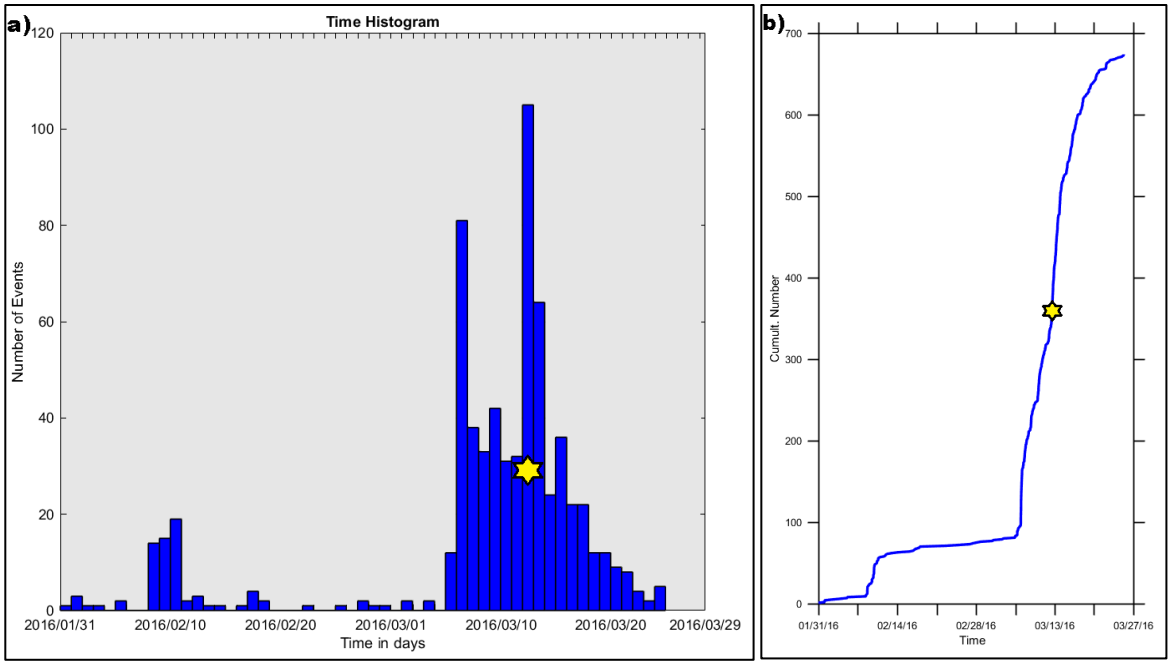

Figure 5.2.29 a) the time histogram present the daily rate of the 2016 Chania swarm sequence. b) the cumulative curve, the yellow star denotes the strong event with moment magnitude M_w= 4.6 (figures obtained by Zmap).

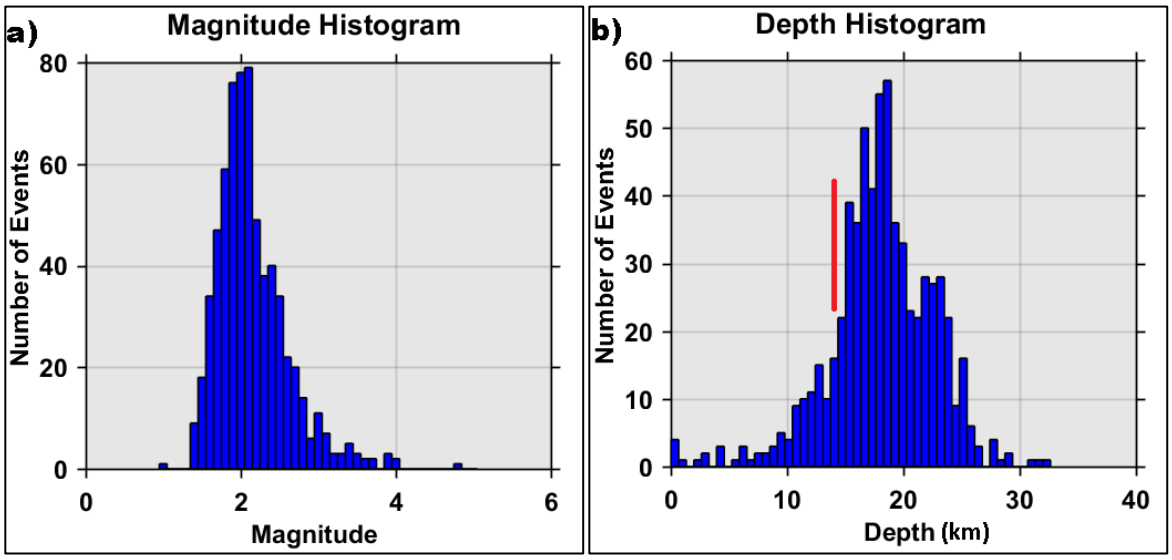

Figure 5.2.30 The magnitude (a) and the depth histogram (b) of the 12/03/2016 strong earthquake and its aftershock sequence. The red line indicates the depth of the largest event (figures obtained by Zmap).

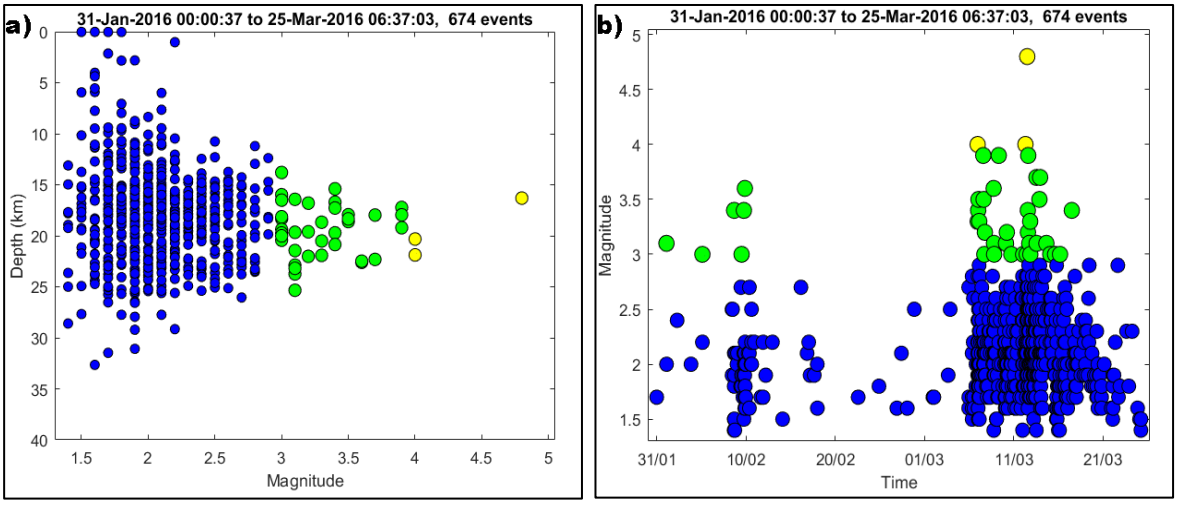

Figure 5.2.31 a) The magnitude versus depth diagram and b) the magnitude versus time diagram of the 2016 Chania swarm sequence. The circles colour and the size change as the magnitude increases.

Omori's law has been used to validate if this sequence is a swarm. The decay rate parameters have been estimated for the events after the 'mainshock' that occurred on 12/03/2016. The catalogue was limited spatially and temporally to with the same procedure as on the previous aftershocks sequences (sections 5.2.1 and 5.2.2). The Magnitude of completeness and the *b*-value have calculated for the whole swam period with the best combination option in Z-map software with 50 times bootstrapping as in section 3.2.1. These values (M_c and *b*) were rejected because a new estimation was carried out in the time interval before and after the main event, which showed a slight change in estimated parameters between the two-time windows. The Gutenberg-Richer' law fits for the two-time windows are illustrated in figure 5.2.32 a and b. The Magnitude of completeness and the *b*-value increase from 1.9 to 2 and from 0.92 to 1.09 after the main event. The modified Omori's law has been applied to the 'aftershocks' with the new M_c. The fitting was very good as the RMS was about 3.3 while the obtained *p*-value was 2.7, which is a very high value and not typical for aftershock sequences (figure 5.2.33). The *p-value* in the swarm sequences is usually high because aftershocks and swarm events occurs at the same time, so the decay appears to be slow (Utsu, et al., 1995).

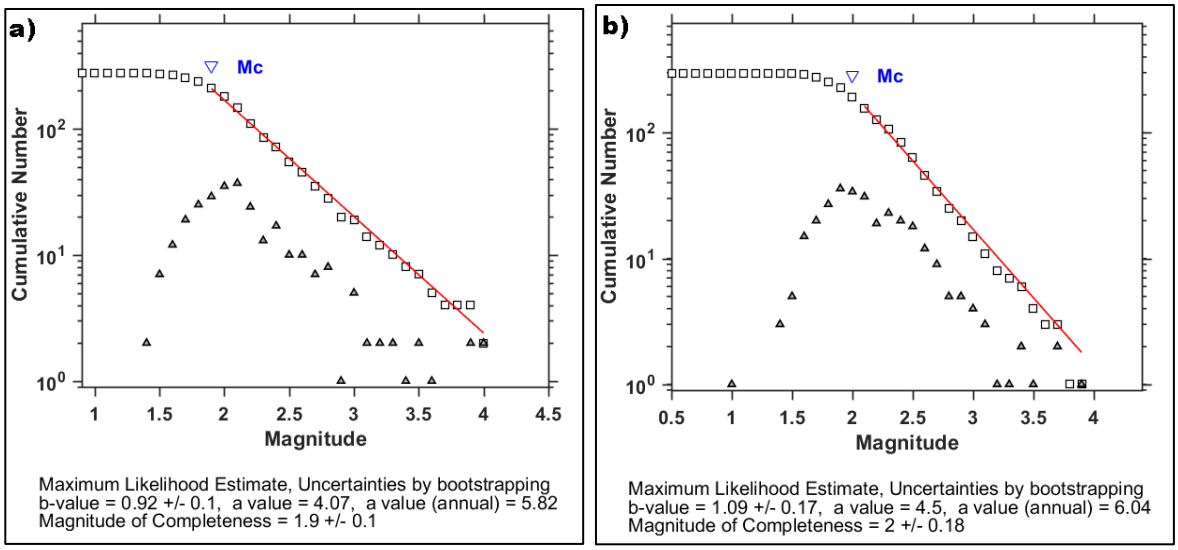

Figure 5.2.32 The Magnitude of completeness and b-value before(a) and after(b) the Mw=4.6 event 12/03/2016 (figures obtained by Zmap).

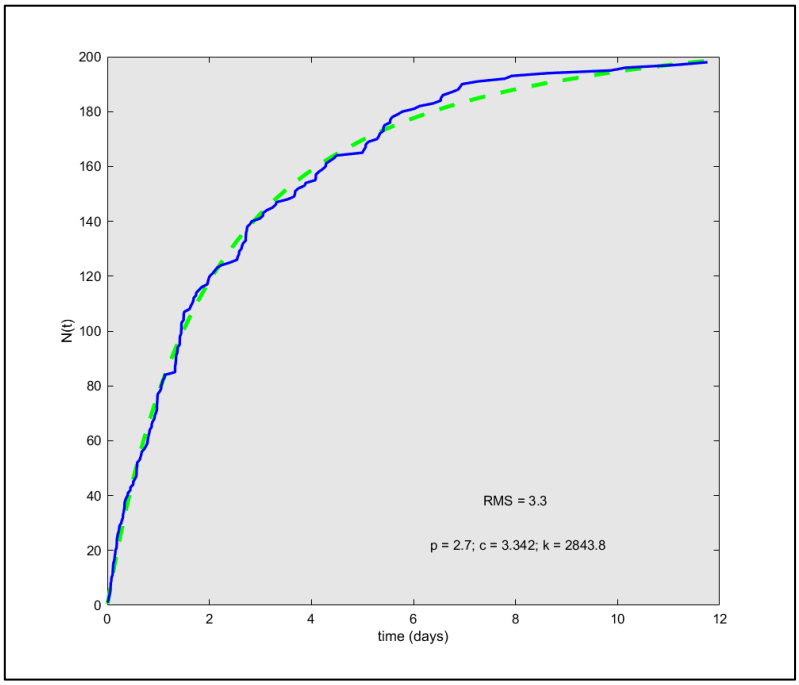

Figure 5.2.33 The modified Omori's law fitted has been applied to examine the swarm decay rate. The p-value is 2.7 which is an indicator that there are swarm events between the aftershocks of the main event (figure obtained by Zmap).

The main event with moment magnitude M_w=4.6 and the spatial distribution of the swarm sequence are presented in figure 5.2.33. In the same figure has been placed the fault plane solution of the main event as well as the trace of the two cross sections. According to the NOA's moment tensor database the fault plane solution of the mainshock has strike=207 dip=52 rake=-4 and the other plane has strike=299 dip= 87 rake=-142 (figure 5.2.33). Very similar results in terms of strike and rake (205 and -4 respectively) are provided from the (HT/Aristotle University of Thessaloniki Seismological Network, 2018) while the dip in this case is much steeper (81), so both suggest a left lateral strike slip fault (dip=90 and rake=0) with a normal component (see section 2.1.3).

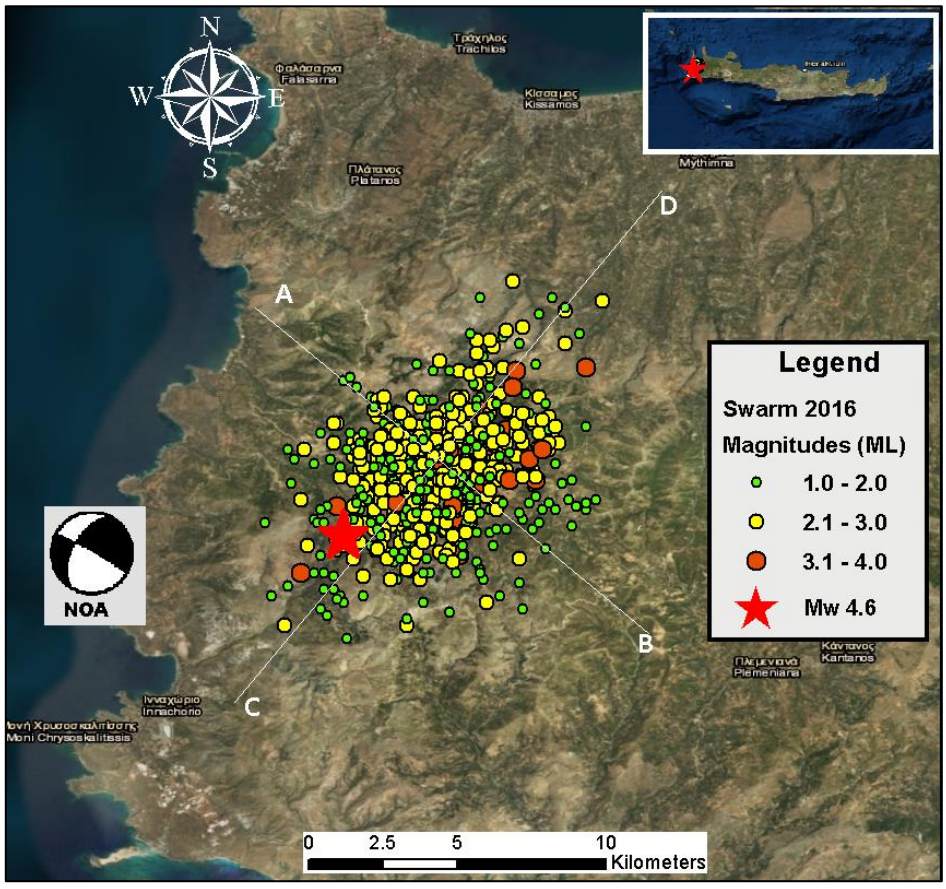

Figure 5.2.33. The spatial distribution the Chania 2016 swarm sequence, the moment tensor of the strongest event and the trace of the two cross sections (NOA, 2018). The strongest event is denoted with a star while the smaller events with circles. The size of the circles scales with the magnitude, the same occurs for the colour (map data are managed in ArcGIS (Esri, 2018)).

The swarm events make it difficult to examine and understand the focal mechanism with the cross sections. The vertical cross section with all the swarm sequence events suggests an incorrect fault plane solution (figure 5.2.34). The catalogue was reduced to have only the events after the main earthquake, the new the cross section vertical to strike appears to have a dipping angle about 58-60 degrees (figure 5.2.35)

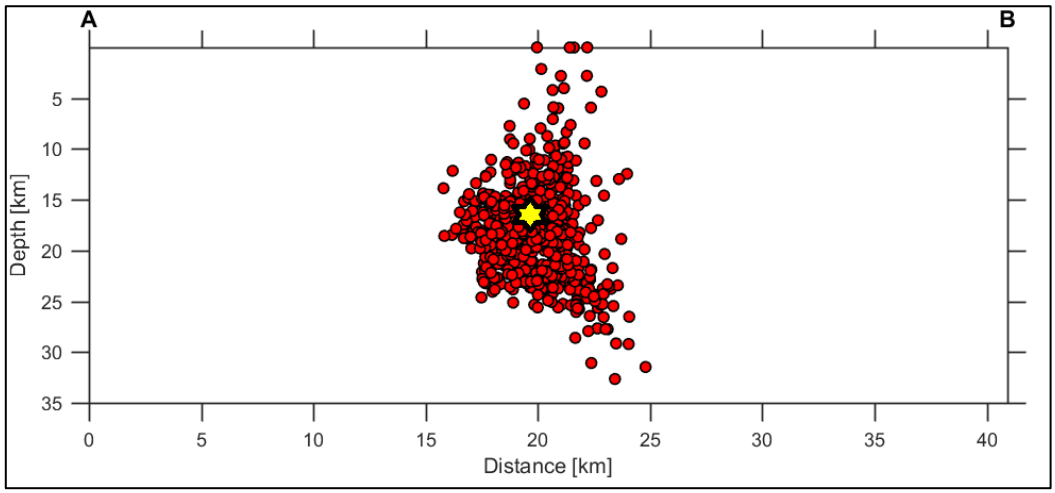

Figure 5.2.34 The perpendicular to the strike cross section that contains all the swarm events (figure obtained by Zmap).

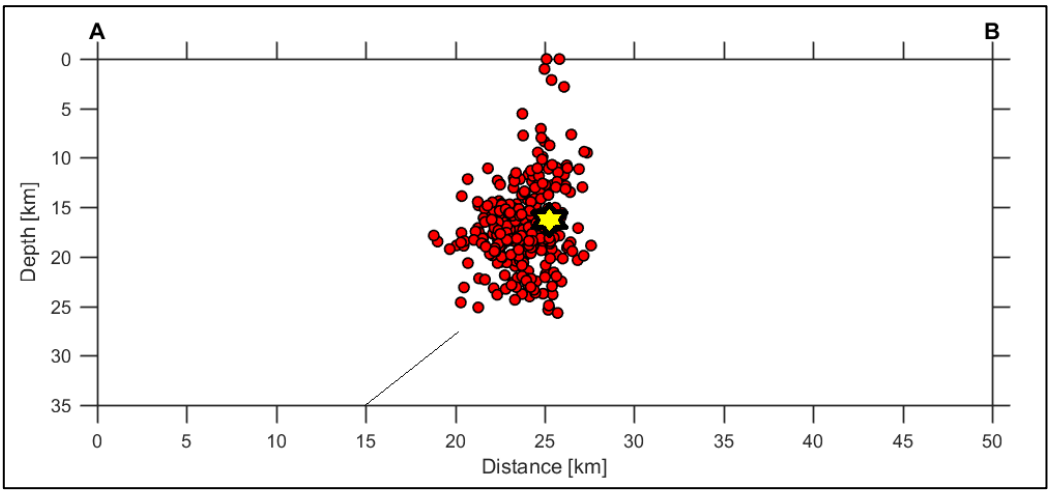

Figure 5.2.35 The perpendicular to the strike cross section of the Chania swarm limited to only show the events after main earthquake. The black line denotes the dip of about 58-60 degrees (figure obtained by Zmap).

The parallel to strike cross section is illustrated in figure 5.2.36, where again the swarm events makes difficult to examine the fracture surface and the rake. The catalogue was reduced to have only the events after the main earthquake (figure 5.2.37).

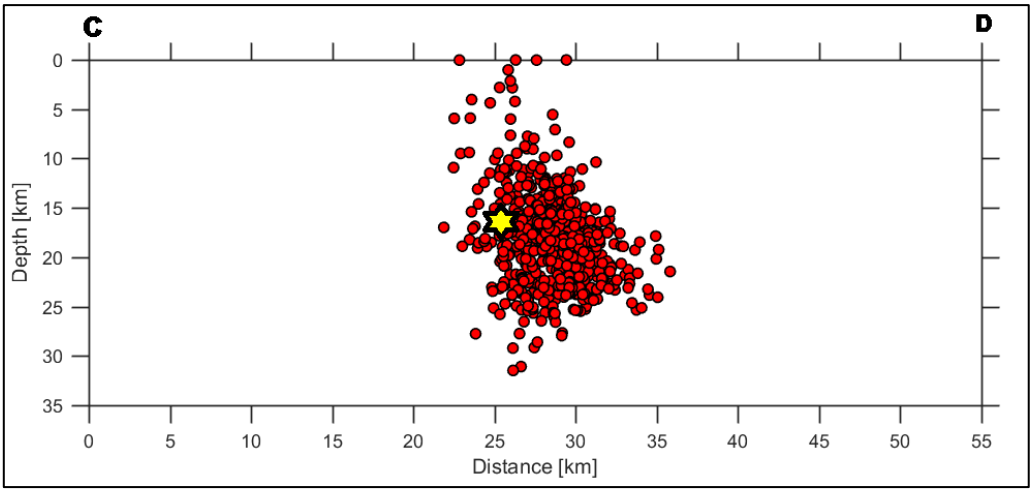

Figure 5.2.36. The parallel to the strike cross section that contains all the swarm events (figure obtained by Zmap).

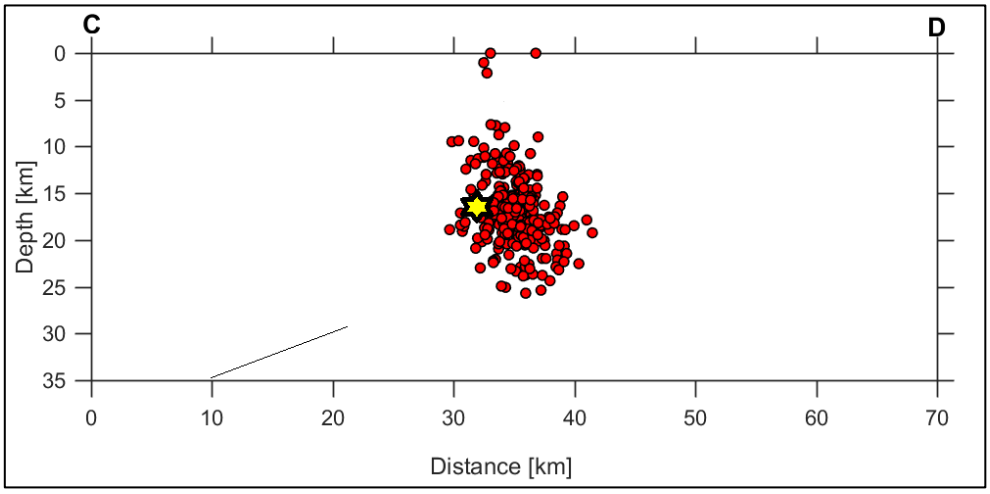

Figure 5.2.37 The parallel to the strike cross section of the Chania swarm limited to only show the events after main earthquake. The black line denotes the direction of the rake (figure obtained by Zmap).

An attempt to correlate the fault parameters of the large earthquake with one of the recorded faults in the NOA digital fault database has been made. The main event and three of the strongest swarm have been placed on the map (figure 5.2.38) but none of the existing fault (red colour) match the focal mechanism. The onshore faults from the hardcopy map for the western part of Crete by Mountrakis, et al. (2012) has been digitized and added in along with the NOA faults. The number of faults in the western part of Crete is considerably higher and for that reason only the ones that were close to the epicentres with similar strike have been digitized. According to focal mechanism and the second vertical to strike cross section (figure 5.2.35), if the fault plane reaches the surface, that will be about 8-10 km east of the main event. The only possible fault that that could match the available data is noted with blue colour. The first fault on the left side of the Mw 4.6 epicentre is a reverse one and the next one on the right is too far away.

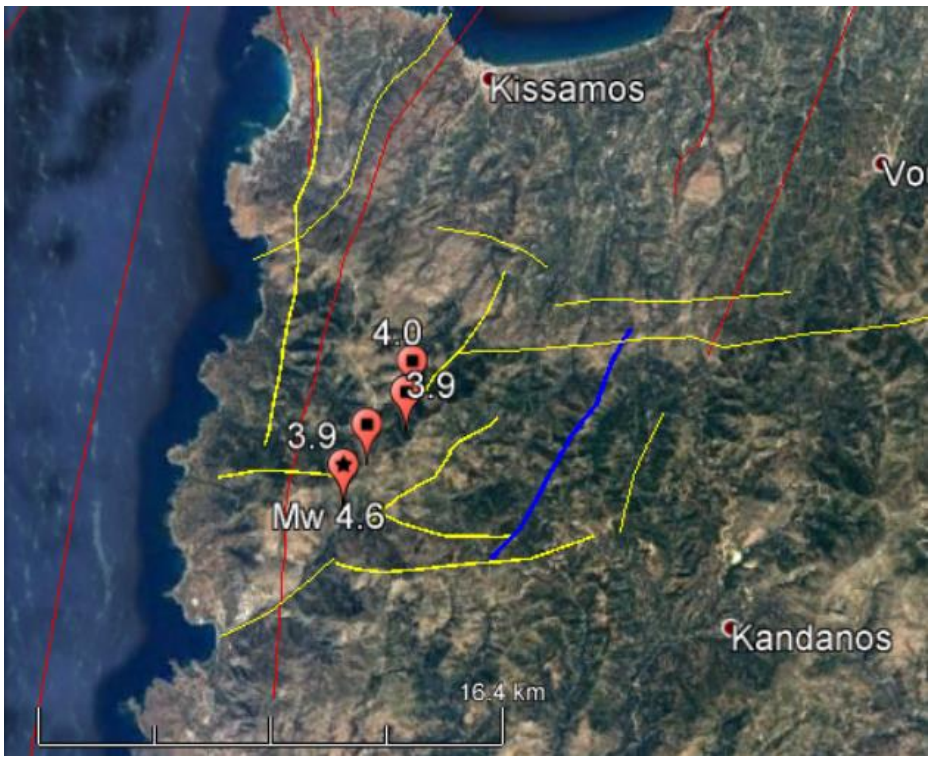

Figure 5.2.38 The registered faults in the NOA database are the red lines (Ganas, et al., 2013), the epicentres of the largest events of the swarm sequence are the red pins with square and the number next to them is the local magnitude. The main event is the red pin with star and the faults from Mountrakis, et al.(2012) work are noted with yellow lines (data processed in Google Earth (Google, 2018)).

In order to relocate the the Chania 2016 swarm sequence, the velocity ratio VP/VS was calculated. The ratio is obtained with the same procedure as for the previous aftershock sequences. The Wadati diagrams have been plotted with the MATLAB script for every event and the mean value have been used in the relocation process. The same criteria have been used so the mean *VP/VS* been calculated with all the event that have been recorded at least in six stations. The arrival times has been normalized so they could plot in the same diagram (figure 5.2.39) and the mean velocity ratio for the Chania 2016 swarm sequence is 1.7475 ≈ 1.75. The clustering pattern in the Wadati plot, where the *S-P* time differences are constrained in specific t_P values is because the swarm events are located in a small area which is very close to the HSNC' stations. The *P* and *S* travel paths and travel times are similar for most events and they create this image which is reflecting the distance between epicenters and stations.

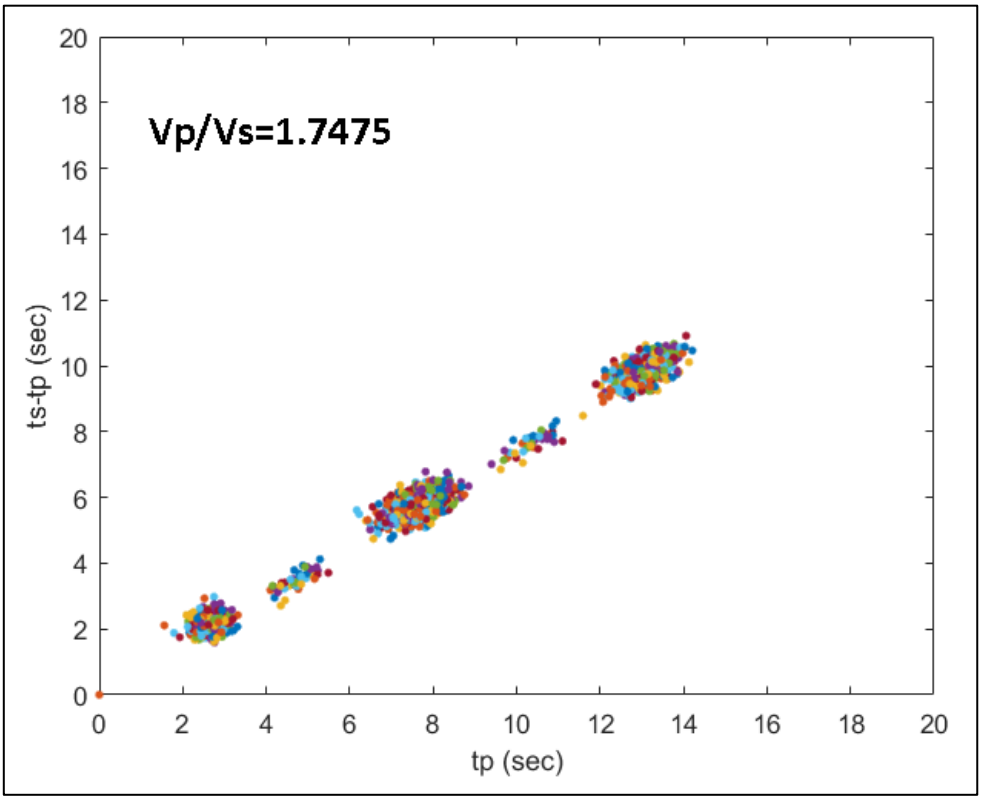

Figure 5.2.39 The Wadati plot obtained from the 2016 swarm sequence. The mean velocity ratio has been estimated 1.7475≈1.75.

The station corrections that have been used to relocate the 2016 Chania swarm events are presented on table 5.2.4. The software that use Wadati plots to compare the theoretical and the observed arrival times has been used with the initial crust model which is the same as the one used for 12/10/2013 aftershock sequence relocation and it has been used for the 1D minimum velocity model obtained from the VELEST software. As far as the station corrections are concerned, the values were acceptable for both crust models but for the second one seems to be more correct. The station GVDS which is considered to be relative close to the swarm epicentres with the first model had large corrections which indicates that the model did not fit well as the obtained 1D.

Table 5.2.4 the Hypoinverse-2000 station file input file with the calculated station corrections for the 2016 Chania Swarm. The letters A and B denotes which values are from the old and which are from the modified crust model respectively.

Station 4 letter codename	**Latitude (Degrees)**	**Longitude (Degrees)**	**Altitude (meters)**	**Station Corrections A (sec)**	**Station Corrections B (sec)**
GVDS	3450.61N	2405.41E	164	0.41	0.14
PRNS	3521.89N	2430.09E	51	-0.62	-0.55
CHAN	3531.15N	2402.55E	34	0.23	0.37
RODP	3533.37N	2345.28E	308	0.07	0.13
VLI	3643.09N	2256.22E	220	0.80	0.91
KTHR	3615.64N	2300.25E	315	-0.05	-0.17
TMBK	3504.35N	2445.97E	10	0.22	0.20

A comparison of the 8 strongest events results obtained from initial and the new crust model are in table 5.2.5. The relocation associated errors for the second velocity model seems to be smaller for the vertical dimensions and the RMS time residuals weighting while for the horizontal errors it seems that there is an improvement in some cases. Table 5.2.6 presents the 10 strongest event relocation errors from the second model which is presented along with the original one in table 5.2.7.

Table 5.2.5 The comparison of the two crust model relocation errors of the 8 largest events of the 2016 Chania sequence.

Date Time UTC	Local Mag	Time residuals A (sec)	Horizontal Error A (Km)	Error in Depth A (km)	Time residuals B (sec)	Horizontal Error B (Km)	Error in Depth B (km)
12/03/16 12:40	4.8	0.23	0.6	1.9	0.22	0.5	1.5
12/03/16 07:49	4	0.23	2.0	0.8	0.23	1.8	0.8
06/03/16 23:18	4	0.22	0.5	1.2	0.22	0.5	1.1
12/03/16 15:22	3.9	0.13	0.4	1.1	0.13	0.4	0.9
09/03/16 8:04	3.9	0.11	0.4	1.1	0.1	0.4	0.9
07/03/16 14:25	3.9	0.19	0.5	1.4	0.18	0.5	1.1
13/0316 13:22	3.7	0.19	1.8	1.0	0.18	1.8	0.6
13/0316 23:26	3.7	0.21	0.6	1.3	0.18	0.5	1.0

Table 5.2.6 The relocation errors of the 10 largest events of the 2016 Chania sequence. The mean square root time residuals are less than 0.23 seconds, the horizontal errors less than 1.8km while the vertical ones less than 1.5km.

Date	Time (UTC)	Magnitude ML	Depth (km)	Rms time Residuals (sec)	Horizontal error in (km)	Vertical error in (km)
12/03/2016	12:40:39	4.8	16.31	0.22	0.5	1.5
06/03/2016	23:18:16	4	20.32	0.22	0.5	1.1
12/03/2016	7:49:59	4	21.88	0.23	1.8	0.8
07/03/2016	14:25:15	3.9	17.23	0.18	0.5	1.1
09/03/2016	8:04:08	3.9	17.95	0.10	0.4	0.9
12/03/2016	15:22:23	3.9	19.21	0.13	0.4	0.9
13/03/2016	13:22:58	3.7	22.32	0.18	1.8	0.6
13/03/2016	23:26:32	3.7	17.97	0.18	0.5	1
09/02/2016	21:11:14	3.6	22.6	0.21	0.6	0.6
08/03/2016	18:25:04	3.6	22.49	0.11	0.5	0.3

Table 5.2.7 The velocity model that has been used in the relocation of the 12/10/2013 aftershocks sequence (Vp A) and the new minimum 1D model derived from VELEST software Vp B.

Depth (km)	Vp A (km/sec)	Vp B (km/sec)
0	4.2	4.34
1	5.7	4.96
3	6.3	6.20
8	6.4	6.36
12	6.45	6.40
20	6.5	6.42
25	6.8	6.74
30	7.3	6.88
33	7.9	7.95

The non-extensive statistical physics q parameter has been estimated to examine the temporal characteristics and scaling relations of the Chania 2016 swarm sequence. The cumulative interevent times $P(>T)$ of the events has been calculated in order to estimate the q. The M_c value from figure 5.2.32 b has been adopted. Having in mind the q-variations that have been noted in the previous aftershock sequence, the q value has been computed for different time windows and the same techniques as the previous sequences have been applied (sections 5.2.1 and 5.2.2). Figures 5.2.40 provides the results from the 'normal' expanding windows method, starting from 200 events, increasing by 25 up to 325 while in the 'reverse' method presented in figures 5.2.41, from 350 and goes down to 225 events. In the figure 5.2.42 are the results from the moving window approach. A large window with 180 events have been selected to be statistically stable and have an as accurate as possible fitting while the overlap window was 25 events.

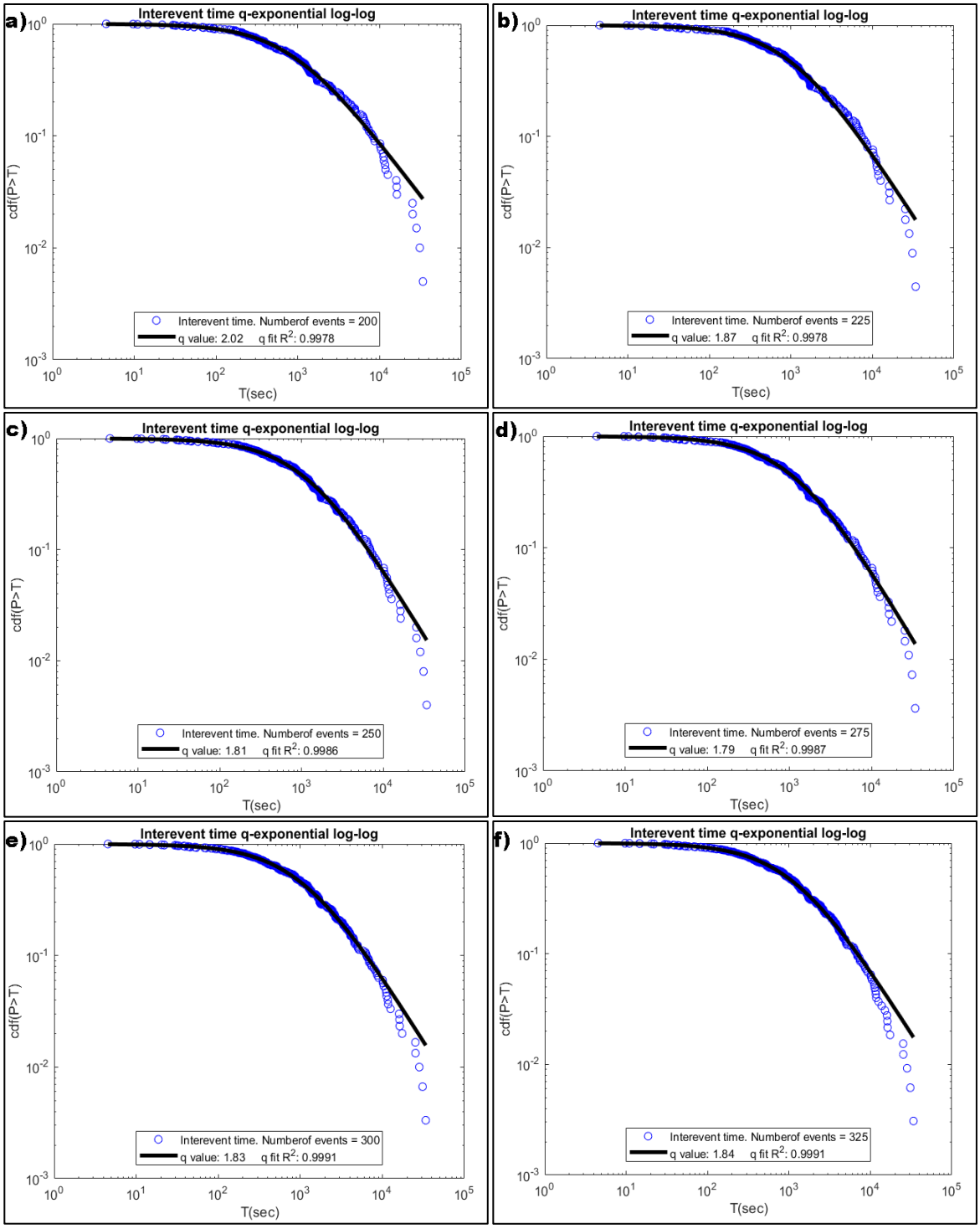

Figure 5.2.40 The normal expanding time window results for 200(a), 225(b), 250(c), 275(d), 300(e), and 325(f) events: a) q=2.02 ±0.0006 to ± 0.0017, b) q=1.87 ±0.006 to ± 0.0016, c) q=1.81 ±0.0004 to ±0.0010, d) q=1.79 ±0.0004 to ±0.0010, e) q=1.83 ±0.003 to = 0.0006 and f) q=1.84 ±0.0003 to ± 0.0006.

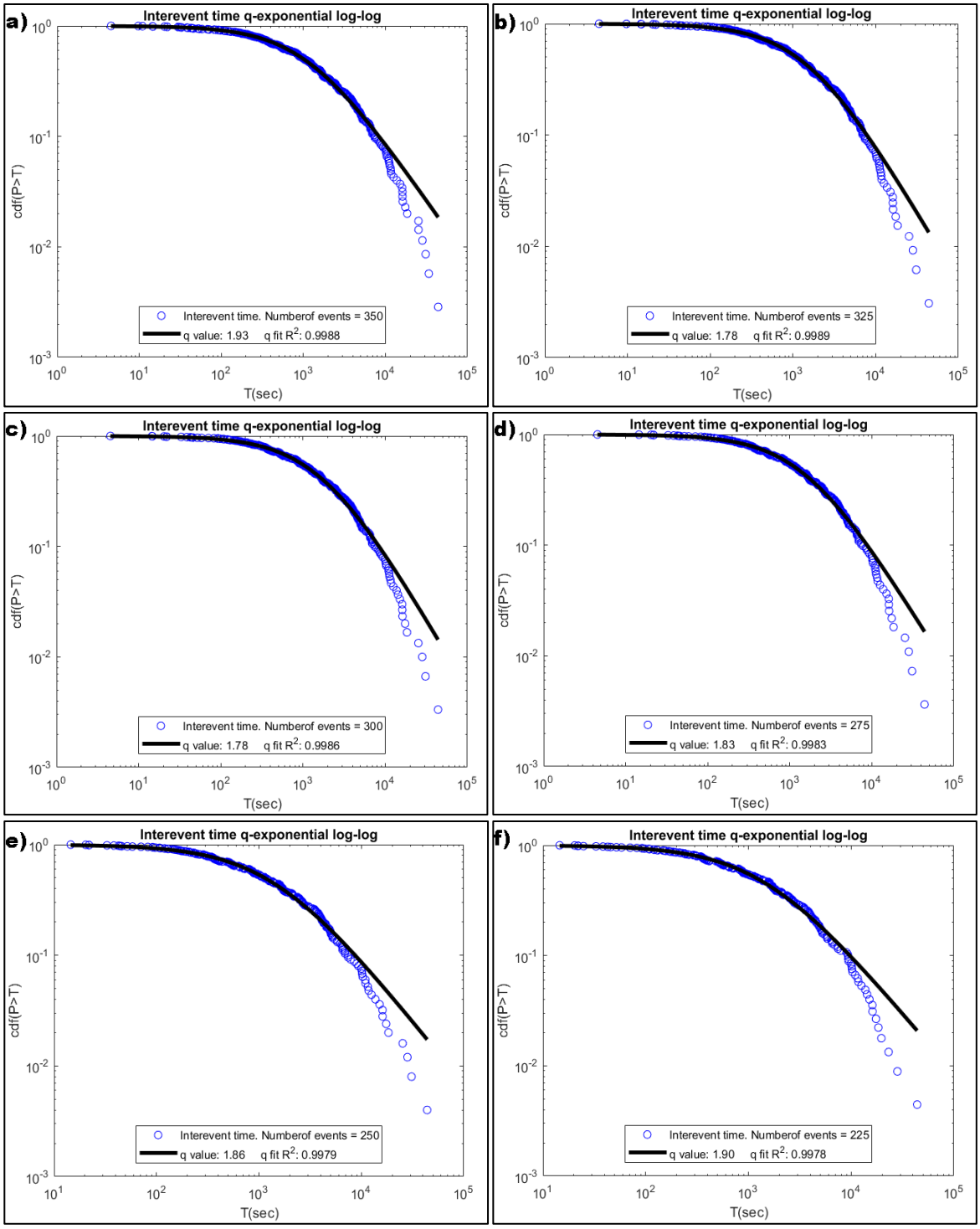

Figure 5.2.41 The reverse expanding time window results for 350(a), 325(b), 300(c), 275(d), 250(e) and 225(f) events:a) *q=1.93 ±0.0004 to ± 0.0008, b) q=1.78 ±0.003 to ± 0.0007, c) q=1.78 ±0.0004 to ±0.0010, d) q=1.83 ±0.0005 to ±0.0012, e) q=1.86 ±0.006 to = 0.0016 and f) q=1.90 ±0.0007 to ± 0.0017.*

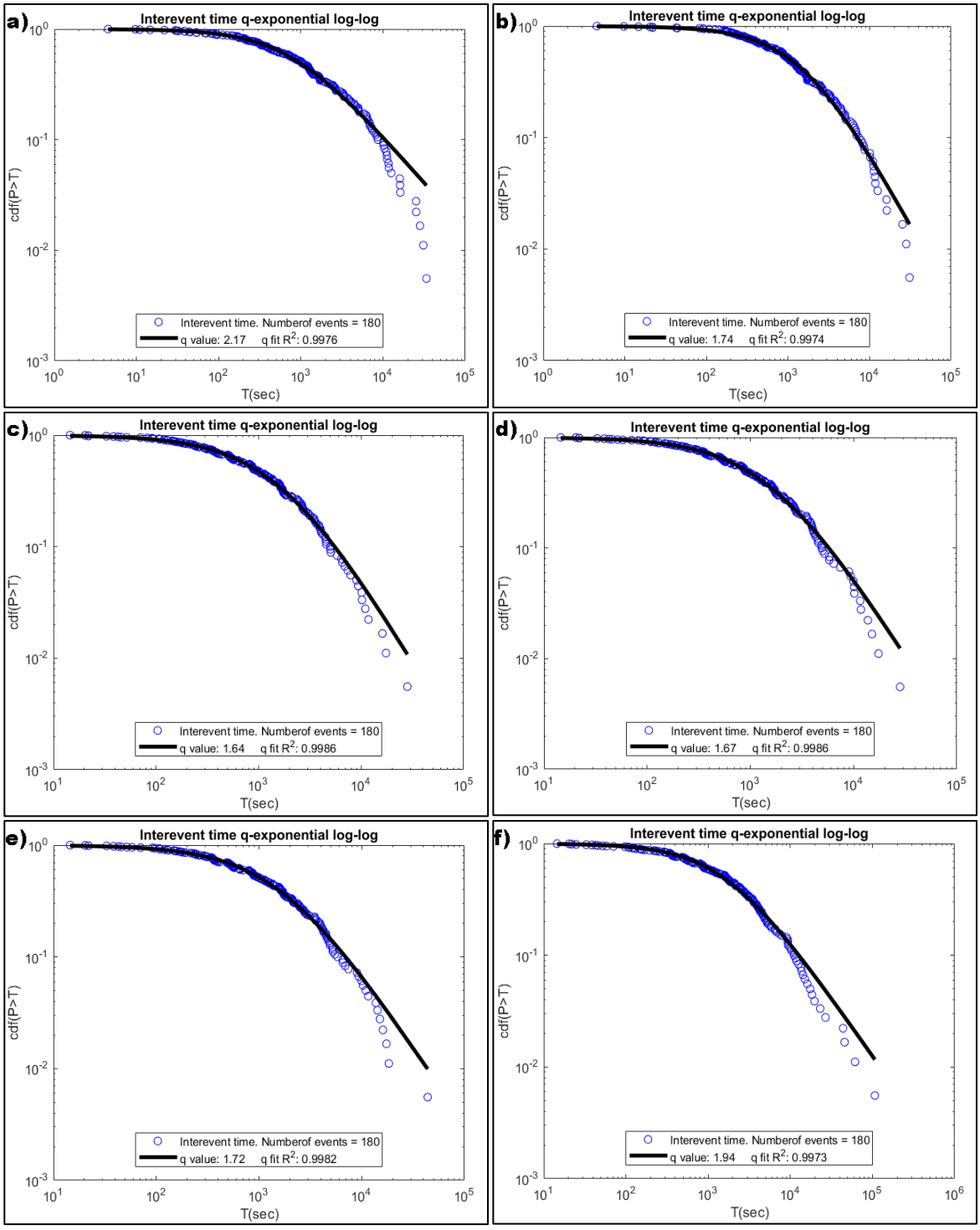

Figure 5.2.42 The moving time window results, time incresse from up to down: q=2.17 ±0.0007 to ±0.0019, q=1.74 ±0.0007 to ±0.0021, q=1.64 ±0.0004 to ±0.0011, q=1.67±0.0004 to ±0.0011, q=1.72 ±0.0005 to ±0.0014, and q=1.94 ±0.0008 to ±0.0022.

The results suggest that the *q-value* has a significant decrease in the time interval after the strongest event of the swarm sequence takes place, then starts to increase again. Another approach to investigate this observation was to separate the available data in 12-hour time windows and examine the temporal attributes of the system before and after the event main event instead of having time windows based on the number of the events (figure 5.2.43). The forward expanding window has been used with two different starting points. The first was from the beginning of the swarm sequence and the second one was from the main event towards the end of the sequence. If the events before the largest activation were removed and the remaining events were treat as an aftershock sequence, then expanding windows suggest that the entropic index increases as the 'aftershock' decays. Unfortunately, the first 12 hours after the main event there was not enough data to produce an accurate fitting in the q-exponential equation.

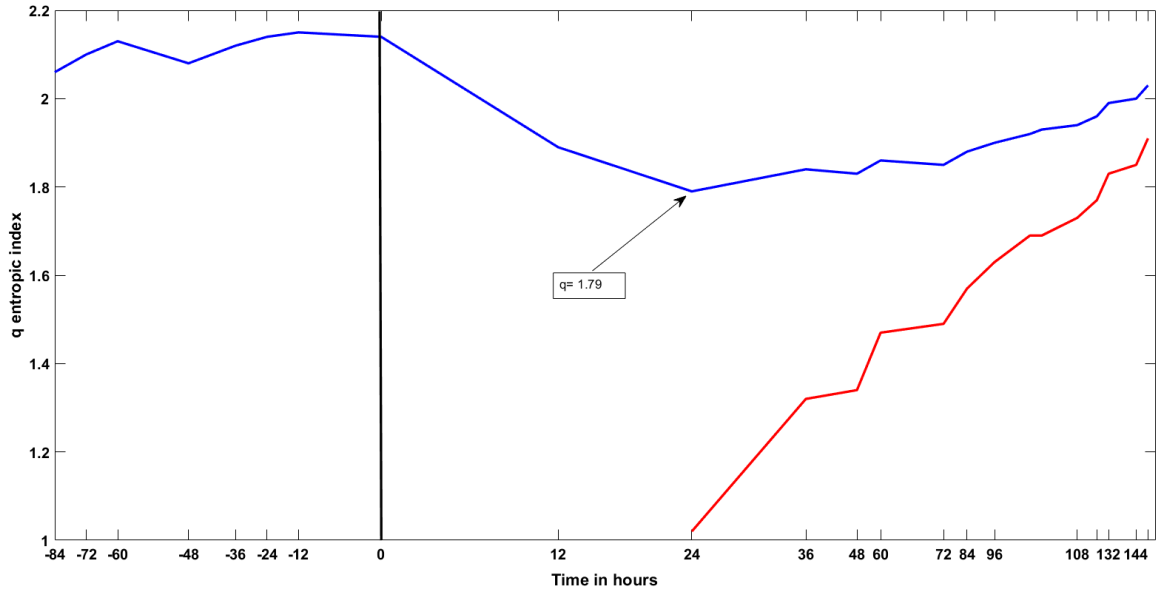

Figure 5.2.43. The distribution of q index with time. The blue line is for the data with starting point at the beginning of the swarm sequence, the black vertical line denotes the time of the main event while red line is the catalogue with starting point set at the main event.

Chapter 6 Discussion

6.1 Seismicity patterns

This thesis examines the seismicity patterns and provides a foundation between the classical physics and the modern ideas of the non-extensive statistical physics. The primary focus was to provide a better understanding of the hazard associated with large earthquakes in subduction zones. These areas exhibit frequent strong events with large amounts of seismic energy release from foreshocks and aftershocks. An effort to understand the large earthquake driving mechanism in the complex geotectonic environment of the South Aegean has been made with remarkable results. Several important questions mention in chapter 1 that could help to understand seismicity and evaluate the hazard associated with large earthquakes and their likelihood have been addressed.

6.1.1 Is there a relationship between foreshock sequences and large earthquakes?

A considerable number of researchers support the observational based hypothesis, that many large earthquakes are preceded by accelerating-decelerating seismicity patterns (see section 3.1.1). The increase in the intermediate magnitude earthquake population has been linked by various independent researchers with the critical point theory where the large event is the end of a preparation process. As seismic energy flows within the fractured volume, it is stored in subvolumes which becomes coherently self-organized and leads to the large event. There is also an alternative approach which claims that foreshock patterns are the result of the stress loading and they does not participate in the large event preparation process (see section 2.2.2). In this point of view, the energy release and storage procedures are ignored, and the large earthquakes are a product of the stress loading parameters, which limits the hazard estimation process.

6.1.2 What is the nature of the relationship between foreshocks and major events in South Aegean?

The quantification of the energy release is the cornerstone to understand these phenomena. The cumulative Benioff strain, which is equal to the cumulative square root of the seismic energy release, has been used to explain the mechanism of the seismicity patterns that have been observed before the large events. To estimate the cumulative Benioff strain, an empirical power law time-to-failure equation has been proposed by Bufe & Varnes (1993) and widely adopted by other scientists (see section 3.1.1). This method has been applied in various cases, mainly as a prediction tool, but not all of the results had the expected outcome for several reasons: Since a sufficient physical model did not existed, the power law fitting results was filtered by statistic indexes which do not reflect the physical mechanism of the earthquake preparation. In addition, the increase in the number and the quality of the seismological stations allowed to have more accurate and complete catalogues. In order to understand and enhance the predictive capabilities of the accelerated seismic release model, different theoretical models and statistical filters have been proposed to increase the stability of the power law fitting (see subchapter 2.2). These efforts did not make the method stable enough, not many successful predictions have been made and the ASR approach has been criticized by Hardebeck, et al. (2008). The last couple years some new ideas were proposed by different researchers but without presenting a satisfactory model yet. To provide a new perspective to this problem, a theoretical framework has been developed (section 3.1.2) which explains with analytical expressions of the physical processes of the energy flow and storage in a stressed faulted crustal volume can be addressed with the novel ideas of the non-extensive statistical physics (section 3.1.2).

6.1.3 Can a generalized model of Tsallis entropy explain the accelerating-decelerating seismicity patterns in South Aegean?

The initial motivation to address the seismicity patterns as a fractal distribution and express with an analytic approach the seismic energy flow in an under stress crustal volume was by the Di Giovambattista & Tyupkin (2001) work. The idea to explain the accelerating seismic

release with complexity and non-extensive statistical physics comes from Vallianatos, et al. (2015) work. As the fault systems and by extension the earthquakes (Mandelbrot, 1983; Scholz & Mandelbrot, 1989; Turcotte, 1997), present a fractal distribution the correlations between the elements of the fault system are described by long-range dependence effects which can be explained by the NESP ideas (Zaslavsky, 1999; Tsallis, 2001; Vallianatos, et al., 2018). The power-law time-to-failure equation that has been used to describe seismicity patterns, the generalized Benioff strain: $\Omega_\xi(t) = \sum_{i=1}^{n(t)} E^\xi(t)$ where $0 \leq \xi \leq 1$, describes a fault system that obeys a hierarchical distribution. In the stressed volume, the system's subvolumes where the seismic energy is stored also follow a hierarchical distribution. As the fractal dimension of the subvolumes is a function of the non-extensive statistical physics entropic parameter *q,* which is a measure of long range interactions and of the complexity of the system, the subvolumes distribution in the critical area is controlled by the Euclidean dimension. In this case, the analytic expressions in 3.1.3 proves that m_ξ is defined by the Euclidean dimension and entropic parameter q and it is independent of ξ *(0≤ξ≤1).* This leads to the conclusion that a common critical exponent m_ξ exists as a function of the non-extensive entropic parameter q. Since m_ξ is independent on the characteristic cases: number of events, Benioff stain and seismic energy release, then it can be used as a criterion of the power law equation stability.

6.1.4 What could be the process for assessing the future earthquake hazards in South Aegean?

The identification of the foreshock patterns has always been a great challenge for researchers. The proposed method in subchapter 3.3 can be used as a new tool to estimate the hazard relates with future large events. In contrast with the previous 'versions' of this method, this one relies more on the physical parameters such as the fractal dimension and the existence of a common critical exponent which is a function of the entropic parameter q. Although the findings help to estimate the risk in the South Aegean and to be able to explain the large earthquake likelihood in the specific area, there are additional aspects that need to be better understood. For instance, the center of the circle in each accelerating seismic release case presented in section 5.1.2, denotes an approximation of the areas

where the events are nucleated before the large event. The shape of the search area is convenient but does not reflect the physical properties of the stressed volume. Although the critical areas were identified successfully, another shape is possible to improve slightly the results. Also, an attempt to correlate the geotectonic environment with the stressed area has been made. The fault plane solution provided in sections 5.2.1 and 5.2.2 for the 2013 strong events, suggests that the activated faults were mainly reverse or thrust. A similar type of fault activated in the 2015 strong event. The focal mechanisms provided by the National Observatory of Athens (NOA, 2018), the Global Centroid-Moment-Tensor (CMT, 2018), and the Helmholtz Centre Potsdam GFZ German Research Centre for Geosciences (GFZ, 2018) suggest a fault with dip between 44 and 74 degrees while the rake is about 120-130 degrees which is a reverse fault with a right lateral strike slip component. Taking the focal mechanisms and locations of the critical areas into account, it is suggested that the foreshocks of these three cases were located in the hanging wall side of the faults (figures 6.1.1 to 6.1.3). Another example of this observation is the 08/01/2006 Kythira Mw 6.4 strong earthquake. According to (NOA, 2018) the fault plane solution of this event has strike=239 dip=49 and rake 79 degrees which was also verified by examining the spatial distribution of the aftershocks. The foreshock sequence has been predicted by (Tzanis & Vallianatos, 2003; Papazachos, et al., 2002) while the critical areas in both studies are located in the western part of the Kythira Island which suggest again that the nucleation occurred in the hanging wall of the reverse fault. It is worth to mention that in the 12/10/2013 study case the foreshock and the aftershocks have a continuity. This suggest that the fault which caused the accelerating seismic crustal deformation, is in the same fault network with the one where the mainshocks occurred. Probably some of the aftershocks are in the fault plane of the foreshock fault. These results demonstrate that the proposed method with the common critical exponent criterion, can be used for assessing the future earthquake hazards in tectonically stressed areas with reverse faults like the front of the of the South Aegean subduction zone.

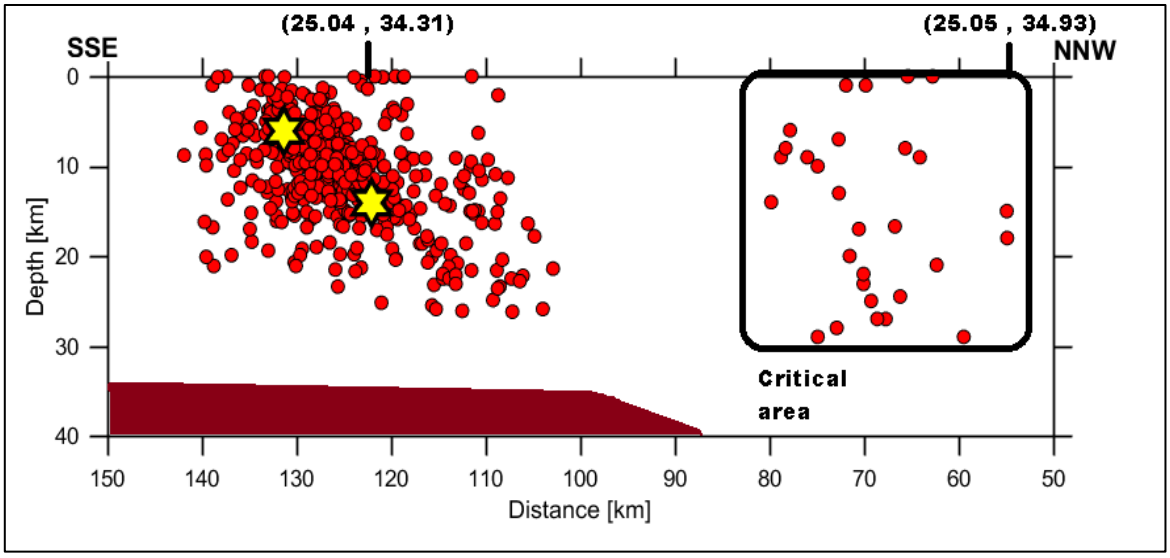

Figure 6.1.1 Cross section of the 15/06/2013 aftershocks sequence as well as the foreshocks that give the best power law fitting results with the common critical exponent. The brown area approximates the subducting plate (figure obtained from Zmap).

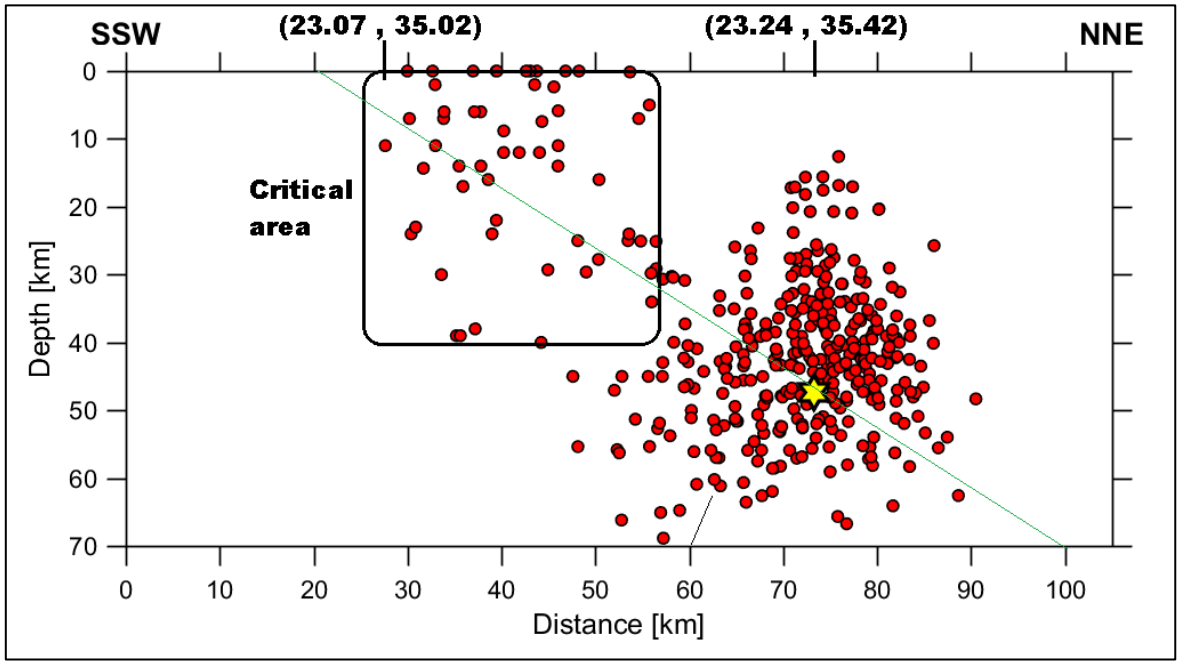

Figure 6.1.2 Cross section of the 12/10/2013 aftershocks sequence as well as the foreshocks that give the best power law fitting results with the common critical exponent. The green line denotes the fault plane of the fault activated in the critical area (figure obtained from Zmap).

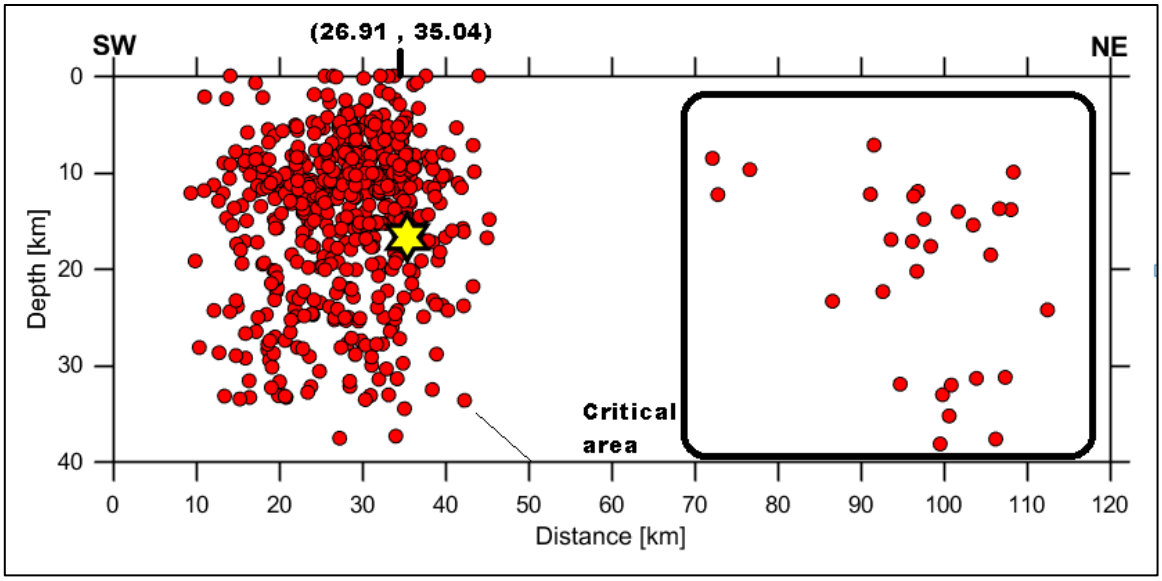

Figure 6.1.3 Cross section of the 16/04/2015 aftershocks sequence as well as the foreshocks that give the best power law fitting results with the common critical exponent (figure obtained from Zmap).

A question that might arise from these results, has to do with the applicability of the proposed method in different geotectonic settings. Is it working only for reverse fault or it explain the nature of a strike slip motion? Although in literature the accelerated seismic release model has been applied in other geotectonic environments such as the San Andreas transform fault (Bufe & Varnes, 1993; Bowman, et al., 1998; Bowman & King, 2001), a further investigation should be carried out with the use of the new proposed common critical exponent m_ξ to validate the limits of the method.

6.1.5 Can the hazard associated with large earthquakes in subduction zones be better understand?

The proposed model uses the common critical exponent m_ξ as a criterion for to identify the seismicity patters. The critical exponent is independent from the measured quantity and reflects the physical parameters of the critical area, such as the Euclidian dimension, the Guttenberg-Richer *b-value* and the extensivity of the system during the large earthquake preparation period. The obtained results suggest that the ideas of non-extensive statistical physics along with the basic principles of physics, explain the physical process that leads to

the critical point, the large earthquake which is an important step to evaluate the future hazard.

6.2 Aftershock-swarm sequences

6.2.1 Can the aftershock sequences be correlated with the foreshock patterns?

The two aftershock sequences of the 2013 strong earthquakes, as well as the 2016 swarm events, have been identified. All the events has been located and relocated with the appropriate crust model (sections 4.4.3 and 4.4.4). The detailed relocation procedure was necessary to study the geotectonic environment and the parameters of the activated faults as well as to be able to apply the non-extensive statistical physics. During the investigation procedure, some new interesting results regarding the temporal attributes of these sequences come out.

The first strong event took place in south from central Crete in the front of the Hellenic Arc (section 5.2.1). Within 29 hours another almost the same magnitude event occurs. These events have special interest as they appear to be the same fault plane according to the cross sections. The Omori's law fitting, the as the *b-value* of the Gutenberg Richter law as well as the cumulative number curve, suggest that the event that occurred in 16/06/2013 is not a large aftershock but it is a second activation (see section 5.2.1). The focal mechanism of the 15/06/2013 presents an activation according to the NOA which is an oblique reverse fault while the 16/06/2013 is presented as a normal fault. These results suggest three possible scenarios:

- The hanging wall of fault after the first upward motion, it has moved backwards by gravitational forces.

- An overextension caused by the intense slip of the first strong event has been elastically 'healed' with a second slip with an opposite direction motion.

- A seismometer that has been used for the estimation of the second moment tensors for the second event and its aftershocks is miss wired. Most of the available fault plane solutions for these two large events, are from in the European-Mediterranean Seismological Centre webpage (EMSC, 2018) presented in figure 6.2.1. According to the focal mechanism every reporting centre agrees that the first event occurred on an oblique reverse fault, while for the second large activation, there is only one out of the nine reported focal mechanisms suggest that the slip occurred on a normal fault. This evidence suggests that probably one of the NOA's stations has a defect. This conclusion is supported by the observation that he moment tensors estimated with the use of the SIVA station present opposite rake while it is the only station that is absent in the first strong event solution.

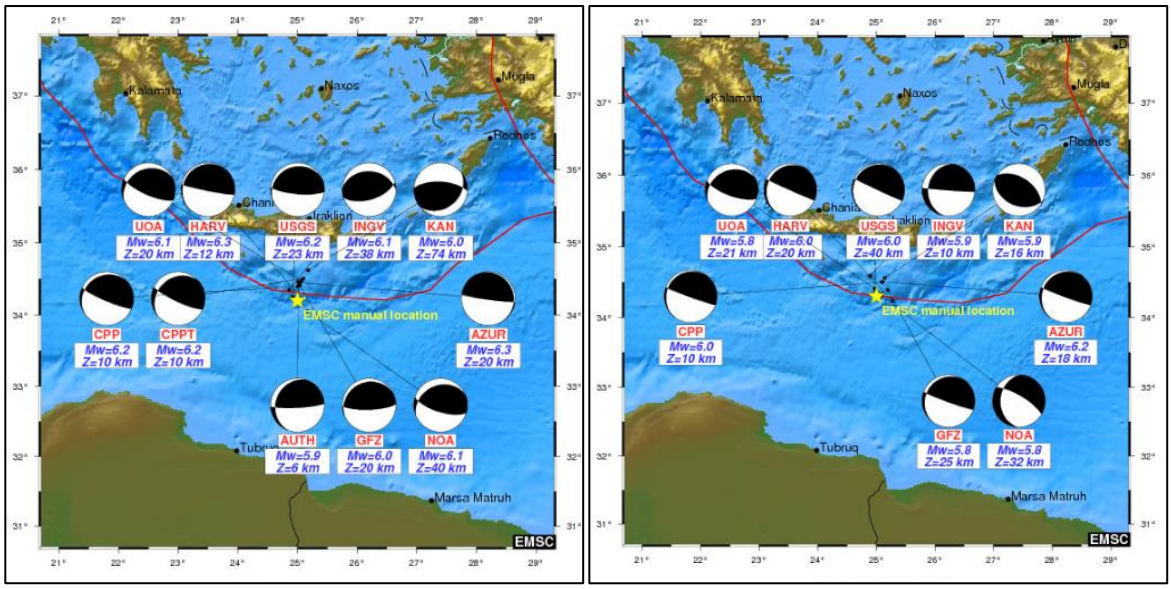

Figure 6.2.1 The reported fault plane solution for the 15/06/2016(a) and the 16/06/2016 events (figures obtained from (EMSC, 2018)).

The second strong event of the 2013 has occurred in a considerable greater depth. Although the 12/10/2013 mainshock has significant larger magnitude than the first large activation of the 2013 in South Aegean, it is noticeable that the number of aftershocks and the magnitude range have lower values compared to the 15/06/2013 event. This can be explained by the intermediate hypocentral depth of the events (>40), where the materials have different

mechanical properties and the plates have uncoupled response (Ruff & Kanamori, 1983). The occurrence of microearthquakes at depth ≈45km located inside the overriding plate have been also mention by (Shaw, 2012). The fault plane solution and the cross section suggest that the 2013 Mw 6.4 has been occurred in reverse fault with very steep dipping angle. The examination of the vertical to strike cross section reveals some characteristic linear features, these hypocentres have been aligned almost perpendicular to the fault plane. The initial though was that this secondary fault could indicate another activation in the same area-fault network. The results from section 5.2.2 (magnitude vs time and cumulative number of events) does not show any new mainshock-aftershocks relation during the decay of the sequence that could explain the existence of this feature. This observation is enhanced if the aftershock catalogue is limited to only present the strongest earthquakes. Plotting the foreshocks along with the aftershocks in the same cross section (figure 6.1.2) gives a new perspective of the activation process. The hypocentres of the foreshocks and some aftershocks appear to have a continuity between them. Probably the fault that has been activated in the critical area before the second strong mainshock of the 2013 is related to the 12/10/2013 fault or it belongs to the same fault network. An interesting observation is that the location, the dip and the depth of the fault that activated before the 12/10/2013 event, have similarities with the AD 365 reverse fault described by the work of Shaw (2012).

The 16/04/2015 aftershocks sequence is still under investigation. About the first 600 aftershocks have been located and relocated, but this number only corresponds to the first 48 hours and the actual total aftershock number is larger. The reason for using this preliminary data is only to have a first image for this fault plane and examine the aftershocks-foreshocks distribution.

6.2.2 Can the aftershock and the swarm type sequence characteristics be explained by complexity theories?

It has been proposed by a number of authors (Abe & Suzuki, 2005; Michas, et al., 2013; Papadakis, et al., 2013; Vallianatos, et al., 2012) that, in an earthquake population with consecutive events, the cumulative distribution of the spatiotemporal properties such as the

interevent times and hypocentral distances can be explained by the non-extensive statistical physics. More specifically the cumulative distribution frequency (CDF) of the interevent times (or hypocentral distances) can be described by a q-exponential distribution. In the 2013 and 2015 sequences that took place in South Aegean, the entropic index q was examined and found to have values larger than 1 for the interevent times of the aftershock sequences, which means in term of Tsallis entropy that that system is sub-additive and the events are strongly correlated (Papadakis, et al., 2013; Michas, et al., 2013; Chochlaki, et al., 2018; Abe & Suzuki, 2005; Vallianatos, et al., 2012). The $q>1$ shows that the frequent interevent times, that have large probability to occur (close to 1) are enhanced (Vallianatos, et al., 2018; Tsallis, 2009). Also, when the entropic index obtains values higher than one, then the q-exponential function behaves as an asymptotical power law (Abe & Suzuki, 2005). The examination of the cumulative distribution of the interevent times for the 2013 aftershock sequences and the 2015 Chania swarm present similar results ($q>1$) as to those report in the literature. A further examination of the q-value with different time window show that the q varies as the aftershock sequences decay. Different techniques have been used to evaluate this information which suggests that the system enhances the frequent interevent times in the end of the energy release process.

A slightly different behaviour has been observed in the swarm sequence, the *q-value* decrease in a time interval after the strongest event of the swarm sequence, before it starts to increase again. The decrease of the entropic index in the middle of the swarm reveals that the rare interevent times are happen more frequently. This behaviour can be attributed to the parallel occurrence of aftershock and swarm events at same time. The *q-value* start to increase after the swarm type events decay, and the system has only aftershocks from the main activation. The quantification of the swarm events in 12 hours-time windows give similar results as expanding-moving window methods but in more detail. These results suggest that about 24 hours after the main activation, the q starts to increase with time as it is observed on the aftershock sequences in sections 5.2.1 and 5.22. Separating and examining the interevent times with two different starting points, it shows that the system becomes additive during the parallel generation of swarm and aftershocks and when the swarms decay, the system becomes non-additive. The cumulative distribution of the interevent times has been investigated with small the time windows which permitted to

observe the q-value variations. In the work of Tsallis (1999); Tsekouras & Tsallis (2005) it is proposed to address the systems that cannot fully explained by the non-extensive statistical mechanics, with a generalized entropic function which instead of using one *q* index value, it will take the entire disruption of the *q-values* into account. The findings on the cumulative distribution of the interevent times as well as the Tsallis (1999); Tsekouras & Tsallis (2005) proposal suggest that the calculation of the *q-value* distribution in some systems is a more appropriate method to examine the extensivity of the system.

6.3 Conclusions

A theoretical model based on energy conservation law and the non-extensive statistical physics has been proposed to explain the foreshock seismicity patterns before the large events in South Aegean. The proposed model proves that the critical exponent is independent from the measured quantity and reflects the physical parameters of the critical area, such as the Euclidian dimension, the Guttenberg-Richer b-value and the extensivity of the system during. The evaluation of the model has been carried out with real data in retrospective analysis on 3 strong magnitude events. Studying additional datasets with this approach is a future work.

A GUI algorithm with improved and faster power law fitting capabilities has been compiled for the purposes of this research. The common critical exponent with values between 0.25 and 0.33 has be used as a criterion to identify accelerated seismic crustal deformation. The identification of the critical area is approximated with a circle which gives good results, but it is possible a different shape to produce a slightly better estimation. A future approach is to try to approximate the critical area with different shapes. Based on the observations acquired from the results, one or more faults has been activated in the critical area. Trying a shape that will include the whole foreshocks fault(s) area could give a better estimation of the critical point parameters. This approach may improve the results from the proposed magnitude estimation relations. Since these equations are more sensitive to the critical exponent and the average Benioff strain, more accurate parameters additional tests are need before it can be used.

The relocation of the aftershocks and swarm sequences permits the detailed examination of the spatial and temporal characteristics of the available events. The activated fault(s) in the critical area is(are) located close to the future shock. Using cross sections in the critical area made possible the examination of the foreshocks-aftershock relation. In the reverse faults the critical area is located on the hanging wall of the fault. In the 12/10/2013 case, the foreshocks appear to be on a fault plane similar with the one descripted by Shaw (2012). A future work is to study more foreshock-aftershock patterns in South Aegean and compare the results with other subduction zones. It is also possible to validate the propose model in transform fault areas.

The cumulative distribution of the temporal characteristics of the system such as the interevent times follows a q-exponential distribution. The aftershock sequences in South Aegean is sub-additive, the events have strong correlations and the high probability interevent times are more likely to occur. The entropic index q in the cumulative distribution of the interevent times, increase with time for the aftershocks sequences, the system becomes more correlated. As the sequence approaches to the end the events follow an exponential distribution which means that the system becomes more random. This is observed in the end of the fitting of the q-exponential plots. In contrast with aftershocks, in the swarm sequence the entropic index q decreases after the main event took place and then it increases again. A further study with more aftershocks-swarm sequences from other areas is necessary to examine this q-variations and better explain the changes in the complexity of the system with time.

References

Earthquake analysis software-seisan, 2018. *Seisan - earthquake analysis software.* [Online]
Available at: http://seisan.info/
[Accessed 12 08 2018].

NEIC, 2018. *National Earthquake Information Center.* [Online]
Available at: https://earthquake.usgs.gov/contactus/golden/neic.php
[Accessed 09 2018].

Thingbaijam, K. K., Mai, P. M. & Goda, K., 2017. New Empirical Earthquake Source-Scaling Laws. *Bulletin of the Seismological Society of America,* 17(5), p. 2225 – 2246.

Abe, S. & Suzuki, N., 2005. Scale-free statistics of time interval between successive earthquakes.. *Physica A,* Volume 350, p. 588 – 596..

Aki, K. & Richards, P. G., 1980. *Quantitative Seismology, Vol. 1..* second ed. s.l.:University Science Books.

Allaby, M., 2013. *A Dictionary of Geology and Earth Sciences.* 4th ed. s.l.:Oxford University Press.

Allen, R., 1978. Automatic earthquake recognition and timing from single traces. *Bull. Seismol. Soc. Am.*, Issue 68, p. 1521–1532.

Ambraseys, N. N., 2001. Reassessment of earthquakes, 1900–1999, in the Eastern Mediterranean and the Middle East. *Geophysical Journal International,* 145(2), pp. 471 - 485.

Amitrano, D., 2012. Variability in the power-law distributions of rupture events, How and why doesb-value change. *European Physical Journal - Special Topics, EDP Sciences,* Volume 205, pp. 199 - 215.

Ammon, C. J., Lay, T. & Simpson, D. W., 2010. Great Earthquakes and Global Seismic Networks. *Seismological Research Letters,* 81(6), pp. 965 - 971.

Baba, A. B. et al., 2000. Unified local magnitude scale for earthquakes of south Balkan area. *Pure Applied Geophysics,* Volume 157, pp. 765 - 783.

Bak, P. & Tang, C., 1989. Earthquakes as a self-organized critical phenomenon. *Journal of Geophysical Research,* Volume 635 - 637, p. 94.

Bak, P., Christensen, K., Danon, L. & Scanlon, T., 2002. Unified scaling law for earthquakes. *Physical Review Letters,* Volume 88.

Becker, D., Meier, T., Bohnhoff, M. & Harjes, H.-P., 2010. Seismicity at the convergent plate boundary offshore Crete, Greece, observed by an amphibian network. *J Seismol,* Volume 14, p. 369–392.

Blake, S. et al., 2008. *An Introduction to: Our dynamic planet.* s.l.:Cambridge University Press.

Boltzmann, L., 1896. *Gastheorie.* Leipzig: Verlag von Johann Ambrosius Barth.

Bonneau, M., Beauvais, L. & Middlemiss, F.-A., 1974. L'unite de Miamou (Crete, Grece) et sa macrofaune d'age Jurassique superieur (Brachiopods, Madreporaires).. *Ann Soc Geol Nord 94*, pp. 71-85.

Bonneau, M. & Fleury, J.-J., 1971. Preisions sur la serie d'Ethia (Crete,Grece): Existence d'un premier flysch mesocretace. *CR Acad Sci Paris 272*, pp. 1840-1842.

Bonneau, M. & Lys, M., 1978. Sur la presence de Permien fossilifere dans l'unite de Vatos (Crete): sa nature interne et l' ampleur des charriages dans l'arc egeen.. *CR Acad Sci Paris 287*, pp. 423--426.

Bormann, P. & Wielandt, E., 2013. Seismic Signals and Noise. In: *New Manual of Seismological Observatory Practice (NMSOP-2).* s.l.:GFZ.

Bowman, D. D. & King, G. C., 2001. Accelerating seismicity and stress accumulation before large earthquakes. 2001, 28, 01 11, pp. 4039-4042.. *Geophysical Research Letters,* Volume 28, pp. 4039 - 4042..

Bowman, D. D. et al., 1988. An observational test of the critical earthquake concept. *J. Geophys. Res,* Volume 103, p. 24359 – 24372..

Bowman, D. D. et al., 1998. An observational test of the critical earthquake concept. *J. Geophys. Res,* Volume 103, p. 24359 – 24372..

Brehm, D. J. & Braile, L. W., 1999. Refinement of the modified time-to-failure method for intermediate-term earthquake prediction. *Journal of Seismology,* Volume 3, p. 121 – 138..

Brief Historical Note - NOA, 2018. *Brief Historical Note.* [Online]
Available at:
http://www.noa.gr/index.php?option=com_content&view=article&id=187&Itemid=490&lang=en
[Accessed 20 06 2018].

British Geological Survey, 2018. [Online]
Available at: http://www.bgs.ac.uk/
[Accessed 06 2018].

Brooklyn College - Geology Department, 2017. *Plate Tectonics, Earthquakes and Volcanoes.* [Online]
Available at: http://academic.brooklyn.cuny.edu/geology/grocha/plates/platetec16.htm
[Accessed 11 2017].

Brouers, F. & Sotolongo-Costa, . O., 2005. Relaxation in heterogeneous systems: A rare events dominated phenomenon. *Physica A: Statistical Mechanics and its Applications,,* 356(2-4), pp. 359 - 374.

Brune, J. N., 1970. Tectonic stress and the spectra of seismic shear waves from earthquakes. *Journal Geophysical Research,* Volume 75, p. 4997 – 5009.

Brunn, J., 1956. Contribution à l'étude du Pinde septentrional et d'une partie de la Macédoine occidentale.. *Annales Géologiques du Pays Helléniques 7*, pp. 1 - 358.

Buck, W. R., 1991. Modes of Continental Lithospheric Extension. *JOURNAL OF GEOPHYSICAL RESEARCH, VOL. 96*, pp. 20161 - 20178.

Bufe, C. G. & Varnes, J. D., 1993. Predictive Modeling of the Seismic Cycle of the Greater San Francisco Bay Region. *Journal of Geophysical Reseach,* Volume 10, pp. 9871 -9883..

California State University, Sacramento State-Tectonic Basins, 2017. *Tectonic Basins.* [Online]
Available at: http://www.csus.edu/indiv/k/kusnickj/geology12/tectonicbasins.html
[Accessed 11 2017].

Castellaro, S., Mulargia, F. & Kagan, Y., 2006. Regression problems for magnitudes. *Geophysical Journal International,* Volume 165, pp. 913-930.

Center for Educational Technologies, 2017. *Transform boundaries.* [Online]
Available at: http://www.cotf.edu/ete/modules/msese/earthsysflr/plates4.html
[Accessed 11 2017].

Chatzopoulos, G., Kouli, M., Papadopoulos, I. & Vallianatos, F., 2018. The Chania (Crete) urban strong ground motion network first results. *16th European Conference on Earthquake Engineering* .

Chatzopoulos, G., Papadopoulos, I. & Vallianatos, F., 2016. The Hellenic Seismological Network of Crete (HSNC): validation and results of the 2013 aftershock sequences. *Advances in Geosciences EGU*, Issue 41, pp. 65-72.

Chingtham, P., Sharma, B. & Chopr, S., 2016. Statistical analysis of aftershock sequences related with two major Nepal earthquakes: April 25, 2015, MW 7.8, and May 12, 2015, MW 7.2. *Annals of Geophysics,* Volume 59.

Chochlaki, K., Vallianatos, F. & Michas, G., 2018. Global regionalized seismicity in view of Non-Extensive Statistical Physics. *Physica A: Statistical Mechanics and its Applications*, pp. 276 - 285.

CMT, 2018. *Global Centroid-Moment-Tensor (CMT).* [Online]
Available at: http://www.globalcmt.org/CMTsearch.html
[Accessed 09 05 2018].

Conrad, C. P. & Lithgow-Bertelloni, C., 2002. How mantle slabs drive plate tectonics.. *Science ,* 207(9).

Contadakis, M. E. et al., 2015. TEC variations over the Mediterranean before and during the strong earthquake (M D6.5) of 12th October2013 in Crete, Greece. *Journal Physics Chemistry of the Earth,.*

corrcoef-MathWorks, 2018. *corrcoef.* [Online]
Available at: https://uk.mathworks.com/help/matlab/ref/corrcoef.html
[Accessed 12 08 2018].

CPPT, 2018. *Centre Polynesien de Prevention des Tsunamis.* [Online]
Available at: http://itic.ioc-unesco.org/index.php?option=com_content&view=featured&Itemid=2441
[Accessed 10 09 2018].

CQ/Cyprus Broadband Seismological Network, 2018. *International Federation of Digital Seismograph Networks..* [Online]
Available at: doi:10.7914/SN/CQ,
[Accessed 09 2018].

Creutzburg, N. & Seidel, E., 1975. Zum Stand der Geologie des praeneogens auf Kreta. *N. Jahrb. Geol. Palaeont. Abh., 149*, pp. 363-383.

datenum-MathWorks, 2018. *datenum.* [Online]
Available at: https://uk.mathworks.com/help/matlab/ref/datenum.html
[Accessed 30 07 2018].

De Chabalier, J. et al., 1992. A detailed analysis of microearthquakes in western Crete from digital three-component seismograms. *Geophys. J. Int.,* Volume 110, pp. 347-360.

De Santis, A., Chianchini, G., Qamili, E. & Frepoli, A., 2010. The 2009 L'Aquila (Central Italy) seismic sequence as a chaotic process. *Tectonophysics,* Volume 496, pp. 44 - 52.

Dercourt, J., 1964. Contribution à l'étude géologique d'un secteur du Péloponnèse septentrional. *Annales Géologiques des Pays Helléniques, 15*, pp. 1 -417.

Dewey, J. F., 2016. Marking 50 years of Wislon cyrcle. *Geoscience Canada,* Volume 43.

Di Giovambattista, R. & Tyupkin, Y., 2001. An analysis of the process of acceleration of seismic energy emission in laboratory experiments on destruction of rocks and before strong earthquakes on Kamchatka and in Italy. *Tectonophysics,* Volume 338, pp. 339 - 351.

Di Giovambattista, R. & Tyupkin, Y., 2004. Seismicity patterns before the M=5.8 2002, Palermo (Italy) earthquake: seismic quiescence and accelerating seismicity. *Tectonophysics,* Volume 384, pp. 243 - 255..

Diehl, T., Kissling, E. & Bormann, P., 2011. Tutorial for consistent phase picking at local to regional distances. In: *New Manual of Seismological Observatory Practice.* s.l.:GFZ.

Dietz, R. S., 1961. Continent and ocean basin evolution by spreading of the sea floor. *Nature*, pp. 854 - 857.

Donaldson, I., 2016. Francis Bacon's comments on the power of negative observations in his Novum Organum, first published in 1620. *Journal of the Royal Society of Medicine*, Volume 109, p. 459–460.

DuMouchel, W. H. & O'Brien, F. L., 1989. *Integrating a Robust Option into a Multiple Regression Computing Environment..* s.l., Proceedings of the 21st Symposium on the Interface. Alexandria. American Statistical Association.

Duni, L., Kuka, S. & Kuka, N., 2010. Local relations for converting ML to Mw in southern-western Balkan region. *Acta Geod. Geoph. Hung.,* Volume 45, pp. 317 - 323.

Dziewonski, A. M., Chou , R. -A. & Woodhouse, . J. H., 1981. Determination of earthquake source parameters from waveform data for studies of global and regional seismicity. *J. Geophys. Res.,* Volume 86, pp. 2825 - 2852.

Earthworm, 2018. *Isti.* [Online]
Available at: http://www.earthwormcentral.org/documentation3/OVERVIEW/1_History.htm#history
[Accessed 30 05 2018].

Efron, B., 1979. Bootstrap methods: Another look at the jackknife. *The Annals of Statistics,* Volume 7, pp. 1-26.

Efron, B. & Tibshirani, R. J., 1993. *An Introduction to the Bootstrap (Chapman & Hall/CRC Monographs on Statistics & Applied Probability.* 1st ed. s.l.:Springer - Science + Busniess Media.

EG/EUROSEISTEST Strong Motion Network, 2018. *https://www.fdsn.org/networks/detail/EG/.* [Online]
Available at: http://euroseisdb.civil.auth.gr/
[Accessed 08 2018].

Ekström, G., Nettles, M. & Dziewonski, . A. M., 2012. The global CMT project 2004-2010: Centroid-moment tensors for 13,017 earthquakes. *Phys. Earth Planet. Inter..,* pp. 1 - 9.

EMSC, 2018. *Euro-Med earthquakes.* [Online]
Available at: https://www.emsc-csem.org/#2
[Accessed 08 2018].

Engdahl, E. R. & Villasenor, A., 2002. Global Seismicity, 1900-1999,. In: *International handbook of Earthquake and Engineering Seismology.* s.l.:Academic Press, pp. 665 - 690.

Entropy, 2018. *Entropy — Open Access Journal.* [Online]
Available at: http://www.mdpi.com/journal/entropy
[Accessed 09 2018].

Epting, M., Kudrass, H., Leppig, U. & Schafer, A., 1972. Geologie der Talea Ori/Kreta. *N. Jb. Geol. Paläont. Abh.,* 141(3), pp. 259 - 285.

Esri, 2018. *ArcGIS Desktop.* [Online]
Available at: http://desktop.arcgis.com/en/
[Accessed 07 2018].

Fassoulas, C., Kilias, A. & Mountrakis, D., 1994. Postnappe stacking extension and exhumation of high-pressure/low temperature rocks in the island of Crete, Greece. *Tectonics, 13*, pp. 127-138.

FDSN, 2018. *International Federation of Digital Seismograph Networks.* [Online]
Available at: http://www.fdsn.org/station_book/
[Accessed 06 08 2018].

FDSN, USGS & IRIS, 2012. SEED Reference Manual.

Fiore, J. M., 2018. *Operational Amplifiers & Linear Intergrates Circuits: Theory and Application.* s.l.:J. Fiore via dissidents.

for-MathWorks, 2018. *for.* [Online]
Available at: https://uk.mathworks.com/help/matlab/ref/for.html?s_tid=srchtitle
[Accessed 14 07 2018].

Fowler, C. M. R., 2005. *The Solid Earth An Introduction to Global Geophysics.* s.l.:Cambridge University Press.

Frankel, H. R., 2012. *The continental drift controversy: Volume I: Wegener and the Early Debate.* ed. New York: Cambridge University Press.

Frisch, W., Meschede, M. & Blakey, R., 2011. *Plate Tectonics Continental Drift and Mountain Building.* s.l.:Springer.

Fuller, W. A., 1987. *Measurement Error Models.* ed. s.l.:John Wiley & Sons.

Fytrolakis, N., 1980. The geological structure of Krete. Probleme, observations and conclusions.. *Habil. Thesis, Nat. Tech. Univ. Athens*, pp. 1-147.

Gamma, E., Helm, R., Johnson, R. & Vlissides, J., 1994. *Design Patterns: Elements of Reusable Object-Oriented Software..* s.l.:Addison-Wesley..

Ganas, A., Oikonomou, I. A. & Tsimi, C., 2013. NOA faults: a digital database for active faults in Greece. *Bulletin of the Geological Society of Greece,* 47(2), pp. 518 - 530.

Ganas, A. & Parsons, T., 2009. Three-dimensional model of Hellenic Arc deformation and origin of the Cretan uplift. *Journal of Geophysical Research,* Volume 114.

Geiger, L., 1912. Probability method for the determination of earthquake epicentres from the arrival time only. *Bull. St. Louis. Univ,* Volume 8, pp. 60-71.

GFZ, 2018. *The Helmholtz Centre Potsdam GFZ German Research Centre for Geosciences.* [Online]
Available at: https://eqarchives.wordpress.com/gfz-moment-tensors/
[Accessed 07 05 2018].

Giardini, D. et al., 2013. *European Seismic Hazard Map for Peak Ground Acceleation, 10% Exceedance Probabilities in 50 years,* s.l.: s.n.

Gibbs, W., 1902. *Elementary Principles in Statistical Mechanics.* s.l.:s.n.

Google, 2018. *Google Earth.* [Online]
Available at: https://earth.google.com/web/

Grotzinger, J. P. & Jordan, Thomas, T. H., 2010. *Understanding Earth.* 6 th ed. s.l.:W. H. Freeman, ISBN 978-1429219518.

Guglielmi, A. V., 2016. Interpretation of the Omori law. *Izvestiya, Physics of the Solid Earth,* Volume 5.

Gutenberg , B. & Richter, . C., 1954. *Seismicity of the Earth and Associated Phenomena.* 2nd ed. s.l.:Princeton University Press.

HA/Seismological Laboratory of the National and Kapodistrian University of Athens, 2018. *International Federation of Digital Seismograph Networks.* [Online]
Available at: doi:10.7914/SN/HA
[Accessed 20 05 2018].

Hanks, T. C. & Kanamori, H., 1979. A moment magnitude scale. *Journal Geophysical Research,* Volume 84, p. 2348–2350.

Hardebeck, J., Felzer, K. R. & Michael, A. J., 2008. Improved tests reveal that the accelerating moment release hypothesis is statistically insignificant. *Journal of Geophysical Research,* Volume 113.

Harrison, C. G., 2016. The present-day number of tectonic plates. *Earth, Planets and Space a Springer open Journal*, pp. 1 - 14.

Hatzfeld, D., Pedotti, G., Hatzidimitriou, P. & Makropoulos, K., 1990. The strain pattern in the western Hellenic arc deduced from a microearthquake survey. *Geophys. J. Int,* Volume 101, pp. 181-202.

HC/Hellenic Seismological Network of Crete, 2018. *International Federation of Digital Seismograph Networks.* [Online]
Available at: https://doi.org/10.7914/SN/HC
[Accessed 21 06 2018].

Helmholtz Centre Potsdam, GFZ German Research Centre for Geosciences, 2018. *SeisComP3.* [Online]
[Accessed 30 05 2018].

Hess, H., 1962. History of ocean basins. *Petrologic Studies: A Volume in Honour of A. E. Buddington*, p. 599–620.

HI/Institute of Engineering Seismology and Earthquake Engineering, 2018. *International Federation of Digital Seismograph Networks..* [Online]
[Accessed 05 06 2018].

History of the Department of Geophysics - AUTH, 2018. *History of the Department of Geophysics.* [Online]
Available at: http://geophysics.geo.auth.gr/new_web_site_2007/EN/history/historyall.html
[Accessed 20 06 2018].

HL/National Observatory of Athens Seismic Network, 2018. *International Federation of Digital Seismograph Networks..* [Online]
Available at: https://doi.org/10.7914/SN/HL
[Accessed 21 06 2018].

Hloupis, G. & Vallianatos, F., 2013. Wavelet-based rapid estimation of earthquake magnitude oriented to early warning,. *IEEE Geosci. Remote S.,* Volume 10, pp. 43 - 47.

Holland, P. W. & Welsch, R. E., 1977. Robust Regression Using Iteratively Reweighted Least-Squares.. *Communications in Statistics: Theory and Methods,* p. 813 – 827.

Holmes, A., 1931. Radioactivity and Earth movement. *Geological Society of Glasgow 18*, pp. 559 - 606.

HP/Seismological Laboratory of the University of Patras, 2018. *International Federation of Digital Seismograph Networks.* [Online]
Available at: ith doi:10.7914/SN/HP
[Accessed 05 06 2018].

HSNC, 2018. *GAIA.* [Online]
Available at: http://gaia.chania.teicrete.gr/uk/?cat=11
[Accessed 05 09 2018].

HT/Aristotle University of Thessaloniki Seismological Network, 2018. *International Federation of Digital Seismograph Networks.* [Online]
Available at: https://doi.org/10.7914/SN/HT
[Accessed 21 06 2018].

Hurukawa, N., 2012. *Practical Analyses of Local Earthquakes,* s.l.: Japan International Cooperation Agency.

Husen, S. & Hardebeck, J., 2010. Earthquake location accuracy. *Community Online Resource for Statistical Seismicity Analysis*.

Husen, S. et al., 2003. Probabilistic earthquake location in complex three-dimensional velocity models: Application to Switzerland. *J. Geophys. Res.,* Volume 108.

Husen, S. & Smith, R., 2004. Probabilistic earthquake relocation in three-dimensional velocity models. *Bull. Seismol. Soc. Am*, pp. 880-896.

idirect, 2018. *VT iDirect.* [Online]
Available at: www.idirect.net
[Accessed 01 2018].

if-MathWorks, 2018. *if.* [Online]
Available at: https://uk.mathworks.com/help/simulink/slref/if.html?s_tid=doc_ta
[Accessed 30 07 2018].

Incorporated Research Institutions for Seismology, 2018. *Software Downloads – PQLX.* [Online]
Available at: https://ds.iris.edu/ds/nodes/dmc/software/downloads/pqlx/
[Accessed 09 06 2018].

Isacks Bryan, O. J. S. L. R., 1968. Seismology and the new global tectonics. *Journal of Geophysical Research 73*, p. 5855–5899.

ISC, 2018. *International Seismological Centre.* [Online]
Available at: http://www.isc.ac.uk/
[Accessed 09 2018].

Johnson, . C. R., Sethares, W. A. & Klein, A. G., 2011. *Software Receiver Design: Build Your Own Digital Communication System in Five Easy Steps.* s.l.:Cambridge University Press.

Johnston, A. C., 1996. Seismic moment assessment of earthquakes in stable continental regions—I. Instrumental seismicity. *Geophysical Journal International,* 124(2), pp. 381-414.

Kagan, . Y. Y., 2010. Earthquake size distribution: Power-law with exponent β=1/2?. *Tectonophysics,* Volume 490, pp. 103-114.

Kagan, Y. Y. & Houston, H., 2005. Relation between mainshock rupture process and Omori's law for aftershock moment release rate. *Geophys. J. Int.,* Volume 163, p. 1039 – 1048.

Kanamori, H., 1977. The energy release in great earthquakes. *Journal of Geophysical research,* 82(20), pp. 2981 - 2987.

Kanamori, H., 1978. Quantification of earthquakes. *Nature,* Volume 271, pp. 411 - 414..

Kanamori, H., 1983. Magnitude scale and quantification of earthquakes. *Tectonophysics*, Issue 93, pp. 185-199.

Karagianni, E. et al., 2002. Rayleigh wave group velocity tomography in the Aegean area. *Tectonophysics,* Volume 358, pp. 187-209.

Karagianni, E. et al., 2005. Shear velocity structure in the Aegean area obtained by inversion of Rayleigh waves. *Geophysical Journal International,* Volume 160, p. 127–143.

Karakostas, V., Karagianni, E. & Paradisopoulou, P., 2012. Space–time analysis, faulting and triggering of the 2010 earthquake doublet in western Corinth Gulf. *Nat Hazards,* Volume 63, p. 1181 – 1202.

Karnik, V., 1996. *Seismicity of Europe and the Mediterranean.* s.l.:Academy of Sciences of the Czech Repuplic .

Kennett, B., 2005. Seismological Tables: ak135. *Research School of Earth Sciences, The Australian National University*.

Kennett, B. & Engdahl, E., 1991. lASPEI 1991 SEISMOLOGICAL TABLES. *Geophys. J. Int.*, Issue 105, pp. 429-465.

Kilias, A., Falalakis, G. & Mountrakis, D., 1999. Cretaceous-Tertiary structures and kinematics of the Serbomacedonian metamorphic rocks and their relation to the exhumation of the Hellenic Hinterland (Macedonia, Greece). *Intern. J. of Earth Scien., 88*, pp. 513-531.

Kilias, A., Fassoulas, C. & Mountrakis, D., 1994. Tertiary extension of continental crust and uplift of Psiloritis metamorphic core complex in the central part of the Hellenic Arc (Crete, Greece). *Geol. Rundsch., 83*, pp. 417-430.

King, G. C. P. & Bowman, D. D., 2003. The evolution of regional seismicity between large earthquakes. *Journal of Geophysical Research: Solid Earth,* Volume 108.

Kissling, E., Ellsworth,, W. L., Eberhart-Phillips, D. & Kradolfer, U., 1994. Initial reference models in seismic tomography. *Journal Of Geophysical Research,* Volume 99, pp. 19.635 - 19.646.

Kissling, E., Kradolfer, U. & Maurer, H., 1995. *Program VELEST USER'S GUIDE - Short Introduction,* s.l.: Institute of Geophysics and Swiss Seismological Service, ETH-Hoenggerberg.

Klein, F. W., 2002. *User's Guide to HYPOINVERSE-2000, a Fortran Program to Solve for Earthquake Locations and Magnitudes,* s.l.: U. S. Geological Survey.

KO/Kandilli Observatory and Earthquake Research Institute, Bosphorus Univ., 2018. *International Federation of Digital Seismograph Networks.* [Online]
Available at: https://doi.org/10.7914/SN/KO
[Accessed 09 2018].

KOERI, 2018. *Kandili Observatory and Earthquake Research Institute.* [Online]
Available at: http://www.koeri.boun.edu.tr/
[Accessed 09 2018].

Kokinou, E. et al., 2006. Crustal velocity models for the wide area of Crete island in the southern Hellenic suduction zone. *First European Conference on Earthquake Engineering and Seismology.*

Kolligri, M. et al., 2014. A homogeneous earthquake catalogue of relocated recent shallow events of the Hellenic arc. *E.G.U. General Assembly Vienna, Austria.*

Kopp,, K.-O. & Ott, E., 1977. Spezialkartierungen in Umkreis neuer Fossilfunde im Trypali- und Tripolitsa-Kalken West-Kretas.. *N Jahrb Geol Palfiontol Mh*, pp. 217-238.

Kourouzidis , M. C., 2003. *Study of seismic sequences in Greece and its contribution to earthquake prediction..* s.l.:Ph.D Thesis Univ. of Thessaloniki.

Krahl, j. et al., 1983. Neue Daten zur Biostratigraphie und zur tektonischen Lagerung der Phyllit-Gruppe und der Trypali-Gruppe auf der Insel Kreta (Griechenland). *Geol Rundsch 72*, pp. 1147-1166.

Kulhanek, O., Persson, L. & Nuannin, P., 2018. Variations of b-values preceding large earthquakes in the shallow subduction zones of Cocos and Nazca plates. *Journal of South American Earth Sciences,* Volume 82, pp. 207 - 214.

Lahr, J. C., 1989. *HYPOELLIPSE/version 2.0; a computer program for determining local earthquake hydrocentral parameters, magnitude, and first motion pattern,* s.l.: U.S. Geological Survey.

Latorre, D. et al., 2016. Assessment of earthquake locations in 3D deterministic velocity models: a case study from the Altotiberina Near Fault Observatory (Italy). *J. Geophys. Res. Solid Earth*.

Le Pichon, X. & Angelier, J., 1979. The hellenic arc and trench system: A key to the neotectonic evolution of the eastern mediterranean area. *Tectonophysics,* Volume 60, pp. 1 - 42.

Le Pichon, X., Chamot-Rooke, N. & Lallemant, S., 1995. Geodetic determination of the kinematics central Greece with respect to Europe. *Journal Geophysical Research,* Volume 100.

Le Pichon, X. & Kreemer, C., 2010. The Miocene-to-Present Kinematic Evolution of the Eastern Mediterranean and Middle East and Its Implications for Dynamics. *Annu. Rev. Earth Planet. Sci.,* Volume 38, pp. 323 - 351.

Lee, W. H. K. & Lahr, J. C., 1972. *HYPO71: a computer program for determining hypocenter, magnitude, and first motion pattern of local earthquakes,* s.l.: U.S. Geological Survey,.

Lei, X., 2003. How do asperities fracture? An experimental study of unbroken asperities. *Earth and Planetary Science Letters,* Volume 213, pp. 347 - 359..

length-MathWorks, 2018. *length.* [Online]
Available at: https://uk.mathworks.com/help/matlab/ref/tscollection.length.html
[Accessed 30 07 2018].

Lermo, J. & Chavez-Garcia, F., 1993. Site effect evaluation on using spectral ratios with only one station. *Bulletin of the Seismological Society of America, VoL 83, No. 5*, pp. 1574-1594.

Lolli, B. & Gasperini, P., 2012. A comparison among general orthogonal regression methods applied to earthquake magnitude conversions. *Geophysical Journal International,* Volume 190, p. 1135–1151.

Lolli, B., Gasperini, P. & Vannucci, G., 2014. Empirical conversion between teleseismic magnitudes (mb and Ms) and moment magnitude (Mw) at the Global, Euro-Mediterranean and Italian scale. *Geophysical Journal International,* 199(2), p. 805–828.

Lomax, A., Berge-Thierry, C., Volant, P. & Virieux, J., 2000. Probabilistic earthquake location in 3-D. *Advances in Seismic Event Location*, pp. 101-134.

lsqcurvefit-MathWorks, 2018. *lsqcurvefit.* [Online]
Available at:
https://uk.mathworks.com/help/optim/ug/lsqcurvefit.html?searchHighlight=lsqcurvefit&s_tid=doc_srchtitle
[Accessed 25 08 2018].

Lyon-Caen, H. et al., 1988. The 1986 Kalamata (South Peloponnesus) earthquake: detailed study of a normal fault, evidences of East-West extension in the Hellenic arc. *J. Geophys. Res. ,* Volume 93, p. 14967 – 15000.

Makris, J., Papoulia, J. & Yegorova, T., 2013. A 3-D density model of Greece constrained by gravityand seismic data. *Geophysical Journal International,* Volume 194, pp. 1 - 17.

Mandelbrot, B. B., 1983. The fractal geometry of nature. San Francisco: Freeman. *W. H. Freeman and Company.*

Maochen, G., 2003. Analysis of source location algorithms Part II: Iterative methods. *J. Acoustic Emission,* Volume 21, pp. 29 - 51.

Mascle , J., Le Quellec, P., Leité, O. & Jongsma, D., 1982. Structural sketch of the Hellenic continental margin between the western Peloponnesus and eastern Crete. *Geology,* 10(2).

MathWorks, 2018. *find.* [Online]
Available at: https://uk.mathworks.com/help/matlab/ref/find.html?searchHighlight=find&s_tid=doc_srchtitle
[Accessed 30 07 2018].

MATLAB-Mathworks, 2018. *MATLAB.* [Online]
Available at: https://uk.mathworks.com/products/matlab.html
[Accessed 25 08 2018].

Mc Namara, D. E. & Boaz, R. I., 2005. Seismic Noise Analysis System,Power Spectral Density Probability Density Function: Stand-Alone Software Package. *United States Geological Survey Open File Report, NO 2005–1438.*

McKenzie, D., 1972. Active Tectonics of the Mediterranean Region. *The Geophysical Journal of the Royal Astronomical Society,* Volume 30, p. 109 – 185.

ME/Montenegrian Seismic Network of the Montenegro Seismological Observatory, 2018. *International Federation of Digital Seismograph Networks.* [Online]
Available at: (DOI) https://doi.org/10.7914/SN/ME
[Accessed 09 2018].

Meier, T. et al., 2004. Seismicity of the Hellenic subduction zone in the area of western and central Crete observed by temporary local seismic networks. *Tectonophysics,* Volume 383, pp. 149-169.

Mercier, J., 1968. Etude geologique des zones Internes des Hellenides en Macedoine centrale.. *Ann. Géologique des Pays Hélléniques, 20,*, pp. 1 - 739.

Michas, G., Vallianatos, F. & Sammonds, P., 2013. Non-extensivity and long-range correlations in the earthquake activity at the West Corinth rift (Greece). *Nonlin. Processes Geophys.,* Volume 20, p. 713 – 724.

Mignan, A., 2008b. The stress accumulation model: Accelerating moment release and seismic hazard. *Advances in Geophysics ,* Volume 49, pp. 67-201.

Mignan, A., 2008. Non-Critical Precursory Accelerating Seismicity Theory (NC PAST) and limits of the power-law fit methodology. *Tectonophysics,* Volume 452, pp. 42 - 50.

Mignan, A., 2012. Seismicity precursors to large earthquakes unified in a stress accumulation framework. *Geophys. Res. Lett,* Volume 39.

Mignan, A., Bowman, D. & King, G., 2006. An observational test of the origin of accelerating moment release before large earthquakes. *Journal of Geophysical Research,* Volume 111.

Mignan, A. & Di Giovambattista, R., 2008. Relationship between accelerating seismicity and quiescence, two precursors to large earthquakes. *Geophysical Research Letters,* Volume 35.

Mignan, A., King, G. & Bowman, D., 2007. A mathematical formulation of accelerating moment release based on the stress accumulation model. *Journal of Geophysical Research,* Volume 112.

Mignan, A. & Woessner, J., 2012. Estimating the magnitude of completeness for earthquake catalogs. *Community Online Resource for Statistical Seismicity Analysis, Version: 1.0,* pp. 1 - 45.

Mogi, K., 1962. Magnitude frequency relations for elastic shocks accompanying fractures of various materials and some rerelated problems in earthquake. *Bull. Earthquake Res. Inst. Tokyo,* Volume 40, p. 831 – 853.

Molchan, G. M. & Dmitrieva, O. E., 1992. Aftershock identification: methods and new approaches. *Geophys. J. Int.,* Volume 109, pp. 501-516.

Mollova, G., 2007. Effect of Digital Filtering in Data Processing of Seismi Acceleration Recors. *EURASIP Journal on Advances in Signal Processing,* p. 9.

Morgan, J. W., 1968. Rises, trenches, great faults, and crustal blocks. *Journal of Geophysics 73*, p. 959–1982.

Mori , J. & Abercombie, R. E., 1997. Depth dependence of earthquake frequency-magnitude distributions in california: Implication for rupture initiation. *Journal of Geophysical Research,* p. 102.

Mountrakis, D., Killias, A., Pavlaki, A. & Fassoulas, C., 2012. Neotectonic study of Western Crete and implications for seismic hazard assessment. *J Virtual Explor ,* Volume 42, pp. 19-20.

Mountrakis, D., 1986. The Pelagonian zone in Greece: A polyphase deformed fragment of the Cimmerian continent and its role in the geotectonic evolution of the Eastern Mediterranean. *Journal of Geology, 94*, pp. 335 - 347.

Mountrakis, D., 2006. Tertiary and Quaternary tectonics of Greece. *Special Paper of the Geological Society of America,* Volume 409, pp. 125 - 136.

Nakamura, Y., 1989. A method for dynamic characteristics estimation of subsurface using ambient noise on the ground surface. *QR Railway Tech Res. Inst.,* Volume 30, p. 25 – 33.

National Oceanic and Atmospheric Administration , 2015. *Marine Trackline Geophysical Data.* [Online]
Available at: https://www.ngdc.noaa.gov/mgg/geodas/trackline.html
[Accessed 10 12 2015].

Nikolintaga, I., Karakostas, V., Papadimitriou, E. & Vallianatos, F., 2007. Velocity models inferred from P-waves travel time curves in South Aegean. *Bulletin of the Geological Society of Greece.*

nlinfit-Mathworks, 2018. *nlinfit.* [Online]
Available at: https://uk.mathworks.com/help/stats/nlinfit.html
[Accessed 11 08 2018].

NOA, 2018. *Hellenic Seismic Network (HL).* [Online]
Available at: http://bbnet.gein.noa.gr/HL/seismicity/seismicity/last-24-hours
[Accessed 06 09 2018].

NOA, 2018. *Revised moment tensors.* [Online]
Available at: http://bbnet.gein.noa.gr/HL/seismicity/mts/revised-moment-tensors
[Accessed 22 08 2018].

norm-MathWorks, 2018. *norm.* [Online]
Available at: https://uk.mathworks.com/help/matlab/ref/norm.html
[Accessed 30 07 2018].

Nuannin, P., Kulhanek, O. & Persson, L., 2012. Variations of b-values preceding large earthquakes in the Andaman-Sumatra subduction zone. *Journal of Asian Earth Sciences,* Volume 61, pp. 237 - 242.

Nuannun, P., Kulhanek, O. & Persson, L., 2005. Spatial and temporal b value anomalies preceding the devastating off coast of NW Sumatra earthquake of December 26, 2004. *Geophysical Research Letters,* 32(1), pp. 1 - 4 .

Obi, E., Abong, A. A. & Ogbeche, J. U., 2017. Empirical Study of the Frequency and Severity of Earthquakes in Taiwan. *Journal of Geosciences and Geomatics,* 5(4), pp. 167 - 172.

Olivieri, M. & Clinton, J., 2012. An Almost Fair Comparison Between Earthworm and SeisComp3. *Seismological Society of America*, Volume 83, pp. 720-727.

Omori, F., 1894. On the after-shocks of earthquakes. *Journal of the College of Science Imperial University of Tokyo,* Volume 7, pp. 111 - 200..

ORFEUS the European Infrastructure for seismic waveform data in EPOS, 2018. *European Integrated Data Archive.* [Online]
Available at: https://www.orfeus-eu.org/data/eida/
[Accessed 06 09 2018].

Ottemöller, . L., Havskov, J. & Voss, P., 2017. *SEISAN: THE EARTHQUAKE ANALYSIS SOFTWARE FOR WINDOWS, SOLARIS, LINUX and MACOSX,* s.l.: s.n.

Pacheco, J. F. & Sykes, L., 1992. Seismic moment catalog of large shallow earthquajes, 1900 to 1989. *Bullentin Seimological Society America,* Volume 82, pp. 1306 - 1349.

Padman, R., 2007. *Computational Physics Self-study guide 2 Programming in Fortran 95.* Michaelmas: University of Cambridge Department of Physics.

Papadakis, G., Vallianatos, F. & Sammonds, P., 2013. Evidence of Nonextensive Statistical Physics behavior of the Hellenic Subduction Zone seismicity. *Tectonophysics,* Volume 608, p. 1037 – 1048.

Papadakis, G., Vallianatos, F. & Sammonds, . P., 2014. A Nonextensive Statistical Physics Analysis of the 1995 Kobe, Japan Earthquake.. *Pure and Applied Geophysics,* Volume 172, pp. 1923 - 1931.

Papadakis, G., Vallianatos, F. & Sammonds, P., 2016. Non-extensive statistical physics applied to heat flow and the earthquake frequency-magnitude distribution in Greece. *Physica A Statistical Mechanics and its Applications,* Volume 456, pp. 135 - 144.

Papadimitriou, E., Karakostas, V., Mesimeri, M. & Vallianatos, F., 2016. The M w6.7 12 October 2013 western Hellenic Arc main shock and its aftershock sequence: implications for the slab properties. *International Journal of Earth Sciences ,* 105(7), p. 2149–2160.

Papadopoulos, G. A., 1986. Long term earthquake prediction in western Hellenic arc,. *Earthquake Pred. Res,* Volume 4, pp. 131 - 137.

Papadopoulos, G. A., 1988. Long-term accelerating foreshock activity may indicate the occurrence time of a strong shock in the Western Hellenic Arc. *Tectonophysics,* 152(09), pp. 179 - 192.

Papadopoulos, G. A., Charalampakis, M. & Fokaefs, A., 2010. Strong foreshock signal preceding the L'Aquila (Italy) earthquake (Mw6.3) of 6 April 2009. *Natural Hazards and Earth System Science,* 10(1), pp. 19-24.

Papadopoulos, G. A., Drakatos, G. & Plessa, A., 2000. Foreshock activity as a precursor of strong earthquakes in Corinthos Gulf, Central Greece. *Physics and Chemistry of the Earth, Part A: Solid Earth and Geodesy,* 25(3), pp. 239 - 245.

Papadopoulos, G. A. & Minadakis, G., 2016. Foreshock Patterns Preceding Great Earthquakes in the Subduction Zone of Chile,, 2016, 173, 10-11, 3247-3271. *Pure and Applied Geophysics,* 173(10 - 11), pp. 3247 - 3271.

Papazachos , C. & Papazachos, B., 2001. Precursory accelerated Benioff strain in the Aegean area. *Annali Di Geofisica,* 44(04), pp. 461 - 474..

Papazachos, B. C., 1990. Seismicity of the Aegean and surrounding area. *Tectonophysics,* Volume 178, p. 287 – 308.

Papazachos, B. C. et al., 2005. Deep structure and active tectonics of the southern Aegan volcanic arc. In: F. M. V. G.E., ed. *The South Aegean Active Volcanic Arc.* s.l.:Elsevier.

Papazachos, B. C., Karakostas, V. G., Papazachos, C. B. & Scordilis, E. M., 2002. The geometry of the Wadati–Benioff zone and lithospheric kinematics in the Hellenic arc. *Tectonophysics*, Issue 319, p. 275–300.

Papazachos, B. C., Papaioannou, C. A., Papazachos, C. B. & Savvaidis, A. S., 1999. Rupture zones in the Aegean region. *Tectonophysics,* Volume 308, p. 205–221.

Papazachos, B. & Papazachos, C., 2000. Accelerated Preshock Deformation of Broad Regions in the Aegean. *Pure appl. geophys.*, Volume 157, p. 1663–1681.

Papazachos, B. & Papazachou, K., 2003. *The earthquakes of Greece..* s.l.:Ziti Publications.

Papazachos, C. B., Karakaisis , G. F., Scordilis, E. M. & Papazachos, B. C., 2005. Global observational properties of the critical earthquake model. *Bulletin of the Seismological Society of America,* 95(10), p. 1841 – 1855..

Papazachos, C. B., Karakaisis, G. F., Savvaidis, A. & Papazachos, B. C., 2002. Accelerating Seismic Crustal Deformation in the Southern Aegean Area. 2002. *Bulletin of the Seismological Society of America,* 92(03), pp. 570 - 580.

Papazachos, C. B. & Nolet, G., 1997. P and S deep velocity structure of the Hellenic area obtained by robust nonlinear inversion of travel times. *J. Geophys. Res,* Volume 102, pp. 8349-8367.

Papazachos, C. B. & Papaioannou, C. A., 1997. The macroseismic field of the Balkan area. *J. Seismology,* Volume 1, pp. 181 - 201.

Peng, Z., 2011. *Basic statistical seismology tutorial.* [Online]
Available at: http://geophysics.eas.gatech.edu/people/bsullivan/tutorial/StatisticalSeismology.htm
[Accessed 2018 08 22].

Piper, D. J. W. & Perissoratis, C., 2003. Quaternary neotectonics of the South Aegean arc. *Marine Geology,* Volume 198, pp. 259 - 288.

Pujol, J., 2003. *Elastic Wave Propagation and Generation in Seismology.* U. S. A.: Cambridge University Press,.

Reasenberg, P., 1985. Second-Order Moment of Central California Seismicity, 1969-1982. *Journal of Geophysical Research ,* Volume 90, pp. 5479-5495.

Reasenberg, P. & Jones, L. M., 1989. Earthquake hazard after a mainshock in California. *Science,* Volume 243, pp. 1173 - 1176..

Ref Tek, 2018. *Refraction Technology, Inc..* [Online]
Available at: www.reftek.com
[Accessed 2018 08 22].

Reilinger, R. et al., 2006. GPS constraints on continental deformation in the Africa–Arabia–Eurasia continental collisional zone and implications for the dynamics of plate interactions. *J. Geophys. Res.,* Volume 111.

Richter, C. F., 1935. An istrumental earthquake magnitude scale. *Bulletin of the Seismological Society of America*, pp. 1 - 32.

Ruff, L. & Kanamori, H., 1983. Seismic coupling and uncouping at subduction zones. *Tectonophysics,* Volume 99, pp. 99 - 117.

Rundle, J. B., Klein, W., Turcotte, D. & Malamud, B. D., 2000. Precursory Seismic Activation and Critical-point Phenomena. *Pure and Apprlied Geophysics,* Volume 157, pp. 2165 - 2182.

Saleur, H., Sammis, C. G. & Sornette, D., 1996. Discrete scale invariance, complex fractal dimensions, and log-periodic fluctuations in seismicity. *J. Geophys. Res.,* Volume 101, pp. 17661 - 17677.

Schmitz, J. E., 2007. *The Second Law of Life: Energy, Technology, and the Future of Earth as We Know It.* s.l.:William Andrew Publishing.

Scholz, C. H., 1968. The frequency-magnitude relation of microfracturing in rock and its relation to earthquakes. *Bulletin of the Seismological Society of America,* Volume 58 , p. 399 – 415.

Scholz, C. H. & Mandelbrot, B. B., 1989. *Fractals in geophysics.* s.l.:Basel: Birkhuser.

Schorlemmer, D. & Wiemer, S., 2005. Microseismicity data forecast rapture area,. *Nature,* Volume 434.

Schorlemmer, D., Wiemer, S. & Wyss, M., 2005. Variations in earthquake-size distribution across different stress regimes. *Nature,* Volume 437, p. 539 – 542.

Scordilis, E. M., 2005. Globally valid relations converting Ms, mb and Mjma to Mw.. *NATO Advanced Research Workshop on Earthquake Monitor and Seismic Hazard Mitigaion in Balkan Countires 11- 17.*

Scordilis, E. M., 2006. Decelerating precursory seismicity in Vrancea. *Tectonophysics,* Volume 420, pp. 509 - 517.

Scordilis, E. M., 2006. Empirical global relations converting MS and mb to moment magnitude. *Journal of Seismology*, Issue 10, pp. 225-236.

Scordilis, E. M., Kementidou, D. & Papazachos, B. C., 2015. Local magnitude calibration of the Hellenic Unified Seismic Network. *J. Seismology.*

Scordilis, E. M., Papazachos, C. B., Karakaisis, G. F. & Karakostas, V. G., 2004. Accelerating seismic crustal deformation before strong mainshocks in Adriatic and its importance for earthquake prediction. *J. Seismology,* Volume 8, p. 57 – 70.

Seber, G. A. F. & Wild, C. J., 2003. *Nonlinear Regression.* s.l.:John Wiley & Sons, Inc.

Seidel, E., 1978. Petrologie der Phyllit-Quarzit-Serie Kretas.. *Habil Schr Tech Univ Braunschweig: 145 S.*

Seidel, E., Kreuzer, H. & Harre, W., 1982. A Late Oligocene/Early Miocene high pressure belt in the external Hellenides. *Geol. Jahrb., E 23,*, pp. 65-206.

Shaw, B., 2012. *Active Tectonics of the Hellenic Subduction Zone.* s.l.:Springer.

Shcherbakov, R. & Turcotte, D. L., 2003. Damage and Self-similarity in fracture. *Theoretical and Applied Fracture Mechanics,* Volume 39, pp. 245 - 258.

Sheriff, R. E., 1984. *Encyclopedic Dictionary of Applied Geophysics.* s.l.:The Society of Exploration Geophysicists.

Shire, S. B. & Richardson, S. H., 2011. Start of the Wilson Cycle at 3 Ga Shown by Diamonds from Subcontinental Mantle. *Science,* Volume 333, p. 434 – 436.

Siedel, E., 1971. Die Pindos-Serie in West Kreta, auf der Insel Gavdos und im Kedros-Gebiet (Mittelkreta).. *Jahrb Geol Pal/iontol Abh 137*, pp. 443-460.

Siedel, E. et al., 1981. Eo-Alpine metamorphism in the uppermost unit of the Cretan nappe system,. *Ppetrology and geochronology : Part 2. Synopsis of high temperature metamorphics and associated ophiolites.,* pp. 351-361.

Siedel, M., Schliestedt, M., Kreuzer, H. & Harre, W., 1977. Metamorphic rocks of Late Jurassic age as components of the ophiolitic melange on Gavdos and Crete (Greece). *Geol Jb B28*, pp. 3-21.

Silva, R., Franca, G. S., Vilar, C. S. & Alcaniz, J. S., 2006. Nonextensive models for earthquakes. *Phys. Rev. E,* Volume 73.

Smith, P. L., 2006. *A Primer for Sampling Solids, Liquids, and Gases.* Philadelphia, Pennsylvania: American Statistical Association and the Society for Industrial and Applied Mathematics.

Sornette, A. & Sornette, D., 1989. Self-organized criticality and earthquakes. *Europhysics Letters,* Volume 9, pp. 197 - 202.

Sornette, A. & Sornette, D., 1990. Earthquake rapture as a critical point: consequences for telluric precursors. *Tectonophysics,* Volume 179, pp. 327 - 334.

Sornette, D. & Sammis, C. G., 1995. Complex critical exponents from renormalization group theory of earthquakes: Implications for earthquake prdictions. *J. Phys,* 1(5), pp. 607 - 619.

Sornette, D. & Vanneste, C., 1992. Dynamics and Memory Effects in Rupture of Thermal Fuse Networks. *Physical Review Letter,* Volume 68, pp. 612 - 616..

Sotolongo-Costa, O. & Posadas, A., 2004. Fragment-asperity interaction model for earthquakes. *Phys. Rev. Lett.,* 92(4).

Stork, A. L., Verdon, J. P. & Kendall, J. -M., 2014. The robustness of seismic moment and magnitudes estimated using. *Geophysical Prospecting,* Volume 62, pp. 862 - 878.

Theye, T., Seidel, E. & Vidal, O., 1992. Carphollite, sudoite and chloritoid in low high-pressure metapelites from Crete and the Peloponnesese Grecce. *Eur J Mineral 4:*, pp. 487--507.

Tiampo, K., Bowman, D. D., Colella, H. & Rundle, J. B., 2008. The Stress Accumulation Method and the Pattern Informatics Index: Complementary Approaches to Earthquake Forecasting. *Pure and Applied Geophysics,* Volume 165, p. 693 – 709.

Tiedemann, H., 1992. Disaster Prevention and Mitigation: Some Prerequisites. *Disaster Prevention and Management: An International Journal,* 1(1).

Timoshenko, S., 1953. *History of the strength of materials.* New York: McGraw-Hill.

Torsvik, T. H. & Cocks, L. R. M., 2012. From Wegener until now: the development of our understanding of Earth's Phanerozoic evolution. *GEOLÓGICA BÉLGICA*, Volume 15/3, pp. 181-192.

Trnkoczy, A., 2009. Understanding and parameter setting of STA/LTA trigger. In: *New Manual of Seismological Observatory Practice.* s.l.:s.n.

Tsallis, C., 1988. Possible generalization of Boltzmann-Gibbs statistics. *Journal of Statistical Physics*, Issue 52, pp. 479-487.

Tsallis, C., 1999. Nonextensive statistics: Theoretical, experimental and computational evidences and connections. *J. Phys.,* Volume 29, pp. 1 - 35.

Tsallis, C., 2001. *Non extensive statistical mechanics and its applications.* s.l.:Springer.

Tsallis, C., 2009. *Introduction to Nonextensive Statistical Mechanics - Approaching a Complex World.* s.l.:Springer.

Tsampas, A., 2006. The critical earthquake model in low seismicity areas of Europe.. *MSc Thesis Aristotle University of Thessaloniki.*

Tsekouras, G. A. & Tsallis, C., 2005. Generalized entropy arising from a distribution of q indices. *Physical Review E,* 71(4).

Turcotte, D. L., 1997. *Fractals and chaos in geology and geophysics.* 2nd ed. s.l.:Cambridge.

Turcotte, D. L. & Schubert, G., 2002. *Geodynamics.* s.l.:Cambridge University Press.

Tzanis, A. & Vallianatos, F., 2003. Distributed power-law seismicity changes and crustal deformation in the SW Hellenic Arc.. *Natural Hazards and Earth System Sciences,* Volume 3, p. 179 – 195.

Tzanis, A., Vallianatos, F. & Makropoulos, K., 2000. Seismic and electrical precursors to the 17-1-1983, M7 Kefallinia earthquake, Greece: Signatures of a SOC system. *Physics and Chemistry of the Earth Part A: Solid Earth and Geodesy,* Volume 25, pp. 281 - 287..

Udias, A., 1999. *Principles of Seismology.* United Kingdom : Cambridge university press.

URAHA FOUNDATION GERMANY E.V., 2017. *How earthquakes work.* [Online]
Available at: http://uraha.de/de/?p=250
[Accessed 11 2017].

USGS - Historical perspective, 1999. [Online]
Available at: https://pubs.usgs.gov/gip/dynamic/historical.html
[Accessed 04 2018].

USGS - Undestanding plate motions, 2017. *Undestanding plate motions.* [Online]
Available at: https://pubs.usgs.gov/gip/dynamic/understanding.html
[Accessed 12 2017].

USGS, 1996. *Focal Mechanism.* [Online]
Available at: https://earthquake.usgs.gov/learn/topics/beachball.php
[Accessed 2018].

Utsu, T., 1961. A statistical study of the occurrence of aftershocks. *Geophysical Magazine,* Volume 30, p. 521 – 605.

Utsu, T., Ogata, , Y. & Matsu'ura, R., 1995. The centenary of the Omori formula for a decay law of aftershock activity. *Journal of Physics of the Earth,* Volume 43, p. 1 – 33.

Vallianatos, F., Michas, G. & Papadakis, G., 2018. *Non Extensive statistical Seismology: An overview , in Complexity of Seismic Time Series .Measurement and Application.* 1st edition, ed. s.l.:Elsevier.

Vallianatos, F., Baziotis, I., Udry, A. & Taylor, L., 2014. Application of non-extensive statistical physics on Martian nakhlites: A first-order approach on the crystal size distribution of pyroxene using Tsallis entropy. *Eur. Phys. Let. (EPL),* Volume 108.

Vallianatos, F., Michas, G. & Papadakis, G., 2014. Non-extensive and natural time analysis of seismicity before the Mw6.4, October12, 2013 earthquake in the South West segment of the Hellenic Arc. *Physica A-Statistical Mechanics and its Applications,* Volume 414, p. 163 – 173.

Vallianatos, F., Michas, G. & Papadakis, G., 2015. *A description of seismicity based on non-extensive statistical physics: A review. In Earthquakes and Their Impact on Society..* s.l.:Springer Natural Hazard.

Vallianatos, F., Michas, G., Papadakis, G. & Sammonds, P., 2012. A non-extensive statistical physics view to the spatiotemporal properties of the June 1995, Aigion earthquake (M6.2) aftershock sequence (West Corinth rift, Greece). *Acta Geophysica,* 60(3), p. 758 – 768.

Vallianatos, F., Papadakis, G. & Michas, G., 2016. Generalized statistical mechanics approaches to earthquakes and tectonics. *Proc. R. Soc. A Math. Phys. Eng. Sci.*.

van Stiphout, T., Zhuang, T. & Marsan, D., 2012. Seismicity declustering,. *Community Online Resource for Statistical Seismicity Analysis,* pp. 1 - 25.

Varnes, D. G., 1989. Predicting Earthquakes by Analyzing Accelerating Precursory Seismic Activity. *Pure applied geophysics,* Volume 130, pp. 661 - 686..

Vine, F. J. M. D., 1963. Magnetic anomalies over oceanic ridges. *Nature*, pp. 947 - 949.

Voight, B., 1989. A relation to describe rate-dependent material failure. *Science,* Volume 243, pp. 200 - 203.

Wadati, K., 1933. On the travel time of earthquake waves.Part. II. *Geophys. Mag. (Tokyo),* Volume 7, pp. 101-111.

Waldhauser, F., 2001. *hypoDD—A Program to Compute Double-Difference Hypocenter Locations,* s.l.: U.S. Geological Survey.

Wang, J. H., 2016. A mechanism causing b- value anomalies prior to a mainshock. *Bulletin of the Seismological Society of America,* Volume 106, pp. 1663 - 1671..

Wielandt, E., 2003. Seismometry. In: K. K. Jennings, ed. *International Handbook of Earthquake and Engineering Seismology.* s.l.:Academic Press.

Wiemer, S. & Wyss., M., 2000. Minimum magnitude of complete reporting in earthquake catalogs: Examples from Alaska, the Western US, and Japan. *Bull. Seismol. Soc. Am., 90, , 2000.,* Volume 90, p. 859 – 869.

Wilson, J. T., 1966. Did the Atlantic close and then re-open?. *Nature vol. 211*, pp. 676 - 681.

Woessner, J., Hardebeck, J. & Haukkson, E., 2010. What is an instrumental seismicity catalog. *Community Online Resource for Statistical Seismicity Analysis*, pp. 1-14.

Wyss, M., Hasegawa, A., Wiemer, S. & Umino, N., 1999. Quantitative mapping of precursory seismic quiescence before the 1989, m7.1 O-sanriku earthquake, Japan. *Annali di Geofisica,* Volume 42, p. 851 – 869.

Wyss, M., Wiemer, S. & Zuniga, R., 2001. *ZMAP A tool for analyses of seismicity patterns,* s.l.: s.n.

Xue, Y., Liu, J., Yu, H. & Liu, S. Q., 2012. Seismicity characteristics of the 2011 M9.0 Tohuku earthquake near the East Cost of Honshu in Japan. *Chinese Science Bulletin,* Volume 57, pp. 886 - 893.

Zager, D., 1972. Sedimentologie der Tripolitsakarbonate im nordlichen Mittelkreta. *Dissertation, Univ Freiburg*, pp. 1--165.

Zandt, G. & Ammon, C. J., 1995. Continental crust composition constrained by measurements of crustal Poisson's ratio. *Nature,* Volume 374, pp. 152 - 154.

Zaslavsky, G. M., 1999. Chaotic dynamics and the origin of statistical laws. *Physics Today,* Volume 52.

zeros-MathWorks, 2018. *zeros.* [Online]
Available at: https://uk.mathworks.com/help/matlab/ref/zeros.html
[Accessed 30 07 2018].

Appendix 1 Foreshock catalogues

Foreshocks of the 15/06/2013 strong event

Longitude Degrees	Latitude *Degrees*	Year	Month	Day	Magnitude M_L	Depth (km)	Hour	Minutes	Seconds
24.9550	34.7860	2012	1	18	2.8	25	10	53	51
24.9050	34.8250	2012	3	8	3.3	9	11	16	3
24.9465	34.8127	2012	3	11	3.2	24.5	22	16	29
25.0416	34.7927	2012	3	16	2.9	23.1	16	11	33
25.0550	34.9340	2012	4	9	2.8	18	17	52	50
25.1320	34.7180	2012	4	9	2.7	14	21	26	52
25.0890	34.7460	2012	7	7	2.8	9	17	17	11
25.0430	34.7760	2012	7	15	2.7	1	20	0	9
24.8943	34.7991	2012	8	7	3.3	16.7	12	57	15
24.9010	34.7720	2012	9	16	2.8	1	5	7	49
24.9100	34.8380	2012	10	17	2.7	0	18	10	36
24.9940	34.8820	2012	12	18	3.4	29	3	39	1
25.0000	34.7060	2012	12	26	2.9	9	12	30	25
24.8990	34.7910	2013	1	1	3.0	27	15	23	59
25.1607	34.7890	2013	1	9	2.7	7	4	8	39
25.0000	34.7600	2013	1	12	2.7	28	8	34	21
24.9440	34.7530	2013	1	30	3.1	13	16	8	16
25.1870	34.8590	2013	2	9	3.0	0	21	51	20
24.9890	34.7130	2013	3	12	2.8	6	2	42	34
24.8790	34.8370	2013	3	18	2.7	21	9	43	21
24.9900	34.7400	2013	4	3	2.7	29	9	57	34
25.1900	34.8300	2013	4	7	2.7	27	13	17	41
24.9600	34.7660	2013	4	17	3.4	20	8	4	4
25.0090	34.7120	2013	4	17	2.9	8	10	13	44
24.9660	34.7360	2013	4	29	2.7	10	7	20	15
25.1980	34.8180	2013	5	10	2.9	22	10	18	59
24.9040	34.9090	2013	5	19	2.9	15	20	51	57
25.0770	34.7940	2013	5	20	2.7	17	12	45	29
24.9920	34.8250	2013	5	24	2.7	8	22	27	57
25.0453	34.3170	2013	6	15	6.0	14.1	16	11	1.8

Foreshocks of the 12/10/2013 strong event

Longitude Degrees	Latitude Degrees	Year	Month	Day	Magnitude ML	Depth (km)	Hour	Minutes	Seconds
23.1718	35.1507	2011	1	4	3.1	7.4	7	11	49
23.2550	35.2073	2011	1	10	2.9	0.1	14	35	14
23.2724	35.1960	2011	1	11	3.5	25	23	35	4
23.0933	35.1482	2011	1	15	3.0	8.8	0	36	38
23.1478	35.0289	2011	1	15	3.1	14.3	19	38	25
23.1470	35.0880	2011	3	15	2.7	38	17	26	47
23.1863	35.2418	2011	4	20	3.0	24	18	47	2
23.2670	35.0930	2011	5	1	3.1	2	20	4	4
23.1800	35.0900	2011	10	5	2.7	24	1	50	14
23.0500	35.1000	2011	10	18	3.0	30	13	12	45
23.1100	35.1800	2011	10	18	3.4	12	13	23	2
23.0160	35.1880	2011	11	8	3.1	12	23	47	25
23.2380	35.2260	2011	11	12	3.2	7	11	38	3
23.1670	35.0840	2011	12	16	2.9	14	19	52	2
23.1600	35.0600	2012	2	6	2.7	39	8	21	45
23.1300	35.0800	2012	2	8	2.7	39	23	22	57
23.0760	35.0230	2012	4	24	2.8	11	22	4	43
22.9940	35.2370	2012	5	31	3.4	0	6	7	36
23.0960	35.0690	2012	6	22	2.8	2	0	54	38
23.0161	35.2448	2012	8	14	3.0	2.3	8	23	18
23.2690	35.1270	2012	8	25	2.9	0	2	44	38
23.0460	35.2340	2012	9	1	2.7	14	0	41	42
23.1400	35.1540	2012	9	18	2.8	0	10	31	5
23.2581	35.1243	2012	9	25	3.5	5.9	9	27	40
23.2130	35.1940	2012	10	6	3.1	16	22	13	13
23.0720	35.2430	2012	10	22	3.5	25	1	40	44
22.9800	35.1720	2012	11	28	2.8	0	16	46	24
23.1470	35.0430	2012	12	20	2.8	11	19	22	1
23.2100	35.1300	2013	1	31	2.7	40	8	43	30
23.1700	35.1700	2013	2	8	2.7	11	2	27	24
23.1700	35.100	2013	2	8	2.9	22	2	31	40
23.1840	35.0330	2013	2	8	3.3	7	2	34	55
22.9530	35.1140	2013	3	3	2.8	7	11	56	55
23.1540	35.0990	2013	3	31	3.0	16	5	53	59
23.0160	35.1420	2013	3	31	3.0	17	11	0	8

23.1040	35.0620	2013	4	23	2.7	0	17	36	35
23.1320	35.1020	2013	5	28	3.2	6	11	12	7
23.0430	35.1410	2013	5	31	3.3	6	4	41	39
23.1060	35.0910	2013	6	13	3.0	14	1	56	58
23.0230	35.2020	2013	6	24	2.7	12	2	24	29
23.1170	35.0310	2013	7	3	3.8	24	21	3	35
23.1230	35.0330	2013	7	13	3.4	23	23	45	13
23.0180	35.0780	2013	8	1	2.9	0	4	3	49
23.1480	35.2050	2013	8	7	2.7	0	0	50	55
23.1550	35.2810	2013	8	21	2.7	5	20	46	17
23.1870	35.0320	2013	8	30	3.0	6	17	55	35
23.1950	35.0870	2013	9	5	3.2	0	3	48	30
23.2020	35.0840	2013	9	8	3.2	0	6	44	57
23.1330	35.1530	2013	9	21	3.2	0	14	46	41
23.2425	35.4218	2013	10	12	6.2	47.4	13	11	53.6

Foreshocks of the 16/04/2015 strong event

Longitude Degrees	Latitude Degrees	Year	Month	Day	Magnitude ML	Depth (km)	Hour	Minutes	Seconds
27.4400	35.4400	2011	1	16	3	12	12	39	40
27.4800	35.4000	2011	1	21	3.1	32	21	42	46
27.5997	35.4755	2011	5	21	2.7	31.3	13	3	9
27.5785	35.4045	2012	1	11	2.6	38.2	20	9	31
27.4535	35.5523	2012	6	13	2.5	10	8	42	24
27.4493	35.5513	2012	12	16	2.5	13.9	12	4	17
27.4608	35.5317	2012	12	16	2.5	13.8	12	42	5
27.4993	35.4817	2012	12	16	3.2	15.5	13	41	14
27.6115	35.4583	2013	5	6	2.5	37.7	4	14	49
27.5652	35.4330	2013	6	24	2.5	14.1	11	33	50
27.5113	35.3642	2013	7	2	2.5	22.4	11	8	3
27.3138	35.4963	2013	10	14	2.8	20.3	1	36	11
27.3530	35.3740	2014	2	3	2.6	23.4	5	18	18
27.4090	35.5268	2014	4	23	2.8	31.4	11	48	44
27.4735	35.3660	2014	4	25	2.5	12.3	17	47	22
27.5257	35.5617	2014	8	8	2.5	24.3	11	18	45

27.5138	35.3732	2014	9	19	3.1	17	23	11	54
27.5535	35.3815	2014	9	20	2.7	17.2	1	48	16
27.3802	35.4833	2014	10	31	3.1	17.7	14	58	1
27.4895	35.4123	2014	12	31	2.7	12.5	18	32	35
27.3892	35.4090	2015	1	3	3	7.2	16	2	22
27.3640	35.5053	2015	1	25	2.8	33.1	9	30	32
27.4195	35.5397	2015	1	29	2.5	18.6	4	57	41
27.3178	35.5033	2015	3	15	2.5	14.9	16	44	1
27.5405	35.4330	2015	4	2	3.4	35.3	8	49	45
27.5873	35.4142	2015	4	6	3.1	32.1	10	59	42
26.9172	35.0435	2015	4	6	6.1	5.3	18	7	42

Appendix 2 Aftershock- swarm catalogues

Catalogue of 15/06/2013 sequence

Longitude Degrees	Latitude Degrees	Year	Month	Day	Magnitude M_L	Depth (km)	Hour	Minutes	Seconds	Horizontal error	Vertical error
25.0453	34.3170	2013	6	15	6.0	14.1	16	11	1.8	0.5	0.7
24.8785	34.3775	2013	6	15	3.7	26.1	16	16	29.8	1.1	1.3
24.8968	34.3077	2013	6	15	3.9	15.5	16	20	33.2	0.8	0.6
25.0768	34.2818	2013	6	15	3.4	15.1	16	21	50.4	1.4	1.2
25.0825	34.3115	2013	6	15	4.5	12.6	16	23	17.0	0.7	0.6
24.9765	34.2278	2013	6	15	4.7	9.7	16	28	56.1	0.8	0.9
25.0250	34.4602	2013	6	15	3.4	22.2	16	39	15.4	0.8	0.9
24.9102	34.2582	2013	6	15	3.2	3.6	16	41	5.6	0.8	1.1
24.9192	34.2632	2013	6	15	3.3	15.6	16	42	24.5	1.3	1.1
25.0163	34.2398	2013	6	15	3.9	7.9	16	45	48.3	0.6	0.8
24.9787	34.2548	2013	6	15	3.7	11.2	16	47	29.9	1.0	0.6
24.9467	34.2193	2013	6	15	3.3	12.6	16	49	13.4	1.0	0.8
24.9877	34.2562	2013	6	15	4.5	8.2	16	51	14.0	0.9	1.0
24.9338	34.4745	2013	6	15	3.8	21.4	16	54	16.5	1.1	0.9
24.8082	34.2263	2013	6	15	3.2	4.5	16	56	27.5	1.1	1.5
25.0920	34.4422	2013	6	15	4.4	24.9	16	59	37.9	1.1	1.8

25.0947	34.3200	2013	6	15	2.8	11.5	17	5	50.5	2.1	2.0
25.1075	34.1927	2013	6	15	3.4	7.5	17	9	29.1	0.9	1.0
25.0593	34.2643	2013	6	15	3.9	11.3	17	10	39.4	1.0	0.7
24.8400	34.2432	2013	6	15	2.6	8.9	17	14	21.3	1.3	1.4
24.9973	34.2683	2013	6	15	3.0	7.7	17	19	13.8	0.8	0.8
25.0302	34.2585	2013	6	15	4.8	8.0	17	22	6.3	0.7	0.9
25.0032	34.2330	2013	6	15	3.9	13.6	17	24	13.2	1.4	1.5
25.0003	34.2968	2013	6	15	3.2	13.8	17	26	22.2	2.5	3.9
24.8818	34.1873	2013	6	15	3.2	0.0	17	28	37.6	0.9	1.1
25.0715	34.4108	2013	6	15	3.5	12.6	17	29	21.8	1.0	1.3
24.8805	34.2747	2013	6	15	2.7	8.4	17	38	38.0	0.8	0.8
25.0350	34.2528	2013	6	15	2.9	11.7	17	41	26.7	1.5	0.8
24.9835	34.2588	2013	6	15	2.9	7.6	17	44	38.0	0.5	0.7
24.9230	34.2968	2013	6	15	2.6	11.3	17	46	59.0	0.9	0.6
25.0393	34.2953	2013	6	15	3.1	9.5	17	52	54.4	0.6	0.6
25.0505	34.2773	2013	6	15	3.2	9.7	17	54	21.3	0.6	0.8
25.0030	34.4342	2013	6	15	3.2	23.4	17	55	56.4	0.8	0.7
24.9445	34.2120	2013	6	15	3.3	9.9	17	57	50.3	1.2	1.0
25.1038	34.2022	2013	6	15	2.6	6.6	18	0	20.8	0.9	1.0
24.9337	34.2698	2013	6	15	2.8	8.7	18	2	9.3	1.1	1.1
24.9948	34.3445	2013	6	15	2.8	9.1	18	5	46.3	0.9	1.1
25.1975	34.3293	2013	6	15	3.0	12.1	18	8	14.3	1.4	0.8
24.9890	34.2158	2013	6	15	2.6	16.1	18	12	7.1	1.4	1.8
25.1673	34.3042	2013	6	15	2.9	12.8	18	15	41.1	0.7	0.7
25.0083	34.2493	2013	6	15	3.3	5.1	18	16	49.0	0.5	0.6
24.9252	34.1435	2013	6	15	3.1	16.8	18	20	26.7	1.2	1.7
25.2465	34.3355	2013	6	15	2.5	10.6	18	22	19.4	1.6	1.6
25.0088	34.2125	2013	6	15	3.9	8.0	18	24	50.3	0.5	0.5
24.8027	34.3008	2013	6	15	2.7	20.3	18	27	21.8	1.8	1.4
25.0940	34.2630	2013	6	15	3.3	7.8	18	33	36.5	0.9	1.1
24.9672	34.2732	2013	6	15	3.0	11.0	18	36	15.0	1.1	1.3
24.8785	34.2205	2013	6	15	2.7	9.2	18	38	41.0	1.2	1.2
24.9963	34.2922	2013	6	15	3.3	10.4	18	41	13.8	1.4	1.2
25.0332	34.2568	2013	6	15	3.0	11.3	18	42	34.7	1.0	0.7
25.0065	34.2677	2013	6	15	3.2	6.6	18	43	58.6	0.6	0.8
25.1465	34.3072	2013	6	15	2.5	9.9	18	45	21.4	1.2	1.0
25.0648	34.3967	2013	6	15	2.8	19.9	18	46	52.9	0.9	1.2
25.0275	34.2730	2013	6	15	3.7	7.8	19	2	5.2	0.6	0.7
24.9093	34.2808	2013	6	15	3.2	9.2	19	3	11.6	0.8	0.9
25.0340	34.2713	2013	6	15	4.4	8.2	19	4	4.7	0.6	0.6
25.0592	34.2535	2013	6	15	2.6	13.7	19	10	22.9	1.0	1.2
25.0062	34.2578	2013	6	15	3.5	11.1	19	14	3.7	1.0	0.7
24.9012	34.2090	2013	6	15	2.7	0.1	19	17	1.2	1.8	1.9

24.9847	34.2175	2013	6	15	3.2	8.8	19	18	34.9	0.9	0.9
25.0592	34.1800	2013	6	15	3.5	13.7	19	21	56.4	2.5	2.3
25.0953	34.3047	2013	6	15	3.7	11.4	19	27	41.8	0.8	0.5
24.9555	34.2443	2013	6	15	2.5	9.5	19	31	33.8	1.0	0.8
25.0285	34.3395	2013	6	15	3.4	15.9	19	36	7.8	0.7	0.8
24.9408	34.4353	2013	6	15	3.2	22.5	19	37	31.0	1.0	1.2
24.9763	34.1917	2013	6	15	2.8	3.3	19	42	11.5	1.7	2.1
24.9925	34.1845	2013	6	15	2.6	5.7	19	53	57.3	1.7	1.6
25.0545	34.2940	2013	6	15	2.4	10.4	20	6	21.9	2.0	1.9
24.9640	34.3133	2013	6	15	2.6	25.2	20	12	44.2	1.2	1.4
24.9517	34.2783	2013	6	15	3.2	7.4	20	13	40.1	0.9	1.2
24.9712	34.2270	2013	6	15	2.8	3.1	20	15	44.5	1.0	1.2
25.0723	34.2835	2013	6	15	2.8	8.8	20	20	24.6	0.6	0.6
24.9175	34.1892	2013	6	15	2.5	1.5	20	22	22.3	1.0	1.2
24.9507	34.2610	2013	6	15	2.7	13.6	20	24	42.5	1.0	1.1
24.9217	34.2220	2013	6	15	3.0	15.5	20	25	33.8	1.5	1.3
24.9560	34.2667	2013	6	15	2.7	7.3	20	29	36.6	1.3	1.7
25.1232	34.2687	2013	6	15	2.3	7.8	20	36	19.8	1.0	1.2
25.0452	34.3067	2013	6	15	3.2	10.1	20	47	22.2	0.7	0.9
25.0168	34.2618	2013	6	15	3.3	6.8	20	48	24.1	0.7	0.7
24.8918	34.2802	2013	6	15	3.1	13.0	20	57	4.3	1.0	0.7
24.8642	34.2767	2013	6	15	2.9	9.6	20	57	38.0	1.8	1.6
24.9017	34.2348	2013	6	15	2.5	15.9	21	2	17.6	1.2	0.9
25.0197	34.2908	2013	6	15	2.7	8.0	21	5	59.4	1.1	1.1
25.0195	34.2830	2013	6	15	3.5	8.6	21	8	22.8	0.8	0.7
25.0330	34.3118	2013	6	15	3.5	10.7	21	14	57.5	0.5	0.6
24.9432	34.2608	2013	6	15	2.6	8.6	21	26	27.9	0.9	0.9
25.0465	34.4003	2013	6	15	2.5	20.8	21	31	35.4	1.7	1.7
25.0025	34.2388	2013	6	15	2.4	8.5	21	34	14.2	1.3	1.3
25.0402	34.3018	2013	6	15	3.3	8.7	21	37	24.7	1.8	1.6
24.9703	34.4483	2013	6	15	2.5	22.8	21	41	46.0	1.2	0.9
25.0722	34.3465	2013	6	15	3.9	11.8	21	51	58.0	1.1	0.7
25.0120	34.2908	2013	6	15	3.1	8.2	21	58	9.8	0.8	0.9
24.9397	34.2895	2013	6	15	2.5	0.5	22	7	47.1	1.7	1.8
24.9840	34.3063	2013	6	15	2.2	11.9	22	10	25.4	1.2	0.8
25.0300	34.2753	2013	6	15	3.1	6.9	22	19	44.5	0.5	0.7
25.1680	34.3360	2013	6	15	2.3	9.3	22	26	15.3	1.3	1.5
25.0678	34.2705	2013	6	15	2.8	8.7	22	27	7.9	1.0	1.0
25.0970	34.4212	2013	6	15	2.0	10.0	22	28	39.9	5.4	7.3
24.7937	34.2635	2013	6	15	2.6	9.6	22	43	23.0	1.6	1.4
25.0077	34.3692	2013	6	15	2.6	20.1	22	48	34.0	1.3	0.9
24.9027	34.2175	2013	6	15	2.6	8.6	22	53	59.7	0.9	0.9
25.0140	34.2647	2013	6	15	3.1	9.3	22	56	4.6	0.7	0.7

25.0022	34.2378	2013	6	15	3.2	6.0	23	5	44.9	0.8	1.1
25.0335	34.2228	2013	6	15	2.4	13.9	23	8	45.4	2.4	2.4
25.0482	34.2980	2013	6	15	2.8	8.9	23	9	27.2	0.7	0.7
25.0188	34.2833	2013	6	15	2.7	10.1	23	16	21.3	0.9	0.8
25.0973	34.2490	2013	6	15	2.5	12.7	23	17	26.0	1.3	1.1
24.9338	34.1752	2013	6	15	2.3	4.6	23	19	60.0	0.8	1.0
24.9378	34.2852	2013	6	15	2.5	10.4	23	29	8.0	1.3	1.2
24.9570	34.3003	2013	6	15	2.5	10.0	23	29	56.5	1.1	1.5
24.9797	34.2503	2013	6	15	3.1	12.8	23	30	34.6	1.4	1.0
25.0242	34.2975	2013	6	15	3.3	10.7	23	34	5.6	0.7	0.8
25.2108	34.3172	2013	6	15	2.6	12.0	23	37	54.9	1.5	1.0
24.9300	34.1982	2013	6	15	2.5	0.0	23	38	50.1	3.0	2.8
25.1112	34.2287	2013	6	15	2.3	4.3	23	47	39.2	2.0	2.4
25.2350	34.3173	2013	6	15	2.8	16.5	23	57	31.4	1.3	1.4
24.9845	34.2985	2013	6	16	2.4	9.1	0	6	44.0	1.0	0.8
24.9782	34.2102	2013	6	16	2.3	6.9	0	8	13.3	0.8	0.9
25.2137	34.3073	2013	6	16	2.8	10.1	0	12	6.0	1.2	1.3
24.9205	34.1805	2013	6	16	2.6	5.8	0	12	37.7	1.9	2.6
25.1558	34.4023	2013	6	16	2.2	12.0	0	25	58.5	2.2	2.7
25.1105	34.3267	2013	6	16	2.3	11.7	0	33	11.2	1.1	0.6
24.9353	34.2282	2013	6	16	2.8	9.3	0	40	18.3	1.3	1.1
24.9650	34.2473	2013	6	16	2.7	11.9	0	44	31.1	0.8	0.4
24.9485	34.3080	2013	6	16	2.9	8.8	0	46	21.3	1.1	1.0
25.0975	34.2672	2013	6	16	2.3	11.1	0	48	14.2	0.8	0.7
25.0363	34.2870	2013	6	16	2.5	9.5	0	49	22.1	0.8	0.7
25.0988	34.3802	2013	6	16	4.1	20.7	0	53	38.0	0.7	0.6
24.9827	34.2663	2013	6	16	2.4	7.3	0	58	25.1	1.4	1.1
25.1563	34.2947	2013	6	16	2.3	18.5	0	59	14.5	1.2	1.6
25.1140	34.2158	2013	6	16	2.1	6.6	1	0	18.9	1.5	1.5
25.1625	34.2783	2013	6	16	2.5	10.5	1	5	13.1	1.6	1.2
24.9547	34.2585	2013	6	16	2.8	5.7	1	6	4.2	1.5	1.1
25.1070	34.2953	2013	6	16	2.3	7.2	1	8	25.7	1.0	1.2
25.0673	34.2945	2013	6	16	3.5	10.4	1	10	36.2	0.4	0.5
25.0082	34.2893	2013	6	16	2.3	8.9	1	17	52.1	1.3	0.9
25.0278	34.4462	2013	6	16	2.3	11.3	1	23	56.2	1.7	1.3
25.1038	34.2638	2013	6	16	2.1	15.1	1	25	13.7	1.3	2.0
24.9172	34.2643	2013	6	16	3.4	6.9	1	29	49.4	1.6	1.6
24.9808	34.2808	2013	6	16	2.4	14.9	1	36	9.3	0.9	0.9
25.1832	34.2065	2013	6	16	2.3	10.5	1	37	1.5	0.7	0.6
25.0452	34.2875	2013	6	16	2.9	12.9	2	13	38.2	0.8	0.5
24.9563	34.1418	2013	6	16	2.1	8.7	2	17	29.0	5.4	4.3
25.0168	34.2870	2013	6	16	2.8	11.4	2	19	43.2	0.7	0.5
24.9698	34.2957	2013	6	16	2.8	8.8	2	29	48.9	1.0	0.9

24.9163	34.2607	2013	6	16	2.5	7.2	2	35	3.3	1.1	1.1
25.1252	34.1862	2013	6	16	2.1	8.8	2	37	41.3	1.1	0.8
25.0863	34.4272	2013	6	16	2.0	15.0	2	39	46.1	1.3	1.9
24.7835	34.3147	2013	6	16	2.3	9.2	2	42	44.7	1.5	1.9
24.8713	34.2587	2013	6	16	2.8	4.9	2	49	56.3	1.2	1.7
24.9883	34.2330	2013	6	16	2.2	20.7	2	58	0.1	1.4	2.1
25.0942	34.2695	2013	6	16	2.3	10.2	3	8	41.1	1.0	1.2
25.0585	34.3025	2013	6	16	2.9	12.2	3	18	11.9	0.8	0.7
24.9647	34.2750	2013	6	16	2.5	9.0	3	21	25.4	1.4	1.5
25.0427	34.4413	2013	6	16	2.7	13.6	3	25	53.3	0.9	1.2
25.0317	34.2363	2013	6	16	2.7	4.6	3	27	7.1	0.7	0.8
25.0282	34.2502	2013	6	16	3.0	6.2	3	30	3.3	0.6	0.6
24.7927	34.2500	2013	6	16	2.3	10.1	3	37	3.2	1.6	1.8
25.1472	34.3365	2013	6	16	2.2	14.3	3	40	24.1	1.3	1.6
24.9387	34.2233	2013	6	16	2.7	15.2	3	56	24.0	1.4	1.0
24.9607	34.2632	2013	6	16	2.4	1.8	4	1	56.6	0.8	1.5
25.0718	34.2818	2013	6	16	2.8	13.1	4	12	7.7	1.1	0.8
25.0402	34.2860	2013	6	16	2.6	10.9	4	20	7.6	1.2	1.2
25.0637	34.3103	2013	6	16	4.1	8.5	4	32	49.2	0.6	0.7
25.0475	34.3375	2013	6	16	2.9	14.0	4	59	6.6	1.5	2.1
25.0595	34.4407	2013	6	16	3.2	21.6	5	2	58.5	0.8	0.9
24.9512	34.4085	2013	6	16	2.1	11.5	5	19	58.0	2.0	1.4
25.0153	34.3878	2013	6	16	2.2	14.4	5	23	7.7	1.5	2.1
25.0950	34.3770	2013	6	16	2.0	11.0	5	34	47.3	2.1	3.7
25.2570	34.3202	2013	6	16	2.2	9.5	5	46	59.4	2.0	3.2
24.9948	34.2752	2013	6	16	2.4	6.5	5	57	33.9	1.4	1.6
25.2280	34.3308	2013	6	16	2.2	10.9	6	18	45.8	1.6	2.4
25.0438	34.3788	2013	6	16	2.0	13.3	6	22	20.5	1.2	1.7
25.1282	34.2907	2013	6	16	2.2	5.1	6	31	42.7	1.5	2.0
25.0967	34.2882	2013	6	16	2.3	6.4	6	33	45.0	1.9	2.7
24.9473	34.3300	2013	6	16	2.2	4.3	6	35	59.1	1.8	3.4
24.9035	34.2433	2013	6	16	2.8	7.9	6	58	34.6	1.6	1.8
24.9190	34.3230	2013	6	16	2.5	14.3	7	14	41.6	2.3	2.8
25.0387	34.3378	2013	6	16	3.5	13.5	7	26	42.6	0.7	0.6
25.1190	34.2800	2013	6	16	2.2	4.7	7	30	46.6	1.0	1.4
24.9715	34.2677	2013	6	16	2.2	5.7	7	38	14.8	0.8	1.0
24.9780	34.2638	2013	6	16	2.9	6.3	7	44	49.8	0.9	0.8
24.9303	34.2737	2013	6	16	2.5	7.8	8	13	7.2	1.1	1.1
25.1742	34.3185	2013	6	16	2.2	5.3	8	14	22.9	1.1	1.3
25.0733	34.3435	2013	6	16	4.2	15.7	8	15	17.8	0.6	0.7
25.0792	34.2018	2013	6	16	2.3	8.6	8	23	46.7	0.7	0.7
25.0042	34.2442	2013	6	16	2.5	5.4	8	38	20.2	0.6	0.7
25.0747	34.2775	2013	6	16	3.0	11.0	9	15	23.7	0.9	1.0

24.8662	34.3047	2013	6	16	2.3	12.1	9	21	28.4	1.2	0.8
25.0977	34.2842	2013	6	16	3.0	11.3	9	41	53.1	0.9	0.6
25.1025	34.2855	2013	6	16	2.4	9.3	10	4	19.5	1.2	1.6
25.0492	34.2490	2013	6	16	2.6	10.1	10	16	21.6	0.7	0.8
25.0888	34.2785	2013	6	16	2.3	13.3	10	26	55.0	0.7	0.7
25.0655	34.2673	2013	6	16	2.5	9.8	10	33	17.6	1.0	1.0
25.1115	34.3117	2013	6	16	2.2	5.3	10	48	24.1	1.0	1.1
24.9755	34.2977	2013	6	16	2.8	11.3	11	13	54.0	1.4	0.8
25.0513	34.2748	2013	6	16	2.3	7.7	11	25	21.0	1.1	1.3
24.9857	34.2722	2013	6	16	2.2	21.5	11	48	52.8	2.8	4.1
25.0550	34.3600	2013	6	16	2.6	16.9	12	15	6.7	0.7	0.5
25.1037	34.2497	2013	6	16	2.7	13.9	12	16	20.9	1.2	1.2
24.9707	34.2807	2013	6	16	2.7	4.7	12	21	32.4	1.3	2.0
25.0923	34.2437	2013	6	16	3.3	9.5	12	25	37.3	1.9	2.4
25.1217	34.2965	2013	6	16	2.7	13.8	12	29	35.3	1.4	1.3
24.9180	34.3592	2013	6	16	2.2	19.4	12	32	14.3	1.8	2.6
25.0898	34.2723	2013	6	16	2.5	10.3	12	56	31.1	1.1	0.9
25.2413	34.3602	2013	6	16	2.2	0.1	13	1	38.3	2.8	2.9
25.0373	34.2468	2013	6	16	2.2	6.9	13	20	27.1	1.0	1.0
25.0838	34.2785	2013	6	16	3.0	8.5	13	28	4.5	0.9	0.8
24.9693	34.3042	2013	6	16	3.1	9.6	14	1	41.7	1.1	1.3
24.9655	34.2820	2013	6	16	2.4	15.5	14	4	58.8	1.8	1.1
24.9648	34.2488	2013	6	16	2.4	12.6	14	36	35.3	1.3	1.0
25.0900	34.2977	2013	6	16	3.0	7.7	14	43	3.2	1.3	1.3
24.9100	34.2443	2013	6	16	2.5	3.1	15	5	20.9	0.7	1.0
25.2605	34.2877	2013	6	16	2.5	6.4	15	44	56.5	1.8	2.2
24.9412	34.2853	2013	6	16	2.6	9.1	16	49	23.7	1.3	1.1
24.9075	34.2403	2013	6	16	2.4	4.4	17	4	39.5	1.5	2.7
25.0172	34.4390	2013	6	16	3.0	20.4	17	10	39.3	1.0	1.0
25.0802	34.3427	2013	6	16	2.6	19.2	17	53	40.4	1.5	2.9
25.1032	34.4180	2013	6	16	2.2	18.6	18	4	50.1	2.3	3.8
25.2365	34.3377	2013	6	16	2.3	14.9	18	22	28.3	2.1	2.8
25.0978	34.3142	2013	6	16	2.5	13.3	18	54	32.3	1.3	0.9
25.3277	34.2102	2013	6	16	2.2	21.1	19	3	5.7	3.4	5.4
25.1533	34.3053	2013	6	16	2.2	13.7	20	6	50.3	1.8	1.8
25.0085	34.2497	2013	6	16	2.6	7.2	20	22	15.0	0.8	0.9
25.1117	34.3883	2013	6	16	2.7	23.2	20	56	58.6	2.1	3.3
25.1935	34.2900	2013	6	16	2.3	11.6	21	0	13.9	1.9	1.3
25.2150	34.2485	2013	6	16	2.2	8.5	21	2	32.7	1.8	2.4
25.0372	34.1540	2013	6	16	2.2	16.2	21	20	23.9	1.3	1.5
25.0148	34.2657	2013	6	16	2.3	6.6	21	26	19.9	2.2	6.3
24.9000	34.2838	2013	6	16	2.8	1.0	21	33	42.8	1.9	2.0
25.0635	34.2835	2013	6	16	3.3	7.4	21	35	3.3	0.8	1.1

25.0925	34.2398	2013	6	16	5.9	6.1	21	39	4.8	0.6	0.8
25.1032	34.2945	2013	6	16	4.4	13.7	21	42	41.7	0.8	0.7
25.0768	34.2682	2013	6	16	4.9	13.5	21	43	17.0	0.9	0.9
25.0700	34.2208	2013	6	16	3.6	3.8	21	46	33.4	0.7	0.8
24.9958	34.2633	2013	6	16	4.5	9.5	21	47	36.1	1.2	1.0
25.0313	34.2475	2013	6	16	3.7	19.2	21	51	4.1	1.2	1.7
24.9872	34.1640	2013	6	16	3.2	26.5	21	52	0.4	2.9	5.5
25.0172	34.4702	2013	6	16	3.1	17.8	21	54	35.3	2.0	2.5
25.1222	34.4043	2013	6	16	3.0	21.2	21	57	13.8	2.3	2.3
25.0837	34.2688	2013	6	16	3.1	6.5	21	58	33.8	1.1	1.1
25.0993	34.2627	2013	6	16	2.9	8.7	22	0	8.3	0.6	0.6
25.0108	34.3790	2013	6	16	2.9	18.6	22	1	34.7	1.8	3.1
25.0548	34.2838	2013	6	16	3.1	10.2	22	4	16.5	1.0	0.8
24.9145	34.2055	2013	6	16	3.2	4.6	22	5	48.5	1.3	1.5
24.9777	34.4187	2013	6	16	2.6	9.3	22	8	56.5	1.6	2.4
24.9823	34.2665	2013	6	16	2.7	10.6	22	11	1.4	0.6	0.7
24.8998	34.4127	2013	6	16	2.4	16.4	22	14	5.8	1.6	2.4
25.0977	34.2942	2013	6	16	3.2	11.9	22	15	27.2	1.2	0.8
25.0517	34.2973	2013	6	16	3.0	8.5	22	20	36.3	0.6	0.7
25.0790	34.3312	2013	6	16	3.2	12.8	22	21	49.4	0.7	0.6
25.1523	34.2733	2013	6	16	3.3	9.8	22	23	50.9	1.8	1.9
24.9528	34.2598	2013	6	16	2.5	12.0	22	28	5.6	1.4	0.7
24.9498	34.2345	2013	6	16	2.9	5.3	22	30	25.5	1.2	1.3
24.9105	34.1593	2013	6	16	3.3	19.9	22	31	8.7	2.8	3.7
25.0462	34.2913	2013	6	16	2.5	9.3	22	33	14.0	0.9	0.9
24.9593	34.2342	2013	6	16	3.0	7.6	22	34	8.0	1.2	1.6
25.0487	34.2413	2013	6	16	2.9	7.7	22	37	59.1	0.5	0.7
25.1308	34.3778	2013	6	16	2.4	18.6	22	41	52.6	2.1	3.4
25.1133	34.3660	2013	6	16	2.4	15.4	22	44	1.8	1.0	0.9
25.2478	34.3843	2013	6	16	2.5	6.4	22	48	23.3	2.1	3.1
25.1762	34.3505	2013	6	16	2.4	15.9	22	56	33.9	0.9	0.5
25.2507	34.2830	2013	6	16	2.5	9.5	22	57	21.6	2.2	2.7
25.0547	34.3552	2013	6	16	2.5	15.9	22	58	42.1	1.0	0.9
25.0613	34.2222	2013	6	16	2.8	3.5	23	3	48.7	0.9	1.1
25.1100	34.2803	2013	6	16	2.9	7.1	23	4	58.5	1.0	1.2
25.0053	34.3690	2013	6	16	3.1	25.5	23	5	23.8	1.7	2.4
25.0202	34.2135	2013	6	16	2.8	4.4	23	8	31.2	1.1	1.4
25.0427	34.3103	2013	6	16	2.7	10.1	23	10	8.3	2.5	2.9
25.0740	34.2890	2013	6	16	2.9	10.1	23	11	11.8	0.7	0.6
25.2075	34.3215	2013	6	16	2.7	11.1	23	13	59.9	1.1	0.8
24.9965	34.2787	2013	6	16	3.2	14.0	23	15	0.4	1.3	1.2
25.0750	34.2792	2013	6	16	2.6	4.0	23	16	38.0	1.2	1.4
25.1730	34.2370	2013	6	16	2.5	12.9	23	20	41.0	1.0	0.9

24.9397	34.3313	2013	6	16	2.9	10.0	23	22	22.3	2.0	2.9
25.1060	34.3008	2013	6	16	2.8	11.3	23	25	3.2	1.5	1.0
25.0252	34.2270	2013	6	16	2.5	6.2	23	26	43.0	0.8	0.9
25.0588	34.3082	2013	6	16	2.5	8.0	23	30	40.9	0.9	1.1
25.1035	34.2397	2013	6	16	2.3	1.4	23	33	20.8	1.1	1.8
25.0678	34.2462	2013	6	16	3.4	13.3	23	35	27.1	0.7	0.6
25.0192	34.2860	2013	6	16	2.9	8.1	23	40	9.3	1.4	1.4
24.9968	34.2753	2013	6	16	3.8	5.0	23	43	35.5	1.0	1.3
25.0298	34.2465	2013	6	16	2.8	5.0	23	51	44.5	1.1	1.4
25.0420	34.2697	2013	6	16	3.9	8.3	23	53	35.3	1.3	1.5
25.1903	34.2973	2013	6	16	2.3	11.7	23	57	31.5	1.6	1.0
25.0675	34.2252	2013	6	17	2.5	5.5	0	4	7.5	1.6	2.0
25.0558	34.1588	2013	6	17	2.2	9.9	0	5	11.4	7.6	0.9
25.0263	34.1687	2013	6	17	2.1	7.0	0	19	47.1	3.8	4.7
25.1290	34.2353	2013	6	17	2.5	2.4	0	21	35.5	1.0	1.1
25.0167	34.2653	2013	6	17	2.6	2.3	0	23	32.4	1.1	2.1
25.0282	34.2498	2013	6	17	2.3	2.1	0	28	50.4	2.1	3.8
25.0758	34.2735	2013	6	17	2.2	2.7	0	36	58.4	4.0	9.9
25.1133	34.3007	2013	6	17	2.4	12.7	0	38	30.1	0.9	0.9
25.1380	34.2763	2013	6	17	2.2	2.7	0	46	5.4	1.8	2.6
25.0332	34.2587	2013	6	17	2.1	9.9	0	48	26.2	0.8	0.7
25.1603	34.3073	2013	6	17	2.8	11.5	0	57	56.0	0.9	0.5
25.0958	34.2242	2013	6	17	2.3	12.3	0	59	21.7	1.3	0.9
25.1778	34.2968	2013	6	17	2.6	12.9	1	2	6.3	2.1	2.0
25.0062	34.4095	2013	6	17	2.5	15.3	1	3	57.4	1.1	1.0
25.1130	34.2535	2013	6	17	3.4	12.4	1	7	53.8	1.0	0.7
24.9375	34.1828	2013	6	17	2.4	15.2	1	15	15.6	1.0	0.7
25.1132	34.4248	2013	6	17	2.6	21.6	1	17	40.3	10.1	4.1
25.1297	34.2742	2013	6	17	2.9	12.0	1	20	27.7	1.0	0.7
25.0298	34.2875	2013	6	17	2.3	9.9	1	22	54.1	1.5	1.4
25.0105	34.2382	2013	6	17	2.6	8.2	1	28	30.2	1.1	1.1
25.0627	34.4163	2013	6	17	2.6	9.5	1	48	58.1	0.8	1.4
25.0170	34.3357	2013	6	17	2.4	20.4	1	51	51.5	2.1	1.5
24.9375	34.2960	2013	6	17	3.2	14.7	1	53	43.1	0.9	0.9
25.0828	34.2077	2013	6	17	2.3	11.6	1	57	3.6	1.3	1.1
25.0845	34.4092	2013	6	17	2.3	11.8	2	3	47.6	1.9	1.9
25.0478	34.4070	2013	6	17	2.0	11.1	2	12	33.6	1.4	1.5
25.0128	34.2335	2013	6	17	2.2	3.7	2	16	50.4	1.4	2.2
25.2157	34.4417	2013	6	17	2.9	0.0	2	18	9.4	5.1	5.9
25.0077	34.2398	2013	6	17	2.2	11.9	2	24	6.0	3.2	3.5
25.1662	34.4323	2013	6	17	2.1	15.0	2	30	51.1	1.8	0.2
24.9892	34.2665	2013	6	17	2.6	5.5	2	33	33.0	1.0	1.2
25.0137	34.3110	2013	6	17	2.3	7.4	2	34	16.4	2.2	3.5

25.1073	34.3473	2013	6	17	3.4	12.6	2	44	35.3	0.5	0.6
25.1305	34.2928	2013	6	17	3.9	10.2	2	55	2.3	1.0	1.2
25.0503	34.3325	2013	6	17	2.2	16.8	3	2	18.1	2.3	4.2
25.0172	34.2608	2013	6	17	2.6	12.3	3	18	15.6	2.5	3.5
25.1678	34.4063	2013	6	17	2.0	22.5	3	24	2.1	2.1	3.6
24.8957	34.3132	2013	6	17	2.7	3.5	3	37	2.7	0.7	1.1
25.0915	34.3360	2013	6	17	2.2	15.4	3	57	6.1	2.4	3.7
25.0872	34.2450	2013	6	17	3.9	8.8	3	58	31.1	0.9	1.2
25.0518	34.3233	2013	6	17	2.1	17.1	4	1	28.1	7.1	8.3
25.0325	34.2425	2013	6	17	2.1	10.5	4	3	54.7	2.2	4.2
25.1222	34.2350	2013	6	17	2.5	4.0	4	6	22.6	2.7	4.5
25.0740	34.2320	2013	6	17	2.6	7.2	4	16	18.0	1.1	1.3
25.0022	34.3122	2013	6	17	2.6	14.0	4	16	59.2	2.4	3.5
24.9507	34.4055	2013	6	17	2.1	10.5	4	28	56.0	6.2	4.0
25.0752	34.3030	2013	6	17	2.8	8.0	4	37	9.5	2.0	2.8
25.0695	34.2905	2013	6	17	2.6	19.8	4	44	5.8	1.6	2.1
25.0720	34.3705	2013	6	17	2.1	18.6	4	51	59.4	1.1	1.8
25.0977	34.2838	2013	6	17	3.2	12.8	5	2	12.2	0.8	0.9
25.0728	34.2585	2013	6	17	3.1	8.2	5	15	11.6	0.6	0.8
24.9405	34.1398	2013	6	17	2.5	20.1	5	23	34.8	11.1	5.4
25.0213	34.1860	2013	6	17	2.8	9.3	5	27	0.0	0.9	1.1
24.9823	34.2123	2013	6	17	2.1	25.8	5	42	17.0	7.7	5.0
25.0115	34.4315	2013	6	17	1.9	10.9	5	46	8.2	2.4	4.4
25.0325	34.3267	2013	6	17	2.0	10.1	6	10	32.8	6.8	7.2
25.1870	34.2868	2013	6	17	2.4	19.0	6	12	35.0	2.1	3.6
25.0937	34.2938	2013	6	17	3.2	13.7	6	46	45.0	0.6	0.7
24.9668	34.3165	2013	6	17	2.3	10.0	7	12	9.7	4.0	2.0
24.7332	34.2763	2013	6	17	2.8	0.1	7	13	55.0	2.5	2.4
24.9903	34.4302	2013	6	17	2.2	23.6	7	26	31.8	2.4	5.2
25.1613	34.3360	2013	6	17	3.8	14.7	7	34	44.6	0.8	0.9
25.1742	34.2693	2013	6	17	3.5	11.7	7	57	34.9	0.7	0.6
25.0383	34.2813	2013	6	17	3.0	9.9	7	58	48.4	0.7	0.8
25.0267	34.2168	2013	6	17	2.6	4.0	8	30	23.8	1.8	2.5
25.0168	34.3813	2013	6	17	2.2	22.0	9	5	3.2	1.0	0.8
25.0700	34.3922	2013	6	17	2.3	14.2	9	5	55.0	1.1	2.1
24.9387	34.3620	2013	6	17	2.9	25.9	9	40	59.7	1.5	2.2
25.1667	34.3142	2013	6	17	3.0	12.6	10	0	13.8	0.6	0.6
25.1363	34.3083	2013	6	17	3.5	8.3	11	7	10.2	0.6	0.7
25.0865	34.2753	2013	6	17	2.9	5.3	11	20	38.0	0.6	0.7
25.0808	34.2518	2013	6	17	4.0	9.7	11	36	2.5	0.8	1.1
25.0802	34.2812	2013	6	17	2.9	11.1	11	44	25.8	0.6	0.5
25.1810	34.2765	2013	6	17	3.0	16.8	11	46	17.8	0.8	1.0
24.8892	34.2478	2013	6	17	2.8	8.5	11	51	52.5	1.0	0.9

25.0948	34.2560	2013	6	17	3.6	19.9	11	52	33.9	1.3	1.6
25.1410	34.2990	2013	6	17	2.5	10.0	12	2	18.3	1.5	1.9
25.0807	34.2858	2013	6	17	3.2	10.7	12	6	7.2	0.7	0.9
25.1997	34.2815	2013	6	17	2.3	13.0	12	41	3.7	1.0	1.1
25.1128	34.2433	2013	6	17	2.7	2.5	12	44	21.8	2.0	1.9
25.1083	34.3303	2013	6	17	2.6	0.0	13	38	22.9	3.5	5.4
25.1377	34.2767	2013	6	17	2.6	8.8	13	39	21.0	1.3	1.6
25.1050	34.2743	2013	6	17	2.6	9.6	13	46	42.1	1.2	1.2
25.1250	34.2397	2013	6	17	2.6	3.7	13	48	52.1	0.9	1.2
25.0840	34.2405	2013	6	17	2.9	7.2	13	49	33.9	1.0	1.3
25.1317	34.3142	2013	6	17	2.4	0.1	13	54	29.5	2.8	3.1
25.0635	34.3430	2013	6	17	2.2	0.0	14	41	47.8	3.5	4.3
25.0673	34.3958	2013	6	17	3.1	22.5	15	5	53.9	0.8	1.0
25.1100	34.2502	2013	6	17	2.7	1.6	15	11	25.2	1.4	1.9
25.0820	34.2710	2013	6	17	2.9	8.9	15	13	58.0	0.6	0.8
25.1028	34.2663	2013	6	17	4.1	9.9	15	27	7.5	0.7	0.9
25.2980	34.2842	2013	6	17	2.7	9.9	15	42	23.0	1.3	2.0
25.1430	34.4145	2013	6	17	2.4	22.1	15	46	47.6	1.1	1.3
25.0498	34.2843	2013	6	17	3.2	7.8	16	0	18.9	0.8	0.9
25.2385	34.2565	2013	6	17	2.3	15.5	16	21	13.4	1.4	1.3
25.1258	34.3238	2013	6	17	2.4	11.8	17	20	23.4	2.4	2.5
25.2118	34.3913	2013	6	17	2.6	14.7	17	41	41.5	1.1	1.5
25.1528	34.1968	2013	6	17	3.3	4.0	18	5	29.0	1.2	1.5
25.1242	34.2880	2013	6	17	2.5	10.7	18	14	26.9	1.0	1.2
25.2453	34.3180	2013	6	17	2.9	11.0	18	25	16.5	1.8	1.8
25.0558	34.2490	2013	6	17	4.0	9.6	19	8	53.1	0.7	0.7
25.2045	34.2270	2013	6	17	2.3	18.4	19	29	7.8	1.2	1.4
24.9682	34.4112	2013	6	17	2.0	16.3	19	36	22.5	2.2	3.9
25.0967	34.2215	2013	6	17	2.9	8.2	19	36	48.8	1.4	1.7
25.1407	34.3052	2013	6	17	2.3	16.7	20	18	57.5	1.6	1.3
25.0872	34.2398	2013	6	17	2.6	4.3	20	20	10.6	2.3	3.5
25.0647	34.1660	2013	6	17	2.3	1.0	20	43	56.7	0.7	1.0
25.0730	34.4215	2013	6	17	2.1	14.9	21	4	48.7	0.9	2.0
25.0373	34.2618	2013	6	17	2.9	9.4	21	50	44.0	1.2	1.5
25.1493	34.2318	2013	6	17	2.5	5.0	23	15	55.8	1.0	1.6
25.2380	34.3257	2013	6	17	2.3	15.2	23	35	59.6	1.6	1.2
25.2273	34.2757	2013	6	17	2.3	13.0	23	44	35.9	0.7	0.8
25.0032	34.3118	2013	6	18	2.2	8.5	0	4	0.8	0.9	1.4
25.1970	34.3063	2013	6	18	2.6	4.0	0	17	35.6	1.6	2.5
25.1668	34.3112	2013	6	18	2.4	11.8	0	39	4.2	1.1	0.9
25.0522	34.4400	2013	6	18	2.0	15.1	0	45	22.2	1.8	5.8
25.1335	34.4540	2013	6	18	2.3	2.1	4	24	41.5	1.5	4.1
25.1132	34.2307	2013	6	18	2.7	6.3	4	55	15.6	0.7	1.1

25.2010	34.2118	2013	6	18	2.6	4.7	4	59	6.5	2.2	4.1
25.0840	34.3392	2013	6	18	2.3	4.3	5	31	41.2	1.0	1.8
24.9572	34.3972	2013	6	18	2.5	13.0	5	51	54.8	1.2	2.0
25.1405	34.3635	2013	6	18	1.9	0.1	7	15	17.6	3.3	4.6
25.0197	34.4162	2013	6	18	2.8	6.3	8	25	22.5	1.3	2.6
25.0155	34.1947	2013	6	18	2.9	4.2	15	6	16.6	0.8	1.3
24.9202	34.3942	2013	6	18	2.3	15.0	16	2	57.4	1.7	4.7
25.0548	34.2207	2013	6	18	2.8	14.7	18	46	33.1	0.9	1.0
25.0617	34.3530	2013	6	18	2.0	14.4	19	29	40.9	1.4	2.8
25.0877	34.2335	2013	6	18	2.7	12.6	20	40	52.0	4.3	4.0
25.0672	34.3108	2013	6	18	4.6	15.6	22	27	7.1	0.7	0.6
25.0177	34.2043	2013	6	18	3.9	12.2	22	33	14.6	0.9	1.0
25.0567	34.2413	2013	6	18	3.0	8.5	22	35	43.5	0.7	1.0
25.0867	34.2612	2013	6	18	3.5	5.6	22	39	29.9	0.5	0.7
25.1693	34.3687	2013	6	18	2.0	0.0	22	48	4.7	3.6	4.9
25.0258	34.2743	2013	6	18	2.3	13.8	23	4	23.0	1.8	2.9
24.9050	34.1762	2013	6	18	2.5	17.0	23	11	25.5	1.8	2.2
25.0938	34.2450	2013	6	18	3.6	7.4	23	15	57.1	0.8	1.1
24.9548	34.2383	2013	6	18	2.0	9.6	23	20	17.4	3.3	2.7
25.1260	34.2373	2013	6	18	2.5	11.7	23	22	58.7	1.1	0.8
25.0660	34.2472	2013	6	18	2.4	21.1	23	26	8.4	1.8	2.8
25.0308	34.2320	2013	6	18	2.3	7.3	23	27	7.6	2.2	4.0
24.9467	34.3292	2013	6	18	2.0	8.5	23	32	30.8	1.9	5.3
25.0268	34.2470	2013	6	18	3.4	1.9	23	36	18.2	0.7	1.0
25.0528	34.2420	2013	6	18	3.4	7.5	23	46	34.3	0.6	0.8
25.1937	34.2868	2013	6	18	2.4	15.6	23	55	13.8	2.1	2.2
25.1303	34.2770	2013	6	19	3.9	9.7	0	0	13.8	0.9	1.4
24.9907	34.2183	2013	6	19	3.4	2.8	0	1	38.0	1.0	1.4
24.9593	34.2583	2013	6	19	2.9	8.2	0	2	51.2	0.6	0.9
25.1148	34.3435	2013	6	19	2.4	17.6	0	6	11.5	1.5	2.4
25.2485	34.3333	2013	6	19	2.3	19.8	0	12	39.7	0.6	1.0
24.9582	34.3457	2013	6	19	2.4	11.1	0	23	28.4	0.9	1.7
25.0957	34.3133	2013	6	19	2.5	16.9	0	24	52.9	1.0	1.0
25.1938	34.2807	2013	6	19	2.0	12.0	0	40	1.7	1.8	1.8
25.0913	34.2322	2013	6	19	2.3	2.1	0	48	55.5	1.2	1.9
25.0705	34.4027	2013	6	19	1.9	9.1	0	56	22.0	2.7	0.4
25.1553	34.3477	2013	6	19	1.8	5.3	2	20	14.6	2.3	0.8
24.9857	34.2747	2013	6	19	2.4	23.4	2	46	54.0	1.3	2.0
25.1352	34.2507	2013	6	19	2.5	8.3	3	15	48.7	2.2	3.5
25.0652	34.2475	2013	6	19	3.6	6.3	4	32	57.6	0.8	1.1
25.1495	34.3135	2013	6	19	2.6	15.3	4	40	52.3	2.2	1.9
24.9660	34.2567	2013	6	19	3.3	1.3	7	6	52.4	1.0	1.6
25.1998	34.3012	2013	6	19	2.6	7.8	9	36	52.4	1.6	2.1

25.0622	34.3008	2013	6	19	2.5	8.5	9	55	13.4	1.5	2.7
25.2947	34.2385	2013	6	19	2.7	1.0	12	54	29.1	1.5	2.6
24.9977	34.2483	2013	6	19	3.0	5.9	14	22	57.0	0.6	0.7
25.0305	34.3692	2013	6	19	2.4	18.2	14	52	40.3	2.0	3.9
25.0233	34.3037	2013	6	19	4.8	10.9	19	5	9.5	0.6	0.6
24.8947	34.2248	2013	6	19	2.7	6.7	19	10	0.1	1.3	1.6
25.0150	34.2795	2013	6	19	2.7	7.7	19	17	17.9	1.1	1.4
24.9022	34.2065	2013	6	19	2.6	16.2	19	24	31.1	1.3	2.0
24.9393	34.2485	2013	6	19	2.5	7.5	19	47	47.4	0.8	1.0
25.0135	34.2792	2013	6	19	2.6	7.5	19	54	14.3	0.7	0.9
24.9692	34.2302	2013	6	19	2.5	4.1	20	3	12.0	1.4	1.7
24.9980	34.2587	2013	6	19	2.4	7.6	20	28	49.7	0.8	1.1
25.3823	34.3135	2013	6	19	2.3	2.6	23	10	43.2	2.2	3.3
24.9877	34.2880	2013	6	20	2.0	11.0	0	30	45.0	1.7	3.0
25.1013	34.3607	2013	6	20	1.9	3.1	1	12	25.0	2.1	7.4
25.0635	34.2757	2013	6	20	1.8	4.9	1	30	24.5	1.1	1.8
25.1093	34.2602	2013	6	20	2.5	7.8	4	48	16.3	1.6	2.0
25.0623	34.2652	2013	6	20	3.6	10.8	18	9	47.9	0.7	0.9
24.9462	34.2907	2013	6	20	2.7	21.3	21	20	17.9	2.3	1.4
25.0990	34.2580	2013	6	20	2.2	12.5	22	30	14.3	1.9	1.8
25.0760	34.2195	2013	6	21	2.4	6.4	0	50	32.1	1.5	1.7
25.1932	34.2302	2013	6	21	2.2	9.5	1	56	41.7	1.6	2.1
25.0242	34.2372	2013	6	21	2.7	8.0	23	45	14.8	1.3	1.2
25.1027	34.3172	2013	6	22	2.4	7.7	3	47	46.9	0.7	1.0
25.1177	34.3825	2013	6	22	2.9	17.8	7	27	57.1	1.3	1.6
24.9947	34.2207	2013	6	22	4.5	5.3	8	50	14.6	0.8	1.0
24.9560	34.2437	2013	6	22	2.9	10.9	8	55	46.1	1.4	1.8
24.9912	34.3117	2013	6	22	2.1	13.1	9	38	14.8	1.8	3.0
25.0937	34.2815	2013	6	22	2.7	8.7	15	16	30.7	1.2	1.7
25.0448	34.2833	2013	6	22	3.0	9.1	17	47	38.0	0.7	0.8
25.0490	34.2673	2013	6	22	2.7	2.5	22	10	12.2	1.5	2.8
25.0365	34.2975	2013	6	23	2.2	13.2	1	17	35.5	1.5	2.4
25.1103	34.1868	2013	6	23	2.5	0.0	2	22	56.8	1.3	1.2
25.1057	34.2153	2013	6	23	3.5	8.8	2	57	45.7	0.6	0.8
25.0617	34.1382	2013	6	23	2.4	8.8	5	41	15.4	2.0	3.2
25.0882	34.2243	2013	6	23	2.7	1.5	10	22	27.8	1.0	1.3
25.0110	34.3522	2013	6	23	2.4	12.8	11	16	16.5	0.6	0.7
25.0042	34.3215	2013	6	23	2.3	11.8	15	52	3.5	2.0	1.4
25.0398	34.3427	2013	6	23	2.2	14.9	16	35	51.2	0.9	1.0
25.1053	34.3127	2013	6	23	2.3	19.1	16	42	44.5	2.0	3.7
25.0888	34.2325	2013	6	23	2.0	10.1	22	40	12.2	1.7	3.3
25.0248	34.3658	2013	6	24	1.6	9.1	1	53	58.0	1.0	2.1
25.1092	34.1787	2013	6	24	2.3	0.1	15	11	59.1	2.1	2.4

24.8922	34.2763	2013	6	24	2.7	21.7	19	13	24.4	0.7	1.0
24.9890	34.2595	2013	6	25	2.2	9.9	5	54	34.9	1.1	1.4
25.0402	34.3125	2013	6	25	2.6	1.4	9	34	18.0	2.6	4.8
25.1137	34.4097	2013	6	25	3.3	23.1	19	25	16.4	1.0	1.5
24.9288	34.1782	2013	6	25	1.9	6.0	23	33	0.4	1.3	1.4
24.9403	34.2578	2013	6	26	2.5	6.2	9	49	8.4	0.8	1.0
25.0613	34.3220	2013	6	26	2.6	11.4	18	44	50.2	0.9	0.8
24.9632	34.2488	2013	6	26	3.1	7.3	19	43	28.7	1.5	1.8
25.0693	34.1827	2013	6	26	3.4	8.2	20	33	21.1	1.4	1.3
25.0567	34.2588	2013	6	26	2.5	5.8	21	7	17.0	0.7	0.8
25.0297	34.2563	2013	6	26	1.3	13.3	21	31	20.7	1.8	1.9
25.0872	34.3445	2013	6	27	2.3	11.1	13	7	50.1	1.7	2.5
25.1037	34.2512	2013	6	27	2.4	8.0	22	51	5.9	1.5	1.8
24.9192	34.2902	2013	6	28	2.0	10.5	1	55	3.0	1.2	1.4
25.0042	34.4617	2013	6	28	2.5	16.4	7	13	0.7	1.9	2.1
25.1155	34.3508	2013	6	28	1.7	3.9	15	44	56.0	1.7	5.0
25.0157	34.2767	2013	6	30	2.8	9.8	10	55	56.0	0.6	0.7
25.0000	34.2860	2013	6	30	2.0	5.9	15	5	30.1	0.7	0.8
25.0285	34.2327	2013	6	30	2.6	2.3	19	57	40.6	0.8	1.0
25.1323	34.1660	2013	6	30	2.6	5.7	23	55	50.4	1.0	1.2
25.1255	34.2510	2013	7	1	3.1	6.2	22	56	41.1	1.4	2.3
25.3002	34.2992	2013	7	1	2.2	8.7	23	27	22.3	1.5	2.1
25.0800	34.2227	2013	7	2	2.3	19.4	6	11	30.6	1.3	1.6
24.9530	34.2435	2013	7	2	2.5	4.2	7	42	8.2	1.1	2.2
25.0742	34.2223	2013	7	2	2.9	5.8	11	13	40.0	1.5	1.9
25.0420	34.4528	2013	7	3	2.2	26.2	0	34	13.8	1.3	1.0
25.0128	34.1848	2013	7	3	1.9	12.4	1	43	18.2	1.5	1.6
24.9138	34.4613	2013	7	5	3.4	25.9	5	51	1.2	1.6	2.2
24.9847	34.3058	2013	7	7	2.2	8.5	4	45	1.4	0.8	0.9
25.3800	34.2392	2013	7	9	2.6	5.9	3	25	34.6	2.4	3.1

Catalogue of 12/10/2013 aftershock sequence

Longitude Degrees	Latitude Degrees	Year	Month	Day	Magnitude M_L	Depth (km)	Hour	Minutes	Seconds	Horizontal error	Vertical error
23.2425	35.4218	2013	10	12	6.2	47.4	13	11	53.6	0.7	0.8
23.2735	35.3002	2013	10	12	4.0	42.8	13	17	0.4	0.7	0.9
23.2673	35.3815	2013	10	12	3.1	55.9	13	19	32.9	0.8	0.9
23.2717	35.2677	2013	10	12	3.3	50.0	13	21	3.3	0.7	0.5
23.3313	35.3212	2013	10	12	3.3	38.6	13	21	54.8	0.5	0.7
23.2800	35.2665	2013	10	12	3.0	46.8	13	23	57.7	0.7	0.8
23.3818	35.4432	2013	10	12	2.9	51.2	13	24	44.9	1.0	1.0
23.2823	35.3793	2013	10	12	2.7	49.8	13	26	22.0	0.7	0.4
23.2768	35.4247	2013	10	12	2.7	42.8	13	28	20.3	1.0	1.3
23.3148	35.3832	2013	10	12	2.9	47.4	13	29	39.4	0.6	0.6
23.3857	35.4405	2013	10	12	2.6	48.7	13	32	1.5	0.8	0.8
23.3412	35.4387	2013	10	12	3.1	38.3	13	33	11.1	0.7	0.9
23.3695	35.3643	2013	10	12	2.9	51.5	13	34	53.9	0.8	0.8
23.3130	35.3412	2013	10	12	3.2	58.5	13	35	17.1	0.7	0.7
23.3148	35.2522	2013	10	12	2.4	40.9	13	38	8.7	0.7	0.9
23.3570	35.3397	2013	10	12	3.0	41.7	13	40	36.5	0.6	0.7
23.3438	35.3853	2013	10	12	2.8	43.4	13	44	57.6	0.7	0.9
23.3212	35.3445	2013	10	12	2.1	43.4	13	47	30.5	0.6	0.7
23.3380	35.2648	2013	10	12	2.0	57.0	13	51	48.8	1.1	1.3
23.3260	35.3223	2013	10	12	2.0	49.2	13	53	14.0	1.0	1.2
23.3617	35.3787	2013	10	12	3.3	42.6	13	55	28.3	0.6	0.7
23.3237	35.3417	2013	10	12	1.8	58.2	13	57	56.0	2.1	2.8
23.3855	35.4317	2013	10	12	2.8	41.3	14	1	46.5	0.8	1.0
23.3513	35.3657	2013	10	12	2.4	35.3	14	2	56.6	0.5	0.7
23.3568	35.3592	2013	10	12	2.1	37.6	14	5	25.8	0.6	0.9
23.3477	35.4263	2013	10	12	4.0	43.7	14	5	50.7	0.6	0.8
23.3697	35.4183	2013	10	12	1.8	57.2	14	11	1.2	0.7	0.8
23.3157	35.1660	2013	10	12	2.0	66.2	14	12	8.6	0.9	0.9
23.3110	35.3902	2013	10	12	2.9	46.1	14	14	45.0	0.6	0.7
23.3997	35.4072	2013	10	12	3.0	58.1	14	15	3.4	0.7	0.8
23.3418	35.3267	2013	10	12	2.9	38.5	14	16	54.2	0.7	0.9
23.2532	35.3367	2013	10	12	2.1	45.6	14	21	2.0	0.7	1.0
23.2988	35.3803	2013	10	12	2.1	52.6	14	23	16.0	1.2	1.5
23.2575	35.2427	2013	10	12	2.4	30.7	14	26	8.4	0.9	1.3

23.3797	35.3878	2013	10	12	1.9	66.7	14	29	11.6	0.7	0.8
23.3362	35.3602	2013	10	12	2.4	39.1	14	32	28.5	1.4	1.6
23.2362	35.3355	2013	10	12	1.8	25.9	14	36	10.4	0.9	0.7
23.3998	35.4038	2013	10	12	2.0	55.4	14	37	25.2	0.9	1.0
23.3520	35.3780	2013	10	12	2.5	37.9	14	38	31.8	0.8	1.1
23.3537	35.3850	2013	10	12	2.0	52.8	14	40	7.5	0.7	0.9
23.3402	35.3872	2013	10	12	2.1	40.5	14	42	45.4	0.8	1.2
23.3005	35.2810	2013	10	12	2.0	57.0	14	44	8.7	1.0	1.2
23.3683	35.3490	2013	10	12	2.0	49.1	14	46	23.2	1.1	1.2
23.3447	35.3882	2013	10	12	2.0	36.5	14	47	21.3	1.0	1.5
23.3148	35.2985	2013	10	12	1.9	51.6	14	49	46.6	1.2	1.4
23.3815	35.4050	2013	10	12	1.8	41.8	14	52	55.4	0.7	1.0
23.3570	35.4318	2013	10	12	1.7	38.2	14	54	9.5	0.7	1.1
23.2995	35.3145	2013	10	12	2.3	37.2	14	55	59.5	0.8	1.1
23.3643	35.4508	2013	10	12	2.1	56.3	14	56	22.6	1.2	1.3
23.2748	35.3337	2013	10	12	3.2	35.7	14	57	7.6	0.7	0.8
23.3428	35.3462	2013	10	12	2.0	32.8	15	0	19.7	1.0	1.4
23.3062	35.3867	2013	10	12	1.9	42.7	15	1	12.4	0.6	0.9
23.4467	35.3432	2013	10	12	1.9	65.7	15	3	36.9	0.9	0.8
23.2585	35.2997	2013	10	12	1.9	51.5	15	5	29.5	0.6	0.8
23.3328	35.3573	2013	10	12	2.0	41.4	15	5	52.3	0.6	1.0
23.3660	35.4113	2013	10	12	2.0	36.8	15	10	2.1	0.8	1.0
23.3148	35.3625	2013	10	12	2.0	43.4	15	11	24.0	0.9	1.1
23.3280	35.3728	2013	10	12	2.8	42.2	15	11	58.1	0.6	0.8
23.3388	35.4177	2013	10	12	2.8	41.7	15	13	41.9	0.6	0.8
23.3843	35.4160	2013	10	12	2.4	48.3	15	14	27.3	0.6	0.7
23.3223	35.2813	2013	10	12	2.3	43.6	15	14	54.7	0.6	0.9
23.3968	35.4048	2013	10	12	2.0	44.6	15	18	28.9	0.7	1.0
23.3435	35.2952	2013	10	12	2.0	55.9	15	20	6.9	1.0	1.1
23.3320	35.3380	2013	10	12	1.9	52.4	15	23	22.6	0.9	1.1
23.3000	35.3997	2013	10	12	3.4	42.5	15	27	5.2	0.7	0.9
23.3485	35.4062	2013	10	12	1.9	51.7	15	34	3.4	0.8	0.9
23.3740	35.2955	2013	10	12	1.9	62.6	15	34	35.0	1.0	1.0
23.3568	35.3060	2013	10	12	1.8	53.4	15	36	40.7	0.8	0.9
23.3032	35.3300	2013	10	12	2.1	39.1	15	47	49.7	0.6	0.9
23.3237	35.3327	2013	10	12	1.9	58.6	15	49	53.9	1.3	1.6
23.3250	35.3953	2013	10	12	1.9	45.4	15	55	56.1	0.7	1.1
23.2715	35.3868	2013	10	12	2.0	40.0	16	5	55.0	1.1	1.5
23.2802	35.2313	2013	10	12	2.0	45.0	16	8	33.5	2.9	4.3
23.3217	35.2447	2013	10	12	2.1	56.1	16	14	9.9	0.7	0.8
23.3500	35.3367	2013	10	12	1.9	33.2	16	15	42.3	0.9	1.3
23.4215	35.4115	2013	10	12	1.9	39.1	16	19	47.6	0.7	0.9
23.3508	35.3110	2013	10	12	1.8	47.9	16	25	0.8	1.2	1.5

23.3520	35.4190	2013	10	12	2.1	42.5	16	31	2.6	0.6	0.9
23.4422	35.4210	2013	10	12	1.8	51.9	16	33	43.8	1.2	1.3
23.3840	35.2605	2013	10	12	1.9	51.6	16	37	6.0	1.3	1.4
23.3742	35.3425	2013	10	12	2.1	41.1	16	45	32.3	0.9	1.2
23.3112	35.4135	2013	10	12	2.7	40.8	16	52	13.2	0.6	0.8
23.3892	35.4388	2013	10	12	2.5	42.3	17	15	13.9	0.6	0.7
23.3645	35.3400	2013	10	12	2.1	51.2	17	21	23.8	0.8	0.8
23.2830	35.3122	2013	10	12	2.0	51.2	17	27	11.8	0.9	1.0
23.4358	35.4582	2013	10	12	1.8	25.7	17	49	45.6	0.8	1.3
23.4107	35.4440	2013	10	12	2.0	39.1	17	53	8.8	0.6	0.8
23.3443	35.3797	2013	10	12	1.8	51.0	18	0	50.8	0.8	0.9
23.3410	35.3913	2013	10	12	2.3	36.8	18	6	27.1	1.2	1.6
23.3548	35.2840	2013	10	12	1.7	60.7	18	8	54.2	1.0	1.3
23.3437	35.4452	2013	10	12	1.9	34.4	18	15	29.0	0.8	1.2
23.4025	35.4628	2013	10	12	2.2	46.6	18	22	0.1	1.0	1.2
23.3662	35.3997	2013	10	12	2.0	38.2	18	46	34.8	1.0	1.3
23.3195	35.3228	2013	10	12	2.4	52.2	19	3	30.0	0.7	0.8
23.3448	35.4257	2013	10	12	2.0	41.6	19	10	5.3	1.0	1.5
23.3957	35.4260	2013	10	12	1.9	43.1	19	21	55.4	1.0	1.5
23.3278	35.4347	2013	10	12	2.1	42.6	19	26	34.6	1.2	1.6
23.3255	35.4165	2013	10	12	3.8	48.6	19	36	26.3	0.5	0.5
23.3443	35.4783	2013	10	12	2.3	58.3	19	41	12.7	0.9	1.0
23.3503	35.3072	2013	10	12	1.9	55.9	19	42	40.0	0.9	1.1
23.3577	35.4558	2013	10	12	2.2	39.4	19	44	37.3	1.0	1.4
23.3203	35.3730	2013	10	12	1.9	27.0	19	46	35.7	1.0	1.0
23.4675	35.4692	2013	10	12	1.7	62.6	20	13	8.8	1.2	1.7
23.3137	35.2223	2013	10	12	1.9	53.8	20	16	45.7	0.6	0.8
23.3477	35.3457	2013	10	12	2.0	35.6	20	23	39.1	0.7	0.8
23.2630	35.1938	2013	10	12	2.0	45.0	20	31	6.3	3.6	5.7
23.3327	35.4100	2013	10	12	3.0	40.4	20	54	28.8	0.8	1.0
23.3560	35.4293	2013	10	12	1.8	36.0	21	1	2.7	1.1	1.7
23.3778	35.3318	2013	10	12	1.9	29.5	21	1	51.5	1.4	0.8
23.2143	35.2597	2013	10	12	2.4	52.7	21	8	6.8	0.7	0.8
23.2818	35.2995	2013	10	12	2.0	52.3	21	21	57.5	0.7	0.8
23.2913	35.4020	2013	10	12	2.3	36.7	21	42	40.8	0.7	1.0
23.2690	35.3180	2013	10	12	2.1	35.0	21	47	15.3	0.6	0.8
23.3477	35.3408	2013	10	12	2.4	43.3	21	48	22.9	0.6	0.8
23.3378	35.3883	2013	10	12	2.6	45.3	21	58	11.8	0.6	0.7
23.3902	35.4043	2013	10	12	2.5	39.8	22	16	44.2	0.5	0.7
23.3122	35.4347	2013	10	12	2.1	46.2	22	17	49.1	0.8	1.1
23.3365	35.4167	2013	10	12	1.8	39.9	22	41	56.6	0.7	1.1
23.4777	35.4410	2013	10	12	1.7	55.5	22	45	26.8	1.2	1.3
23.3520	35.4055	2013	10	12	2.4	41.7	22	50	14.5	1.3	1.9

23.3480	35.4255	2013	10	12	1.7	43.2	22	57	22.1	1.1	1.7
23.4230	35.3200	2013	10	12	2.3	41.2	23	0	20.6	0.5	0.7
23.2983	35.1915	2013	10	12	1.8	51.3	23	7	1.2	1.3	1.4
23.3838	35.4138	2013	10	12	1.7	39.1	23	7	54.1	0.8	1.2
23.3478	35.3892	2013	10	12	3.3	43.7	23	14	5.6	0.5	0.6
23.3452	35.3880	2013	10	12	1.9	35.6	23	27	52.1	1.1	1.5
23.3727	35.4443	2013	10	12	1.8	38.9	23	45	58.3	1.1	1.8
23.3737	35.3887	2013	10	12	2.1	34.0	23	47	2.0	0.7	1.0
23.3138	35.3452	2013	10	13	3.6	36.4	0	1	23.6	0.5	0.7
23.3712	35.3703	2013	10	13	1.7	34.3	0	12	1.0	0.7	1.1
23.4358	35.4730	2013	10	13	1.6	54.0	0	24	17.9	0.7	0.8
23.2680	35.3393	2013	10	13	1.8	40.5	0	30	11.5	0.9	1.4
23.3793	35.4635	2013	10	13	2.2	48.1	0	30	36.5	0.9	0.9
23.3593	35.2943	2013	10	13	1.7	54.6	0	43	41.4	1.1	1.5
23.2933	35.3202	2013	10	13	1.6	38.0	0	46	26.9	0.8	1.4
23.3078	35.3087	2013	10	13	1.9	38.1	0	46	57.2	0.6	1.0
23.2853	35.3918	2013	10	13	1.7	28.4	1	48	30.0	1.1	0.8
23.3900	35.4543	2013	10	13	1.7	42.5	2	2	21.1	0.6	1.0
23.3603	35.3530	2013	10	13	1.9	33.8	2	7	12.1	0.8	1.1
23.3775	35.3612	2013	10	13	1.8	35.6	2	20	17.9	0.9	1.1
23.3865	35.4408	2013	10	13	1.7	36.1	2	38	18.3	1.1	1.4
23.2795	35.2173	2013	10	13	1.8	55.3	2	39	32.9	1.7	2.1
23.2793	35.3002	2013	10	13	1.9	47.5	2	40	54.8	0.6	0.8
23.4027	35.4572	2013	10	13	1.8	50.9	2	42	50.0	0.8	0.8
23.2990	35.4108	2013	10	13	2.5	41.2	3	2	23.7	0.7	1.0
23.3422	35.3930	2013	10	13	1.6	20.7	3	11	23.7	0.7	1.4
23.3198	35.2755	2013	10	13	1.7	61.1	3	15	11.4	1.4	1.6
23.2590	35.2710	2013	10	13	2.5	46.2	3	17	19.5	0.5	0.7
23.2550	35.2283	2013	10	13	1.8	45.0	3	18	52.4	3.4	5.4
23.3502	35.4217	2013	10	13	3.2	47.3	3	43	12.8	0.5	0.5
23.2700	35.2833	2013	10	13	1.9	44.3	3	55	53.9	0.7	1.1
23.2840	35.2275	2013	10	13	1.7	65.1	4	22	59.2	1.6	1.9
23.3130	35.3720	2013	10	13	2.0	47.3	4	53	54.5	1.1	1.3
23.3600	35.3908	2013	10	13	1.6	49.7	5	1	55.0	0.8	0.9
23.3617	35.3227	2013	10	13	1.8	47.9	5	2	49.9	1.4	0.8
23.3300	35.4195	2013	10	13	2.4	34.8	6	19	49.8	1.3	1.4
23.3278	35.3885	2013	10	13	1.9	37.4	6	39	28.0	1.0	1.3
23.2660	35.3647	2013	10	13	1.7	42.6	6	57	21.3	0.6	1.1
23.3007	35.4382	2013	10	13	1.7	37.2	7	1	42.5	0.8	1.5
23.3250	35.3658	2013	10	13	1.9	52.1	7	4	20.4	1.0	1.1
23.3548	35.3957	2013	10	13	1.7	31.4	7	42	31.1	1.0	1.5
23.3632	35.3830	2013	10	13	1.7	42.3	8	56	36.4	0.6	0.9
23.3580	35.4318	2013	10	13	1.9	47.5	10	23	43.7	0.9	1.0

23.3452	35.4183	2013	10	13	2.0	33.6	10	52	33.0	1.2	1.7
23.1968	35.2672	2013	10	13	1.9	29.1	11	12	22.1	1.2	0.8
23.4248	35.4133	2013	10	13	1.9	29.0	11	32	51.3	1.0	0.6
23.3338	35.4057	2013	10	13	1.8	31.4	11	58	1.3	1.4	2.3
23.3362	35.3383	2013	10	13	2.0	48.1	12	0	3.8	0.8	1.0
23.3540	35.4590	2013	10	13	1.7	47.0	12	15	3.9	1.0	1.6
23.3435	35.4133	2013	10	13	1.8	20.9	12	55	15.3	0.6	1.2
23.3765	35.3333	2013	10	13	1.8	57.1	13	3	6.3	0.9	1.1
23.3993	35.3515	2013	10	13	2.0	31.1	14	10	48.5	0.5	0.7
23.2312	35.2675	2013	10	13	1.9	30.3	14	46	57.1	1.6	2.6
23.3637	35.2203	2013	10	13	2.0	51.1	14	49	58.6	1.1	1.1
23.2987	35.3192	2013	10	13	2.1	39.4	14	50	46.8	0.8	1.0
23.3337	35.3653	2013	10	13	1.9	18.2	14	53	52.9	0.5	1.0
23.2430	35.1985	2013	10	13	1.9	55.8	15	1	55.4	0.7	1.0
23.2498	35.2470	2013	10	13	2.0	43.0	16	18	50.8	0.6	1.1
23.3405	35.3298	2013	10	13	2.1	41.6	16	22	57.9	0.9	1.3
23.3393	35.3250	2013	10	13	1.9	62.0	16	48	47.3	1.3	1.5
23.3535	35.4095	2013	10	13	1.9	27.9	17	1	7.7	0.8	0.6
23.3050	35.3750	2013	10	13	4.1	47.8	17	43	51.8	0.5	0.6
23.3872	35.3978	2013	10	13	2.3	36.5	17	50	34.8	0.6	0.8
23.3455	35.3708	2013	10	13	2.2	54.1	18	23	50.1	0.9	1.0
23.3600	35.4355	2013	10	13	2.7	49.2	19	18	19.7	0.7	0.7
23.3647	35.3202	2013	10	13	1.8	53.2	19	22	14.6	0.6	0.7
23.3820	35.2390	2013	10	13	1.9	52.9	20	4	21.3	0.8	0.8
23.3793	35.4490	2013	10	13	1.7	32.6	21	52	7.4	1.6	2.5
23.3798	35.3683	2013	10	13	1.9	55.4	21	59	18.9	0.9	1.0
23.2837	35.3842	2013	10	13	1.8	43.8	22	25	54.0	1.4	2.3
23.3308	35.3390	2013	10	14	1.8	34.3	0	26	26.9	1.1	1.6
23.3470	35.3443	2013	10	14	2.5	38.6	0	34	54.8	0.6	0.8
23.3950	35.3615	2013	10	14	1.9	36.8	1	9	52.3	0.7	0.9
23.3360	35.2573	2013	10	14	1.8	55.9	3	52	44.2	1.2	1.5
23.4062	35.4033	2013	10	14	1.7	42.3	5	51	26.9	0.7	1.1
23.3315	35.3978	2013	10	14	2.9	47.3	7	11	59.0	0.9	1.0
23.3553	35.3918	2013	10	14	1.8	16.9	7	54	46.0	1.4	2.9
23.3903	35.4222	2013	10	14	2.0	45.6	8	0	58.9	0.8	1.1
23.4000	35.3810	2013	10	14	2.2	44.8	8	16	57.1	0.7	0.9
23.3258	35.3527	2013	10	14	1.9	17.2	8	24	5.2	0.6	1.2
23.2982	35.3695	2013	10	14	1.9	23.8	9	24	23.2	1.6	2.5
23.2902	35.4225	2013	10	14	2.0	49.0	10	35	42.7	1.5	1.6
23.3468	35.3445	2013	10	14	1.8	20.1	11	5	28.6	0.6	1.1
23.3690	35.4188	2013	10	14	1.8	45.5	12	5	10.4	0.9	1.3
23.3508	35.4267	2013	10	14	2.0	35.2	12	57	50.7	0.5	0.8
23.2077	35.1673	2013	10	14	1.9	45.0	13	11	48.2	3.7	6.4

23.2860	35.3993	2013	10	14	1.7	44.3	13	14	16.3	0.8	1.4
23.3852	35.4167	2013	10	14	2.1	46.6	13	21	43.9	1.0	1.3
23.3383	35.3333	2013	10	14	1.8	53.0	15	21	36.2	0.8	1.0
23.3430	35.3388	2013	10	14	1.8	47.2	17	2	45.0	0.7	0.9
23.2478	35.3308	2013	10	14	1.7	40.6	19	2	24.6	0.9	1.5
23.3500	35.3933	2013	10	14	2.0	40.3	20	2	6.6	0.9	1.1
23.3547	35.3740	2013	10	14	1.6	15.6	20	5	9.3	0.9	2.1
23.2165	35.1683	2013	10	14	1.9	55.4	20	11	17.1	0.9	1.3
23.3383	35.3702	2013	10	14	1.7	34.0	21	54	1.1	1.0	1.5
23.3370	35.3687	2013	10	14	1.7	20.7	23	10	11.9	0.8	2.0
23.2042	35.2902	2013	10	15	2.0	64.8	0	0	50.5	0.9	1.1
23.3500	35.3453	2013	10	15	1.5	27.7	2	6	0.1	0.8	1.1
23.3635	35.1890	2013	10	15	1.6	68.9	2	37	16.8	1.0	1.0
23.3877	35.3497	2013	10	15	1.7	34.6	3	17	17.9	0.6	0.9
23.3665	35.3037	2013	10	15	2.5	39.0	4	46	10.9	0.5	0.6
23.3122	35.3605	2013	10	15	1.8	30.2	5	5	11.1	1.0	1.4
23.3612	35.3958	2013	10	15	1.7	43.4	7	7	19.8	0.6	0.9
23.3673	35.3323	2013	10	15	2.0	35.3	8	42	18.0	2.0	2.8
23.3743	35.2210	2013	10	15	1.5	60.9	8	47	29.8	1.0	0.8
23.3925	35.3630	2013	10	15	1.4	59.1	10	4	13.8	1.0	1.3
23.3043	35.3983	2013	10	15	1.6	32.9	10	22	40.0	1.2	1.8
23.3187	35.3988	2013	10	15	1.4	32.6	11	6	13.4	1.2	2.0
23.3752	35.4088	2013	10	15	1.5	55.2	12	20	31.1	1.0	1.2
23.3382	35.3628	2013	10	15	1.5	15.6	12	25	39.4	0.7	1.5
23.3167	35.3878	2013	10	15	1.8	45.6	15	1	27.4	1.2	1.9
23.3482	35.3985	2013	10	15	1.9	53.7	15	17	39.9	1.0	1.1
23.2300	35.2857	2013	10	15	1.9	42.9	15	47	38.1	0.9	1.6
23.2947	35.3227	2013	10	15	1.9	26.5	17	4	40.6	0.7	1.1
23.2650	35.3093	2013	10	15	1.8	43.9	19	9	42.5	0.7	1.2
23.2283	35.3233	2013	10	15	1.8	33.1	19	16	45.7	1.2	2.0
23.3345	35.4217	2013	10	15	1.6	44.1	22	16	58.1	0.6	1.0
23.2637	35.1527	2013	10	15	2.1	29.6	23	50	30.0	1.7	1.0
23.4610	35.4347	2013	10	16	2.9	53.3	1	49	6.9	1.2	1.3
23.3880	35.4048	2013	10	16	1.7	31.1	3	27	41.7	0.8	1.8
23.4047	35.4593	2013	10	16	2.7	43.5	4	5	12.5	0.6	1.0
23.3603	35.4122	2013	10	16	2.4	45.7	4	10	56.7	0.7	1.3
23.3053	35.3467	2013	10	16	2.3	41.0	7	59	5.3	1.2	2.0
23.2755	35.2212	2013	10	16	2.1	34.0	9	31	32.0	0.8	1.2
23.3577	35.2733	2013	10	16	2.1	45.9	11	28	50.7	0.8	1.0
23.3867	35.4042	2013	10	16	3.8	41.0	13	47	59.5	0.8	1.0
23.1873	35.3042	2013	10	16	1.8	46.6	16	11	5.5	2.2	3.4
23.3568	35.2993	2013	10	16	2.2	57.5	20	15	19.5	1.3	1.5
23.3818	35.4387	2013	10	16	2.5	38.1	22	8	53.8	0.6	0.8

23.3255	35.3598	2013	10	17	2.2	27.6	3	15	51.7	1.0	1.4
23.2403	35.2390	2013	10	17	2.2	29.8	5	1	31.5	0.8	0.5
23.3442	35.3690	2013	10	18	2.2	36.1	1	57	47.2	0.5	0.8
23.3703	35.3435	2013	10	18	2.0	52.5	6	58	18.6	0.9	1.0
23.2892	35.2228	2013	10	18	2.7	51.9	11	42	42.8	0.6	0.7
23.3332	35.3978	2013	10	18	1.9	27.5	14	5	18.8	1.3	1.0
23.3510	35.3390	2013	10	18	1.8	27.6	14	51	43.9	0.6	0.8
23.4485	35.4313	2013	10	18	2.3	47.4	15	26	40.5	1.0	1.1
23.3205	35.3605	2013	10	18	2.2	37.4	18	28	7.8	0.7	0.9
23.3795	35.4175	2013	10	18	2.9	48.4	19	34	9.0	0.7	0.7
23.3743	35.3922	2013	10	18	1.9	58.0	19	54	27.7	1.2	1.3
23.2860	35.3200	2013	10	19	1.9	43.5	0	33	51.5	0.6	1.0
23.2605	35.4180	2013	10	19	3.9	51.4	2	19	21.1	0.6	0.7
23.2830	35.3740	2013	10	19	2.7	47.5	2	45	33.2	0.6	0.6
23.3408	35.4373	2013	10	19	3.2	39.5	3	39	58.6	0.6	0.9
23.2717	35.3305	2013	10	19	1.8	32.8	4	41	29.9	1.0	1.6
23.3745	35.3722	2013	10	19	1.9	51.6	4	55	8.5	0.7	0.8
23.4005	35.3302	2013	10	19	1.8	29.5	5	4	5.3	0.7	0.4
23.2330	35.2007	2013	10	19	1.9	47.1	7	13	39.2	1.3	2.2
23.4835	35.4812	2013	10	19	2.3	48.3	13	44	37.1	0.9	0.7
23.3140	35.4140	2013	10	19	1.7	39.7	17	39	21.0	0.6	0.9
23.3272	35.3978	2013	10	19	1.7	26.3	19	42	15.7	1.1	1.7
23.3558	35.3845	2013	10	19	1.9	46.0	20	23	10.5	0.7	1.0
23.3550	35.3520	2013	10	20	3.6	40.1	4	49	48.1	0.6	0.8
23.2588	35.3422	2013	10	20	3.0	45.6	6	20	35.3	0.7	0.8
23.2527	35.2742	2013	10	20	2.1	40.5	7	21	0.8	0.8	1.0
23.4023	35.3265	2013	10	20	2.0	35.0	8	58	6.2	1.7	2.6
23.3175	35.3472	2013	10	20	2.3	52.4	17	51	56.5	0.8	0.6
23.3490	35.3890	2013	10	20	3.0	44.3	22	54	40.3	0.5	0.7
23.3845	35.4242	2013	10	21	2.8	42.8	2	35	31.8	0.5	0.7
23.3792	35.3672	2013	10	21	1.5	34.3	16	13	17.9	0.9	1.3
23.2813	35.1582	2013	10	21	1.6	27.8	17	47	5.4	2.2	2.1
23.3735	35.3668	2013	10	21	1.3	28.7	18	20	41.6	0.8	0.5
23.3888	35.4115	2013	10	21	1.4	56.9	18	31	39.4	1.4	1.6
23.3468	35.4048	2013	10	21	1.8	48.0	18	44	1.3	0.6	0.7
23.3222	35.3803	2013	10	21	2.0	42.7	23	15	47.5	1.0	1.3
23.2742	35.3293	2013	10	22	1.3	63.6	0	3	58.6	0.9	1.1
23.3933	35.4177	2013	10	22	1.1	20.3	0	40	18.1	1.8	4.1
23.4060	35.4470	2013	10	22	1.3	47.3	1	26	56.6	1.5	1.6
23.3607	35.4330	2013	10	22	1.9	38.0	3	11	40.7	1.1	1.4
23.3367	35.4413	2013	10	22	1.6	54.0	16	18	10.9	1.1	1.4
23.4062	35.3833	2013	10	22	1.4	40.8	23	7	29.7	1.0	1.4
23.3180	35.3297	2013	10	22	1.3	48.2	23	10	19.1	1.3	1.6

23.3775	35.3558	2013	10	23	2.2	29.5	2	33	3.9	0.9	0.6
23.3168	35.2243	2013	10	23	1.8	30.4	4	12	24.7	1.2	1.6
23.3793	35.4345	2013	10	23	2.1	41.4	19	14	13.3	0.7	1.1
23.3470	35.3958	2013	10	24	1.8	12.6	1	59	4.5	0.9	3.2
23.3020	35.3798	2013	10	24	2.0	32.2	3	6	53.0	0.9	1.5
23.3960	35.4370	2013	10	24	2.0	42.1	3	13	33.9	0.9	1.3
23.3640	35.4032	2013	10	24	2.5	17.1	5	32	37.4	0.9	1.7
23.3597	35.3748	2013	10	24	2.0	30.3	5	56	33.4	0.7	1.0
23.2718	35.3737	2013	10	24	1.9	11.5	15	8	13.9	0.7	2.2
23.3400	35.3817	2013	10	24	2.1	17.6	15	30	53.2	0.9	1.8
23.2088	35.2192	2013	10	24	2.1	56.3	15	50	49.8	1.6	2.4
23.3667	35.3617	2013	10	24	1.8	26.5	18	47	25.9	0.7	1.0
23.2420	35.1208	2013	10	25	2.1	29.3	9	19	26.1	1.3	0.8
23.3462	35.3787	2013	10	25	1.8	37.1	11	10	42.5	0.8	1.2
23.2717	35.3082	2013	10	25	2.1	42.4	17	10	4.0	0.7	1.0
23.3070	35.4073	2013	10	26	2.2	48.1	10	37	17.8	1.8	2.0
23.3517	35.4207	2013	10	27	2.5	33.5	0	47	39.4	0.5	0.7
23.2768	35.2077	2013	10	27	2.3	25.1	8	5	48.8	0.9	0.9
23.3285	35.4065	2013	10	28	2.8	43.7	0	32	40.0	0.7	0.9
23.4403	35.4235	2013	10	28	1.6	45.9	1	47	53.5	0.6	0.8
23.3868	35.4558	2013	10	28	1.5	37.4	1	58	18.2	1.0	1.6
23.3597	35.4578	2013	10	28	1.5	40.0	6	54	53.1	1.0	1.5
23.3222	35.2015	2013	10	28	1.8	25.1	9	46	31.0	0.7	0.8
23.3350	35.4262	2013	10	28	1.5	30.6	10	10	8.1	1.2	2.0
23.3570	35.4158	2013	10	28	1.4	29.6	13	17	14.2	0.9	0.6
23.2328	35.3490	2013	10	28	1.4	30.2	17	23	6.7	1.4	2.5
23.4277	35.4635	2013	10	28	1.2	5.3	17	43	7.3	0.4	2.0
23.4108	35.3707	2013	10	28	1.7	43.0	22	16	42.9	1.2	0.9
23.3412	35.3280	2013	10	29	1.5	43.4	1	21	6.0	0.7	1.1
23.3917	35.4303	2013	10	29	1.7	40.7	11	17	7.1	0.9	1.3
23.3930	35.3595	2013	10	29	1.3	38.7	11	25	10.3	0.6	0.8
23.3712	35.3015	2013	10	29	3.1	37.2	14	14	46.0	0.8	0.9
23.2712	35.2600	2013	10	29	1.3	42.3	17	51	53.4	0.9	1.4
23.3257	35.3815	2013	10	29	1.5	52.0	21	19	33.7	1.5	0.9
23.2677	35.2628	2013	10	30	1.5	37.3	5	32	52.7	0.8	0.9
23.2855	35.2930	2013	10	30	1.7	35.3	8	42	17.0	0.6	0.9
23.3368	35.3713	2013	10	30	2.4	55.6	11	51	12.3	0.7	0.8
23.2970	35.3138	2013	10	30	1.5	41.8	17	4	1.5	0.7	1.0
23.2562	35.3375	2013	10	30	3.2	42.9	18	35	11.5	0.8	1.2
23.3558	35.3705	2013	10	30	2.2	44.6	18	36	45.4	0.9	1.1
23.3190	35.4120	2013	10	31	1.6	34.1	22	25	16.1	0.7	1.2
23.3468	35.3435	2013	10	31	1.9	46.7	23	19	31.7	0.8	1.0
23.3202	35.3238	2013	11	1	2.1	45.0	4	20	13.3	0.8	1.2

23.2860	35.3357	2013	11	1	1.9	50.6	7	13	29.7	1.1	1.2
23.3982	35.4767	2013	11	1	2.1	40.1	16	16	55.1	1.0	1.5
23.3128	35.3317	2013	11	1	2.2	47.8	20	20	52.0	0.8	1.0
23.3752	35.4273	2013	11	1	1.8	20.4	20	39	21.9	0.9	1.7
23.3853	35.4368	2013	11	2	1.6	31.9	18	45	36.5	0.6	0.9
23.2995	35.4108	2013	11	2	1.3	28.2	19	47	59.6	0.9	0.5
23.3013	35.2335	2013	11	2	1.4	40.0	22	34	32.6	0.7	1.1
23.3000	35.2455	2013	11	2	1.8	30.9	23	41	21.9	1.2	1.7
23.2927	35.3250	2013	11	3	1.5	27.7	6	26	56.9	1.6	1.2
23.2955	35.3732	2013	11	3	1.4	17.1	10	18	43.8	0.9	2.6
23.3602	35.3640	2013	11	3	1.5	25.6	10	44	15.2	0.5	0.8
23.4022	35.4295	2013	11	3	1.2	64.1	12	7	25.5	1.8	2.0
23.2840	35.3872	2013	11	3	1.8	56.9	17	34	28.8	1.1	1.5
23.4218	35.4602	2013	11	4	3.1	36.8	6	30	56.2	0.7	0.9
23.4058	35.4103	2013	11	4	1.8	48.2	6	37	5.8	0.7	0.7
23.2437	35.3323	2013	11	4	1.8	49.4	6	57	58.9	0.8	1.1
23.4030	35.3467	2013	11	4	2.5	44.6	9	26	50.2	0.6	0.9
23.3265	35.2655	2013	11	4	1.7	60.2	10	59	41.6	2.0	1.2
23.2790	35.3403	2013	11	4	1.8	23.1	20	16	50.7	0.7	1.6
23.3967	35.3647	2013	11	5	2.9	37.5	22	3	43.5	0.7	0.9
23.4198	35.4005	2013	11	8	3.0	36.8	0	6	50.5	0.7	0.9
23.2555	35.3170	2013	11	8	1.6	45.3	21	4	13.6	1.4	2.6

Catalogue of Chania 2016 swarm sequence

Longitude Degrees	Latitude Degrees	Year	Month	Day	Magnitude M_L	Depth (km)	Hour	Minutes	Seconds	Horizontal error	Vertical error
23.5638	35.3675	2016	1	31	1.7	16.1	0	0	38.0	0.4	1.3
23.6197	35.3682	2016	2	1	3.1	19.7	2	11	51.6	0.5	1.4
23.6345	35.3600	2016	2	1	3.1	22.9	2	19	57.2	0.5	0.4
23.6145	35.3528	2016	2	1	2.0	25.2	2	26	58.1	0.7	1.2
23.6422	35.3458	2016	2	2	2.4	12.5	6	57	5.7	0.7	2.8
23.6095	35.3618	2016	2	3	2.0	18.9	20	15	12.6	0.4	1.4
23.6085	35.3733	2016	2	5	3.0	13.8	2	52	27.8	0.6	2.0
23.6522	35.3592	2016	2	5	2.2	29.2	2	53	24.5	0.8	1.2
23.6375	35.3702	2016	2	8	2.5	19.0	10	35	5.1	0.5	1.0

23.6428	35.3745	2016	2	8	1.9	14.6	10	49	54.4	0.7	1.9
23.6303	35.3933	2016	2	8	2.5	14.8	12	0	52.7	0.6	1.9
23.6290	35.3878	2016	2	8	3.4	16.7	16	15	29.8	0.8	2.5
23.6263	35.3727	2016	2	8	1.4	15.0	16	19	33.8	0.6	4.2
23.6245	35.3900	2016	2	8	1.5	21.1	16	20	34.2	1.3	2.0
23.6352	35.3808	2016	2	8	1.8	21.2	16	29	58.8	0.8	1.4
23.6375	35.3697	2016	2	8	1.4	28.6	16	31	6.8	1.1	1.6
23.6268	35.3888	2016	2	8	2.1	18.2	16	41	50.1	0.4	1.2
23.6587	35.3738	2016	2	8	1.5	27.7	17	0	24.9	0.8	1.3
23.6547	35.3760	2016	2	8	1.9	27.9	17	2	50.5	0.9	1.4
23.6282	35.3607	2016	2	8	2.1	24.9	17	19	28.0	0.6	0.4
23.6160	35.3790	2016	2	8	1.4	23.6	18	6	1.1	0.6	0.6
23.6122	35.3803	2016	2	8	2.1	16.1	20	53	20.1	0.6	1.7
23.6290	35.3872	2016	2	9	2.0	19.2	0	2	35.9	0.4	0.9
23.6213	35.3875	2016	2	9	2.1	18.8	1	20	22.1	0.6	1.8
23.6270	35.3900	2016	2	9	1.8	20.1	9	43	42.5	0.4	0.8
23.6425	35.3827	2016	2	9	2.7	20.0	10	28	20.8	0.8	2.2
23.6323	35.3923	2016	2	9	1.9	18.0	12	19	19.2	0.6	1.4
23.6377	35.3752	2016	2	9	3.0	19.7	12	20	2.7	0.4	0.9
23.6573	35.3912	2016	2	9	1.8	25.3	12	21	20.1	0.9	0.8
23.6520	35.3853	2016	2	9	1.9	23.4	13	5	14.4	0.9	1.3
23.6122	35.3797	2016	2	9	1.7	16.0	15	59	55.0	0.5	1.7
23.6457	35.3483	2016	2	9	1.9	29.2	17	45	41.6	0.7	1.1
23.6270	35.3940	2016	2	9	2.1	15.7	18	17	59.0	0.6	1.8
23.6252	35.3740	2016	2	9	3.4	17.3	18	31	29.3	0.4	1.4
23.6453	35.3852	2016	2	9	1.5	13.7	18	34	38.7	0.7	5.1
23.6217	35.3723	2016	2	9	2.0	19.0	19	36	35.4	0.5	1.6
23.6188	35.3550	2016	2	9	1.7	25.8	20	49	55.9	0.8	1.3
23.6332	35.3663	2016	2	9	1.6	24.4	20	52	25.2	1.3	1.8
23.6353	35.3600	2016	2	9	1.9	31.1	20	52	58.6	0.8	0.6
23.6345	35.3715	2016	2	9	3.6	22.6	21	11	13.7	0.6	0.6
23.6178	35.3390	2016	2	9	2.1	27.8	21	12	57.2	0.8	1.2
23.6555	35.3807	2016	2	9	2.0	23.3	21	17	10.3	0.6	0.5
23.6348	35.3603	2016	2	9	1.8	21.9	21	21	13.9	1.2	2.0
23.6110	35.3612	2016	2	9	2.2	17.9	21	47	41.3	0.8	2.4
23.6477	35.3823	2016	2	9	1.8	12.0	22	4	15.4	0.5	1.2
23.6157	35.3673	2016	2	9	1.6	4.2	22	34	38.1	0.5	1.9
23.6520	35.3515	2016	2	9	1.7	26.5	23	47	28.4	1.3	2.1
23.6170	35.3870	2016	2	9	2.0	18.1	23	59	41.1	0.7	2.1
23.6613	35.3917	2016	2	10	2.1	23.2	6	8	31.2	0.6	0.5

23.6722	35.3742	2016	2	10	1.6	32.7	9	21	40.3	0.8	0.5
23.6510	35.3900	2016	2	10	2.1	16.2	9	26	16.6	0.6	2.1
23.6460	35.3762	2016	2	10	2.7	26.1	9	26	48.5	0.6	0.7
23.6278	35.3803	2016	2	10	2.0	20.0	13	43	31.1	0.5	1.2
23.6172	35.3688	2016	2	10	2.2	17.4	15	4	34.2	0.8	4.6
23.6305	35.3625	2016	2	10	2.5	23.6	15	8	9.6	0.6	0.5
23.6225	35.3825	2016	2	10	2.0	20.2	15	25	59.1	0.8	4.2
23.5533	35.3458	2016	2	10	2.2	10.5	22	24	23.6	1.3	0.6
23.6263	35.3680	2016	2	11	1.7	17.0	16	8	39.5	1.2	7.6
23.6455	35.3937	2016	2	11	2.2	19.0	22	7	0.7	0.5	1.4
23.6360	35.3695	2016	2	11	1.7	0.0	22	10	21.2	0.5	1.0
23.6425	35.3965	2016	2	12	1.9	15.6	5	14	16.8	0.4	1.3
23.6122	35.3890	2016	2	12	2.2	19.1	23	15	30.3	0.6	1.8
23.5897	35.3553	2016	2	14	1.5	16.9	2	47	6.7	0.9	6.0
23.6258	35.3768	2016	2	16	2.7	16.9	4	0	37.1	0.5	1.7
23.6163	35.3640	2016	2	16	2.1	6.0	20	28	40.3	0.4	1.7
23.6333	35.3645	2016	2	17	2.2	19.5	0	53	16.4	0.5	1.7
23.6318	35.3863	2016	2	17	1.9	18.3	4	42	13.7	0.4	1.2
23.6435	35.3628	2016	2	17	1.9	25.7	15	48	20.2	0.8	1.3
23.6265	35.3735	2016	2	17	2.0	17.7	23	53	47.4	0.5	1.7
23.6253	35.3550	2016	2	18	1.6	24.7	0	13	45.2	1.0	1.4
23.6723	35.3762	2016	2	22	1.7	23.8	13	59	31.5	0.6	0.6
23.6235	35.3932	2016	2	24	1.8	18.1	21	52	33.1	1.6	1.2
23.6318	35.3650	2016	2	26	1.6	23.9	21	59	33.5	0.9	0.9
23.6402	35.3953	2016	2	27	2.1	22.0	10	12	41.5	0.7	0.6
23.6385	35.3765	2016	2	28	1.6	22.7	2	9	46.1	0.7	0.7
23.6338	35.3743	2016	2	28	2.5	17.3	20	50	48.4	0.7	1.5
23.6387	35.3578	2016	3	1	1.7	25.3	23	4	31.2	1.0	1.7
23.6347	35.4045	2016	3	2	1.7	21.0	1	28	0.6	0.5	1.2
23.6565	35.3913	2016	3	3	1.9	14.9	16	1	27.4	0.4	1.3
23.6425	35.3972	2016	3	3	2.5	21.8	21	25	32.3	0.6	0.6
23.6365	35.3718	2016	3	5	2.7	22.8	23	5	2.4	0.4	0.4
23.6138	35.3582	2016	3	5	1.6	20.4	23	13	47.9	0.9	1.4
23.6525	35.3440	2016	3	5	1.7	31.5	23	30	6.2	0.8	0.6
23.6503	35.4030	2016	3	6	2.1	22.0	8	28	24.2	0.6	0.3
23.6077	35.3677	2016	3	6	2.8	11.2	8	29	34.7	0.7	1.9
23.6243	35.3595	2016	3	6	1.5	21.7	8	31	52.9	1.1	1.2
23.6635	35.3735	2016	3	6	1.6	23.8	8	33	50.9	0.7	0.6
23.6907	35.3910	2016	3	6	1.7	25.0	8	47	41.2	0.5	0.4
23.6403	35.3827	2016	3	6	1.6	21.8	8	53	49.6	0.6	0.6

23.6385	35.3840	2016	3	6	2.2	20.3	11	23	1.1	0.5	1.1
23.6355	35.3992	2016	3	6	2.6	22.6	11	51	15.9	0.4	0.2
23.6630	35.3880	2016	3	6	1.7	25.0	12	31	57.1	0.6	0.3
23.6210	35.3637	2016	3	6	1.6	15.5	13	35	29.6	0.4	1.5
23.6400	35.3725	2016	3	6	1.8	16.4	18	28	23.3	1.2	4.2
23.6280	35.3800	2016	3	6	2.0	18.1	18	52	8.0	0.6	1.9
23.6347	35.3927	2016	3	6	4.0	20.3	23	18	16.1	0.5	1.1
23.6475	35.3975	2016	3	6	3.3	21.9	23	22	49.7	0.6	0.3
23.6482	35.3837	2016	3	6	2.2	17.5	23	25	19.7	0.5	1.1
23.6187	35.3643	2016	3	6	2.0	22.7	23	25	58.8	0.9	0.9
23.6255	35.3903	2016	3	6	2.2	21.3	23	32	34.0	0.7	0.7
23.6583	35.3703	2016	3	6	2.0	24.3	23	33	6.1	0.7	0.6
23.6125	35.3773	2016	3	6	1.9	9.0	23	36	29.0	1.2	8.6
23.6078	35.3790	2016	3	6	2.1	20.7	23	37	39.9	0.5	1.0
23.6310	35.3668	2016	3	6	2.0	25.4	23	38	10.8	0.6	0.6
23.6350	35.3683	2016	3	6	2.0	25.3	23	39	46.9	0.8	0.7
23.6407	35.3528	2016	3	6	1.8	21.7	23	42	50.1	0.9	0.9
23.6137	35.3608	2016	3	6	1.8	22.9	23	43	45.6	1.4	1.4
23.6287	35.3668	2016	3	6	1.9	23.9	23	46	27.9	0.6	0.6
23.6307	35.3910	2016	3	6	1.9	22.4	23	59	12.2	0.7	0.7
23.6473	35.3923	2016	3	7	2.4	23.8	0	1	48.8	0.7	0.3
23.5960	35.3652	2016	3	7	2.0	10.1	0	2	42.7	0.5	2.7
23.6133	35.3535	2016	3	7	2.1	23.1	0	9	17.7	1.2	1.2
23.6162	35.3897	2016	3	7	1.8	16.3	0	10	54.5	0.4	1.3
23.6043	35.3642	2016	3	7	2.6	14.6	0	19	14.9	0.4	1.2
23.6388	35.3672	2016	3	7	1.8	21.1	0	21	37.0	0.7	0.8
23.5983	35.3482	2016	3	7	1.6	4.0	0	23	5.2	1.3	6.2
23.6162	35.3837	2016	3	7	2.8	16.5	0	27	7.3	0.4	1.0
23.6298	35.3680	2016	3	7	2.8	22.6	0	27	18.3	0.6	0.3
23.6183	35.3842	2016	3	7	2.0	13.9	0	32	37.4	0.5	1.8
23.6292	35.3710	2016	3	7	2.4	18.3	0	33	22.4	0.6	1.4
23.6243	35.3745	2016	3	7	2.1	16.8	0	37	3.7	0.5	1.4
23.6103	35.3788	2016	3	7	2.0	18.3	0	37	57.4	0.4	1.1
23.6163	35.3757	2016	3	7	1.9	11.5	0	38	20.3	0.4	1.6
23.6427	35.4112	2016	3	7	2.0	21.2	0	39	23.2	1.7	0.6
23.6017	35.3590	2016	3	7	2.1	18.5	0	41	15.9	2.1	2.5
23.5857	35.3545	2016	3	7	3.4	15.4	0	41	45.5	1.0	1.5
23.6575	35.4178	2016	3	7	1.6	21.8	0	50	13.8	1.7	0.5
23.6722	35.4160	2016	3	7	1.5	19.3	0	57	45.0	3.1	2.1
23.6765	35.4365	2016	3	7	2.2	21.5	1	0	13.2	2.5	0.6

23.6218	35.3535	2016	3	7	1.9	2.8	1	0	54.9	1.4	2.6
23.6703	35.4267	2016	3	7	2.0	23.8	1	5	17.4	2.8	0.7
23.6347	35.4083	2016	3	7	2.1	18.3	1	10	37.5	1.8	1.1
23.6410	35.4167	2016	3	7	2.2	20.7	1	18	36.9	1.1	0.7
23.6220	35.3807	2016	3	7	3.5	17.9	1	27	26.9	1.2	1.2
23.6142	35.3822	2016	3	7	2.5	16.3	1	28	34.9	1.6	1.5
23.6410	35.4197	2016	3	7	1.8	18.7	1	33	20.6	1.6	0.9
23.6460	35.3943	2016	3	7	2.1	21.4	1	41	37.5	1.7	0.7
23.6577	35.4333	2016	3	7	1.9	23.2	1	47	43.4	1.7	0.4
23.6325	35.4028	2016	3	7	1.9	18.9	1	53	22.7	1.4	0.9
23.6940	35.4343	2016	3	7	2.0	24.3	2	4	47.5	2.3	0.5
23.6152	35.3782	2016	3	7	1.7	15.5	2	9	35.3	1.6	2.0
23.6412	35.4022	2016	3	7	2.4	19.1	2	19	0.7	1.2	1.0
23.6427	35.4050	2016	3	7	1.9	21.4	2	21	20.3	1.5	0.5
23.5997	35.3348	2016	3	7	1.5	5.9	2	30	58.9	1.0	1.9
23.5992	35.3465	2016	3	7	1.5	18.2	2	45	17.4	1.0	3.3
23.6450	35.3737	2016	3	7	1.9	15.6	2	49	29.6	0.5	1.7
23.6485	35.4025	2016	3	7	1.8	15.1	2	58	52.5	0.5	1.4
23.6285	35.3830	2016	3	7	2.0	24.0	3	0	0.5	1.5	1.4
23.6292	35.3882	2016	3	7	2.9	19.9	3	6	2.5	0.5	1.0
23.6065	35.3793	2016	3	7	1.7	17.9	3	14	50.2	0.5	1.4
23.6215	35.3533	2016	3	7	2.3	23.2	3	18	46.5	0.9	0.8
23.6120	35.3953	2016	3	7	1.8	19.8	3	38	58.7	2.2	1.9
23.6398	35.4043	2016	3	7	3.3	20.5	3	39	42.4	0.4	0.8
23.6028	35.3768	2016	3	7	1.5	15.3	3	50	29.2	0.7	2.4
23.6040	35.3745	2016	3	7	2.0	14.3	4	1	19.1	0.7	2.7
23.6065	35.3628	2016	3	7	2.0	16.9	4	4	50.2	0.9	3.0
23.6415	35.3838	2016	3	7	1.9	16.7	4	6	26.0	0.6	1.7
23.6747	35.3773	2016	3	7	1.9	25.5	4	28	31.0	0.8	0.7
23.6675	35.3828	2016	3	7	2.0	24.3	4	32	57.4	1.2	1.0
23.6212	35.3598	2016	3	7	1.7	17.4	4	34	6.2	1.2	4.0
23.6415	35.3895	2016	3	7	2.5	18.5	4	49	55.2	0.5	1.1
23.6167	35.3713	2016	3	7	2.8	23.5	4	50	33.4	1.0	0.5
23.5995	35.3663	2016	3	7	2.0	17.3	5	12	6.8	0.5	1.4
23.6282	35.3805	2016	3	7	2.3	19.5	5	16	21.1	0.7	1.6
23.6375	35.3828	2016	3	7	1.9	16.4	5	28	55.8	2.2	2.0
23.6135	35.3947	2016	3	7	2.2	20.1	7	2	13.9	0.4	0.8
23.6427	35.3668	2016	3	7	1.9	23.8	9	0	42.9	1.3	1.2
23.6585	35.3970	2016	3	7	2.1	10.4	9	3	38.5	0.7	2.7
23.6365	35.3763	2016	3	7	1.8	22.7	9	4	13.6	0.7	0.7

23.6562	35.3855	2016	3	7	2.4	25.4	10	29	39.8	0.8	0.5
23.6622	35.3972	2016	3	7	2.7	20.5	10	29	49.5	0.4	0.8
23.6563	35.4000	2016	3	7	2.4	23.2	10	45	9.0	0.7	0.6
23.6593	35.3983	2016	3	7	2.2	24.2	11	10	54.7	0.7	0.6
23.6667	35.3768	2016	3	7	1.9	25.3	12	49	11.6	0.6	0.5
23.6242	35.3887	2016	3	7	3.9	17.2	14	25	15.2	0.5	1.1
23.6363	35.3672	2016	3	7	2.3	18.2	14	29	3.1	0.4	1.0
23.6533	35.3958	2016	3	7	2.0	18.6	14	31	59.4	0.4	1.1
23.6217	35.3875	2016	3	7	2.2	18.3	14	45	42.8	0.6	1.7
23.6268	35.3927	2016	3	7	3.5	18.6	15	19	45.6	0.5	1.1
23.6132	35.3688	2016	3	7	2.1	16.6	15	34	10.5	0.8	2.8
23.6342	35.3768	2016	3	7	2.2	25.6	16	2	20.2	1.0	1.0
23.6308	35.3428	2016	3	7	2.0	23.4	16	9	32.4	2.0	0.9
23.6488	35.3953	2016	3	7	2.0	22.3	16	22	8.3	0.8	0.7
23.6550	35.3882	2016	3	7	2.1	12.8	16	30	50.5	0.5	1.7
23.6368	35.3942	2016	3	7	2.0	15.0	16	51	6.7	0.7	2.1
23.6367	35.3893	2016	3	7	3.0	16.5	17	13	59.5	0.4	1.0
23.6052	35.3543	2016	3	7	2.2	18.9	17	28	58.9	0.9	2.9
23.6332	35.3732	2016	3	7	1.9	10.9	18	5	32.0	2.2	4.1
23.6378	35.3910	2016	3	7	3.2	19.6	18	46	44.5	0.4	0.9
23.6112	35.3773	2016	3	7	2.1	19.1	18	49	42.5	0.7	2.0
23.6278	35.4193	2016	3	7	2.1	19.8	19	45	7.0	1.6	0.9
23.6468	35.4167	2016	3	7	2.6	23.3	19	47	13.8	1.5	0.5
23.6370	35.3937	2016	3	7	2.1	13.1	20	20	46.7	0.4	1.3
23.6300	35.3598	2016	3	7	2.1	9.5	20	31	10.4	0.5	2.8
23.6183	35.3597	2016	3	7	1.9	11.4	20	32	18.7	0.7	2.8
23.6430	35.4027	2016	3	7	2.5	23.1	22	48	0.4	2.0	0.7
23.6200	35.3987	2016	3	7	1.8	21.3	22	53	58.1	2.1	0.9
23.6143	35.3827	2016	3	7	1.8	17.8	23	37	28.4	1.9	2.0
23.6555	35.4012	2016	3	8	2.2	16.5	0	2	6.2	1.7	1.1
23.6637	35.3938	2016	3	8	2.1	19.4	0	2	20.9	1.8	1.0
23.6473	35.4265	2016	3	8	1.7	21.3	0	57	18.9	1.9	1.0
23.6462	35.3975	2016	3	8	1.8	17.3	2	55	6.1	1.9	1.8
23.6323	35.3582	2016	3	8	2.2	17.8	4	32	58.7	0.6	1.8
23.6322	35.4000	2016	3	8	2.3	17.3	5	14	16.0	0.6	1.4
23.6418	35.3778	2016	3	8	2.4	16.2	5	52	12.7	0.5	1.2
23.6177	35.3615	2016	3	8	1.7	13.8	7	20	52.2	0.8	3.3
23.6222	35.3683	2016	3	8	2.3	20.2	7	47	7.2	0.7	1.6
23.5768	35.3482	2016	3	8	1.7	10.9	8	28	20.3	0.4	2.1
23.6275	35.3958	2016	3	8	2.5	20.5	8	41	50.3	0.4	0.8

23.6437	35.3880	2016	3	8	2.2	21.7	9	3	4.3	1.0	0.9
23.6533	35.3935	2016	3	8	2.1	18.7	9	12	31.8	0.4	1.1
23.6415	35.3817	2016	3	8	2.2	23.3	12	20	20.3	1.2	1.1
23.6197	35.3592	2016	3	8	2.1	20.8	15	26	19.7	0.6	0.6
23.6337	35.3825	2016	3	8	2.8	23.4	15	43	2.4	0.6	0.3
23.6222	35.3935	2016	3	8	2.0	23.6	15	48	28.0	0.8	0.8
23.6477	35.3857	2016	3	8	2.3	19.6	17	41	16.8	0.4	0.9
23.6412	35.3908	2016	3	8	3.6	22.5	18	25	3.7	0.5	0.3
23.6453	35.3675	2016	3	8	1.9	26.5	18	39	27.2	0.6	0.6
23.6530	35.3705	2016	3	8	1.4	25.0	18	42	48.3	2.1	0.5
23.6328	35.3553	2016	3	8	2.0	17.0	18	45	40.1	0.8	2.0
23.6403	35.3850	2016	3	8	2.1	15.1	19	8	4.1	0.4	1.0
23.6553	35.3893	2016	3	8	3.1	21.5	19	15	28.9	0.6	0.6
23.6223	35.3965	2016	3	8	2.5	18.6	19	33	33.0	0.4	0.8
23.6383	35.3970	2016	3	8	3.0	18.3	19	33	37.5	0.5	1.1
23.6363	35.3993	2016	3	8	1.9	21.2	19	47	59.1	0.5	0.5
23.6302	35.4035	2016	3	8	2.1	19.1	20	2	9.4	0.4	0.8
23.6177	35.3658	2016	3	8	2.3	15.8	20	8	58.2	0.4	1.0
23.6217	35.3847	2016	3	8	2.1	18.5	20	17	41.8	0.5	1.4
23.6377	35.3880	2016	3	8	2.4	22.9	20	21	16.9	0.9	0.8
23.6255	35.3850	2016	3	8	1.9	20.1	20	55	42.5	0.4	1.1
23.6223	35.3720	2016	3	8	2.1	14.1	21	16	35.7	0.5	1.4
23.6447	35.3832	2016	3	8	2.1	22.6	23	40	59.6	0.7	0.7
23.6125	35.3863	2016	3	9	2.6	15.6	0	2	54.6	0.6	1.4
23.5980	35.3838	2016	3	9	2.4	17.9	0	20	3.5	0.6	1.3
23.6307	35.3845	2016	3	9	2.4	13.9	1	1	56.5	0.5	1.4
23.6262	35.4158	2016	3	9	1.5	15.2	1	28	59.0	1.4	1.1
23.6320	35.3840	2016	3	9	1.5	19.5	2	36	7.9	0.8	2.3
23.6395	35.4078	2016	3	9	1.9	17.4	3	54	36.3	0.4	1.0
23.6110	35.3900	2016	3	9	1.7	19.4	4	42	50.4	0.6	1.4
23.6383	35.3912	2016	3	9	1.8	17.6	6	53	31.3	0.4	1.2
23.6428	35.4142	2016	3	9	1.7	20.4	7	16	28.6	0.4	1.0
23.6098	35.3792	2016	3	9	3.9	18.0	8	4	8.0	0.4	0.9
23.6313	35.3888	2016	3	9	2.2	22.1	8	9	50.8	0.5	0.5
23.6358	35.3912	2016	3	9	2.0	16.4	8	38	12.2	0.4	1.1
23.6290	35.4010	2016	3	9	2.4	20.5	12	7	45.2	0.6	1.2
23.6513	35.3967	2016	3	9	2.5	24.2	12	12	32.3	0.9	0.5
23.6080	35.3613	2016	3	9	2.0	17.8	14	34	28.7	0.6	1.8
23.6178	35.3698	2016	3	9	1.8	21.8	19	20	51.3	1.3	0.6
23.6272	35.3947	2016	3	9	2.1	16.5	23	9	50.1	0.4	1.1

23.6265	35.3940	2016	3	9	2.5	17.1	23	12	32.0	0.4	1.0
23.6333	35.4082	2016	3	9	2.3	20.0	23	33	8.0	1.5	1.1
23.6472	35.4268	2016	3	9	2.0	22.1	23	39	50.9	2.1	0.6
23.6345	35.4163	2016	3	9	2.2	22.0	23	42	44.7	1.6	0.5
23.6387	35.4123	2016	3	9	2.2	17.7	23	48	11.9	2.3	1.5
23.6352	35.3628	2016	3	10	1.7	24.1	0	31	29.8	2.2	0.9
23.6287	35.3595	2016	3	10	1.7	15.1	1	3	15.4	3.8	5.5
23.6228	35.3465	2016	3	10	1.6	4.4	1	28	48.8	0.7	1.8
23.6660	35.4342	2016	3	10	2.4	20.2	1	31	59.2	1.2	0.7
23.6580	35.4082	2016	3	10	2.1	21.0	1	43	50.2	1.4	0.5
23.6255	35.3828	2016	3	10	2.2	16.3	2	2	58.8	2.2	2.6
23.6110	35.3985	2016	3	10	1.7	19.7	2	46	42.2	1.7	1.1
23.6458	35.4093	2016	3	10	2.1	21.2	3	6	11.1	1.4	0.5
23.5943	35.3422	2016	3	10	1.8	0.0	3	8	24.8	1.4	1.6
23.6523	35.3957	2016	3	10	2.5	21.5	3	9	38.6	1.4	0.5
23.6045	35.3478	2016	3	10	2.0	13.1	3	13	9.2	2.3	3.6
23.6718	35.4167	2016	3	10	3.1	25.3	3	33	0.3	1.7	0.5
23.5807	35.3385	2016	3	10	2.7	17.0	3	33	44.3	2.0	3.0
23.5932	35.3502	2016	3	10	1.6	5.9	3	58	42.5	1.0	1.9
23.6387	35.3817	2016	3	10	1.8	9.7	4	35	41.7	0.4	2.5
23.6608	35.3935	2016	3	10	2.7	18.7	4	42	2.0	0.5	0.9
23.6255	35.3917	2016	3	10	2.6	16.5	5	18	28.1	0.5	1.2
23.6212	35.3792	2016	3	10	2.0	14.1	5	25	0.8	0.4	1.6
23.6360	35.3802	2016	3	10	2.0	23.0	5	29	59.4	0.9	0.8
23.6425	35.3895	2016	3	10	3.2	22.0	5	46	1.9	0.6	0.3
23.6477	35.3683	2016	3	10	1.9	24.5	5	56	37.0	1.2	1.1
23.6685	35.3752	2016	3	10	1.9	23.5	6	38	0.4	0.7	0.6
23.6517	35.3733	2016	3	10	1.9	22.6	6	47	19.0	1.0	0.9
23.6470	35.3928	2016	3	10	2.4	23.1	7	1	51.3	0.8	0.4
23.6455	35.3857	2016	3	10	2.0	21.6	7	10	38.1	0.9	0.8
23.6297	35.3893	2016	3	10	1.9	21.3	7	38	48.4	0.7	0.7
23.6525	35.4290	2016	3	10	2.1	21.6	8	3	34.7	1.5	0.4
23.6402	35.3558	2016	3	10	1.8	27.7	8	40	0.7	2.5	0.9
23.6250	35.3712	2016	3	10	1.6	19.4	9	6	19.6	2.0	2.0
23.6382	35.3817	2016	3	10	2.2	22.9	10	14	45.3	0.9	0.8
23.6425	35.3885	2016	3	10	1.9	23.7	10	28	5.0	0.6	0.5
23.6580	35.3697	2016	3	10	1.9	26.6	10	55	15.8	0.9	0.8
23.6315	35.3800	2016	3	10	2.1	16.2	11	37	56.0	0.4	1.1
23.6448	35.3745	2016	3	10	2.3	22.4	12	38	58.6	0.6	0.3
23.6177	35.3832	2016	3	10	2.6	21.9	12	56	20.6	0.6	0.3

23.6298	35.3847	2016	3	10	2.1	25.6	14	51	38.1	0.8	0.8
23.6380	35.3875	2016	3	10	2.0	16.0	15	47	35.0	0.4	1.1
23.6145	35.3807	2016	3	10	2.1	18.8	15	49	58.6	0.5	1.2
23.6405	35.3553	2016	3	10	1.7	23.3	15	56	19.4	0.6	0.6
23.6378	35.3930	2016	3	10	2.7	23.1	16	2	8.5	0.5	0.3
23.6483	35.3935	2016	3	10	3.0	19.4	17	51	23.3	1.2	1.0
23.6213	35.3885	2016	3	10	2.0	17.8	17	58	41.3	1.7	1.4
23.6430	35.4160	2016	3	10	2.1	22.7	18	42	58.6	2.1	0.7
23.6380	35.4122	2016	3	10	1.8	18.6	19	29	36.1	1.5	0.9
23.6427	35.3958	2016	3	10	2.1	18.4	19	33	30.2	1.7	1.2
23.6543	35.4093	2016	3	10	1.7	16.1	20	8	49.9	0.4	1.1
23.6345	35.3773	2016	3	10	1.7	11.9	20	42	13.1	0.6	1.6
23.6440	35.3937	2016	3	10	2.1	17.2	22	36	32.8	0.3	0.8
23.6255	35.3647	2016	3	10	2.4	14.4	22	40	28.0	0.5	1.5
23.6207	35.3767	2016	3	10	2.3	14.8	23	3	57.2	0.5	1.4
23.6175	35.3845	2016	3	11	1.8	12.0	1	9	27.5	0.6	1.6
23.6320	35.4007	2016	3	11	1.9	16.7	1	36	37.4	1.2	1.0
23.6390	35.3948	2016	3	11	1.8	21.0	3	17	56.7	0.7	0.6
23.6312	35.3960	2016	3	11	1.6	11.4	3	21	11.0	0.9	3.2
23.6400	35.3947	2016	3	11	2.0	20.1	3	32	55.6	0.4	0.7
23.6170	35.3960	2016	3	11	2.6	19.0	4	57	0.5	1.9	1.7
23.6283	35.3970	2016	3	11	2.5	19.4	7	0	43.9	0.5	1.1
23.6385	35.3838	2016	3	11	2.3	18.2	7	28	3.0	0.5	1.0
23.6148	35.3888	2016	3	11	1.8	13.4	7	30	7.2	0.4	1.5
23.6240	35.4068	2016	3	11	1.6	16.4	8	45	45.9	0.6	1.4
23.6390	35.3892	2016	3	11	2.1	17.1	9	14	53.7	0.3	0.8
23.6420	35.3873	2016	3	11	2.2	22.2	9	21	49.8	0.8	0.8
23.6255	35.3917	2016	3	11	2.2	19.3	10	5	36.3	0.4	0.8
23.6235	35.3933	2016	3	11	2.3	17.3	11	13	6.2	0.4	0.8
23.6227	35.3898	2016	3	11	1.7	17.4	16	32	31.2	0.5	1.3
23.6325	35.3770	2016	3	11	2.7	22.4	19	3	14.6	0.9	0.5
23.6257	35.3975	2016	3	11	1.6	16.6	19	48	2.0	0.5	1.2
23.6440	35.3983	2016	3	11	2.6	23.7	21	51	49.0	0.9	0.5
23.6315	35.3683	2016	3	11	1.7	22.2	22	19	9.8	1.4	1.4
23.6218	35.3910	2016	3	11	2.4	20.1	22	36	20.8	0.5	1.0
23.6078	35.3838	2016	3	11	1.9	9.1	22	56	30.4	0.5	3.2
23.6200	35.3808	2016	3	11	2.8	19.0	23	59	47.3	1.5	1.5
23.6323	35.3663	2016	3	12	2.6	21.0	0	0	9.2	1.3	0.8
23.6520	35.4243	2016	3	12	2.0	22.7	0	1	31.3	2.0	0.6
23.6403	35.3902	2016	3	12	1.4	13.1	0	11	32.8	2.4	3.3

23.6387	35.4212	2016	3	12	2.2	22.8	0	22	15.4	2.1	0.7
23.6662	35.4347	2016	3	12	1.8	24.1	0	55	35.9	1.9	0.5
23.6018	35.3753	2016	3	12	2.4	15.9	1	26	49.0	1.3	1.8
23.6122	35.3850	2016	3	12	2.0	17.6	1	40	47.7	1.9	2.1
23.6080	35.3745	2016	3	12	3.0	16.0	1	44	4.0	0.9	1.2
23.6330	35.3953	2016	3	12	1.8	19.0	2	11	2.2	1.7	1.1
23.6122	35.4047	2016	3	12	1.8	13.4	3	3	22.8	1.4	1.3
23.6140	35.3888	2016	3	12	2.1	16.8	5	0	26.1	0.5	1.2
23.6385	35.4067	2016	3	12	1.8	17.5	5	13	16.4	0.4	0.9
23.6257	35.3977	2016	3	12	4.0	21.9	7	49	59.1	1.8	0.8
23.6198	35.4085	2016	3	12	2.2	18.0	7	56	17.9	1.3	0.8
23.6467	35.4255	2016	3	12	2.0	23.1	8	7	52.8	1.6	0.4
23.6220	35.3985	2016	3	12	2.1	18.8	8	18	26.4	1.3	0.9
23.6373	35.4150	2016	3	12	2.8	22.2	9	55	31.5	2.0	0.7
23.6655	35.4237	2016	3	12	2.6	25.1	9	59	3.2	1.4	0.4
23.6477	35.4042	2016	3	12	2.8	23.3	10	10	54.9	1.5	0.5
23.6393	35.4247	2016	3	12	2.3	17.6	10	12	27.2	1.5	0.8
23.6122	35.3595	2016	3	12	2.1	13.5	10	17	36.3	0.7	2.2
23.6180	35.3910	2016	3	12	1.9	13.0	10	19	33.2	2.3	2.6
23.6457	35.3868	2016	3	12	1.7	22.5	10	29	16.4	1.1	1.0
23.6115	35.3683	2016	3	12	2.4	23.8	10	44	39.7	0.8	0.4
23.6260	35.3937	2016	3	12	2.2	15.8	10	47	31.5	0.5	1.2
23.6395	35.3968	2016	3	12	3.0	19.7	11	18	8.0	0.4	0.9
23.6152	35.3767	2016	3	12	2.1	14.1	11	35	10.5	0.5	1.5
23.6423	35.3808	2016	3	12	2.7	21.8	11	38	6.8	0.5	0.5
23.6583	35.3968	2016	3	12	2.5	17.9	11	39	38.6	0.5	1.0
23.6078	35.3612	2016	3	12	2.0	11.7	11	44	51.4	0.7	1.9
23.6365	35.3880	2016	3	12	2.4	24.0	11	49	14.4	0.8	0.4
23.6163	35.3902	2016	3	12	2.1	14.9	12	12	0.3	0.5	1.2
23.5992	35.3665	2016	3	12	4.8	16.3	12	40	39.5	0.5	1.5
23.6103	35.3772	2016	3	12	2.7	18.0	12	47	15.2	0.7	1.5
23.6240	35.3857	2016	3	12	1.9	19.5	12	56	57.9	0.8	1.7
23.6367	35.4042	2016	3	12	2.4	19.5	13	13	16.1	1.4	1.1
23.6177	35.3638	2016	3	12	1.8	2.8	13	14	45.4	0.5	1.3
23.6110	35.3662	2016	3	12	2.8	19.8	13	27	18.1	0.5	1.2
23.6097	35.3630	2016	3	12	2.4	22.5	13	49	59.4	0.6	0.3
23.6270	35.3915	2016	3	12	2.5	14.7	13	59	9.6	0.5	1.2
23.6252	35.3937	2016	3	12	2.7	17.0	14	8	5.3	0.4	1.0
23.6270	35.3860	2016	3	12	3.4	19.7	14	14	35.2	0.4	0.8
23.6125	35.3922	2016	3	12	2.2	17.9	14	18	40.0	0.4	1.1

23.6297	35.3728	2016	3	12	1.9	21.6	14	28	14.1	1.0	1.0
23.6218	35.3990	2016	3	12	2.4	20.5	14	34	10.7	0.4	0.9
23.5972	35.3752	2016	3	12	3.2	16.8	14	37	15.3	0.5	1.3
23.6237	35.3877	2016	3	12	1.6	5.6	14	51	13.4	0.5	1.8
23.6037	35.3865	2016	3	12	2.7	21.0	15	5	53.0	0.7	0.5
23.6178	35.3927	2016	3	12	2.3	20.1	15	14	24.6	0.7	1.6
23.6053	35.3695	2016	3	12	2.6	13.8	15	18	25.3	0.7	2.1
23.6320	35.3750	2016	3	12	3.9	19.2	15	22	23.7	0.4	0.9
23.6052	35.3773	2016	3	12	2.5	17.6	15	28	25.1	0.6	1.4
23.6030	35.3695	2016	3	12	2.2	1.0	15	47	17.8	0.7	1.4
23.6178	35.3827	2016	3	12	2.0	11.7	16	3	26.5	0.4	1.2
23.6607	35.4023	2016	3	12	2.3	16.4	16	11	47.9	1.4	1.3
23.6112	35.3793	2016	3	12	2.9	12.4	16	26	26.9	1.6	2.7
23.6395	35.3903	2016	3	12	2.6	17.7	16	29	14.9	1.4	1.3
23.6570	35.3933	2016	3	12	1.8	17.5	16	40	7.4	1.9	1.8
23.7010	35.4387	2016	3	12	2.3	24.9	16	53	42.1	1.8	0.4
23.6228	35.3717	2016	3	12	2.3	19.2	16	59	31.1	1.5	1.5
23.6172	35.3717	2016	3	12	2.0	11.1	17	4	24.0	1.6	3.1
23.6420	35.4167	2016	3	12	2.3	17.1	17	9	15.8	1.4	1.2
23.6245	35.3740	2016	3	12	2.5	25.1	17	9	37.8	1.5	0.6
23.6440	35.4228	2016	3	12	2.6	20.7	17	24	8.6	1.3	0.8
23.6300	35.3788	2016	3	12	1.7	9.9	17	25	59.6	2.9	7.4
23.6485	35.4275	2016	3	12	2.5	24.6	17	37	40.4	1.7	0.5
23.6113	35.3948	2016	3	12	2.5	18.2	18	4	51.3	1.7	1.6
23.6408	35.3820	2016	3	12	3.1	23.7	18	14	6.0	1.1	0.6
23.6078	35.3848	2016	3	12	2.3	16.1	18	25	48.1	0.5	1.4
23.6090	35.3680	2016	3	12	1.7	2.1	19	4	22.0	0.7	1.7
23.6605	35.4060	2016	3	12	2.0	15.4	19	12	14.9	0.6	1.6
23.6025	35.3897	2016	3	12	2.2	17.9	19	33	20.8	0.5	1.2
23.6090	35.3897	2016	3	12	2.4	16.7	20	1	55.2	0.5	1.2
23.6237	35.3925	2016	3	12	2.4	22.9	20	2	15.6	0.6	0.3
23.6148	35.3992	2016	3	12	2.6	14.5	20	21	12.3	0.5	1.3
23.5895	35.3712	2016	3	12	1.9	15.1	20	24	51.9	0.5	2.0
23.6570	35.3830	2016	3	12	3.3	18.7	20	35	38.0	0.5	1.1
23.6415	35.4022	2016	3	12	1.9	20.1	20	43	20.1	0.6	1.5
23.6395	35.3863	2016	3	12	2.5	15.8	20	44	21.9	0.4	1.0
23.6208	35.3768	2016	3	12	2.5	19.4	20	45	4.6	0.5	1.1
23.6123	35.3883	2016	3	12	3.0	20.4	20	59	50.5	0.4	0.8
23.6677	35.3687	2016	3	12	1.9	13.0	21	7	44.5	1.7	6.2
23.5912	35.3697	2016	3	12	1.8	9.5	21	19	22.8	0.7	5.3

23.6567	35.3837	2016	3	12	2.1	25.4	21	27	51.6	1.3	1.2
23.6375	35.3818	2016	3	12	1.8	7.1	21	51	21.8	0.4	1.2
23.6235	35.3653	2016	3	12	1.7	12.8	22	7	43.8	0.5	2.1
23.6612	35.3982	2016	3	12	2.0	21.5	22	9	3.8	0.9	0.8
23.6178	35.3565	2016	3	12	2.1	11.2	22	26	30.5	0.7	2.9
23.6430	35.3800	2016	3	12	2.4	15.1	23	31	44.5	0.5	1.3
23.6445	35.3887	2016	3	12	2.7	15.2	23	33	33.0	0.6	1.5
23.6283	35.3713	2016	3	13	2.1	11.0	0	48	41.2	0.6	2.1
23.5955	35.3503	2016	3	13	2.0	17.1	0	52	57.1	0.9	3.0
23.6497	35.3843	2016	3	13	2.0	8.4	1	37	34.3	0.5	3.8
23.6345	35.3880	2016	3	13	2.1	22.9	2	17	36.9	0.7	0.7
23.6390	35.3838	2016	3	13	2.4	17.3	2	23	49.3	0.5	1.2
23.6178	35.3775	2016	3	13	2.8	13.0	2	26	21.7	0.6	1.6
23.6295	35.3803	2016	3	13	2.2	16.8	2	31	35.6	0.6	1.3
23.6265	35.3947	2016	3	13	2.5	16.4	2	41	7.6	0.5	1.2
23.6015	35.3935	2016	3	13	2.1	14.4	2	43	15.6	0.5	1.9
23.6252	35.3920	2016	3	13	1.9	15.3	3	5	30.6	0.5	1.5
23.6110	35.3758	2016	3	13	2.1	16.1	3	51	33.4	0.5	1.2
23.6445	35.3870	2016	3	13	2.3	15.6	4	17	50.2	0.4	0.9
23.6193	35.3892	2016	3	13	1.7	16.4	4	27	53.5	0.4	1.3
23.6190	35.3878	2016	3	13	2.0	20.4	4	38	7.0	0.6	1.4
23.6242	35.3720	2016	3	13	2.2	12.8	4	54	58.0	0.5	1.5
23.6282	35.3925	2016	3	13	1.9	18.6	5	14	49.4	0.6	1.6
23.6273	35.4000	2016	3	13	1.9	14.6	5	23	14.4	0.4	1.2
23.6373	35.3947	2016	3	13	1.8	18.5	5	41	8.1	0.4	1.1
23.6017	35.3713	2016	3	13	1.5	10.2	5	48	3.9	0.7	4.1
23.6130	35.3855	2016	3	13	1.7	12.2	5	50	35.4	0.8	3.1
23.6035	35.3938	2016	3	13	1.7	12.7	5	53	15.6	0.8	3.2
23.5972	35.3613	2016	3	13	1.9	11.5	6	4	29.3	0.6	2.5
23.6142	35.3730	2016	3	13	2.6	22.1	6	6	1.4	0.6	0.3
23.6072	35.3697	2016	3	13	1.9	17.5	6	14	32.3	0.4	1.3
23.6430	35.3855	2016	3	13	1.8	15.3	6	23	43.8	0.4	1.3
23.6723	35.3988	2016	3	13	1.8	21.4	6	47	36.1	0.5	0.5
23.6312	35.3945	2016	3	13	2.7	22.6	6	49	6.2	0.6	0.3
23.6027	35.3760	2016	3	13	2.0	18.9	7	28	38.8	0.8	2.4
23.6435	35.3868	2016	3	13	2.1	23.7	7	39	25.8	1.3	1.2
23.6192	35.3995	2016	3	13	2.0	16.7	7	48	34.3	0.5	1.5
23.6237	35.3997	2016	3	13	1.8	15.4	8	9	50.0	0.5	0.8
23.6363	35.3987	2016	3	13	2.3	17.9	8	11	12.4	0.5	0.8
23.6593	35.4015	2016	3	13	2.1	22.1	8	26	7.9	0.7	0.6

23.6340	35.3810	2016	3	13	1.9	13.4	8	35	49.6	0.7	2.7
23.6467	35.3953	2016	3	13	2.7	23.8	8	39	56.4	0.6	0.3
23.6327	35.3937	2016	3	13	2.3	23.1	9	31	37.8	1.0	0.9
23.6248	35.3848	2016	3	13	2.4	15.4	9	32	48.4	0.5	1.2
23.6328	35.3878	2016	3	13	2.1	22.2	9	59	48.7	0.7	0.6
23.6207	35.3872	2016	3	13	1.7	18.0	10	40	38.9	0.5	1.4
23.6300	35.3702	2016	3	13	2.4	17.9	10	48	4.9	0.6	1.5
23.6240	35.3970	2016	3	13	2.0	20.5	10	58	59.4	0.5	1.1
23.6290	35.3847	2016	3	13	2.2	19.7	11	25	49.9	0.4	0.9
23.6183	35.3830	2016	3	13	2.1	15.9	11	55	23.1	0.4	1.0
23.6068	35.3830	2016	3	13	2.5	20.4	12	1	5.3	0.7	1.4
23.6060	35.3778	2016	3	13	2.3	22.2	12	1	43.7	1.0	0.6
23.6282	35.3835	2016	3	13	2.3	23.4	12	7	44.3	0.7	0.3
23.6087	35.3617	2016	3	13	2.8	20.2	12	13	39.5	0.5	1.1
23.6627	35.3990	2016	3	13	2.1	20.6	12	14	31.4	0.5	1.0
23.6465	35.3947	2016	3	13	2.1	22.0	12	23	13.9	0.8	0.4
23.6553	35.4030	2016	3	13	1.7	22.9	12	27	47.3	0.7	0.7
23.6248	35.4017	2016	3	13	1.4	18.9	13	9	3.0	3.7	3.1
23.6427	35.4018	2016	3	13	1.9	20.6	13	14	4.8	1.5	0.8
23.6508	35.4157	2016	3	13	3.7	22.3	13	22	58.0	1.8	0.6
23.6502	35.4108	2016	3	13	3.1	23.2	13	58	25.2	1.7	0.6
23.6222	35.3958	2016	3	13	2.4	17.8	14	2	23.7	0.4	0.9
23.6395	35.3828	2016	3	13	1.9	16.9	14	8	55.6	0.4	1.2
23.6315	35.3923	2016	3	13	2.7	19.9	14	25	30.7	0.5	0.9
23.6345	35.4018	2016	3	13	2.5	20.1	14	46	39.2	0.4	0.9
23.6337	35.3958	2016	3	13	2.4	17.2	15	32	13.2	1.2	1.2
23.6092	35.3912	2016	3	13	2.0	16.8	15	40	59.3	0.6	1.9
23.6338	35.3822	2016	3	13	1.9	12.4	17	10	18.9	0.4	1.2
23.6398	35.3863	2016	3	13	1.9	13.0	20	7	23.2	0.7	1.9
23.6147	35.3917	2016	3	13	2.3	16.8	20	31	54.7	0.5	1.2
23.6095	35.3810	2016	3	13	2.7	14.3	20	32	9.2	0.4	1.1
23.6462	35.3865	2016	3	13	2.1	17.4	20	32	54.9	0.4	1.0
23.6130	35.3972	2016	3	13	2.1	18.8	20	47	34.7	0.6	1.3
23.6043	35.3908	2016	3	13	2.0	18.3	20	54	24.2	0.6	1.4
23.6200	35.3907	2016	3	13	2.0	16.1	20	57	37.2	0.4	1.0
23.6305	35.3830	2016	3	13	2.0	17.1	21	3	42.9	0.6	1.6
23.6212	35.3657	2016	3	13	1.9	15.6	21	26	34.2	0.7	1.8
23.6150	35.3763	2016	3	13	3.5	18.4	21	32	34.7	0.4	0.9
23.6370	35.3917	2016	3	13	2.0	18.9	21	42	9.5	0.4	0.9
23.6050	35.3867	2016	3	13	2.6	15.1	21	44	10.3	0.7	1.8

23.5922	35.3970	2016	3	13	1.8	15.2	21	47	28.6	0.5	1.3
23.6390	35.4050	2016	3	13	2.0	16.3	22	42	16.2	0.5	1.3
23.6198	35.3807	2016	3	13	2.4	16.6	22	44	4.7	0.5	1.2
23.6320	35.3828	2016	3	13	2.9	14.7	22	46	15.3	0.5	1.3
23.6117	35.3970	2016	3	13	2.5	16.3	22	48	15.4	0.6	1.5
23.6438	35.4058	2016	3	13	2.3	18.9	23	23	54.8	0.4	0.9
23.6593	35.3917	2016	3	13	3.7	18.0	23	26	32.2	0.5	1.0
23.6305	35.3732	2016	3	13	2.3	16.5	23	30	10.3	0.5	1.2
23.6400	35.3908	2016	3	13	2.3	18.9	23	30	43.2	0.6	1.3
23.6202	35.3760	2016	3	13	2.1	18.0	23	34	31.8	0.5	1.3
23.6350	35.3840	2016	3	14	1.6	18.3	0	1	47.6	0.8	2.3
23.6228	35.3875	2016	3	14	2.1	13.7	0	33	7.3	0.4	1.1
23.6288	35.3835	2016	3	14	2.1	14.1	0	34	54.3	0.5	1.3
23.6102	35.3838	2016	3	14	2.3	16.9	0	37	22.8	0.5	1.2
23.6473	35.3837	2016	3	14	2.2	18.4	0	51	49.5	0.4	0.9
23.6058	35.3770	2016	3	14	1.8	11.9	1	34	51.1	0.6	1.7
23.6303	35.3733	2016	3	14	1.7	18.1	2	6	5.7	0.6	1.8
23.6325	35.3873	2016	3	14	2.1	16.7	3	22	0.5	0.5	1.3
23.5993	35.3628	2016	3	14	2.7	15.1	3	51	11.4	0.7	1.9
23.6187	35.3722	2016	3	14	1.9	8.8	4	4	44.0	0.4	2.9
23.6128	35.3975	2016	3	14	1.6	20.7	4	6	3.7	0.9	2.1
23.6320	35.3992	2016	3	14	2.2	16.1	4	32	41.0	0.5	1.3
23.6342	35.4075	2016	3	14	2.4	19.9	5	7	8.1	0.4	0.8
23.6270	35.4018	2016	3	14	2.5	18.4	5	15	38.5	0.4	0.9
23.6053	35.3818	2016	3	14	1.6	7.8	5	26	6.1	0.8	1.2
23.6212	35.3613	2016	3	14	2.1	7.7	6	22	25.7	0.4	1.2
23.6328	35.3860	2016	3	14	2.8	17.7	6	33	7.5	0.6	1.3
23.6370	35.4268	2016	3	14	2.0	18.9	7	49	9.8	1.8	0.9
23.6395	35.4158	2016	3	14	2.1	17.5	9	3	55.6	0.6	1.4
23.6063	35.3928	2016	3	14	2.4	16.7	11	39	56.8	0.6	1.4
23.6277	35.3997	2016	3	14	2.8	17.3	11	59	55.7	0.5	1.0
23.6407	35.4010	2016	3	14	2.1	18.4	12	19	4.8	0.4	1.1
23.6093	35.4018	2016	3	14	2.4	15.2	12	49	53.5	0.5	1.2
23.6318	35.3893	2016	3	14	2.2	13.5	14	11	19.8	0.4	1.5
23.6067	35.4077	2016	3	14	2.0	17.5	15	11	6.0	0.4	1.0
23.6305	35.3918	2016	3	14	3.1	16.4	16	14	18.8	0.4	0.9
23.6283	35.3900	2016	3	14	2.5	18.4	18	18	13.1	0.6	1.4
23.6263	35.3900	2016	3	14	2.5	18.3	22	29	19.2	0.7	1.6
23.6307	35.3930	2016	3	15	2.2	16.0	1	42	22.9	1.4	1.2
23.6428	35.4245	2016	3	15	2.2	18.9	1	58	25.2	1.6	0.8

23.6050	35.3813	2016	3	15	3.0	16.5	2	34	59.3	0.4	0.9
23.6345	35.3972	2016	3	15	2.6	16.9	2	40	3.9	0.6	1.4
23.6403	35.3867	2016	3	15	2.5	16.4	3	45	57.9	0.5	1.3
23.6218	35.4052	2016	3	15	2.4	15.5	3	59	18.8	0.5	1.1
23.6433	35.3845	2016	3	15	2.6	17.9	4	34	35.2	0.5	1.0
23.6075	35.3933	2016	3	15	2.6	16.0	5	45	27.2	0.5	1.2
23.6092	35.4068	2016	3	15	2.4	14.8	5	46	25.4	0.8	2.0
23.6095	35.4037	2016	3	15	2.5	15.2	5	52	29.4	0.4	1.1
23.6163	35.3872	2016	3	15	2.1	17.1	6	0	34.6	0.4	0.9
23.6220	35.3920	2016	3	15	2.2	12.1	6	18	30.9	1.0	2.8
23.6157	35.4005	2016	3	15	2.5	15.3	6	27	42.4	0.7	1.8
23.6513	35.4002	2016	3	15	2.1	24.4	7	49	37.5	1.1	0.9
23.6173	35.4018	2016	3	15	2.3	14.5	8	35	41.5	0.6	1.5
23.6252	35.3883	2016	3	15	2.0	17.3	12	24	40.6	0.4	1.1
23.6030	35.3920	2016	3	15	2.3	18.1	13	51	57.2	0.4	0.9
23.6228	35.3828	2016	3	15	2.0	19.1	13	57	54.0	0.4	1.0
23.6047	35.3923	2016	3	15	1.9	15.9	14	53	44.9	0.5	1.2
23.6095	35.3958	2016	3	15	1.9	16.1	15	14	30.5	0.6	1.8
23.6265	35.3997	2016	3	15	3.0	20.0	15	34	59.9	0.4	0.9
23.6032	35.4108	2016	3	15	1.9	12.2	16	28	40.5	1.5	1.7
23.6402	35.4378	2016	3	15	1.6	18.5	17	20	59.7	1.9	1.2
23.6318	35.4030	2016	3	15	2.4	18.6	18	21	16.0	0.4	0.8
23.5950	35.3890	2016	3	15	1.5	16.3	18	47	46.1	0.6	2.1
23.5940	35.3747	2016	3	15	1.7	17.6	19	33	30.0	0.5	1.7
23.6095	35.4053	2016	3	15	2.9	18.2	19	48	0.0	0.4	0.9
23.5977	35.3867	2016	3	15	1.5	17.3	20	0	51.5	0.6	1.9
23.6308	35.3827	2016	3	15	2.2	16.3	20	20	25.7	0.7	2.2
23.6157	35.4002	2016	3	15	1.6	19.5	20	38	11.7	0.7	1.7
23.6008	35.3970	2016	3	15	1.5	17.7	21	17	28.5	0.5	1.2
23.5915	35.3602	2016	3	15	1.8	12.4	21	41	46.0	0.5	1.7
23.5902	35.3882	2016	3	15	1.8	18.2	23	10	50.6	0.4	1.0
23.6622	35.4380	2016	3	16	1.4	19.2	0	23	53.4	2.1	1.2
23.6147	35.4040	2016	3	16	1.6	14.8	1	12	22.5	2.0	1.8
23.6147	35.3987	2016	3	16	2.0	17.8	1	27	10.7	1.4	1.3
23.6212	35.4182	2016	3	16	1.6	18.4	1	43	32.7	1.3	0.8
23.6118	35.3943	2016	3	16	1.8	15.2	2	20	7.9	1.1	1.0
23.5915	35.3438	2016	3	16	1.6	9.5	2	26	24.9	1.1	3.1
23.5987	35.4127	2016	3	16	1.7	13.9	2	57	57.1	2.5	2.3
23.6488	35.3908	2016	3	16	1.4	17.8	3	39	56.0	0.6	1.6
23.6113	35.4003	2016	3	16	1.8	16.6	4	5	29.4	0.6	1.3

23.6128	35.3892	2016	3	16	1.9	12.4	4	15	14.3	0.4	1.3
23.5845	35.3895	2016	3	16	2.0	18.7	4	29	32.3	0.4	1.0
23.6088	35.3885	2016	3	16	3.0	18.1	4	56	25.4	0.5	1.1
23.6103	35.3873	2016	3	16	1.8	15.4	5	2	0.8	0.5	1.4
23.6158	35.4028	2016	3	16	2.4	19.7	5	2	44.6	0.4	0.8
23.5920	35.3742	2016	3	16	1.6	11.3	5	48	38.4	0.8	3.3
23.6132	35.3982	2016	3	16	2.5	12.3	6	34	15.7	0.6	1.8
23.6462	35.3898	2016	3	16	1.6	14.5	7	25	14.9	0.5	1.6
23.6127	35.3953	2016	3	16	2.3	16.0	9	26	2.7	0.4	0.9
23.6240	35.3928	2016	3	16	2.1	18.4	10	1	47.3	0.5	1.5
23.6202	35.3953	2016	3	16	1.8	16.9	10	53	27.8	0.5	1.5
23.6095	35.3885	2016	3	16	1.9	15.6	11	34	10.0	0.6	2.1
23.6107	35.3858	2016	3	16	2.0	15.2	14	30	12.0	0.5	1.4
23.6038	35.3895	2016	3	16	2.6	14.7	14	43	51.7	0.4	1.1
23.5957	35.3943	2016	3	16	2.4	16.7	14	45	29.4	0.4	1.0
23.6208	35.3768	2016	3	16	1.8	8.0	15	50	45.4	0.8	2.1
23.6152	35.3967	2016	3	16	2.2	15.6	16	4	57.3	0.5	1.4
23.6312	35.4163	2016	3	16	1.9	18.3	16	25	36.4	1.9	1.1
23.6082	35.4040	2016	3	16	2.7	16.1	17	54	7.3	1.5	1.2
23.6173	35.3607	2016	3	16	1.8	18.8	19	2	33.3	0.6	1.8
23.6093	35.3870	2016	3	16	2.0	11.5	19	21	23.1	0.6	2.2
23.6038	35.3947	2016	3	16	2.2	16.5	19	32	12.9	0.5	1.2
23.5830	35.3822	2016	3	16	1.9	19.8	20	7	30.6	0.8	2.5
23.6043	35.3942	2016	3	16	1.7	12.7	21	1	35.2	0.8	2.9
23.5868	35.3920	2016	3	16	2.6	17.1	21	21	12.3	0.5	1.1
23.6228	35.3640	2016	3	16	2.5	10.8	23	16	28.9	0.5	1.5
23.6100	35.3663	2016	3	16	1.7	13.0	23	37	3.1	0.7	2.9
23.6108	35.3970	2016	3	17	2.0	17.3	0	25	55.0	1.5	1.1
23.6180	35.3740	2016	3	17	1.6	12.7	1	32	19.2	2.1	3.8
23.5877	35.4168	2016	3	17	1.8	16.2	1	32	47.4	1.8	1.9
23.6000	35.3918	2016	3	17	1.7	14.8	4	24	3.2	0.5	1.8
23.6488	35.3832	2016	3	17	3.4	20.9	12	37	44.1	0.6	0.5
23.6087	35.3925	2016	3	17	2.3	17.6	13	19	31.9	0.4	0.9
23.6078	35.3872	2016	3	17	2.0	16.4	14	8	19.7	0.5	1.2
23.6042	35.3802	2016	3	17	2.0	22.4	14	14	11.4	0.6	0.6
23.6055	35.3782	2016	3	17	2.0	15.8	15	32	11.5	0.4	1.4
23.5968	35.3472	2016	3	17	1.7	9.4	17	7	45.1	1.0	3.3
23.6375	35.3765	2016	3	17	1.9	18.5	19	25	2.3	0.4	1.1
23.6310	35.3932	2016	3	17	2.1	18.1	19	30	9.9	0.5	1.0
23.6527	35.3840	2016	3	17	2.2	18.2	20	21	41.6	0.4	0.9

23.6105	35.3957	2016	3	17	2.8	15.4	20	52	8.4	0.6	1.4
23.6043	35.3908	2016	3	17	2.1	15.2	22	30	3.1	0.5	1.2
23.6203	35.3917	2016	3	17	2.1	15.9	22	30	27.9	0.5	1.3
23.6140	35.3613	2016	3	17	1.8	11.0	22	54	19.0	0.5	2.3
23.6430	35.3840	2016	3	17	2.0	18.1	23	1	10.5	0.4	0.9
23.6253	35.3847	2016	3	17	1.8	17.0	23	41	13.4	0.6	1.4
23.6233	35.3945	2016	3	18	1.7	15.6	1	3	25.1	0.4	1.3
23.6273	35.3733	2016	3	18	1.8	10.7	1	7	54.8	0.5	1.7
23.6025	35.3830	2016	3	18	2.1	15.9	1	38	43.3	0.4	1.0
23.6095	35.3805	2016	3	18	2.1	15.4	1	45	16.8	0.5	1.5
23.5998	35.3713	2016	3	18	2.0	14.1	2	40	1.3	0.5	1.4
23.6358	35.3923	2016	3	18	2.0	15.7	5	15	47.4	0.5	1.3
23.5860	35.3773	2016	3	18	2.3	20.9	7	27	35.4	0.4	0.4
23.6187	35.3658	2016	3	18	2.1	16.0	12	55	57.2	0.6	1.5
23.5935	35.3548	2016	3	18	1.9	19.1	12	57	28.6	0.4	1.4
23.6143	35.3805	2016	3	18	2.4	17.7	15	30	48.3	0.4	1.0
23.5925	35.3698	2016	3	18	1.9	11.9	20	56	20.3	0.5	1.5
23.6300	35.3787	2016	3	18	2.2	12.6	21	56	46.2	0.5	1.6
23.6307	35.3893	2016	3	19	2.0	13.4	1	26	28.0	0.5	1.7
23.5970	35.4000	2016	3	19	2.4	16.5	1	36	49.7	0.6	1.5
23.6045	35.3972	2016	3	19	1.9	19.2	1	41	27.6	0.5	1.1
23.6500	35.4428	2016	3	19	2.3	17.9	2	33	33.8	2.0	0.9
23.5960	35.3995	2016	3	19	2.3	18.8	6	17	47.6	0.6	1.2
23.6375	35.3778	2016	3	19	1.9	13.8	7	59	44.6	0.4	1.6
23.6238	35.3805	2016	3	19	1.9	11.1	8	6	48.4	0.7	2.1
23.6362	35.3880	2016	3	19	2.6	18.8	9	36	39.7	0.4	0.9
23.6115	35.4082	2016	3	19	2.2	14.5	10	37	40.0	0.5	1.4
23.6150	35.3915	2016	3	19	2.9	15.6	11	28	39.5	0.6	1.6
23.6322	35.3852	2016	3	19	1.8	18.4	17	7	20.7	1.7	1.7
23.6527	35.4025	2016	3	19	2.1	18.2	18	55	59.9	0.5	1.4
23.6223	35.3800	2016	3	19	1.8	16.6	22	10	30.1	0.7	1.8
23.6393	35.3928	2016	3	20	1.9	17.9	1	16	39.4	1.3	1.2
23.6333	35.3788	2016	3	20	1.8	16.6	2	47	26.0	1.3	1.2
23.5962	35.3540	2016	3	20	1.9	18.5	6	49	14.9	0.6	1.6
23.6077	35.4047	2016	3	20	1.7	18.7	7	13	40.1	0.6	1.2
23.6193	35.3995	2016	3	20	2.3	23.9	7	40	40.5	0.7	0.3
23.6468	35.3763	2016	3	20	1.8	25.7	7	50	9.4	0.9	0.9
23.6177	35.3407	2016	3	20	1.7	14.6	9	22	51.6	0.5	1.7
23.6563	35.3677	2016	3	20	2.0	20.4	10	45	49.3	0.9	0.9
23.6218	35.3827	2016	3	20	1.6	23.1	10	53	18.4	0.7	0.7

23.6223	35.4065	2016	3	20	1.9	19.0	14	8	13.8	0.4	0.9
23.5818	35.3507	2016	3	20	1.9	18.9	15	32	2.9	0.5	1.2
23.6027	35.3663	2016	3	20	1.7	23.0	20	38	29.8	1.3	1.3
23.6607	35.3760	2016	3	20	1.8	13.2	20	39	42.9	0.5	1.4
23.6095	35.3712	2016	3	20	1.6	0.0	21	8	59.8	0.6	1.1
23.6140	35.3870	2016	3	21	2.0	19.3	3	49	16.9	0.5	1.0
23.6230	35.3547	2016	3	21	1.6	19.9	22	43	58.9	1.0	3.0
23.6313	35.4048	2016	3	22	1.5	19.5	2	50	20.9	1.3	1.1
23.6598	35.3622	2016	3	22	1.0	18.9	3	29	55.0	0.6	1.6
23.5817	35.3920	2016	3	22	1.8	16.3	3	37	12.5	0.4	1.1
23.6413	35.3960	2016	3	22	1.9	18.2	3	39	44.2	0.5	1.1
23.5728	35.3823	2016	3	22	1.6	20.8	3	54	56.5	0.5	1.5
23.6652	35.3822	2016	3	22	1.9	22.0	4	53	18.7	0.6	0.6
23.6160	35.3588	2016	3	22	1.9	19.4	6	1	2.8	0.5	1.3
23.6200	35.3722	2016	3	22	2.2	20.2	9	32	58.0	0.4	1.0
23.6125	35.3933	2016	3	22	2.9	18.3	16	21	20.8	1.5	1.5
23.6010	35.4142	2016	3	22	1.7	18.6	18	7	6.8	2.1	1.8
23.5745	35.3702	2016	3	22	1.8	18.4	22	7	8.0	2.0	2.4
23.5883	35.3630	2016	3	23	2.3	18.1	15	53	7.5	1.2	1.1
23.5623	35.3658	2016	3	23	1.8	12.8	21	54	36.5	2.1	4.1
23.6140	35.3710	2016	3	24	2.3	16.9	6	56	51.0	1.8	1.8
23.6263	35.4070	2016	3	24	1.6	11.1	21	43	30.2	3.5	5.2
23.6565	35.3777	2016	3	25	1.5	0.0	2	48	33.5	1.0	1.3
23.6452	35.4055	2016	3	25	1.4	17.7	6	29	11.0	1.9	1.7
23.6212	35.3732	2016	3	25	1.5	24.9	6	37	3.0	2.3	0.6

Appendix 3 MATLAB code

%catmaker.m

```
%this code creates a catalogue compatible for the
%accelerated deformation scanner
clear all; close all; clc;
%get the text tab delimited file
filename = 'C:\Users\Gehas-Office\Desktop\cat_2014.txt';
delimiter = '\t';
formatSpec = '%q%q%f%f%f%f%[^\n\r]';
fileID = fopen(filename,'r');
dataArray = textscan(fileID, formatSpec, 'Delimiter', delimiter, 'TextType',
'string', 'EmptyValue', NaN, 'ReturnOnError', false);
fclose(fileID);
%assign each colomn the correct parameter
t1 = cellstr(dataArray{:, 1});
t2 = cellstr(dataArray{:, 2});
y = dataArray{:, 3};
x = dataArray{:, 4};
d = dataArray{:, 5};
m = dataArray{:, 6};
clearvars filename delimiter formatSpec fileID dataArray ans;
%connect the date with time in one column
ta=[t1 t2]; ta=join(ta);
%convert date time in serial date format
t=datenum(ta,'dd/mm/yyyy HH:MM:SS');
clearvars t1 t2 ta
%create the catlogue and sort it base on date
cat =[t d m x y];
cat=sortrows(cat,1,'ascend');
t=cat(:,1)' ;d=cat(:,2)';m=cat(:,3)';x=cat(:,4)';y=cat(:,5)';
%save the catalogue as MATLAB file
save ('newcat.mat', 'd','m','t','x','y' )
```

%hyp2velest.m

```
clear all; close all; clc
%get hypo71 phase file and make it velest input phase file
filename = 'C:\Users\Gehas-Office\Documents\MATLAB\relocation\sw_pl.txt';
formatSpec = '%4s%4s%11s%5s%12s%[^\n\r]';
fileID = fopen(filename,'r');
dataArray = textscan(fileID, formatSpec, 'Delimiter', '', 'WhiteSpace',...
    '', 'TextType', 'string', 'ReturnOnError', false);
dataArray{1} = strtrim(dataArray{1});dataArray{2} = strtrim(dataArray{2});
dataArray{3} = strtrim(dataArray{3});dataArray{4} = strtrim(dataArray{4});
dataArray{5} = strtrim(dataArray{5});fclose(fileID);
inicat = [dataArray{1:end-1}];
%empty some memory
clearvars filename formatSpec fileID dataArray ans;

%get the hypo71 location file, this version support up to 50 phases per event
filename = 'C:\Users\Gehas-Office\Documents\MATLAB\relocation\hypsum.out';
%set the format of the saved output - open, read, close file
formatSpec = '%2s%2s%2s%3s%2s%6s%3s%6s%4s%*1s%5s%7s%[^\n\r]';
fileID = fopen(filename,'r');
dataArray = textscan(fileID, formatSpec, 'Delimiter', '', 'WhiteSpace',...
'','TextType', 'string', 'ReturnOnError', false);
fclose(fileID);
%assign columns to variables
yy = (dataArray{:, 1});mm = (dataArray{:, 2});dd = (dataArray{:, 3});hh
=(dataArray{:, 4});
min =(dataArray{:, 5});sec = (dataArray{:, 6});La= str2double(dataArray{:, 7});
```

```
at    =str2double(    dataArray{:,    8});Lo=    str2double(dataArray{:,    9});ng=
str2double(dataArray{:, 10});
Depth= (dataArray{:, 11});
%empty some memory
clearvars filename formatSpec fileID dataArray ans;
%change coordinate system to decimal degrees
x1=Lo; x2=ng./60;x=x1+x2;
y1=La; y2=at./60;y=y1+y2;

%get the header
frm=('%2s%2s%2s%0s%2s%2s%0s%5s%1s%2.4f%0s%2.4f%1s%5s');
for re=1:length(yy)
head(re,:)=sprintf(frm,yy(re),mm(re),dd(re),'',hh(re),min(re),'',...
   sec(re),'',y(re),'N  ',x(re),'W',Depth(re));
end

%Keep or remove stations from the list
names=['VLI';'PRNS';'KTHR';'TMBK';'CHAN';'RODP';'GVDS';""];     % station list
[kn1,kn2]=size(names);       % the size of station list used for the iterations
    for kn=1:kn1                            % up to Number of stations
Findstation=strcmp(inicat(:,1), names(kn,:));   % logical find the stations =1
Newsta(:,kn)=Findstation;
     end
Newsta= sum(Newsta,2); Newsta=logical(Newsta);
catal=inicat(Newsta,:);
%add 1st line space for header
catal(2:end+1,:) = catal(1:end,:);catal(1,:) = '';
%find gaps
gap=strcmp(catal(:,1),'');lg= find(gap==1);
lg=lg+1;lop1=length(lg);
for r=1:lop1-1
    n=lg(r);catal(n+1:end+1,:) = catal(n:end,:);
catal(n,1) = (head(r,:));catal(n,2:end) = '';
lg=lg+1;
end
%remove the first line
catal=catal(2:length(catal),:);lg2=strcmp(catal(:,1),'');
icat = find(lg2==1);icat=icat-1;ee=length(head);
clearvars kn kn1 kn2 Findstation Newsta Depth mm names lop1 dd at ng r n head
clearvars yy y2 y1 y frm x2 x1 x sec lg lg2 La  Lo gap  hh inicat min re
%prepare new variables
mov=1; catalogue=[];
for i=1:ee
fincat2=[];fincat1=[];fincat3=[];fincat4=[];
%get 1 event phases only
cc=catal(mov:icat(i),:);cc=sortrows(cc,2,'ascend');cc=sortrows(cc,1);
[m,m1]=size(cc);mov=mov+m+1;
% remove second S phase
for dtc=length(cc):-1:2
chi=strcmp(cc(dtc,1),cc(dtc-1,1));    chi2=strcmp(cc(dtc,4),'');
    if chi==1 && chi2==1
    ccc(dtc,1) =0;
    else
        ccc(dtc,1) =1;
    end
 end
ccc(1,1)=1;
%ccc(length(ccc)+1,1)=1;ccc=logical(ccc);cc=cc(ccc,:);ccc=[];
nfile(1,1)=cc(1,1);
for k=1:length(cc)-1
    ch=strcmp(cc(k+1,5),'');%find if phase is P or S
if ch==1  % P phase
nfile(2,1+k+k)= cc(k+1,1)+'P0';nfile(2,k+k+2)=cc(k+1,4);
```

```
else      % P phase
 nfile(2,1+k+k)=cc(k+1,1)+'S0';   nfile(2,k+k+2)=cc(k+1,5);
end
end
%start setting the velest phase file format
%find how long is the file and set tittle
con=length(nfile);fincat(1,1)=cc(1,1);frm=('%1s');

%every 6 phases go a new line
%line 1 = header
%line 2
for it1=3:2:14
if it1 <con
fict1= sprintf(frm,nfile(2,it1),'',nfile(2,it1+1));
else
fict1='';
end
fincat1=strcat(fincat1,fict1);
end
fincat(2,1)=fincat1;
fincat1=[];
%line 3
if con>14
for it2=15:2:26
if it2 <con
fict2= sprintf(frm,nfile(2,it2),'',nfile(2,it2+1));
else
fict2='';
end
fincat2=strcat(fincat2,fict2);
end
fincat(3,1)=fincat2;
check2=strcmp(fincat(3,1),'');
if  check2==1
  fincat = fincat(1:2,:);
end
fincat2=[];
end
% line4
if con>26
for it3=27:2:38
if it3 <con
fict3= sprintf(frm,nfile(2,it3),'',nfile(2,it3+1));
else
fict3='';
end
fincat3=strcat(fincat3,fict3);
end
fincat(4,1)=fincat3;
check3=strcmp(fincat(4,1),'');
if  check3==1
fincat = fincat(1:3,:);
end
fincat3=[];
end
%line 5
if con>38
for it4=39:2:50
if it4 <con
fict4= sprintf(frm,nfile(2,it4),'',nfile(2,it4+1));
else
fict4='';
end
```

```
fincat4=strcat(fincat4,fict4);
end
fincat(5,1)=fincat4;
check4=strcmp(fincat(5,1),'');
if  check4==1
        fincat = fincat(1:4,:);
end
fincat4=[];
end
%put every itteration in an appending catalogue
catalogue=[catalogue;fincat];
%add blank line below event
catalogue(length(catalogue)+1)='';
%controllers for catal startstop
clearvars nfile fincat fincat1 fincat2 fincat3 fincat4
end
```

%main.m

```
function varargout = main(varargin)
% MAIN MATLAB code for main.fig
% Begin initialization code - DO NOT EDIT
gui_Singleton = 1;
gui_State = struct('gui_Name',       mfilename, ...
    'gui_Singleton',  gui_Singleton, ...
    'gui_OpeningFcn', @main_OpeningFcn, ...
    'gui_OutputFcn',  @main_OutputFcn, ...
    'gui_LayoutFcn',  [] , ...
    'gui_Callback',   []);
if nargin && ischar(varargin{1})
    gui_State.gui_Callback = str2func(varargin{1});
end

if nargout
    [varargout{1:nargout}] = gui_mainfcn(gui_State, varargin{:});
else
    gui_mainfcn(gui_State, varargin{:});
end
% End initialization code - DO NOT EDIT


% --- Executes just before main is made visible.
function main_OpeningFcn(hObject, eventdata, handles, varargin)
% This function has no output args, see OutputFcn.
% hObject    handle to figure
% eventdata  reserved - to be defined in a future version of MATLAB
% handles    structure with handles and user data (see GUIDATA)
% varargin   command line arguments to main (see VARARGIN)
 % Choose default command line output for main
handles.output = hObject;
 % Update handles structure
guidata(hObject, handles);
 % UIWAIT makes main wait for user response (see UIRESUME)
% uiwait(handles.figure1);
clc;
handles.cat = [];
% load initial Greek map
handles.map = load('maps/GREECE.mat');

PlotMap(handles.axes1,handles.map);
FixMapAxis(handles.axes1,hObject,handles);

% --- Outputs from this function are returned to the command line.
```

```
function varargout = main_OutputFcn(hObject, eventdata, handles)
% varargout  cell array for returning output args (see VARARGOUT);
% hObject    handle to figure
% eventdata  reserved - to be defined in a future version of MATLAB
% handles    structure with handles and user data (see GUIDATA)
% Get default command line output from handles structure
varargout{1} = handles.output;
% --- Executes on button press in Open_Catalog.
function Open_Catalog_Callback(hObject, eventdata, handles)
% hObject    handle to Open_Catalog (see GCBO)
% eventdata  reserved - to be defined in a future version of MATLAB
% handles    structure with handles and user data (see GUIDATA)
[FileName,PathName,FilterIndex] = uigetfile('*.mat');

if FileName~=0

    full_path = [PathName FileName];

    % load the original catalogue
    handles.cat = load(full_path);

    % plot the catalogue

plot(handles.axes1,handles.map.coastline(:,1),handles.map.coastline(:,2),'k');
    hold on

PlotEqs(handles.axes1,handles.cat.x,handles.cat.y,handles.cat.m,handles.cat.d);
    FixMapAxis(handles.axes1,hObject,handles);
    grid on, box on
    hold off

    % set initial coordinates for analysis
    set(handles.edit2, 'String',min(handles.cat.x));
    set(handles.edit3, 'String',max(handles.cat.x));
    set(handles.edit4, 'String',min(handles.cat.y));
    set(handles.edit5, 'String',max(handles.cat.y));
    str = sprintf('Catalog:%s, %d events',FileName,length(handles.cat.t));
    set(handles.mapTitle, 'String',str);

    % set the analysed scat catalogue, according to initial coordinates
    handles.scat.t = handles.cat.t;
    handles.scat.x = handles.cat.x;
    handles.scat.y    =    handles.cat.y;    handles.scat.m    =    handles.cat.m;
handles.scat.d = handles.cat.d;

    % keep a variable for the filename
    [pathstr,name,ext] = fileparts(full_path);    handles.file_name = name;

    % update GUI data
    guidata(hObject, handles);
end

function edit2_Callback(hObject, eventdata, handles)
% hObject    handle to edit2 (see GCBO)
% eventdata  reserved - to be defined in a future version of MATLAB
% handles    structure with handles and user data (see GUIDATA)

% Hints: get(hObject,'String') returns contents of edit2 as text
%        str2double(get(hObject,'String')) returns contents of edit2 as a double
% --- Executes during object creation, after setting all properties.
function edit2_CreateFcn(hObject, eventdata, handles)
% hObject    handle to edit2 (see GCBO)
% eventdata  reserved - to be defined in a future version of MATLAB
```

```
% handles    empty - handles not created until after all CreateFcns called

% Hint: edit controls usually have a white background on Windows.
%       See ISPC and COMPUTER.
if            ispc            &&            isequal(get(hObject,'BackgroundColor'),
get(0,'defaultUicontrolBackgroundColor'))
    set(hObject,'BackgroundColor','white');
end

function edit3_Callback(hObject, eventdata, handles)
% hObject    handle to edit3 (see GCBO)
% eventdata  reserved - to be defined in a future version of MATLAB
% handles    structure with handles and user data (see GUIDATA)

% Hints: get(hObject,'String') returns contents of edit3 as text
%        str2double(get(hObject,'String')) returns contents of edit3 as a double

% --- Executes during object creation, after setting all properties.
function edit3_CreateFcn(hObject, eventdata, handles)
% hObject    handle to edit3 (see GCBO)
% eventdata  reserved - to be defined in a future version of MATLAB
% handles    empty - handles not created until after all CreateFcns called

% Hint: edit controls usually have a white background on Windows.
%       See ISPC and COMPUTER.
if            ispc            &&            isequal(get(hObject,'BackgroundColor'),
get(0,'defaultUicontrolBackgroundColor'))
    set(hObject,'BackgroundColor','white');
end
function edit4_Callback(hObject, eventdata, handles)
% hObject    handle to edit4 (see GCBO)
% eventdata  reserved - to be defined in a future version of MATLAB
% handles    structure with handles and user data (see GUIDATA)

% Hints: get(hObject,'String') returns contents of edit4 as text
%        str2double(get(hObject,'String')) returns contents of edit4 as a double
% --- Executes during object creation, after setting all properties.
function edit4_CreateFcn(hObject, eventdata, handles)
% hObject    handle to edit4 (see GCBO)
% eventdata  reserved - to be defined in a future version of MATLAB
% handles    empty - handles not created until after all CreateFcns called
% Hint: edit controls usually have a white background on Windows.
%       See ISPC and COMPUTER.
if            ispc            &&            isequal(get(hObject,'BackgroundColor'),
get(0,'defaultUicontrolBackgroundColor'))
    set(hObject,'BackgroundColor','white');
end
function edit5_Callback(hObject, eventdata, handles)
% hObject    handle to edit5 (see GCBO)
% eventdata  reserved - to be defined in a future version of MATLAB
% handles    structure with handles and user data (see GUIDATA)
% Hints: get(hObject,'String') returns contents of edit5 as text
%        str2double(get(hObject,'String')) returns contents of edit5 as a double
% --- Executes during object creation, after setting all properties.
function edit5_CreateFcn(hObject, eventdata, handles)
% hObject    handle to edit5 (see GCBO)
% eventdata  reserved - to be defined in a future version of MATLAB
% handles    empty - handles not created until after all CreateFcns called
% Hint: edit controls usually have a white background on Windows.
%       See ISPC and COMPUTER.
if            ispc            &&            isequal(get(hObject,'BackgroundColor'),
get(0,'defaultUicontrolBackgroundColor'))
    set(hObject,'BackgroundColor','white');
```

```
end
% --- Executes on button press in pushbutton2.
function pushbutton2_Callback(hObject, eventdata, handles)
% hObject    handle to pushbutton2 (see GCBO)
% eventdata  reserved - to be defined in a future version of MATLAB
% handles    structure with handles and user data (see GUIDATA)
[FileName,PathName,FilterIndex] = uigetfile('*.mat');
if FileName~=0
    handles.map = load([PathName FileName]);
    x = handles.map.coastline(:,1);
    y = handles.map.coastline(:,2);
    plot(handles.axes1,x,y,'k'), grid on, box on
    guidata(hObject, handles);
end
% --- Executes on selection change in popupmenu3.
function popupmenu3_Callback(hObject, eventdata, handles)
% hObject    handle to popupmenu3 (see GCBO)
% eventdata  reserved - to be defined in a future version of MATLAB
% handles    structure with handles and user data (see GUIDATA)
% Hints: contents = cellstr(get(hObject,'String')) returns popupmenu3 contents as
cell array
%        contents{get(hObject,'Value')} returns selected item from popupmenu3
% --- Executes during object creation, after setting all properties.
function popupmenu3_CreateFcn(hObject, eventdata, handles)
% hObject    handle to popupmenu3 (see GCBO)
% eventdata  reserved - to be defined in a future version of MATLAB
% handles    empty - handles not created until after all CreateFcns called

% Hint: popupmenu controls usually have a white background on Windows.
%       See ISPC and COMPUTER.
if           ispc           &&           isequal(get(hObject,'BackgroundColor'),
get(0,'defaultUicontrolBackgroundColor'))
    set(hObject,'BackgroundColor','white');
end
% --- Executes on button press in checkbox1.
function checkbox1_Callback(hObject, eventdata, handles)
% hObject    handle to checkbox1 (see GCBO)
% eventdata  reserved - to be defined in a future version of MATLAB
% handles    structure with handles and user data (see GUIDATA)
 % Hint: get(hObject,'Value') returns toggle state of checkbox1
 % --- Executes on button press in pushbutton3.
function pushbutton3_Callback(hObject, eventdata, handles)
% hObject    handle to pushbutton3 (see GCBO)
% eventdata  reserved - to be defined in a future version of MATLAB
% handles    structure with handles and user data (see GUIDATA)
 if ~isempty(handles.cat)
    data=getrect(gca);
    xi=[data(1) data(1)+data(3) data(1)+data(3)  data(1)        data(1)];
    yi=[data(2) data(2)         data(2)+data(4)  data(2)+data(4) data(2)];
    in = inpolygon(handles.cat.x,handles.cat.y,xi,yi);

    handles.scat.t = handles.cat.t(in); handles.scat.x = handles.cat.x(in);
    handles.scat.y = handles.cat.y(in); handles.scat.m = handles.cat.m(in);
    handles.scat.d = handles.cat.d(in); guidata(hObject, handles);
    set(handles.edit2, 'String', data(1));
    set(handles.edit3, 'String',data(1)+data(3));
    set(handles.edit4, 'String', data(2));
    set(handles.edit5, 'String', data(2)+data(4));

    rectangle('Position',data,'LineWidth',2)
    guidata(hObject, handles);
else
    disp('PLEASE LOAD CATALOG FIRST!')
```

```
end
function edit6_Callback(hObject, eventdata, handles)
% hObject    handle to edit6 (see GCBO)
% eventdata  reserved - to be defined in a future version of MATLAB
% handles    structure with handles and user data (see GUIDATA)
% Hints: get(hObject,'String') returns contents of edit6 as text
%        str2double(get(hObject,'String')) returns contents of edit6 as a double
% --- Executes during object creation, after setting all properties.
function edit6_CreateFcn(hObject, eventdata, handles)
% hObject    handle to edit6 (see GCBO)
% eventdata  reserved - to be defined in a future version of MATLAB
% handles    empty - handles not created until after all CreateFcns called
% Hint: edit controls usually have a white background on Windows.
%       See ISPC and COMPUTER.
if            ispc            &&            isequal(get(hObject,'BackgroundColor'),
get(0,'defaultUicontrolBackgroundColor'))
    set(hObject,'BackgroundColor','white');
end
% --- Executes on selection change in popupmenu4.
function popupmenu4_Callback(hObject, eventdata, handles)
% hObject    handle to popupmenu4 (see GCBO)
% eventdata  reserved - to be defined in a future version of MATLAB
% handles    structure with handles and user data (see GUIDATA)

% Hints: contents = cellstr(get(hObject,'String')) returns popupmenu4 contents as
cell array
%        contents{get(hObject,'Value')} returns selected item from popupmenu4
% --- Executes during object creation, after setting all properties.
function popupmenu4_CreateFcn(hObject, eventdata, handles)
% hObject    handle to popupmenu4 (see GCBO)
% eventdata  reserved - to be defined in a future version of MATLAB
% handles    empty - handles not created until after all CreateFcns called
% Hint: popupmenu controls usually have a white background on Windows.
%       See ISPC and COMPUTER.
if            ispc            &&            isequal(get(hObject,'BackgroundColor'),
get(0,'defaultUicontrolBackgroundColor'))
    set(hObject,'BackgroundColor','white');
end
% --- Executes on selection change in popupmenu5.
function popupmenu5_Callback(hObject, eventdata, handles)
% hObject    handle to popupmenu5 (see GCBO)
% eventdata  reserved - to be defined in a future version of MATLAB
% handles    structure with handles and user data (see GUIDATA)

% Hints: contents = cellstr(get(hObject,'String')) returns popupmenu5 contents as
cell array
%        contents{get(hObject,'Value')} returns selected item from popupmenu5
% --- Executes during object creation, after setting all properties.
function popupmenu5_CreateFcn(hObject, eventdata, handles)
% hObject    handle to popupmenu5 (see GCBO)
% eventdata  reserved - to be defined in a future version of MATLAB
% handles    empty - handles not created until after all CreateFcns called

% Hint: popupmenu controls usually have a white background on Windows.
%       See ISPC and COMPUTER.
if            ispc            &&            isequal(get(hObject,'BackgroundColor'),
get(0,'defaultUicontrolBackgroundColor'))
    set(hObject,'BackgroundColor','white');
end
% --- Executes on selection change in popupmenu6.
function popupmenu6_Callback(hObject, eventdata, handles)
% hObject    handle to popupmenu6 (see GCBO)
% eventdata  reserved - to be defined in a future version of MATLAB
```

```
% handles    structure with handles and user data (see GUIDATA)

% Hints: contents = cellstr(get(hObject,'String')) returns popupmenu6 contents as
cell array
%        contents{get(hObject,'Value')} returns selected item from popupmenu6
% --- Executes during object creation, after setting all properties.
function popupmenu6_CreateFcn(hObject, eventdata, handles)
% hObject    handle to popupmenu6 (see GCBO)
% eventdata  reserved - to be defined in a future version of MATLAB
% handles    empty - handles not created until after all CreateFcns called

% Hint: popupmenu controls usually have a white background on Windows.
%       See ISPC and COMPUTER.
if            ispc            &&            isequal(get(hObject,'BackgroundColor'),
get(0,'defaultUicontrolBackgroundColor'))
    set(hObject,'BackgroundColor','white');
end
% --- Executes on button press in checkbox2.
function checkbox2_Callback(hObject, eventdata, handles)
% hObject    handle to checkbox2 (see GCBO)
% eventdata  reserved - to be defined in a future version of MATLAB
% handles    structure with handles and user data (see GUIDATA)
% Hint: get(hObject,'Value') returns toggle state of checkbox2
% --- Executes on button press in pushbutton4.
function pushbutton4_Callback(hObject, eventdata, handles)
% hObject    handle to pushbutton4 (see GCBO)
% eventdata  reserved - to be defined in a future version of MATLAB
% handles    structure with handles and user data (see GUIDATA)
if isempty(handles.cat)
    disp('PLEASE LOAD CATALOG FIRST!');
    return
end
rads = str2num(get(handles.edit6, 'String'));
step = str2num(get(handles.edit8, 'String'));
model = get(handles.popupmenu5,'Value');
Mcut = str2num(get(handles.edit11, 'String'));
Dcut = str2num(get(handles.edit12, 'String'));
min_events = str2num(get(handles.edit13, 'String'));
from = (get(handles.edit9, 'String'));
to = (get(handles.edit10, 'String'));

switch get(handles.popupmenu4,'Value');
    case 1
        ksi = 0.0;
    case 2
        ksi = 0.5;
    case 3
        ksi = 1.0;
end

switch get(handles.checkbox2,'Value');
    case 0
        plotmode = '';
    case 1
        plotmode = 'plot';
end

% load data according to edit controls
GetAreaFromEdits(hObject,handles);
% load selected period
[ti,xi,yi,mi,di] = LoadEqs(handles.scat.t',...
    handles.scat.x',handles.scat.y',...
    handles.scat.m',handles.scat.d',from,to,0);
```

```
 % find EQs according to filter
[ti,xi,yi,mi,di] = FindEQs(ti,xi,yi,mi,di,mi>=Mcut & di<=Dcut);
% Run The model
[centx,centy,FCur,Fn,FTc,FK,FA,FR] = ACCScanner(ti',xi',yi',mi',di',...
    rads,step,ksi,min_events,model,plotmode);
% set file  name
if model == 1
    acc_name      =      sprintf('%s_%s-%s_M%d_D%d_Q%d_ACC.mat',handles.file_name,
datestr(min(ti),...
        'yyyy'),datestr(max(ti),'yyyy'),Mcut *10,max(rads),ksi *10);
end
if model == 2
    acc_name = sprintf('%s-%s_M%d_D%d_Q%d_DEC_%s.mat', datestr(min(ti),...
        'yyyy'),datestr(max(ti),'yyyy'),Mcut                    *10,max(rads),ksi
*10,handles.file_name);
end
 % save filename
catalog = handles.scat;
save(acc_name,'catalog','ti','xi','yi','mi','di','rads','ksi','Mcut','Dcut','min_
events',...
    'centx','centy','FCur','Fn','FTc','FK','FA','FR');
function edit8_Callback(hObject, eventdata, handles)
% hObject    handle to edit8 (see GCBO)
% eventdata  reserved - to be defined in a future version of MATLAB
% handles    structure with handles and user data (see GUIDATA)
% Hints: get(hObject,'String') returns contents of edit8 as text
%        str2double(get(hObject,'String')) returns contents of edit8 as a double
% --- Executes during object creation, after setting all properties.
function edit8_CreateFcn(hObject, eventdata, handles)
% hObject    handle to edit8 (see GCBO)
% eventdata  reserved - to be defined in a future version of MATLAB
% handles    empty - handles not created until after all CreateFcns called
% Hint: edit controls usually have a white background on Windows.
%       See ISPC and COMPUTER.
if            ispc            &&            isequal(get(hObject,'BackgroundColor'),
get(0,'defaultUicontrolBackgroundColor'))
    set(hObject,'BackgroundColor','white');
end


function edit9_Callback(hObject, eventdata, handles)
% hObject    handle to edit9 (see GCBO)
% eventdata  reserved - to be defined in a future version of MATLAB
% handles    structure with handles and user data (see GUIDATA)
% Hints: get(hObject,'String') returns contents of edit9 as text
%        str2double(get(hObject,'String')) returns contents of edit9 as a double
% --- Executes during object creation, after setting all properties.
function edit9_CreateFcn(hObject, eventdata, handles)
% hObject    handle to edit9 (see GCBO)
% eventdata  reserved - to be defined in a future version of MATLAB
% handles    empty - handles not created until after all CreateFcns called
% Hint: edit controls usually have a white background on Windows.
%       See ISPC and COMPUTER.
if            ispc            &&            isequal(get(hObject,'BackgroundColor'),
get(0,'defaultUicontrolBackgroundColor'))
    set(hObject,'BackgroundColor','white');
end
function edit10_Callback(hObject, eventdata, handles)
% hObject    handle to edit10 (see GCBO)
% eventdata  reserved - to be defined in a future version of MATLAB
% handles    structure with handles and user data (see GUIDATA)
% Hints: get(hObject,'String') returns contents of edit10 as text
%        str2double(get(hObject,'String')) returns contents of edit10 as a double
```

```
% --- Executes during object creation, after setting all properties.
function edit10_CreateFcn(hObject, eventdata, handles)
% hObject    handle to edit10 (see GCBO)
% eventdata  reserved - to be defined in a future version of MATLAB
% handles    empty - handles not created until after all CreateFcns called
% Hint: edit controls usually have a white background on Windows.
%       See ISPC and COMPUTER.
if           ispc           &&           isequal(get(hObject,'BackgroundColor'),
get(0,'defaultUicontrolBackgroundColor'))
    set(hObject,'BackgroundColor','white');
end
 function edit11_Callback(hObject, eventdata, handles)
% hObject    handle to edit11 (see GCBO)
% eventdata  reserved - to be defined in a future version of MATLAB
% handles    structure with handles and user data (see GUIDATA)
% Hints: get(hObject,'String') returns contents of edit11 as text
%        str2double(get(hObject,'String')) returns contents of edit11 as a double


% --- Executes during object creation, after setting all properties.
function edit11_CreateFcn(hObject, eventdata, handles)
% hObject    handle to edit11 (see GCBO)
% eventdata  reserved - to be defined in a future version of MATLAB
% handles    empty - handles not created until after all CreateFcns called
% Hint: edit controls usually have a white background on Windows.
%       See ISPC and COMPUTER.
if           ispc           &&           isequal(get(hObject,'BackgroundColor'),
get(0,'defaultUicontrolBackgroundColor'))
    set(hObject,'BackgroundColor','white');
end
function GetAreaFromEdits(hObject,handles)
d(1)        =        str2double(get(handles.edit2,        'String'));d(2)        =
str2double(get(handles.edit3, 'String'));
d(3)        =        str2double(get(handles.edit4,        'String'));d(4)        =
str2double(get(handles.edit5, 'String'));
data(1) = d(1);data(2) = d(3);data(3) = d(2)-d(1);data(4) = d(4)-d(3);
xi=[data(1) data(1)+data(3) data(1)+data(3)  data(1)        data(1)];
yi=[data(2) data(2)         data(2)+data(4)  data(2)+data(4) data(2)];
in = inpolygon(handles.cat.x,handles.cat.y,xi,yi);
handles.scat.t = handles.cat.t(in);handles.scat.x = handles.cat.x(in);
handles.scat.y = handles.cat.y(in);handles.scat.m = handles.cat.m(in);
handles.scat.d = handles.cat.d(in);
% plot the catalogue
plot(handles.axes1,handles.map.coastline(:,1),handles.map.coastline(:,2),'k');
hold on
PlotEqs(handles.axes1,handles.scat.x,handles.scat.y,handles.scat.m,handles.scat.d
);
rectangle('Position',data,'LineWidth',2);
FixMapAxis(handles.axes1,hObject,handles)
grid on, box on
hold off
drawnow
guidata(hObject, handles);
function edit12_Callback(hObject, eventdata, handles)
% hObject    handle to edit12 (see GCBO)
% eventdata  reserved - to be defined in a future version of MATLAB
% handles    structure with handles and user data (see GUIDATA)
% Hints: get(hObject,'String') returns contents of edit12 as text
%        str2double(get(hObject,'String')) returns contents of edit12 as a double
% --- Executes during object creation, after setting all properties.
function edit12_CreateFcn(hObject, eventdata, handles)
% hObject    handle to edit12 (see GCBO)
% eventdata  reserved - to be defined in a future version of MATLAB
```

```
% handles    empty - handles not created until after all CreateFcns called
% Hint: edit controls usually have a white background on Windows.
%       See ISPC and COMPUTER.
if            ispc            &&            isequal(get(hObject,'BackgroundColor'),
get(0,'defaultUicontrolBackgroundColor'))
    set(hObject,'BackgroundColor','white');
end
function edit13_Callback(hObject, eventdata, handles)
% hObject    handle to edit13 (see GCBO)
% eventdata  reserved - to be defined in a future version of MATLAB
% handles    structure with handles and user data (see GUIDATA)
% Hints: get(hObject,'String') returns contents of edit13 as text
%        str2double(get(hObject,'String')) returns contents of edit13 as a double
% --- Executes during object creation, after setting all properties.
function edit13_CreateFcn(hObject, eventdata, handles)
% hObject    handle to edit13 (see GCBO)
% eventdata  reserved - to be defined in a future version of MATLAB
% handles    empty - handles not created until after all CreateFcns called
% Hint: edit controls usually have a white background on Windows.
%       See ISPC and COMPUTER.
if            ispc            &&            isequal(get(hObject,'BackgroundColor'),
get(0,'defaultUicontrolBackgroundColor'))
    set(hObject,'BackgroundColor','white');
end
% --- Executes on button press in pushbutton6.
function pushbutton6_Callback(hObject, eventdata, handles)
% hObject    handle to pushbutton6 (see GCBO)
% eventdata  reserved - to be defined in a future version of MATLAB
% handles    structure with handles and user data (see GUIDATA)
system('accres.m');
% --- Executes on button press in pushbutton7.
function pushbutton7_Callback(hObject, eventdata, handles)
% hObject    handle to pushbutton7 (see GCBO)
% eventdata  reserved - to be defined in a future version of MATLAB
% handles    structure with handles and user data (see GUIDATA)
accres();
```

%ACCScaner.m

```
%Accelerated Deformation Scanner

function [centx,centy,FCur,Fn,FTc,FK,FA,FR] = ACCScanner(t,x,y,m,d,...
    radarray,step,ksi,min_events,model,plotmode)

md = {'ACCELERATED' 'DECELERATED'};
disp('============================')
fprintf('Scanning    %s    regions         please    wait...    \n%s    -    %s
\n',char(md(model)),datestr(min(t)),datestr(max(t)))
fprintf('Mmin: %.2f, Dmax: %.2f, ksi: %.2f\n',min(m),max(d),ksi);

disp('============================')
% initialize the output parameters with empty matrices
centx=[]; centy=[]; FCur=[]; Fn=[]; FTc=[]; FA=[]; FK=[]; FR = [];

% validate if the input exist
if isempty(m),
    disp('ERROR DATA NOT FOUND')
    return
end

% set the start parameters for scanner
xstart = floor(min(x)); xend = ceil(max(x)); ystart = floor(min(y)); yend =
ceil(max(y));
```

```
Lr = length(radarray);
% create the grid with user defined step
for yepi=ystart:step:yend
    tic
    for xepi=xstart:step:xend
         % Set the distances from epicenter
        xp =(xepi-x)*85; yp =(yepi-y)*111; D = sqrt(xp.^2+yp.^2);

        % Initialize local model array parameters for speed
        La  = length(radarray);
        CVR = zeros(1,La); nR = zeros(1,La); Tc  = zeros(1,La); b  = zeros(1,La);
        K   = zeros(1,La); A  = zeros(1,La); R = zeros(1,La);
         % Run the model
        for i=1:Lr
            % index the area according to a spesific radius
            idx = find(D<=radarray(i));

            % run the model if the number of events is satisfied
            if length(idx)>=min_events
                [K(i),A(i),Tc(i),nR(i),b(i),CVR(i),R(i)]                                =
GetCurvature(t(idx),m(idx),model,ksi,plotmode);
            end
        end
        % set the minimum value of C(Rc)as best criteria
        if ~isempty(min(CVR(CVR>0)))
            I = find(CVR~=0 & CVR==min(CVR(CVR>0.0)));
            %set outpouts
            centx  =  [centx;  xepi];  centy  =  [centy;  yepi];  FCur  =  [FCur;
CVR(I(1))];
            Fn = [Fn; nR(I(1))]; FTc = [FTc; Tc(I(1))]; FA = [FA; A(I(1))];
            FK = [FK; K(I(1))];   FR = [FR; R(I(1))];
        end
    end
    % dislay every iteration statistics
    if ~isempty(FCur)
    disp(sprintf('line:  %4.1f,  %5.2f  s,  C:[%.2f-%.2f],  n:[%.2f-%.2f],r:[%.2f-
%.2f]',...
        yepi,toc,min(FCur),max(FCur),min(Fn),max(Fn),min(FR),max(FR)))
    end
end
%display the search is finished and play a sound
fprintf('DONE!\n')
finsound

%GetCurvature.m
function [K,A,Tc,n,b,CRV,R] = GetCurvature(T,M,model,ksi,plotmode)
% remove all warning for speed
warning off all
% convert time to elepsed time
N = length(T);t=zeros(N-1,1);
for i=1:N
    t(i)= daysact(T(1),T(i))*86400;
end
% Get the cummulative benioff strain release of the data
Es=10.^((1.5*M) + 4.7);
[bt,Es]=qbenioff(t,Es,ksi);
% create the model function K + A(tc - t)^n
pwlawfunc = @(p,t) p(1) + p(2)*(p(4) - t).^p(3);
% Apply least square fitting
q=polyfit(t,Es,1); LNfit=polyval(q,t,Es);
%make a preliminary estimation for ACC or DCC respectively
if model==1, beta = [2 0 0.33 max(t)]; end
if model==2, beta = [1 0 3 max(t)];end
```

```
% fit power-law model function non least squares case
[bf,r,J,COVB,mse] = nlinfit(t,Es/max(Es),pwlawfunc,beta);
[bf,r,J,COVB,mse]    =    nlinfit(t,Es/max(Es),pwlawfunc,[bf(1)    bf(2)    bf(3)
bf(4)],statset('MaxIter',100));
PLfit = pwlawfunc(bf,t)*max(Es);
% get correlation coefficient R^2
Crmat = corrcoef(PLfit,Es);R = real(Crmat(1,2)^2);
% Calculate the Power Law and Linear Fit RMSs
RMSlin=norm(Es-LNfit); RMSpow=norm(Es-PLfit);
% Get the curvature parameter C=(Power law fit RMS)/(Linear fit RMS),
CRV=RMSpow/RMSlin;
% Set the output fit parameters
K = bf(1); A = bf(2); Tc = bf(4); n = real(bf(3)); b=real(q(1)); c = q(2);
% Plot if plotmode is set
if(strcmpi(plotmode,'plot')==1)
    pdate = addtodate(min(T),mean(Tc)/3600/24,'day');
    plot(t,Es,'o','markersize',5), hold on
    plot(t,LNfit,'k','LineWidth',2)
    plot(t,PLfit,'r','LineWidth',2)
    %legend('Cum. En. Release',...
     legend('Event',...
        sprintf('LS: b=%5.1e,c=%5.1e',b,c),...
        sprintf('PL: K=%.2f,A=%5.1e,n=%.2f,\nTc=%.1e (%s),\nCRV=%.2f,r=%.3f',...
        K,A,n,Tc,datestr(pdate,'dd-mmm-yyyy'),CRV,R),'Location','NorthWest')
    xlabel('Elapsed Time (sec)')
    if ksi==0.0,    ylabel('N(t)'), end
    if ksi==0.5,    ylabel('BS(t)'), end
    if ksi==1.0,    ylabel('E(t)'), end
    hold off
    drawnow
end

% bring back all warnings
warning on all

function [Et,Es] = qbenioff(t,e,q)

N = length(e);Es =zeros(1,N);Et = t;E = 0.0;
for i=1:N
    E = E + e(i)^q;    Es(i) = E;
end
%     end
Es=Es';
```

%accres.m

```
function varargout = accres(varargin)
% ACCRES MATLAB code for accres.fig
clc;
% Begin initialization code - DO NOT EDIT
gui_Singleton = 1;
gui_State = struct('gui_Name',       mfilename, ...
                   'gui_Singleton',  gui_Singleton, ...
                   'gui_OpeningFcn', @accres_OpeningFcn, ...
                   'gui_OutputFcn',  @accres_OutputFcn, ...
                   'gui_LayoutFcn',  [] , ...
                   'gui_Callback',   []);
if nargin && ischar(varargin{1})
    gui_State.gui_Callback = str2func(varargin{1});
end

if nargout
```

```
    [varargout{1:nargout}] = gui_mainfcn(gui_State, varargin{:});
else
    gui_mainfcn(gui_State, varargin{:});
end
% End initialization code - DO NOT EDIT


% --- Executes just before accres is made visible.
function accres_OpeningFcn(hObject, eventdata, handles, varargin)
% This function has no output args, see OutputFcn.
% hObject    handle to figure
% eventdata  reserved - to be defined in a future version of MATLAB
% handles    structure with handles and user data (see GUIDATA)
% varargin   command line arguments to accres (see VARARGIN)
 % Choose default command line output for accres
handles.output = hObject;
clc;
% load initial greec map
handles.full_path=[];
handles.map = load('maps/GREECE.mat');
PlotMap(handles.axes1,handles.map);FixMapAxis(handles.axes1,hObject,handles);
PlotMap(handles.axes2,handles.map);FixMapAxis(handles.axes2,hObject,handles);
PlotMap(handles.axes3,handles.map);FixMapAxis(handles.axes3,hObject,handles);
 handles.mat = [];
set(handles.edit1,'String',sprintf('%.2f',get(handles.slider1,'Value')));
set(handles.edit2,'String',sprintf('%.2f',get(handles.slider2,'Value')));
set(handles.edit3,'String',sprintf('%.2f',get(handles.slider3,'Value')));
set(handles.edit4,'String',sprintf('%.2f',get(handles.slider4,'Value')));
% Update handles structure
guidata(hObject, handles);
% UIWAIT makes accres wait for user response (see UIRESUME)
% uiwait(handles.figure1);
% --- Outputs from this function are returned to the command line.
function varargout = accres_OutputFcn(hObject, eventdata, handles)
% varargout  cell array for returning output args (see VARARGOUT);
% hObject    handle to figure
% eventdata  reserved - to be defined in a future version of MATLAB
% handles    structure with handles and user data (see GUIDATA)
% Get default command line output from handles structure
varargout{1} = handles.output;

% --- Executes on button press in pushbutton1.
function pushbutton1_Callback(hObject, eventdata, handles)
% hObject    handle to pushbutton1 (see GCBO)
% eventdata  reserved - to be defined in a future version of MATLAB
% handles    structure with handles and user data (see GUIDATA)
[FileName,PathName,FilterIndex] = uigetfile('*.mat');

if FileName~=0
    handles.full_path = [PathName FileName];
      % load the original catalogue
    handles.mat=load( handles.full_path);
    set(handles.textFile,'String',FileName);
        guidata(hObject, handles);
        if ~isempty(handles.mat)
        % set texts
        SetInfolabels(hObject,handles,handles.mat);
        CalculateResults(hObject, handles);
           end
end

% update GUI data
guidata(hObject, handles);
```

```
% --- Executes on slider movement.
function slider1_Callback(hObject, eventdata, handles)
% hObject    handle to slider1 (see GCBO)
% eventdata  reserved - to be defined in a future version of MATLAB
% handles    structure with handles and user data (see GUIDATA)
% Hints: get(hObject,'Value') returns position of slider
%        get(hObject,'Min') and get(hObject,'Max') to determine range of slider
set(handles.edit1,'String',sprintf('%.2f',get(handles.slider1,'Value')));
CalculateResults(hObject, handles);
guidata(hObject, handles);
% --- Executes during object creation, after setting all properties.
function slider1_CreateFcn(hObject, eventdata, handles)
% hObject    handle to slider1 (see GCBO)
% eventdata  reserved - to be defined in a future version of MATLAB
% handles    empty - handles not created until after all CreateFcns called
% Hint: slider controls usually have a light gray background.
if                                          isequal(get(hObject,'BackgroundColor'),
get(0,'defaultUicontrolBackgroundColor'))
    set(hObject,'BackgroundColor',[.9 .9 .9]);
end
% --- Executes on slider movement.
function slider2_Callback(hObject, eventdata, handles)
% hObject    handle to slider2 (see GCBO)
% eventdata  reserved - to be defined in a future version of MATLAB
% handles    structure with handles and user data (see GUIDATA)
% Hints: get(hObject,'Value') returns position of slider
%        get(hObject,'Min') and get(hObject,'Max') to determine range of slider
set(handles.edit2,'String',sprintf('%.2f',get(handles.slider2,'Value')));
CalculateResults(hObject, handles);
% --- Executes during object creation, after setting all properties.
function slider2_CreateFcn(hObject, eventdata, handles)
% hObject    handle to slider2 (see GCBO)
% eventdata  reserved - to be defined in a future version of MATLAB
% handles    empty - handles not created until after all CreateFcns called
% Hint: slider controls usually have a light gray background.
if                                          isequal(get(hObject,'BackgroundColor'),
get(0,'defaultUicontrolBackgroundColor'))
    set(hObject,'BackgroundColor',[.9 .9 .9]);
end
% --- Executes on slider movement.
function slider3_Callback(hObject, eventdata, handles)
% hObject    handle to slider3 (see GCBO)
% eventdata  reserved - to be defined in a future version of MATLAB
% handles    structure with handles and user data (see GUIDATA)

% Hints: get(hObject,'Value') returns position of slider
%        get(hObject,'Min') and get(hObject,'Max') to determine range of slider
set(handles.edit3,'String',sprintf('%.2f',get(handles.slider3,'Value')));
CalculateResults(hObject, handles)
% --- Executes during object creation, after setting all properties.
function slider3_CreateFcn(hObject, eventdata, handles)
% hObject    handle to slider3 (see GCBO)
% eventdata  reserved - to be defined in a future version of MATLAB
% handles    empty - handles not created until after all CreateFcns called
% Hint: slider controls usually have a light gray background.
if                                          isequal(get(hObject,'BackgroundColor'),
get(0,'defaultUicontrolBackgroundColor'))
    set(hObject,'BackgroundColor',[.9 .9 .9]);
end
% --- Executes on slider movement.
function slider4_Callback(hObject, eventdata, handles)
% hObject    handle to slider4 (see GCBO)
% eventdata  reserved - to be defined in a future version of MATLAB
```

```
% handles    structure with handles and user data (see GUIDATA)
% Hints: get(hObject,'Value') returns position of slider
%        get(hObject,'Min') and get(hObject,'Max') to determine range of slider
set(handles.edit4,'String',sprintf('%.2f',get(handles.slider4,'Value')));
CalculateResults(hObject, handles);
% --- Executes during object creation, after setting all properties.
function slider4_CreateFcn(hObject, eventdata, handles)
% hObject    handle to slider4 (see GCBO)
% eventdata  reserved - to be defined in a future version of MATLAB
% handles    empty - handles not created until after all CreateFcns called

% Hint: slider controls usually have a light gray background.
if                                      isequal(get(hObject,'BackgroundColor'),
get(0,'defaultUicontrolBackgroundColor'))
    set(hObject,'BackgroundColor',[.9 .9 .9]);
end


% --- Executes on button press in pushbutton2.
function pushbutton2_Callback(hObject, eventdata, handles)
% hObject    handle to pushbutton2 (see GCBO)
% eventdata  reserved - to be defined in a future version of MATLAB
% handles    structure with handles and user data (see GUIDATA)
set(handles.slider1,'Value',0);
set(handles.slider2,'Value',0.6);
set(handles.slider3,'Value',0.28);
set(handles.slider4,'Value',0.38);
set(handles.edit5,'String','0.95');
guidata(hObject, handles);
SetInfolabels(hObject,handles,handles.mat);
CalculateResults(hObject, handles);


function  SetInfolabels(hObject,handles,mat)

if ~isempty(handles.mat)
    set(handles.text1,'String',sprintf('Total        data        length:        %d
events',length(mat.ti)));
    set(handles.text2,'String',sprintf('î-par:     %.1f,     Mc:     %.1f,     Dc:
%.1f',mat.ksi,mat.Mcut,mat.Dcut));
    set(handles.text3,'String',sprintf('Curvative       Range:       [%.2f       -
%.2f]',min(mat.FCur),max(mat.FCur)));
    set(handles.text4,'String',sprintf('Critical   Exponent   Range:   [%.2f    -
%.2f]',min(mat.Fn),max(mat.Fn)));
end
set(handles.edit1,'String',sprintf('%.2f',get(handles.slider1,'Value')));
set(handles.edit2,'String',sprintf('%.2f',get(handles.slider2,'Value')));
set(handles.edit3,'String',sprintf('%.2f',get(handles.slider3,'Value')));
set(handles.edit4,'String',sprintf('%.2f',get(handles.slider4,'Value')));

function edit3_Callback(hObject, eventdata, handles)
% hObject    handle to edit3 (see GCBO)
% eventdata  reserved - to be defined in a future version of MATLAB
% handles    structure with handles and user data (see GUIDATA)
% Hints: get(hObject,'String') returns contents of edit3 as text
%        str2double(get(hObject,'String')) returns contents of edit3 as a double
% --- Executes during object creation, after setting all properties.
function edit3_CreateFcn(hObject, eventdata, handles)
% hObject    handle to edit3 (see GCBO)
% eventdata  reserved - to be defined in a future version of MATLAB
% handles    empty - handles not created until after all CreateFcns called

% Hint: edit controls usually have a white background on Windows.
```

```
%       See ISPC and COMPUTER.
if            ispc            &&            isequal(get(hObject,'BackgroundColor'),
get(0,'defaultUicontrolBackgroundColor'))
    set(hObject,'BackgroundColor','white');
end
function edit4_Callback(hObject, eventdata, handles)
% hObject    handle to edit4 (see GCBO)
% eventdata  reserved - to be defined in a future version of MATLAB
% handles    structure with handles and user data (see GUIDATA)

% Hints: get(hObject,'String') returns contents of edit4 as text
%        str2double(get(hObject,'String')) returns contents of edit4 as a double
% --- Executes during object creation, after setting all properties.
function edit4_CreateFcn(hObject, eventdata, handles)
% hObject    handle to edit4 (see GCBO)
% eventdata  reserved - to be defined in a future version of MATLAB
% handles    empty - handles not created until after all CreateFcns called

% Hint: edit controls usually have a white background on Windows.
%       See ISPC and COMPUTER.
if            ispc            &&            isequal(get(hObject,'BackgroundColor'),
get(0,'defaultUicontrolBackgroundColor'))
    set(hObject,'BackgroundColor','white');
end
function edit1_Callback(hObject, eventdata, handles)
% hObject    handle to edit1 (see GCBO)
% eventdata  reserved - to be defined in a future version of MATLAB
% handles    structure with handles and user data (see GUIDATA)

% Hints: get(hObject,'String') returns contents of edit1 as text
%        str2double(get(hObject,'String')) returns contents of edit1 as a double
% --- Executes during object creation, after setting all properties.
function edit1_CreateFcn(hObject, eventdata, handles)
% hObject    handle to edit1 (see GCBO)
% eventdata  reserved - to be defined in a future version of MATLAB
% handles    empty - handles not created until after all CreateFcns called

% Hint: edit controls usually have a white background on Windows.
%       See ISPC and COMPUTER.
if            ispc            &&            isequal(get(hObject,'BackgroundColor'),
get(0,'defaultUicontrolBackgroundColor'))
    set(hObject,'BackgroundColor','white');
end
function edit2_Callback(hObject, eventdata, handles)
% hObject    handle to edit2 (see GCBO)
% eventdata  reserved - to be defined in a future version of MATLAB
% handles    structure with handles and user data (see GUIDATA)

% Hints: get(hObject,'String') returns contents of edit2 as text
%        str2double(get(hObject,'String')) returns contents of edit2 as a double
% --- Executes during object creation, after setting all properties.
function edit2_CreateFcn(hObject, eventdata, handles)
% hObject    handle to edit2 (see GCBO)
% eventdata  reserved - to be defined in a future version of MATLAB
% handles    empty - handles not created until after all CreateFcns called
% Hint: edit controls usually have a white background on Windows.
%       See ISPC and COMPUTER.
if            ispc            &&            isequal(get(hObject,'BackgroundColor'),
get(0,'defaultUicontrolBackgroundColor'))
    set(hObject,'BackgroundColor','white');
end
% --- Executes on button press in pushbutton3.
function pushbutton3_Callback(hObject, eventdata, handles)
```

```
% hObject    handle to pushbutton3 (see GCBO)
% eventdata  reserved - to be defined in a future version of MATLAB
% handles    structure with handles and user data (see GUIDATA)
if isempty(handles.full_path)
    disp('PATH NOT FOUND!');
    return
end
 [pathstr,name,ext] = fileparts(handles.full_path);
[FileName,PathName] = uiputfile([name '.png'],'Save file name');
if isequal(FileName,0) || isequal(PathName,0)
    disp('User Selected Cancel')
else
    saveDataName = fullfile(PathName,FileName);
    axes(handles.axes1);
set(gcf,'PaperPositionMode','auto')
    print(saveDataName,'-dpng','-r0')
end
% saveas(gca, saveDataName);
function CalculateResults(hObject, handles)
Cr = [get(handles.slider1,'Value') get(handles.slider2,'Value')];
Nr = [get(handles.slider3,'Value') get(handles.slider4,'Value')];
R = str2double(get(handles.edit5,'String'));

if ~isempty(handles.mat)

PlotGUIRes(handles,handles.map,handles.mat.ti,handles.mat.xi,handles.mat.yi,handl
es.mat.mi,handles.mat.di,...
        handles.mat.centx,handles.mat.centy,handles.mat.FCur,handles.mat.Fn,...
        handles.mat.FTc,handles.mat.FK,handles.mat.FA,handles.mat.FR,...
       1,Cr,Nr,R,1)
   FixMapAxis(handles.axes3,hObject,handles);
end
function edit5_Callback(hObject, eventdata, handles)
% hObject    handle to edit5 (see GCBO)
% eventdata  reserved - to be defined in a future version of MATLAB
% handles    structure with handles and user data (see GUIDATA)
% Hints: get(hObject,'String') returns contents of edit5 as text
%        str2double(get(hObject,'String')) returns contents of edit5 as a double
% --- Executes during object creation, after setting all properties.
function edit5_CreateFcn(hObject, eventdata, handles)
% hObject    handle to edit5 (see GCBO)
% eventdata  reserved - to be defined in a future version of MATLAB
% handles    empty - handles not created until after all CreateFcns called
% Hint: edit controls usually have a white background on Windows.
%       See ISPC and COMPUTER.
if           ispc           &&           isequal(get(hObject,'BackgroundColor'),
get(0,'defaultUicontrolBackgroundColor'))
    set(hObject,'BackgroundColor','white');
end
% --- Executes on button press in pushbutton4.
function pushbutton4_Callback(hObject, eventdata, handles)
% hObject    handle to pushbutton4 (see GCBO)
% eventdata  reserved - to be defined in a future version of MATLAB
% handles    structure with handles and user data (see GUIDATA)
CalculateResults(hObject, handles);
% --- Executes on button press in pushbutton5.
function pushbutton5_Callback(hObject, eventdata, handles)
% hObject    handle to pushbutton5 (see GCBO)
% eventdata  reserved - to be defined in a future version of MATLAB
% handles    structure with handles and user data (see GUIDATA)
```

```
%FindEQs.m
function [T,X,Y,M,D]=FindEQs(t,x,y,m,d,condition)
r = find(condition);
T = t(r); X = x(r); Y = y(r); M = m(r); D = d(r);
```

```
%finsound.m
%play a sound
amp=10 ; fs=700; duration=2;freq=50;
values=0:1/fs:duration;
a=amp*sin(2*pi* freq*values);
sound(a)
```

```
%FixMapAxis.m

function FixMapAxis(ax,hObject,handles)

idx = find (handles.map.coastline(:,1)~=Inf);x = handles.map.coastline(:,1);
y = handles.map.coastline(:,2);
axis(ax,[ min(x(idx))-1 ...
    max(x(idx))+2 ...
    min(y(idx))-2 ...
    max(y(idx))+1])
guidata(hObject, handles);
```

```
%LoadEqs.m
function [t,x,y,m,d] = LoadEqs(tt,xx,yy,mm,dd,date_from,date_to,cut_off)
from = datenum(date_from); to = datenum(date_to); N = length(tt);
% calculate length
k = 0;
for i=1:N
    if tt(i)>=from && tt(i)<=to && mm(i)>=cut_off
       k = k+1;
    end
end

% fill arrays
t = zeros(1,k); x = zeros(1,k); y = zeros(1,k);
m = zeros(1,k); d = zeros(1,k);

k=1;
for i=1:N
    if tt(i)>=from && tt(i)<=to && mm(i)>=cut_off
       t(k) = tt(i); x(k) = xx(i); y(k) = yy(i);
       m(k) = mm(i); d(k) = dd(i); k = k+1;
    end
end
fprintf('Loaded: %d events\n',length(m)
```

```
%PlotEqs.m
function PlotEqs(chart,x,y,m,d)
N = length(m);
fprintf('Ploting %d Earthquakes...\n',N)
cl1 = 'b';
h1                                                                                =
plot(chart,x,y,'o','MarkerSize',3,'MarkerEdgeColor',cl1,'MarkerFaceColor',cl1);
```

```
box on
drawnow
```

%PlotGUIRes.m

```
function
PlotGUIRes(handles,map,t,x,y,m,d,centx,centy,FCur,Fn,FTc,FK,FA,FR,defmodel,Cr,Nr,
SquareR,plottype)
% Get the original full catalog
c = handles.mat.catalog;
[ti,xi,yi,mi,di]   =   FindEQs(c.t,c.x,c.y,c.m,c.d,c.t>=max(t)   &   c.m>=5.8     &
c.t<=max(t)+100); % c.t<=max(t)+8
% Set filter
Rth = SquareR;
idx1  =  find(FCur>=Cr(1)  &  FCur<=Cr(2)  &  FR>=Rth);idx2  =  find(Fn>=Nr(1)  &
Fn<=Nr(2) & FR>=Rth);
idx3 = find(Fn>=Nr(1) & Fn<=Nr(2) & FCur>=Cr(1) & FCur<=Cr(2) & FR>=Rth);

% Set axis handles
ax1 = handles.axes1; ax2 = handles.axes2; ax3 = handles.axes3;

% set point size
squaresize = 55;

% Plot results
if plottype==1

    scatter(ax1,centx,centy,squaresize,FCur,'filled','s')
    hold(ax1,'on');
    PlotMap(ax1,map);
    plot(ax1,xi,yi,'kp','Markersize',16,'MarkerFaceColor','r');
    title(ax1,sprintf('Oiginal C(R_{c})\\in [%.2f-%.2f]',min(FCur),max(FCur)));
    colorbar('peer',ax1);
    hold(ax1,'off');
    FixMapAxis(ax1,handles)

    scatter(ax2,centx,centy,squaresize,Fn,'filled','s');
    hold(ax2,'on');
    PlotMap(ax2,map);
    plot(ax2,xi,yi,'kp','Markersize',16,'MarkerFaceColor','r');
    title(ax2,sprintf('Original n(R_{c})\\in [%.2f-%.2f] ',min(Fn),max(Fn)));
    colorbar('peer',ax2);
    hold(ax2,'off');
    FixMapAxis(ax2,handles)

    scatter(ax3,centx(idx3),centy(idx3),squaresize,Fn(idx3),'filled','s');
    hold(ax3,'on');
    PlotMap(ax3,map);
    h = plot(ax3,xi,yi,'kp','Markersize',16,'MarkerFaceColor','r');
    title(ax3,sprintf('Filtered C(R_{c})\\in [%.2f-%.2f],n(R_{c})\\in [%.2f-%.2f]
',Cr(1),Cr(2),Nr(1),Nr(2)));
    legend(ax3,h,sprintf('%s -- %s',datestr(min(ti)),datestr(max(ti))))
    colorbar('peer',ax3);
    hold(ax3,'off');
    FixMapAxis(ax3,handles)
end

function FixMapAxis(ax,handles)
idx = find (handles.map.coastline(:,1)~=Inf);
x = handles.map.coastline(:,1);y = handles.map.coastline(:,2);
axis(ax,[ min(x(idx))-2 ...
    max(x(idx))+3 ...
```

```
    min(y(idx))-3 ...
    max(y(idx))+2])
```

%PlotMap.m

```
function PlotMap(axis,map)
plot(axis,map.coastline(:,1),map.coastline(:,2),'k')
grid(axis,'on')
box(axis,'on')
```